

Correlating magnetic and structural properties of full Heusler Co_2FeSi films

Irene Azaceta

PhD

University of York

Physics

December 2021

Abstract

The half-metallic properties of Heusler alloys make them ideal spin injectors for numerous spintronic applications. In particular, $\text{Co}_2\text{FeAl}_{1-x}\text{Si}_x$ alloys are very attractive for current-perpendicular-to-plane giant magnetoresistance (CPP-GMR) [Fur13; Li18], tunnel magnetoresistance (TMR) [Oka05; Tez06] and in lateral spin-valve (LSV) devices [Kim12; Ham12; Oki17] due to their high spin polarisation (SP) and high Curie temperature (T_c). However, half-metallicity can be significantly reduced due to structural disorder, defects or interfacial effects [Cui14; Ned16a].

The work in this thesis had two main objectives. The first was building a bespoke molecular beam epitaxy (MBE) system for the growth of $\text{Co}_2\text{FeAl}_{1-x}\text{Si}_x$ Heusler films. The second, was optimizing the growth conditions for Co_2FeSi (CFS) thin films on technologically relevant substrates, namely Si(111) and MgO(001). With that aim, the effect of stoichiometry and growth temperature on the structural and magnetic properties of CFS has been studied. The CFS films grown in this work exhibit properties comparable to those reported in the literature for high quality Heusler films used in spintronic devices. Lastly, the effect of a NiO overlayer on the magnetocrystalline anisotropy (MCA) of CFS is discussed.

Non-annealed CFS films are partially $L2_1$ ordered when grown on Si(111). However, even at temperatures $< 130^\circ\text{C}$, interfacial effects switch the magnetic easy axis (EA) from $[10\bar{1}]$ to $[1\bar{1}0]$ in CFS/Si(111). HAADF-STEM images suggest that the CFS/Si interface has suffered some changes although further studies are required to characterize them. Contrary to CFS/Si(111), the growth temperature has to be increased to 350°C for CFS films to show some degree of $L2_1$ on MgO(001). Whereas uncapped CFS/MgO(001) exhibits a cubic MCA with $K_c > 0$, NiO-capped CFS/MgO(001) samples have a $K_c < 0$, which brings the EA along $\langle 110 \rangle$. To the author's knowledge this change in K_c has not been previously reported in CFS films and should be explored in more detail.

Contents

Abstract	2
List of Tables	6
List of Figures	7
Acknowledgements	19
Author's declaration	20
1 Motivation and structure of the thesis	21
1.1 Motivation	21
1.2 Structure of the thesis	23
2 Theoretical background	25
2.1 Energy contributions of ferromagnetism	25
2.1.1 Exchange energy	25
2.1.2 Magnetocrystalline anisotropy	26
2.1.3 Magnetostatic energy and shape anisotropy	29
2.1.4 The magnetoelastic energy	30
2.1.5 The Zeeman energy	31
2.2 Magnetization dynamics	31
2.3 Spin currents and magnons	33
2.4 Spintronics	38
2.4.1 Spin-orbit coupling effects and thermal effects in spintronics	40
2.5 Generation of spin currents	42
2.6 Half-metals	44
2.7 Heusler compounds	46
2.7.1 Atomic structure of Heusler alloys	46

2.7.2	Chemical disorder and half-metallicity in Heusler alloys	49
3	Principles and design of a MBE system for the growth of Heusler alloys	53
3.1	Introduction	53
3.2	Vacuum generation	54
3.3	Growth modes	60
3.4	Molecular beam epitaxy (MBE)	63
3.5	Design of an MBE system for the growth of $\text{Co}_2\text{FeAl}_{1-x}\text{Si}_x$ films	65
3.5.1	Sample manipulator and sample holder	67
3.5.2	Evaporation sources	69
3.6	In-situ characterization. Rate monitors and RHEED	71
3.6.1	Quartz crystal microbalance (QCM)	72
3.6.2	Reflection High Energy Electron Diffraction (RHEED)	73
4	Ex-situ characterization techniques	76
4.1	X-ray diffraction. Bragg's law and Laue formulation	76
4.1.1	2θ - ω scans	80
4.1.2	X-ray reflectivity (XRR)	83
4.2	Electron microscopy	87
4.2.1	Optics and lenses in TEM	88
4.2.2	Imaging and diffraction in TEM	91
4.2.3	STEM high angle annular dark field imaging (STEM-HAADF)	93
4.2.4	STEM spectroscopy: EELS and EDS	95
4.2.5	Focused Ion Beam (FIB) for cross-sectional specimen preparation	98
4.3	Magnetic characterization	102
4.3.1	Ferromagnetic resonance spectroscopy (FMR)	102
4.3.2	Vibrating sample magnetometry (VSM)	108
5	Growth and characterization of CFS films on Si(111)	110
5.1	Introduction	110
5.2	MBE growth of CFS films	111
5.3	Structural properties of CFS films grown on Si(111)	114
5.3.1	X-ray diffraction and reflectivity measurements	115
5.3.2	Cross-sectional TEM and STEM measurements	125
5.4	Magnetic properties of CFS films grown on Si(111)	132
5.4.1	VSM measurements	132

5.4.2	FMR measurements	134
5.5	Summary and conclusions	144
6	Growth and characterization of CFS films on MgO(001)	145
6.1	Introduction	145
6.2	Optimization of the chemical composition of CFS films on MgO(001)	146
6.3	MBE growth of CFS films at different growth temperatures	154
6.3.1	Structural characterization of CFS/MgO(001) grown at different temperatures	155
6.3.2	Magnetic characterization of CFS/MgO(001) grown at different temperatures	164
6.4	NiO capped-CFS films	171
6.5	Summary and conclusions	178
7	Conclusions and Outlook	181
7.1	Conclusions	181
7.1.1	CFS/Si(111)	181
7.1.2	CFS/MgO(001)	182
7.1.3	NiO[t]/Fe[1]/CFS/MgO(001)	183
7.2	Future work	183
7.2.1	MBE growth and system development	183
7.2.2	CFS/Si(111)	184
7.2.3	CFS/MgO(001)	185
7.2.4	NiO[t]/Fe[1]/CFS/MgO(001)	185
	Abbreviations	185
	Bibliography	188

List of Tables

2.1	General formula and structures of differently ordered full-Heusler compounds. . .	49
2.2	Magnetic properties of some Co_2XY Heusler alloys, including the compound studied in this thesis, CFS.	52
3.1	Comparison of different epitaxial technologies from [KC01]. MOCVD is one of the most competitive alternatives to MBE. CVD techniques operate at high pressure and are more affordable and advantageous for mass-production. However, they are not as precise as MBE in controlling the composition and thickness of the films.	64
4.1	Steps used to thin the lamella to electron transparent thickness. Typical stage angles and the Ga^+ voltage and current used for each angle are shown. The thickness of the lamella after the thinning step is also shown in the last column.	102
5.1	Co and Fe concentrations in at% measured by EDS in the $\text{Co}_x\text{Fe}_{1-x}$ alloy films, and the rates used for their growth.	114
5.2	List of allowed reflections for each possible structural phase of CFS.	115
5.3	Co, Fe and Si concentrations in at% measured by EDS in the Co_2FeSi film extracted from the linescan in Fig. 5.15a (first row) and the spectra in Fig. 5.15b (second and third rows).	129
6.1	Co Fe and Si concentrations in at% measured by EDS in the CFS/MgO(001) samples for different T_{Si}	154
6.2	Magnetic parameters extracted from VSM and FMR experiments for the CFS films grown on MgO(001) at $T_B < 130^\circ\text{C}$, 350°C and 550°C	170
6.3	Magnetic parameters measured with VSM and FMR on NiO [t_{NiO}]/Fe [1]/CFS [25]/MgO(001) samples with $t_{\text{NiO}} = 3\text{nm}$, 5nm and 10nm	177

List of Figures

2.1	MCA energy density of a cubic crystal with (a) a positive K_c and (b) a negative K_c	27
2.2	New coordinate system $\{x', y'$ and $z'\}$ in red, with the [111] direction normal to the film plane.	29
2.3	Formation of magnetic domains in order to minimize the dipolar contribution. (a) corresponds to a single-domain state. Here, the exchange energy is minimum but the dipolar energy is the largest due to the big dipolar fields. In (b) the system splits into two domains reducing the magnetostatic contribution at the expense of creating a domain wall. Finally, in (c) the demagnetizing fields are cancelled minimizing the dipolar energy but introducing several domain walls in a Landau structure.	30
2.4	Undamped (a) and damped (b) motion of the magnetization vector around the effective field \vec{H}_{eff} representing eq. (2.20) without and with the damping term respectively.	32
2.5	Schematic representation of the DOS of: (a) the 3d spin sub-bands in a FM shifted by the exchange interaction energy; (b) the s sub-bands in a NM metal, where there is no spin accumulation; and (c) the s sub-bands in a NM, near the FM/NM interface, where there is spin accumulation (see section § 2.5).	35
2.6	(a) Classical picture of the ground state in a FM where all the spins are aligned due to exchange interactions.(b) A possible excited state where one of the spins is reversed. (c) An alternative form of excitation of much lower energy, called magnons, where the spins precess with a constant phase difference between successive spins separated by the interatomic distance a	38

2.7	Representation of a simple SV device consisting of a FM (pinned)/NM/FM (free) structure in: (a) parallel configuration, where the scattering is minimized and hence, the device shows a low resistance; and (b) antiparallel configuration where the device shows a high resistance.	39
2.8	Representation of: (a) the SHE effect where a charge current leads to the generation of a transverse pure spin current in the NM with high SOC; and (b) the iSHE effect where the injection of a pure spin current gives rise to a charge accumulation and hence, a voltage across the NM.	41
2.9	Typical geometry of a so-called longitudinal SSE experiment where a temperature gradient ∇T creates a spin current in the FM which is injected into the HM (Pt). The thermally induced spin accumulation is measured on the Pt as an inverse spin Hall signal, V_{iSHE}	42
2.10	Spin accumulation μ_s and polarization of the spin-current SP in a FM/NM interface when the corresponding boundary conditions are introduced in eq. (2.33). As one can see, near the FM/NM interface, the polarization of the spin current is reduced nearly by half at the FM. This occurs due to the conductivity mismatch between the two materials. In a FM/SC interface the polarization is reduced even more, making spin-injection into the SC very inefficient.	43
2.11	DOS of the d and s sub-bands of a FM (a) and a HMF (b) where the spin-up channel is conductive but the spin-down channel is insulating. Hence, the HMF is 100% spin-polarized at the Fermi level.	45
2.12	Structure of the fully L2 ₁ ordered CFS alloy (a) and CFAS alloy (b), with the blue, red, green and grey sites representing the location of the Co, Fe, Si and Al atomic species. This and the subsequent figures in this section have been drawn with VESTA.	47
2.13	Repeat unit of CFS: (a) along the [001] growth direction and [100] projection; (b) along the [001] growth direction and [1 $\bar{1}$ 0] projection; (c) along the [111] growth direction and [1 $\bar{1}$ 0] projection; (d) along the [111] growth direction and [11 $\bar{2}$] projection. Colour coding is the same as in Fig. 2.12.	48
2.14	Possible disordered structures of the CFS alloy. (a) shows the Y-Z disorder, (b) shows the X-Y disorder and (c) shows the X-Z disorder. Colour coding follows the Fig. 2.12.	50

2.15	Schematic density of states of CFS with an energy gap Δ_{\downarrow} in the minority-spin band (\downarrow) and metallic band structure in the majority-spin band (\uparrow) when: (a) $T=0K$ and (b) $T \neq 0$. The Fermi-level is positioned very close to the bottom of the conduction band, which makes half-metallicity unstable against temperature increments.	51
3.1	Diagram showing physical vapour deposition (PVD) methods to grow thin films based on the working pressure and the modes of material transport involved. Evaporation takes place at HV pressures whereas sputtering usually operates at 10^{-1} to 10^{-3} mbar because it requires a constant feed of Ar to activate the plasma required to sputter the materials from the source. MBE growth is an advanced form of evaporation deposition which operates at UHV. The figure has been adapted from [Cam15].	55
3.2	(a) Working principle of a rotary pump and (b) pumping mechanism of a scroll pump. One of the scrolls is fixed whereas the other orbits eccentrically trapping pockets of gas between them that are removed through the outlet. The figures were taken from [Hit] and [Ide] respectively.	56
3.3	Representation of a turbomolecular pump that ejects the gas particles away using a set of rapidly moving rotors (in blue) interleaved with non-moving stators (in green).	57
3.4	(a) Schematic diagram of a sputter ion pump and (b) its working principle. . . .	58
3.5	Circuitry of a Pirani Gauge.	59
3.6	Illustration of an ion gauge.	59
3.7	(a) Typical RGA scan taken during the outgassing procedure of the Fe source at $1500^{\circ}C$ with an empty Al_2O_3 crucible (prior to loading the material). The scan shows high partial pressures at $m/e = 2, 14$ and 28 ; (b) time evolution of the $m/e = 12, 14$ and 28 partial pressures as the source was heated. The clear correlation between the pressure rise of $m/e = 14$ and $m/e = 28$ indicates release of N_2 . This was eventually attributed to the decomposition of the PBN insulating rings caused by overheating of the crucible.	60
3.8	Schematic representation of elemental processes involved in film growth on a solid substrate. Adapted from [Lüt01].	60
3.9	Depiction of the three possible growth modes: (a) island growth, (b) layer by layer growth and (c) mixed growth.	62

3.10	Diagram of the forces caused by the surface tension of a film island deposited in the substrate.	62
3.11	Illustration of an electron beam heated source.	65
3.12	(a) side view and (b) top view blueprints of the MBE chamber designed for this thesis.	66
3.13	Left (a) and right (b) side views of the MBE system, including the growth chamber, the FEL chamber and the transfer arm. The working principle of all the main components in the growth chamber has been described throughout this chapter.	67
3.14	(a) Vacgen HPT-WX manipulator, (b) the different elements of the manipulator below the flange and (c) custom-made heating stage and sample holder which withstand substrate temperatures up to 1100°C.	68
3.15	Temperature measured by the stage thermocouple (blue dots) and the setpoint temperature (red line) inputted into the labview program. In the inset, the output heating current has been plotted.	69
3.16	(a) Illustration of a effusion cell with a standard Ta heater. Insulating PBN ceramic parts are fully shielded by tantalum plates to prevent outgassing during operation. (b) Top view of the Fe HTEZ cell used in this project.	70
3.17	(a) Side view and (b) top view of the SUSI showing the different Si elements in the source.	70
3.18	(a) Photograph of the metal MBE system built for the growth of $\text{Co}_2\text{FeAl}_{1-x}\text{Si}_x$ films and which was used to grow the CFS films in this project. Note that the photograph was taken before the system was connected to the oxide chamber. (b) RGA scan showing that H_2 is the only gas present in the chamber after baking; the IG was measuring 3×10^{-10} mbar when the scan was performed. . .	71
3.19	Illustration of the working principle of the quartz crystal microbalance.	72
3.20	Schematic representation of the RHEED set-up in the MBE system designed for $\text{Co}_2\text{FeAl}_{1-x}\text{Si}_x$ growth. Due to the relatively large distance between the electron gun and the sample, and between the sample and the screen, RHEED is very flexible in relation to sample conditions and experiments can be performed in-situ during sample growth.	73
3.21	(a) Working principle of RHEED, a diffraction spot is formed when a rods of the reciprocal lattice intersects the Ewald sphere; Schematic RHEED patterns for (b) a flat single-crystal surface, (c) a rough single-crystal surface and (d) a polycrystalline surface.	74

3.22	Experimental RHEED patterns from (a) a MgO(001) surface along [010], (b) a Si(111) surface along $[11\bar{2}]$ and (c) a STO(001) surface along [010] after cleaning.	75
4.1	X-ray diffraction by a periodic lattice of atoms spaced a distance d apart when an x-ray beam impinges at an angle $\theta_{in} = \theta$.	77
4.2	Path difference between beams scattered by two scatterers separated by \bar{d} .	78
4.3	(a) Direct lattice and (b) reciprocal lattice of a simple cubic crystal. The Ewald sphere is shown for an incident radiation \vec{k}_{in} with wavelength λ . The orientation of the incident beam is such that the (100) diffraction occurs and the reciprocal lattice point 100 is intersected by the Ewald sphere.	80
4.4	Geometry of a symmetric $2\theta - \omega$ scan used to to measure the out of plane momentum transfer, \vec{G} in the CFS films. The measurements were performed with a Rigaku SmartLab diffractometer using a Cu K_α source.	81
4.5	Basic features of a XRD peak fitted by a Voigt distribution, which is the convolution of a Gaussian and a Lorentzian distribution with linewidths Δ_G and Δ_L , respectively. Δ_G is related to the instrumental broadening, whereas Δ_L has to do with the intrinsic broadening.	82
4.6	Reflectivity profiles simulated with GenX for (a): a 20nm-thick Fe film in blue and a 20nm-thick SiO ₂ film in green; and (b) Fe films with: t=20nm and $\sigma_{subs}^q = 0.5\text{nm}$ in blue, t=40nm and $\sigma_{subs}^q = 0.5\text{nm}$ in red, and t=20nm and $\sigma_{subs}^q = 1.0\text{nm}$ in black.	85
4.7	Schematic of a layered material and nomenclature used in this section.	86
4.8	The different signals that can take place after an incident beam of electrons has interacted with the specimen. The thinner the specimen, the more electrons will pass through it.	88
4.9	Schematic representation of the electromagnetic lenses, apertures and detectors in (a) TEM and (b) STEM mode.	89
4.10	(a) Effect of the spherical aberration in an electron lens, where electrons at different angles to the optic axis are brought to a focus at different points; (b) The effect of correcting the spherical aberration which brings all electrons into focus at the same point. Here C_s is the spherical aberration constant which relates to the radius of the disk and so, the smaller C_s is the better.	90
4.11	Simplified ray diagrams of a TEM in (a) imaging and (b) diffraction mode. Taken from [FH12].	92

4.12	Different imaging modes in a conventional TEM; the user can switch between the modes by changing the position of the objective aperture at the back focal plane.	92
4.13	Angular range of the forward scattered electrons which are collected by the different detectors in STEM.	94
4.14	Some of the interaction processes between a high energy electron and an atom that generate x-rays for spectroscopy. Taken from [FH12].	96
4.15	Plan-view EDS spectrum taken for a CFS/MgO(001) sample. The spectrum was taken for an accelerating voltage of 15kV and a 3nA probe current in the JEOL-7800 SEM system. The atomic concentration of the substrate elements (Mg and O) and the film elements (Fe, Co and Si) are shown in the light-blue box on the top-right corner.	97
4.16	(a) Schematics of a combined FIB-SEM system and (b) FEI Nova 200 NanoLab system used for the preparation of lamellas in this thesis.	99
4.17	Images taken during the preparation of a FIB-lamella for cross-sectional TEM. .	100
4.18	Illustration of the FMR effect where a magnetic sample is subjected to a bias field \vec{H} and a transverse RF perturbation \vec{h}	103
4.19	Representation of the magnetization and the magnetic field in spherical coordinates.	105
4.20	FMR set-up using a VNA to measure the RF absorption through a coplanar waveguide.	106
4.21	ΔS_{21} signal for a CFS film measured at an RF frequency of 10GHz; the ferromagnetic resonance is characterized by the resonant field H_r and the linewidth ΔH	107
4.22	(a) Schematic representation of a VSM measurement, (b) sample geometry in in-plane configuration and (c) magnetic hysteresis loop showing the saturation magnetization M_s , the remanent magnetization M_r and the coercive field H_c . . .	108
5.1	(a) X-ray reflectivity curves for a Si, Fe and Co films; and (b) rates as a function of the source temperature for the Si, Fe and Co evaporators.	112
5.2	(a) Ferromagnetic hysteresis loops for the MBE-grown $\text{Co}_x\text{Fe}_{1-x}$ films measured by VSM. (b) M_s values extracted as a function of the concentration of Co, x ; the dashed grey line is the Slater-Pauling curve for bulk $\text{Co}_x\text{Fe}_{1-x}$ alloys shown as a reference from [Boz93].	113

5.3	RHEED patterns of (a) the Si(111) surface and (b) the CFS(111) surface taken along the $[11\bar{2}]$ azimuth; suggesting epitaxial growth of CFS on Si(111).	115
5.4	Out of plane $2\theta - \omega$ scan for the $T_{Si} = 1040^\circ\text{C}$ sample with $\chi = 0^\circ$; which reveals the CFS(hhh) reflections with $h = 1, 2$ and 4.	116
5.5	(a) $2\theta - \omega$ scan for $T_{Si} = 1040^\circ\text{C}$ aligned to the CFS(200) peak, with the goniometer at $\chi = 54.74^\circ$ and $\phi = 90^\circ$; (b) ϕ scan aligned to CFS(200) (in red), CFS(400) (in black) and Si(400) (in blue) showing the twinning of the film. . . .	117
5.6	$2\theta - \omega$ scan aligned to CFS($\bar{1}11$) for $T_{Si} = 1040^\circ\text{C}$	118
5.7	(a) x-ray reflectivity measurements (coloured dots) and fits (red lines) for the CFS/Si(111) samples with varying T_{Si} ; (b) thickness of the CFS layers extracted from the fits; (c) surface (black triangles) and interface (blue squares) roughness; and (d) the three-layer model used to fit the data. The density of CoFe_2O_4 and the substrate were set to $\rho_{\text{CoFe}_2\text{O}_4} = 0.0137 \text{ f.u./\AA}^3$ and $\rho_{\text{Si}} = 0.050 \text{ f.u./\AA}^3$ respectively.	119
5.8	Densities of the CFS layer extracted from the fits with: (blue squares) the density of the CoSi_2 layer fixed, and (red circles) the density of the CoSi_2 layer as a fit parameter. The dashed line corresponds to the density of bulk CFS, $\rho_{\text{CFS}} = 0.0222 \text{ f.u./\AA}^3$	120
5.9	(a) $2\theta - \omega$ scans (coloured dots) and fits (red lines) around the CFS(444) reflection for the CFS/Si(111) samples with varying T_{Si} ; (b) the out of plane lattice constant calculated from the fits using Bragg's law; and (c) the FWHM of the CFS(444) peak.	121
5.10	$2\theta - \omega$ scans (coloured dots) and fits to a Voigt function (red lines) of (a) the CFS (111) reflection and (b) the CFS (222) reflection; (c) the integrated intensities extracted from the fits in a and b; (d) ratios of the integrated intensities representative of the B2 ordering in blue, and the $L2_1$ ordering in red. The inset shows the integrated intensities of the structural peak from the fits in Fig. 5.9a.	123
5.11	(a) FWHM of the CFS(222) (blue squares) and CFS(111) (red circles) diffraction peaks and (b) Lorentzian linewidth of CFS(222).	124
5.12	Micrographs showing the cross-section of $T_{Si} = 1035^\circ\text{C}$ prepared along $[1\bar{1}0]$. (a) is an overview of the lamella showing its different layers and (b) reveals the granular nature of the CFS.	125

5.13	(a) Selected-area-diffraction pattern showing the diffraction spots for CFS and Si; (b) and (c) are the diffraction patterns of CFS $[1\bar{1}0]$ and Si $[\bar{1}10]$ simulated using the software Jems. the DPs perfectly match our observations. The repeating unit of the CFS DP is the red rectangle and the repeating unit of the Si DP is the gold rhombus.	126
5.14	Atomic level HAADF-STEM images displaying the atomic stackings characteristic of (a) the L2 ₁ structure and (d) the B2 structure; (b) and (e) are the intensity profiles of the boxed areas in a and d respectively. The structural models are shown in (c) for L2 ₁ and (f) for B2. The specimen preparation along the $[1-10]$ axis allows the distinction between the structures very clearly. These images were taken from $T_{Si} = 1035^\circ\text{C}$	127
5.15	(a) EDS linescan taken across the CFS for $T_{Si} = 1035^\circ\text{C}$ with a spatial resolution of $< 1\text{nm}$; and (b) EDS spectra from two different areas in the same specimen. The micrographs in (a) and (b) are HAADF and TEM images of the regions from which the linescan and the spectra were taken respectively.	128
5.16	Cross-section of the CFS film for $T_{Si} = 1045^\circ\text{C}$ revealing the two types of ordered structures within the film, the L2 ₁ order in blue and the B2 order in red.	129
5.17	(a) HAADF-STEM micrograph of $T_{Si} = 1025^\circ\text{C}$, also showing the two types of ordering; (b) and (c) are the FFT-s of the areas marked in blue and red respectively, which match the diffraction patterns of a L2 ₁ and a B2 structure respectively. The FFTs were performed with the Digital Micrograph software.	130
5.18	(a) $[1\bar{1}0]$ view of the CFS/Si interface for $T_{Si} = 1025^\circ\text{C}$, and (b) the enlarged image of the region of interest in a; (c) is the intensity profile along the line in (b).	131
5.19	CFS/Si interface of $T_{Si} = 1040^\circ\text{C}$	132
5.20	Magnetic hysteresis loops along the $[1\bar{1}0]$ (empty blue rhombus) and $[11\bar{2}]$ (red dots) for the CFS films with increasing Si content: (a) $T_{Si} = 1015^\circ\text{C}$, (b) $T_{Si} = 1025^\circ\text{C}$, (c) $T_{Si} = 1035^\circ\text{C}$, (d) $T_{Si} = 1040^\circ\text{C}$, (e) $T_{Si} = 1045^\circ\text{C}$ and (f) $T_{Si} = 1050^\circ\text{C}$	133
5.21	M_s (blue squares) and H_c (red circles) extracted from the hysteresis loops in Fig. 5.20.	134
5.22	FMR frequency-field maps for: (a) $T_{Si} = 1015^\circ\text{C}$, (b) $T_{Si} = 1025^\circ\text{C}$, (c) $T_{Si} = 1040^\circ\text{C}$, (d) $T_{Si} = 1045^\circ\text{C}$, (e) $T_{Si} = 1050^\circ\text{C}$ and (f) $T_{Si} = 1055^\circ\text{C}$	135
5.23	FMR linescans (blue dots) for $T_{Si} = 1025^\circ\text{C}$ for (a) $\phi = +60^\circ$, (b) $\phi = 0^\circ$ and (c) $\phi = -60^\circ$; and corresponding fits (red lines) to an asymmetric Lorentzian, allowing the extraction of H_r as a function of ϕ	136

5.24	Azimuthal H_r plots for (a) $T_{Si} = 1015^\circ\text{C}$, (b) $T_{Si} = 1035^\circ\text{C}$, (c) $T_{Si} = 1045^\circ\text{C}$ and (d) $T_{Si} = 1055^\circ\text{C}$; $\phi = 0^\circ$ corresponds to $[1\bar{1}0]$ and $\phi = 90^\circ$ to the $[11\bar{2}]$ direction.	137
5.25	Kittel curves measured at the easy axis, $\phi = 60^\circ$ (blue dots), and the hard axis, $\phi = 330^\circ$ (black triangles), for $T_{Si} = 1015^\circ\text{C}$. The red lines are the fits to eq. (4.33) with shared parameters M_{eff}, K_u, K_c and γ	139
5.26	(a) Fitting parameter M_{eff} extracted from the Kittel curves (black squares) compared to the M_s values measured with the VSM (grey dashed line); perpendicular anisotropy constant K_\perp , proportional to the difference of M_s and M_{eff} , is shown in the inset. (b) Uniaxial anisotropy constant K_u as a function of T_{Si}	141
5.27	(a) ΔH as a function of the RF frequency and the corresponding linear fits for $T_{Si} = 1015^\circ\text{C}$ (grey), $T_{Si} = 1025^\circ\text{C}$ (red), $T_{Si} = 1040^\circ\text{C}$ (yellow), $T_{Si} = 1045^\circ\text{C}$ (green) and $T_{Si} = 1055^\circ\text{C}$ (purple); (b) Gilbert damping parameter and $\Delta H(0)$ extracted from the linear fits in (a).	142
5.28	FMR linescan measured for $T_{Si} = 1050^\circ$ (in blue) showing the two resonances present in this sample. The red line is the fit to the asymmetric Lorentzian which returns a bigger value for ΔH due to the proximity of the second adsorption dip. This effect was worst at low RF frequencies preventing the extraction of reliable linewidths where the behaviour is most linear.	143
6.1	(a) XRR measurements on the CFS/MgO(001) samples for $T_{Si} = 1035^\circ\text{C}$ (yellow), $T_{Si} = 1040^\circ\text{C}$ (green), $T_{Si} = 1045^\circ\text{C}$ (blue) and $T_{Si} = 1050^\circ\text{C}$ (grey), and the corresponding fits in red; (b) thickness of the CFS layers extracted from the GenX fits in (a); (c) roughness of the oxide layer (i.e. the surface) (black triangles) and roughness of the bottom CFS/MgO interface (blue squares); (d) 2-layer model to which the data was fitted.	148
6.2	X-ray scattering length density profile of CFS/MgO(001) for $T_{Si} = 1035^\circ\text{C}$ (a), $T_{Si} = 1040^\circ\text{C}$ (b), $T_{Si} = 1045^\circ\text{C}$ (c) and $T_{Si} = 1050^\circ\text{C}$ (d). The greyed areas define bulk-like MgO and air regions, whereas the gradient areas represent the CFS/MgO interface and the air/CFS surface.	149
6.3	Density of the CFS layers extracted from the fits in Fig. 6.1a versus T_{Si} for the CFS/MgO(001) samples (blue squares) and the CFS/Si(111) samples (grey dashed line).	150
6.4	$2\theta - \omega$ measurements for $T_{Si} = 1035^\circ\text{C}$ (yellow), $T_{Si} = 1040^\circ\text{C}$ (green), $T_{Si} = 1045^\circ\text{C}$ (blue) and $T_{Si} = 1050^\circ\text{C}$ (grey), aligned to MgO(002).	151

6.5	Voigt fits of: (a-d) the CFS(004) peak, and (e-h) the CFS(002) peak for $T_{Si} = 1035^\circ\text{C}$ (pink), $T_{Si} = 1040^\circ\text{C}$ (orange), $T_{Si} = 1045^\circ\text{C}$ (blue) and $T_{Si} = 1050^\circ\text{C}$ (green).	152
6.6	(a) Integrated intensities extracted from the Voigt fits in Fig. 6.5 for CFS(002) (blue squares) and CFS(004) (red circles); (b) out-of plane lattice constants extracted from the CFS(004) reflection; and (c) Lorentzian width of CFS(002).	153
6.7	RHEED images for: (a) the MgO(001) surface along the [010] direction before the growth at RT of CFS; the CFS(001) surface after the growth at (b) $T_B < 130^\circ\text{C}$, (c) $T_B = 350^\circ\text{C}$ and (d) $T_B = 550^\circ\text{C}$ along the $[\bar{1}10]$ azimuth.	156
6.8	(a) XRR scans for the CFS/MgO(001) samples grown at RT (yellow), $T_B = 350^\circ\text{C}$ (green) and $T_B = 550^\circ\text{C}$ (blue); (b) thickness of the CFS layers extracted from the fits to the XRR curves; (c) roughness of the surface (black triangles) and the CFS/MgO interface (blue squares); (d) 2-layer model used to fit the data with GenX.	157
6.9	X-ray scattering length density profile of CFS/MgO(001) grown at (a) $T_B < 130^\circ\text{C}$, (b) $T_B = 350^\circ\text{C}$ and (c) $T_B = 550^\circ\text{C}$. The greyed areas define bulk-like MgO and air regions, and the gradient areas represent the CFS/MgO interface and the air/CoFe ₂ O ₄ surface.	158
6.10	Out-of-plane $2\theta - \omega$ scans for $T_B < 130^\circ\text{C}$ (yellow), $T_B = 350^\circ\text{C}$ (green) and $T_B = 550^\circ\text{C}$ (blue).	158
6.11	(a) CFS(002) and (b) CFS(004) diffraction peaks and the corresponding Voigt fits for the three growth temperatures using the same colour coding in Fig. 6.10; integrated intensities (c), peak positions (d), and Lorentzian linewidth for CFS(002) (blue squares) and CFS(004) (red circles) respectively.	159
6.12	ϕ scans aligned to CFS(111) for $T_B < 130^\circ\text{C}$ (a), $T_B = 350^\circ\text{C}$ (b) and $T_B = 550^\circ\text{C}$ (c) revealing an enhancement of the L2 ₁ ordering in (b) and (c); (d) ϕ scan aligned to MgO (0 $\bar{2}2$) verifying the CFS(1 $\bar{1}0$) MgO(100) epitaxial relationship; and (e) illustration of the 45° rotation of the film with respect to the substrate, with a mismatch between the lattice constant of CFS (5.65Å) and the diagonal length of the lattice constant of MgO ($\sqrt{2} \times 4.2 \text{ nm} = 5.9\text{Å}$) of $\approx 5\%$	160
6.13	$2\theta - \omega$ scan aligned to CFS(111) for $T_B = 350^\circ\text{C}$	161
6.14	(a) TEM image of the CFS/MgO(001) specimen grown at $T_B = 350^\circ\text{C}$ and (b) CFS/MgO interface of the same specimen.	162

6.15	(a) TEM image of the CFS/MgO(001) film for $T_B = 350^\circ\text{C}$; (b) and (c) FFTs of the images enclosed by the red square (film) and yellow square (substrate) respectively; and (d) and (e) simulated diffraction patterns for CFS[1-10] and MgO[100] respectively.	163
6.16	(a) Specimen overview; and (c)-(g) EDS net intensity maps, after background subtraction of the scan area in (b).	163
6.17	Magnetic hysteresis loops along CFS[$\bar{1}10$] for: (a) $T_B < 130^\circ\text{C}$, (b) $T_B = 350^\circ\text{C}$ and (c) $T_B = 550^\circ\text{C}$	164
6.18	M_s (blue squares) and H_c (red circles) extracted from the hysteresis loops in Fig. 6.17 plotted against T_B	165
6.19	Frequency-field maps for fields between $0 < H < 0.38\text{T}$ and frequencies between 100kHz and 20GHz for: (a) $T_B < 130^\circ\text{C}$, (b) $T_B = 350^\circ\text{C}$ and (c) $T_B = 550^\circ\text{C}$, taken along the EA (i.e. along CFS[100]).	166
6.20	$H_r(\phi_{CFS})$ azimuthal graphs at 10GHz for (a) $T_B < 130^\circ\text{C}$, (b) $T_B = 350^\circ\text{C}$ and (c) $T_B = 550^\circ\text{C}$. The orientations specified in (a) are the crystallographic directions of CFS.	167
6.21	(a) Kittel curves along the EA (blue dots), the HA (green squares) and the <i>less hard</i> HA (empty black triangles) fitted to eq. (4.30) (red lines); (b) M_{eff} values (black squares) extracted from the fits in (a), and M_s values (grey dashed line) measured with the VSM shown in comparison; (c) cubic (black rhombus) and uniaxial (red circles) anisotropy constants extracted from the fits.	169
6.22	(a) ΔH as a function of the RF frequency and the corresponding linear fits for $T_B = 130^\circ\text{C}$ (yellow circles), $T_B = 350^\circ\text{C}$ (green squares) and $T_B = 550^\circ\text{C}$ (blue hollow triangles); (b) Gilbert damping parameter and $\Delta H(0)$ extracted from the linear fits in (a).	171
6.23	(a) XRR measurements (coloured dots) and fits (red lines) for the NiO [t_{NiO}]/Fe [1]/Co ₂ FeSi [25]/MgO(001) heterostructures with $t_{\text{NiO}} = 3\text{nm}$ (yellow), 5nm (blue), 10nm (green) and 20nm (grey); (b) thickness of the 3 layers in (c) extracted from the fits; (c) 3-layer model used to fit the data.	172
6.24	X-ray scattering length density extracted from the XRR fits in Fig. 6.23a for $t_{\text{NiO}} = 3\text{nm}$ (a), 5nm (b), 10nm (c) and 20nm (d).	174
6.25	(a) Out-of-plane $2\theta - \omega$ scan aligned to MgO(002) and (b) ϕ scan aligned to CFS(111) for the NiO[20]/Fe[1]/Co ₂ FeSi[25]/MgO(001) sample. Even at large angles, the NiO peaks cannot be resolved for the 20nm-thick layer.	174

6.26	HRTEM images of the NiO[10]/Fe[1]/Co ₂ FeSi[25]/MgO(001) sample. (a) is an overview of the layers in cross-section, and (b) is a high magnification image focused on the interface between NiO and CFS.	175
6.27	Azimuthal plots of the resonant frequency for (a) $t_{\text{NiO}}=3\text{nm}$, (b) $t_{\text{NiO}}=5\text{nm}$ and (c) $t_{\text{NiO}}=10\text{nm}$ revealing a negative K_c in all the capped films.	176
6.28	Magnetic hysteresis loop recorded along the [110] direction for $t_{\text{NiO}} = 5\text{nm}$	177

Acknowledgements

First and foremost I would like to express my gratitude to my academic supervisors, Prof. Vlado Lazarov and Dr. Stuart Cavill for giving me the fantastic opportunity to work on this project, as well as for all their guidance and support over the last five years.

Very special thanks to Dr. Barat Kuerbanjiang for the extensive training on UHV technology, this project could not have been possible without your expertise. Thank you for all your patience and invaluable hard work with the MBE system. I am also very grateful to Dr. Leonardo Lari for his help with the 2200FS microscope and to Dr. Demie Kepaptsoglou from the SuperSTEM laboratory for her collaboration on electron microscopy. I would also like to thank Dr. Jon Barnard for his assistance with the FEI-Nova system, and my fellow PhD students Ohoud Alsaqer and Dan Chesire for their enthusiasm and encouragement.

To my good friends, who made this journey far more enjoyable and who helped me get through the hard times. For all of this I thank Amy, Vera, Jeepy and Antonio. Finalmente, me gustaría agradecer con todo mi cariño a mis padres por hacer posible este Doctorado y por su incondicional apoyo en los momentos más difíciles. Eskerrik asko bihotz bihotzez.

This thesis was supported by the EPSRC DTA strategic studentship.



Author's declaration

I declare that this thesis is a presentation of original work and I am the sole author. This work has not previously been presented for an award at this, or any other, University. All sources are acknowledged as references.

Chapter 1

Motivation and structure of the thesis

1.1 Motivation

In the mid 1930-s, Mott postulated that the anomalous resistivity exhibited by ferromagnetic (FM) metals could be described by considering the spin-up and spin-down conduction electrons as two independent channels of charge carriers, each with its own distinct transport properties [MM33]. This two-channel model is, up to this date, the basis of *spintronics*. The field of spintronics was revolutionised by the discovery of giant magnetoresistance (GMR) in 1988 [Bai88; Bin89]; and since then, has shown great promise in the development of highly efficient spin-based electronic devices which overcome the limitations of conventional electronics where further device miniaturization leads to undesirable effects at the nano scale. In particular, magnetic tunnel junctions (MTJs) are a type of GMR multilayer structures that represented a major breakthrough for use in spin-transfer torque magnetic random access memory (STT-MRAM) [Eve], where the switching of the magnetic free layer is achieved by a spin polarized current instead of a magnetic field.

In addition to spin valves and MTJs that exploit the GMR effect, in the recent years, a second generation of spintronic devices which seeks the use of pure spin currents has emerged [Hua20]. One potential advantage of pure spin currents is the reduction of Joule heating and Oersted fields while retaining the functionality of spin currents to manipulate magnetization. These devices rely mostly on spin-orbit coupling (SOC) effects such as the *spin Hall effect* (SHE) or the *Rashba effect*; and have turned the scientific interest to new device capabilities such as new methods to switch FM entities via *spin-orbit torque* (SOT), improving the writing speed in MRAM [Bap18; Wan18], or the utilization of Rashba SOC to control spin transport in logic devices like the long standing challenge of the spin field-effect transistor (S-FET) [DD90].

For any of these applications, an efficient source of spin currents is needed. FMs are the

classic choice for spin injectors due to their characteristic spin-asymmetry at the Fermi level induced by the exchange interaction. In the extreme limit of spin asymmetry, half-metals are conductive in one spin channel while remaining insulating in the other channel; and hence, are an ideal source of 100% spin polarized currents. Among the half-metallic ferromagnets (HMFs), Co_2YZ full-Heusler alloys are particularly attractive due to their high Curie temperature (T_c), high saturation magnetization (M_s), low coercivity and small Gilbert damping. As such, they have been intensively investigated as FM electrodes for current-perpendicular-to-plane (CPP-) GMR [Fur13; Kub17; Li18], and as spin injectors in hybrid devices [Ham12; Kim12; Oki13; Oki17]. The introduction of HMFs to MTJs using insulating oxide (IO) barriers have been also used as a way to enhance the tunnel magnetoresistance (TMR) ratio [Sak06b; Oka05; Sak06a; STT09; Tez06].

Common methods for the generation of pure spin currents into normal metals (NMs) include ferromagnetic resonance (FMR-) driven spin pumping [YH18; Sán13], SHE-driven charge-to-spin conversion [WAKA13; Roy14] and the *Spin Seebeck effect* (SSE) which is enabled by a thermal gradient [Gan17; Qu13]. In this context, Co-based Heusler alloys have also been studied in the search of materials that provide high spin injection, namely materials with low magnetic damping for spin-pumping [Hus18; Sin21], large spin-Hall angles for SHE [Lei21; Sin21] and large spin Seebeck coefficients for SSE [Boe17] amongst others. With the growing interest in antiferromagnetic spintronics, heavy metal (HM)/antiferromagnetic metal or insulator (AFM or AFI)/HMF structures have also gathered attention since the antiferromagnet can be used to enhance SHE in structures such as Pt/IrMn/ Co_2MnSn [Hua19]. Similar effects have been seen in AFM and AFI containing heterostructures, e.g. Pt/NiO/ $\text{Y}_3\text{Fe}_5\text{O}_{12}$ (YIG), where the NiO interlayer between the Pt and YIG significantly increases the spin to charge conversion via SSE [Lin16]. In the last decade, the injection of giant pure spin currents at room temperature (RT) in lateral spin valve devices (LSVs) has also been achieved using Co_2FeSi (CFS) injectors. These experiments used the non-local geometry in combination with the HMF injectors to suppress the degradation of the spin signals by high bias currents when using conventional FM electrodes [Kim12; Oki13; Oki17].

The magnetic structure of Heusler alloys is strongly dependent on their atomic arrangement. In fact, half-metallicity is usually an exclusive feature of the L_{21} structure and can be significantly reduced in the B2 ordered state. An increase of the Gilbert damping has also been reported due to the existence of disordered phases [Cui14; Kue18]; whereas interfacial effects such as interdiffusion or the presence of additional interfacial layers can in some cases help preserve or destroy the spin polarization at the interface [Ned15; Ned16a]. Hence, a fine control of these properties is needed for the applicability of Co-based Heusler electrodes.

The work presented in this thesis can be divided in two main parts. The first part was the development and commissioning of a molecular beam epitaxy (MBE) growth system for the synthesis of high quality $\text{Co}_2\text{FeAl}_{1-x}\text{Si}_x$ (CFAS) thin films. The second part was the growth of full-Heusler CFS films using the newly built MBE. CFS films were grown on Si(111) and MgO(001) substrates, and their structural and magnetic properties were characterized using x-ray diffraction (XRD), transmission electron microscopy (TEM), vibrating sample magnetometry (VSM) and ferromagnetic resonance spectroscopy (FMR). Using these techniques it will be shown that CFS/Si(111) samples grown at $< 130^\circ\text{C}$ exhibit a mixed L2_1 and B2 ordering and that their magnetic properties are comparable to those found in literature for similar highly-ordered Heusler films, making them suitable for device applications. The same holds true for CFS/MgO(001) when the growth temperature is increased to 350°C . The effects of stoichiometry will be investigated in CFS/Si(111), whereas the effects of growth temperature will be the main focus for the CFS/MgO(001) series. Finally, the growth of NiO on CFS has been explored and the influence of the AFI layer on the properties of CFS has been investigated. Intriguing changes are observed related to the magnetic anisotropy of the films. In CFS/Si(111), the uniaxial anisotropy changes the orientation of the EA as a result of a slight increase in the growth temperature. In CFS/MgO(001) the magnetic anisotropy changes as a result of the NiO overlayer. In the latter case, anisotropic features change due to the sign reversal of the cubic magnetocrystalline anisotropy (MCA) constant.

1.2 Structure of the thesis

This thesis contains seven chapters. Following **Chapter 1** which motivates the project, **Chapter 2** provides the theoretical framework for the present work. After covering the fundamentals of ferromagnetism (§ 2.1 and § 2.2), spin currents are introduced (§ 2.3) paving the way to the field of spintronics. A brief review of the key aspects in spintronics is given in sections § 2.4 to § 2.5; and within that context the role of HMFs, and more particularly the Co-based Heusler alloys, is discussed (§ 2.6 and § 2.7).

Chapter 3 focuses on the construction and commissioning of the MBE system for the growth of $\text{Co}_2\text{FeAl}_{1-x}\text{Si}_x$ alloys. The chapter starts with an introduction to ultra-high vacuum (UHV) technology and thin film growth (sections § 3.2 to § 3.4), and continues with the design of the MBE system (§ 3.5). The key components of the MBE system are described (manipulator, heating stage and evaporation sources) and the working principle of the two main analytical techniques used during growth are also outlined, namely the quartz crystal monitor (QCM) and reflection high-energy electron diffraction (RHEED) (§ 3.6).

In **Chapter 4** the experimental and analytical techniques used for the characterization of the MBE-grown CFS films will be detailed, that is, XRD and XRR (§ 4.1), TEM (§ 4.2), FMR (§ 4.3.1) and VSM (§ 4.3.2). The working principle of each technique will be depicted and the specific experimental set-ups will be discussed in reference to the experiments carried out in this work. The procedure for the preparation of cross-sectional lamellas for TEM studies will also be described step by step in § 4.2.5.

Chapter 5 presents the results of a series of non-annealed CFS films grown on Si(111) with varying stoichiometry. The films have been structurally and magnetically characterised and special attention has been paid to the structural ordering of the films and its correlation with their magnetic properties, specifically the magnetic damping and the magnetic anisotropy.

Chapter 6 provides a discussion of the magnetic and structural properties of a second series of CFS thin films grown on MgO(001). In this case, the main interest is on the effects of substrate temperature during growth. Specifically, three CFS films grown at $< 130^{\circ}\text{C}$, 350°C and 550°C are characterized and compared. After finding the optimal growth conditions and substrate temperature, the effects of an antiferromagnetic (NiO) overlayer on the magnetic properties of CFS is also briefly discussed.

Chapter 7 is a summary of the accomplished works and results obtained in this thesis. Future work related to this project will also be considered.

Chapter 2

Theoretical background

2.1 Energy contributions of ferromagnetism

Magnetism is a purely quantum mechanical effect that occurs when atoms with unpaired electrons and therefore, with a magnetic moment $\vec{\mu} \neq 0$, are arranged in a crystal lattice. If the magnetic moments interact sufficiently strongly with each other, ferromagnetism occurs. The magnetic free energy of a ferromagnetic system is defined by four interactions (exchange, spin orbit coupling, magnetostatic and Zeeman) which give rise to the energy terms shown below.

2.1.1 Exchange energy

The origin of ferromagnetism relies on exchange coupling (EXC). This is a quantum mechanical effect that arises from the combination of Pauli's exclusion principle and the Coulomb interaction. In a two electron system, the orbital part of the wave function of the joint state, Φ , is built from the product of the two single electron states, φ_a and φ_b , in such way that the exchange symmetry between the two electrons is obeyed. This leads to two possible orbital wave functions, one of which is symmetric and the other antisymmetric [Blu03]:

$$\begin{aligned}\Phi_S &\propto [\varphi_a(\vec{r}_1)\varphi_b(\vec{r}_2) + \varphi_b(\vec{r}_1)\varphi_a(\vec{r}_2)] && \text{symmetric} \\ \Phi_T &\propto [\varphi_a(\vec{r}_1)\varphi_b(\vec{r}_2) - \varphi_b(\vec{r}_1)\varphi_a(\vec{r}_2)] && \text{antisymmetric}\end{aligned}\tag{2.1}$$

Electrons have been labelled as 1 and 2. Taking into account the electrostatic repulsion, the two orbital states above are not degenerate, and the energy difference between them is known as the exchange energy. Even if the origin of the exchange interaction is the energy dependence on the orbital symmetry, Pauli's symmetry requirement over the complete wave function, including

orbital and spin parts, results in the correlation between the orbital symmetry and the spin alignment. Consequently, it is possible to express the EXC as a spin-spin interaction, $E_{exch}^{el} = -2J\hat{S}_1 \cdot \hat{S}_2$ where $\hat{S}_{1,2}$ is the spin operator of electron 1, 2, and J is the exchange parameter. In this notation, spin operators are dimensionless and the J has units of energy. In a solid, where the electronic wave functions of nearby atoms overlap, the EXC is generalized with the Heisenberg model [Blu03]:

$$E_{exch} = - \sum_{i,j} J_{ij} \hat{S}_i \cdot \hat{S}_j \quad (2.2)$$

Here, J_{ij} is the exchange parameter between two interacting spins i and j in the lattice. For a ferromagnet (FM) $J_{ij} > 0$ and the EXC favours the spins and hence the magnetic moments, to be aligned in the crystal lattice, leading to a non-vanishing value of the magnetization even at zero magnetic field. For an antiferromagnet (AFM) $J_{ij} < 0$ and it turns energetically favourable for neighbouring spins to point in opposite directions.

The EXC is a short range force. In a FM, the coexistence of short range forces and long range forces such as the magnetostatic (MS) interaction (§ 2.1.3), makes it difficult to describe their macroscopic magnetic behaviour. A method to overcome this is to replace the atomic nature of the matter and the quantum mechanical interactions by a continuum model. In this approach, the magnetization is a continuous field with constant magnitude, $\vec{M}(\vec{r}) = M_s \vec{m}(\vec{r})$, where \vec{m} is the dimensionless unit vector known as reduced magnetization. Considering the spin operators in (2.2) as classical vectors, for a crystal of uniform spins, $|\vec{S}_i| = S$, the exchange energy density¹ becomes [Blu03]:

$$U_{exch} = A_{ex} [|\nabla m_x(\vec{r})|^2 + |\nabla m_y(\vec{r})|^2 + |\nabla m_z(\vec{r})|^2] = A_{ex} |\nabla \vec{m}|^2 \quad (2.3)$$

where $A_{ex} = JS^2C/a_{NN}$ is called the exchange stiffness. a_{NN} is the nearest neighbour distance and C is the number of sites in the unit cell.

2.1.2 Magnetocrystalline anisotropy

Even if the EXC explains the alignment of the spins in a FM, it only gives information on the relative orientation of the spins. There are several contributions to the anisotropy of the system that will eventually define the preferential crystallographic orientations along which the magnetic moments align. One of the main sources of anisotropy is the magnetocrystalline anisotropy (MCA), which refers to the coupling between the lattice symmetry and the magnetic

¹In this section, energies, E , are distinguished from energy densities, U .

configuration of the system.

The origin of MCA is the combination of the spin-orbit coupling (SOC) and the crystal fields. The SOC couples the spin angular momentum and the orbital angular momentum of an electron. It arises from the electromagnetic interaction between the electron spin and the magnetic field generated by the same electron orbiting around the nucleus. Given a certain ion in the crystal, all the neighbouring ions produce an electric field which generates attractive or repulsive forces on the first ion. Depending on the crystal symmetry, the orbitals must arrange differently so that the electrostatic repulsion is minimized. Due to the SOC, such orbital orientations cause certain spin orientations, easy axes (EA), to be energetically favourable.

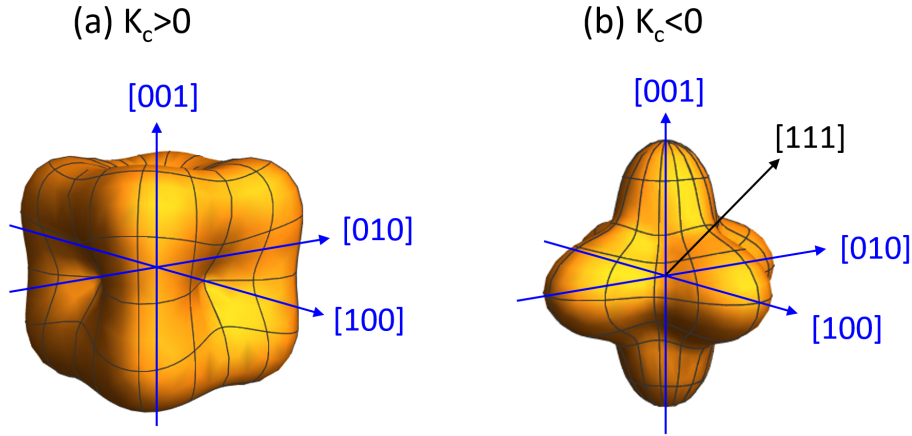


Figure 2.1: MCA energy density of a cubic crystal with (a) a positive K_c and (b) a negative K_c .

The symmetry of the MCA is the same as that of the crystal lattice. Consequently, a cubic crystal like the Heusler compound studied in this thesis, Co_2FeSi (§ 2.7.1), has a cubic anisotropy (CAN) with 3 EAs. The corresponding energy density can be expressed as a series expansion of the direction cosines δ_1 , δ_2 and δ_3 between the magnetization and the principal crystallographic axes $\vec{u}_1 = [100]$, $\vec{u}_2 = [010]$ and $\vec{u}_3 = [001]$. Discarding 2^{nd} and higher order contributions, the MCA energy is given by [Blu03]:

$$U_{can} = K_c (\delta_1^2 \delta_2^2 + \delta_2^2 \delta_3^2 + \delta_3^2 \delta_1^2) \quad (2.4)$$

with K_c the cubic anisotropy coefficient. When the cosines are inserted, the expression simplifies to:

$$U_{can}^{001} = K_c \sin^2 \theta_M \left[\frac{1}{4} \sin^2 \theta_M \sin^2 (2\phi_M) + \cos^2 \theta_M \right] \quad (2.5)$$

where θ_M is the angle of the magnetization with respect to the [001] axis and ϕ_M is the in-plane angle with respect to [100] (see Fig. 4.19). When $K_c > 0$, there are six equivalent energy minima corresponding to the $\langle 100 \rangle$ directions (Fig. 2.1a). Conversely, when $K_c < 0$ a more complex situation arises (Fig. 2.1b). In fact, there are eight equivalent minima along the directions pointing towards the vertices of the cube (i.e. the $\langle 111 \rangle$ directions) and the principle crystallographic axes become now hard axes. Expression (2.5) will be conveniently used when analysing the FMR of (001)-oriented CFS films in Chapter 6. However, since the CFS films grown on Si(111) in Chapter 5 are aligned with the [111] crystal direction, it is preferable to write eq. (2.5) in terms of the new coordinate system $\{x', y' \text{ and } z'\}$ shown in Fig. 2.2 where $x' \parallel [1\bar{1}0]$, $y' \parallel [11\bar{2}]$ and $z' \parallel [111]$. This is achieved using the following transformation matrix:

$$\begin{pmatrix} x \\ y \\ z \end{pmatrix} = \begin{pmatrix} \frac{1}{\sqrt{2}} & \frac{-1}{\sqrt{2}} & 0 \\ \frac{1}{\sqrt{6}} & \frac{1}{\sqrt{6}} & -\sqrt{\frac{2}{3}} \\ \frac{1}{\sqrt{3}} & \frac{1}{\sqrt{3}} & \frac{1}{\sqrt{3}} \end{pmatrix} \cdot \begin{pmatrix} x' \\ y' \\ z' \end{pmatrix} \quad (2.6)$$

Straightforwardly, the expression for the CAN is written in terms of the new polar and azimuthal angles, θ'_M and ϕ'_M respectively:

$$U_{can}^{111} = K_c \left[\frac{1}{3} \cos^4 \theta'_M + \frac{1}{4} \sin^4 \theta'_M - \frac{\sqrt{2}}{3} \sin^3 \theta'_M \cos \theta'_M \sin(3\phi'_M) \right] \quad (2.7)$$

In hexagonal crystals like Co, the crystal symmetry causes a uniaxial anisotropy (UAN) with a single EA. The easy axis coincides with \vec{u}_3 and any direction in the basal plane is an equally hard direction (HA). The expression for the UAN up to 1st contribution is² [Blu03]:

$$U_{uan} = -K_u \delta_3^2 \quad (2.8)$$

²The negative sign has been introduced here so that the easy axis coincides with \vec{u}_3 when $K_u > 0$. This is not always the convention used by other authors.

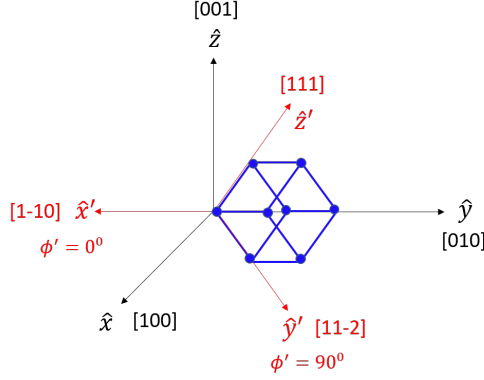


Figure 2.2: New coordinate system $\{x', y' \text{ and } z'\}$ in red, with the $[111]$ direction normal to the film plane.

2.1.3 Magnetostatic energy and shape anisotropy

The magnetostatic (MS) interaction refers to the interaction between the magnetic field generated by the magnetic distribution of the system and the magnetization itself. In a FM, each magnetic dipole, represented by $\vec{\mu}_j$, produces a magnetic field \vec{h}^j centred at the atomic position \vec{r}_j that extends all over the space [Blu03]:

$$\vec{h}^j = \frac{1}{4\pi} \left[-\frac{\vec{\mu}_j}{|\vec{r} + \vec{r}_j|^3} + \frac{3}{|\vec{r} - \vec{r}_j|^5} [\vec{\mu}_j \cdot (\vec{r} - \vec{r}_j)] (\vec{r} - \vec{r}_j) \right] \quad (2.9)$$

As a consequence, a dipole in the i^{th} lattice point $\vec{\mu}_i$, interacts with the dipolar field created by the rest of the dipoles. The energy of $\vec{\mu}_i$ is then $E_i = -\vec{\mu}_i \cdot \sum_{j \neq i} \mu_0 \vec{h}^j$. Summing all the individual contributions, the MS energy can be expressed as:

$$E_{ms} = - \sum_i \vec{\mu}_i \cdot \sum_{j \neq i} \mu_0 \vec{h}^j \quad (2.10)$$

It is usual to write (2.10) as a function of the total dipolar field, known as the MS field, which is the sum of the individual fields (2.9) generated by all the dipoles in the crystal, $E_{ms} = -\frac{\mu_0}{2} \sum_i \vec{\mu}_i \vec{H}_d$, with $H_d = \sum_j \vec{h}^j$. The MS field is usually called the *demagnetizing field* inside the body and the *stray field* outside the body. In the continuum model, it is approximated to:

$$\vec{H}_d = \frac{1}{4\pi} \left[\int_V \frac{\rho_v(\vec{r}') (\vec{r} - \vec{r}')}{|\vec{r} - \vec{r}'|^3} dV' + \int_s \frac{\rho_s(\vec{r}') (\vec{r} - \vec{r}')}{|\vec{r} - \vec{r}'|^3} dS' \right] \quad (2.11)$$

where ρ_v and ρ_s stand for the volume and the surface magnetic charge density respectively. Hence, eq. (2.10) is transformed into:

$$U_{ms} = -\frac{\mu_0 M_s}{2} \vec{m} \cdot \vec{H}_d \quad (2.12)$$

When the FM is uniform, the first integrand of eq. (2.11) is zero. In that case, the MS energy only depends on the shape of the body and the direction of the magnetization, and has the same mathematical form as UAN. Then, the dipolar energy is usually referred to as *shape anisotropy*. In thin films, the shape anisotropy tends to keep the magnetization within the film plane and can be approximated to [Joh96]:

$$U_{ms} \approx \frac{1}{2} \mu_0 M_s^2 \cos^2 \theta_M \quad (2.13)$$

In a small enough structure, the single-domain configuration is energetically favourable. In that case, the cost generated by the demagnetizing fields inside the body is compensated by the minimization of the exchange energy. However, in larger systems, the body splits into several magnetic domains to minimize the MS energy. The formation of domains occurs in spite of an increment in the exchange energy at the domain walls, where there is a gradual rotation of spins. This occurs over lengths of the order of tens to hundreds of nanometers.

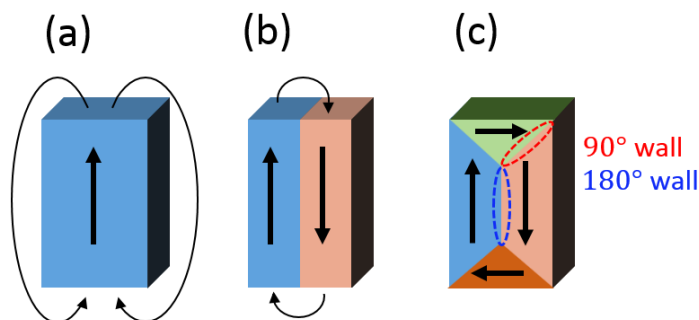


Figure 2.3: Formation of magnetic domains in order to minimize the dipolar contribution. (a) corresponds to a single-domain state. Here, the exchange energy is minimum but the dipolar energy is the largest due to the big dipolar fields. In (b) the system splits into two domains reducing the magnetostatic contribution at the expense of creating a domain wall. Finally, in (c) the demagnetizing fields are cancelled minimizing the dipolar energy but introducing several domain walls in a Landau structure.

2.1.4 The magnetoelastic energy

The magnetoelastic (ME) interaction or magnetostriction stands for the coupling between the magnetization of the body and the strain applied to it. Essentially, if a strain is applied, the distances between atoms change and the lattice is distorted. As a consequence, the crystal

fields change and the spin configuration of the system is modified. The ME energy is a function of $\delta_{1,2,3}$ and the components ϵ_{ij} of the strain tensor. For a cubic crystal [Blu03]:

$$U_{me} = B_1 (\delta_1^2 \epsilon_{xx} + \delta_2^2 \epsilon_{yy} + \delta_3^2 \epsilon_{zz}) + B_2 (\delta_1 \delta_2 \epsilon_{xy} + \delta_2 \delta_3 \epsilon_{yz} + \delta_3 \delta_1 \epsilon_{zx}) \quad (2.14)$$

where B_1 and B_2 are the so-called ME coupling constants in J/m. Nevertheless, because the systems studied in this thesis are not subjected to strain, eq. (2.14) won't be developed further.

2.1.5 The Zeeman energy

Finally, if an external magnetic field (\vec{H}) is applied to the FM, the magnetic moments inside the body tend to align with the external field according to the Zeeman term:

$$U_z = -\mu_0 M_s \vec{m} \cdot \vec{H} \quad (2.15)$$

where the magnetic field is in A/m units. Once again, introducing the spherical coordinates for the magnetization vector and the magnetic field (refer to Fig. 4.19 for the representation of \vec{M} and \vec{H}), the equation for an in-plane field ($\theta_H = 90^\circ$) becomes:

$$U_z = -\mu_0 H M_s \sin \theta_M \cos(\phi_M - \phi_H) \quad (2.16)$$

θ_M and ϕ_M are again the polar and azimuthal angles of the magnetization respectively. Likewise, θ_H is the angle of the magnetic field with respect to the [001] axis and ϕ_H is the in-plane angle with respect to [100].

2.2 Magnetization dynamics

The static approach minimizes the energy of the body with respect to the spatial distribution of $\vec{m}(\vec{r})$ to calculate equilibrium magnetic configurations. Taking into account all the energy contributions in § 2.1, the total energy of an ideal cubic FM with in-plane magnetization is given by:

$$E = \int_V U_{TOT} dV = \int_V [U_{exch} + U_{can} + U_{ms} + U_{me} + U_z] dV \quad (2.17)$$

By using variational principles, it can be shown that the energy minimum satisfies [Blu03]:

$$\vec{m} \times \vec{H}_{eff} = 0 \quad (2.18)$$

where \vec{H}_{eff} is a local effective field that involves all the interactions described:

$$\vec{H}_{eff}(\vec{r}) = -\frac{1}{\mu_0 M_s} \frac{\partial U_{TOT}}{\partial \vec{m}(\vec{r})} \quad (2.19)$$

That is, the equilibrium is reached when $\vec{m}(\vec{r})$ aligns to the local effective field at \vec{r} . On the other hand, the dynamical approach looks for the time evolution of the magnetization. An equation that describes the time dependence of the magnetization was presented by Landau and Lifshitz in 1935 [LL35]. It is known that an external magnetic field causes the precession of the magnetic moment around it, the so-called Larmor precession. Landau and Lifshitz suggested that $\vec{m}(\vec{r})$ also precesses due to the local effective field. To take into consideration dissipative effects, a damping term was introduced giving rise to the Landau-Lifshitz-Gilbert (LLG) differential equation:

$$\frac{\partial \vec{m}}{\partial t} = -\gamma \vec{m} \times \vec{H}_{eff} + \alpha \vec{m} \times \frac{\partial \vec{m}}{\partial t} \quad (2.20)$$

The first term in (2.20) represents the torque exerted by the effective field with γ the electron gyromagnetic ratio. The second term is the damping term, governed by the phenomenological dimensionless Gilbert damping parameter α . By integrating the LLG equation the evolution of the magnetization is obtained until at equilibrium, the magnetization and the effective field are parallel.

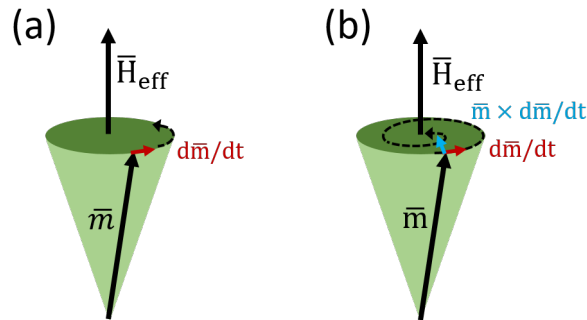


Figure 2.4: Undamped (a) and damped (b) motion of the magnetization vector around the effective field \vec{H}_{eff} representing eq. (2.20) without and with the damping term respectively.

2.3 Spin currents and magnons

Spin currents can be described as spin fluxes caused by electrical or thermal forces in a crystal. The spin current can either be a spin polarized (charge) current or a (pure) spin current³. Spin polarized currents typically occur in materials with an imbalance of spin-up and spin-down conduction electrons (i.e. ferromagnets) where the spin transfer is accompanied with a charge flow. On the contrary, a pure spin current occurs without net charge transfer and it can be thought of as an equal number of spin-up and spin-down electrons moving in opposite directions.

When the spin diffusion length is much longer than the mean free path for spin-dependent scattering, $\lambda_s \gg \lambda$, the *Valet-Fert model* [VF93] successfully describes spin transport in solids. In the diffusive regime, spin-up and spin-down electrons diffuse independently except for a weak scattering from one channel to the other. In such case, the conductivity for each spin channel is [Kri16; YF02]:

$$\sigma_{\uparrow(\downarrow)} = e^2 n_{\uparrow(\downarrow)}(E_F) D_{\uparrow(\downarrow)} \quad (2.21)$$

$D_{\uparrow(\downarrow)}$ is the spin-dependent diffusion constant and $n_{\uparrow(\downarrow)}(E_F)$ is the density of states (DOS) of spin up (down) electrons at the Fermi level⁴. The spin-up (down) current densities are then given by:

$$\vec{j}_{\uparrow(\downarrow)} = \sigma_{\uparrow(\downarrow)} \vec{E} - D_{\uparrow(\downarrow)} \nabla n_{\uparrow(\downarrow)} \quad (2.22)$$

where $n_{\uparrow(\downarrow)}$ is the density of spin-up (down) electrons. The charge current density \vec{j}^c and spin current density \vec{j}^s are defined as:

$$\vec{j}^c = \vec{j}_{\uparrow} + \vec{j}_{\downarrow} = (\sigma_{\uparrow} + \sigma_{\downarrow}) \vec{E} - \frac{e(D_{\uparrow} + D_{\downarrow})}{2} \nabla (n_{\uparrow} + n_{\downarrow}) - \frac{e\beta(D_{\uparrow} + D_{\downarrow})}{2} \nabla (n_{\uparrow} - n_{\downarrow}) \quad (2.23)$$

³Be aware that from now on we will drop the word “pure” to talk about spin currents without flow of charge. If the spin current is accompanied with charge flow, we will refer to it as a “spin polarized current” to distinguish the two.

⁴Note that here, $n_{\uparrow(\downarrow)}(E)$ is the number of spin up (down) states per unit volume per unit energy at E . In some textbooks like in *Solid State Physics* by Ashcroft and Mermin, this quantity is referred to as $g(E)$. Hence, $n_{\uparrow(\downarrow)}(E)$ should not be mistaken with the electronic density, which is the number of states per unit volume (summed for all the occupied energy levels in crystal). Refer to page 44 in [AM76].

$$\vec{j}^s = \vec{j}_\uparrow - \vec{j}_\downarrow = \alpha' (\sigma_\uparrow + \sigma_\downarrow) \vec{E} - \beta \frac{e(D_\uparrow + D_\downarrow)}{2} \nabla (n_\uparrow + n_\downarrow) - \frac{e(D_\uparrow - D_\downarrow)}{2} \nabla (n_\uparrow - n_\downarrow) \quad (2.24)$$

Here, α' is the spin polarization for conductivity and β is a function of α' and the spin polarization for the DOS, $\beta' = \frac{n_\uparrow(E_F) - n_\downarrow(E_F)}{n_\uparrow(E_F) + n_\downarrow(E_F)}$:

$$\alpha' = \frac{\sigma_\uparrow - \sigma_\downarrow}{\sigma_\uparrow + \sigma_\downarrow} \quad (2.25)$$

$$\beta = \frac{\alpha' - \beta'}{1 - \alpha'\beta'} \quad (2.26)$$

In a normal metal (NM), $\sigma_\uparrow = \sigma_\downarrow = \sigma_{NM}$ and therefore there is no spin polarization, $\alpha' = \beta = 0$. If a spin accumulation exists, upon the application of an electric field, a drift spin polarized current can be generated. More interestingly, if the spin accumulation is non-homogeneous, spins will diffuse from the regions with higher spin concentration towards the regions with lower spin concentration, giving rise to a spin current.

In a ferromagnetic metal (FM), the imbalance between spin-up and spin-down conduction electrons (hence, $\alpha' \neq 0$) means that upon the application of an external electric field, a spin polarized current is generated. It should be noted that in itinerant ferromagnets such as Ni, Co or Fe, even if the electrical current is mainly carried by the s-electrons, the band splitting occurring in the 3d sub-bands is responsible for the two independent conduction channels of spin-up and spin-down electrons. This happens due to the hybridization between the s and d bands which leads to the s-electrons being scattered into the DOS of the d bands. One of the s sub-bands, thus, suffers more scattering creating a conductivity imbalance and a net spin polarization of the current [Gre02].

The same way that the charge current is inevitably accompanied by a spin current in a FM, spin accumulation also comes hand in hand with a charge current. If there is spin accumulation, spins will once again diffuse from the areas with higher spin concentration to the areas with lower spin concentration. However, because there is an imbalance in the number of spin-up and spin-down electrons, the number of spin-up electrons diffusing to one side is different from the number of spin-down electrons diffusing to the opposite side and hence, leading to a non-vanishing net flow of charge.

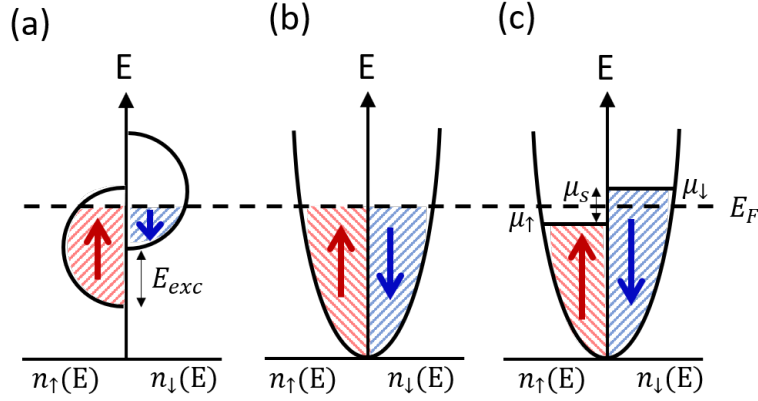


Figure 2.5: Schematic representation of the DOS of: (a) the 3d spin sub-bands in a FM shifted by the exchange interaction energy; (b) the s sub-bands in a NM metal, where there is no spin accumulation; and (c) the s sub-bands in a NM, near the FM/NM interface, where there is spin accumulation (see section § 2.5).

In order to describe spin transport under this formalism, we have to solve the continuity equation for each spin current density [Kri16]:

$$\frac{\partial n_{\uparrow(\downarrow)}}{\partial t} + \nabla \cdot \vec{j}_{\uparrow(\downarrow)} + \left[\frac{n_{\uparrow(\downarrow)}}{\tau_{\uparrow(\downarrow)\uparrow}} - \frac{n_{\downarrow(\uparrow)}}{\tau_{\downarrow(\uparrow)\downarrow}} \right] = 0 \quad (2.27)$$

In contrast to charge, spin is not a conserved quantity and therefore, spin relaxation is introduced in eq. (2.27) through the last two terms in brackets, where spin-up (down) electrons are transformed into spin-down (up) electrons by means of spin-flip scattering with a characteristic relaxation time $\tau_{\uparrow\downarrow}$ ($\tau_{\downarrow\uparrow}$). In the equation for the spin-up current \vec{j}_{\uparrow} , $-(n_{\uparrow}/\tau_{\uparrow\downarrow} - n_{\downarrow}/\tau_{\downarrow\uparrow})$ gives then the net rate of scattering of up electrons to down electrons. Similarly, for the spin-down current \vec{j}_{\downarrow} , $-(n_{\downarrow}/\tau_{\downarrow\uparrow} - n_{\uparrow}/\tau_{\uparrow\downarrow})$ gives the net rate of scattering of down electrons to up electrons. Unlike charge currents, spin currents do not need a spin drain but instead they propagate in the material until they decay.

It is convenient to write the current densities in terms of the electrochemical potential (ECP), μ , which is by definition the amount of energy that has to be added to the system in order to add an extra electron. In the absence of an electric field, μ is equal to the chemical potential (μ_{ch}), which, at $T = 0K$ equals the Fermi energy. If there is an excess of electrons, μ_{ch} is proportional to the excess of particle density $\mu_{ch} = n/n(E_F)$. If the electrons are additionally subjected to an electric field, \vec{E} , the potential energy has to be added to μ_{ch} to obtain the ECP, i.e. $\mu = \mu_{ch} - eV$ (where $\vec{E} = -\nabla V$). A gradient in the ECP then generates a current density that can be both due to the electric field or a spatial variation of the electronic density $\nabla\mu_{ch} \propto \nabla n$:

$$\vec{j}_{\uparrow(\downarrow)} = -\sigma_{\uparrow(\downarrow)} \nabla \left(\frac{\mu_{\uparrow(\downarrow)}}{-e} \right) \quad (2.28)$$

In equilibrium, $\partial n_{\uparrow(\downarrow)}/\partial t = 0$ and there is no net transfer of electrons between spin-up and spin-down states, $n_{\uparrow}/\tau_{\uparrow\downarrow} = n_{\downarrow}/\tau_{\downarrow\uparrow}$. Equations (2.21)-(2.22) and (2.27)-(2.28) are then combined to form the drift-diffusion equation [Kri16; YF02]:

$$\nabla^2 \mu_s(\vec{r}) = \frac{1}{D\tau_{sf}} \mu_s(\vec{r}) \quad (2.29)$$

where μ_s is the difference in the spin-up and spin-down ECP, $\mu_{\uparrow}(\vec{r}) - \mu_{\downarrow}(\vec{r})$, which is defined as the spin accumulation. D is the spin-averaged diffusion coefficient and τ_{sf} the effective spin-relaxation time, i.e. the timescale over which the non-equilibrium spin accumulation decays:

$$D = \frac{D_{\uparrow}D_{\downarrow}[n_{\uparrow}(E_F) + n_{\downarrow}(E_F)]}{D_{\uparrow}n_{\uparrow}(E_F) + D_{\downarrow}n_{\downarrow}(E_F)} \quad (2.30)$$

$$\frac{1}{\tau_{sf}} = \frac{1}{\tau_{\uparrow\downarrow}} + \frac{1}{\tau_{\downarrow\uparrow}} \quad (2.31)$$

It can be seen that τ_{sf} is equal to the spin lattice relaxation times T_1 and T_2 used in the Bloch equations [Blo46] and therefore, represents the average time after which the carrier loses the information of its spin polarization. In metals, the main mechanism for spin relaxation is the *Elliot-Yafet* mechanism [Ell54], whereas in semiconductors (SCs), we also have contributions from the *D'yakonov-Perel'* mechanism [DP71].

If the direction of the current flow is \hat{z} , and there is no current flowing out the sides, applying the divergence theorem, (2.29) can be transformed in a 1D equation [Kri16; YF02]:

$$\frac{\partial^2}{\partial z^2} \mu_s(z) = \frac{1}{D\tau_{sf}} \mu_s(z) \quad (2.32)$$

and its general solution is:

$$\mu_s = Ae^{(-z/\lambda_s)} + Be^{(z/\lambda_s)} \quad (2.33)$$

where we define the spin diffusion length as $\lambda_s = \sqrt{D\tau_{sf}}$. The constants A and B serve to satisfy the boundary conditions at the interfaces. Under the assumption of $\tau_{\uparrow\downarrow} = \tau_{\downarrow\uparrow}$ the dynamics of the spin accumulation μ_s can also be obtained [Dec18]:

$$\frac{\partial \mu_s}{\partial t} + \frac{\mu_s}{\tau_{sf}} + \frac{\partial j_s}{\partial z} = 0 \quad (2.34)$$

In a FM the spin accumulation precesses around the exchange field from the 3d electrons.

In such a case, two extra terms have to be added to the equation above [Dec18; Han13].

$$\frac{\partial \mu_s}{\partial t} + \frac{\mu_s}{\tau_{sf}} + \frac{\partial j_s}{\partial z} + \frac{1}{\tau_{exc}} \vec{\mu}_s \times \vec{m} + \frac{1}{\tau_{dp}} \vec{m} \times (\vec{m} \times \vec{\mu}_s) = 0 \quad (2.35)$$

where τ_{exc} and τ_{dp} are the precession and damping times due to the EXC respectively. The drift-diffusion formalism is applicable to any bulk material. The equations above assume the spin polarization to be polarized along direction \hat{z} . However, if non-collinear systems want to be studied, the spin has to be substituted by a 2 by 2 matrix. The more general equations can be found in [Han13].

Another way to create a pure spin current is through *magnons*. Spin currents generated in ferromagnetic insulators are the perfect example of such spin wave spin currents because a transfer of spin angular momentum is achieved in the absence of conduction electrons [Xia10]. Analogous to the mechanical vibrations or lattice waves in crystals [AM76], spin waves are collective excitations occurring in magnetic lattices as a response to an external stimulus [Blu03]. In such lattices flipping a spin is not a stable solution of the Heisenberg Hamiltonian (2.2) and instead, the flipped spin is “shared” or “distributed” over all lattice sites. This collective excitation has a well defined momentum \vec{k} and energy $\hbar\omega$ called magnon. In the same way lattice waves are quantized as phonons, magnons are quanta of spin waves. That is, they are spin-1 quasiparticles which obey the Bose-Einstein distribution. Magnons can originate due to exchange interaction § 2.1.1 or dipolar interaction § 2.1.3. Exchange mediated magnons are characterized by short wavelengths (< 100 nm) [Che20], whereas dipolar coupling mediated magnons have long wavelengths (> 1 μ m) [Kos05; CSH14].

In the classical picture, spin waves are arrays of precessing spins along a certain axis with frequency ω but with a phase shift between them (see Fig. 2.6). The dispersion relation of these spin waves is calculated by solving eq. (2.20) for the precessing spins under the exchange field:

$$\vec{H}_{eff} = \vec{H}_{exch} = -\frac{A_{ex}}{\mu_0 M_s} \frac{\partial |\nabla \vec{m}|^2}{\partial \vec{m}} \quad (2.36)$$

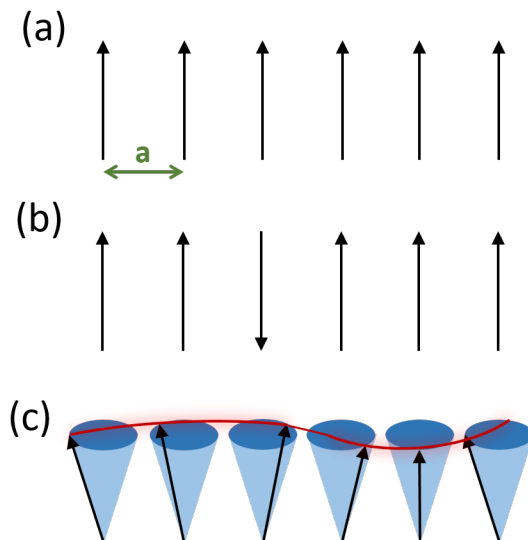


Figure 2.6: (a) Classical picture of the ground state in a FM where all the spins are aligned due to exchange interactions. (b) A possible excited state where one of the spins is reversed. (c) An alternative form of excitation of much lower energy, called magnons, where the spins precess with a constant phase difference between successive spins separated by the interatomic distance a .

2.4 Spintronics

The major interest in spintronics began when GMR was first observed in Fe/Cr superlattices by the groups of Albert Fert and Peter Grönberg in 1988 [Bai88; Bin89]. In these multilayered system, the device shows a dramatic change of resistance when the magnetization of the ferromagnetic layers is switched from parallel to antiparallel configuration. The difference of resistance is significantly higher than the one observed in anisotropic magnetoresistance (AMR) and hence, GMR was quickly implemented in read-head devices for a much faster information readout and a decrease in their dimensions.

In addition to these superlattices, *spin-valves* (SVs) and *magnetic tunnelling junctions* (MTJs) also show GMR. In their simplest form, SVs consist of two ferromagnetic layers separated by a non-magnetic spacer which avoids ferromagnetic coupling between the two. The magnetization of one of the FM is pinned by an adjacent AFM layer via exchange coupling. In a geometry such as the one shown in Fig. 2.7, GMR can be understood from the two channel model introduced in § 2.3. When an electric bias is applied, a spin-polarized current is driven from the FM layer into the NM which gives rise to a change of the ECP and hence, a spin accumulation close to the FM/NM interface. Such spin accumulation diffuses into the NM and enters the second FM. Let us consider that the low resistance channel in the FM metals is the

one of the majority electrons, i.e. the spin-up electrons in the pinned FM. Then, if (a) the majority of the electrons of the free FM are also spin-up (i.e. parallel magnetizations), the spin dependent scattering is minimized and consequently the device shows low resistance. If (b) the majority of the electrons of the second FM are spin-down (i.e. antiparallel magnetizations), the device has a resistance about twice as high as that of the parallel configuration.

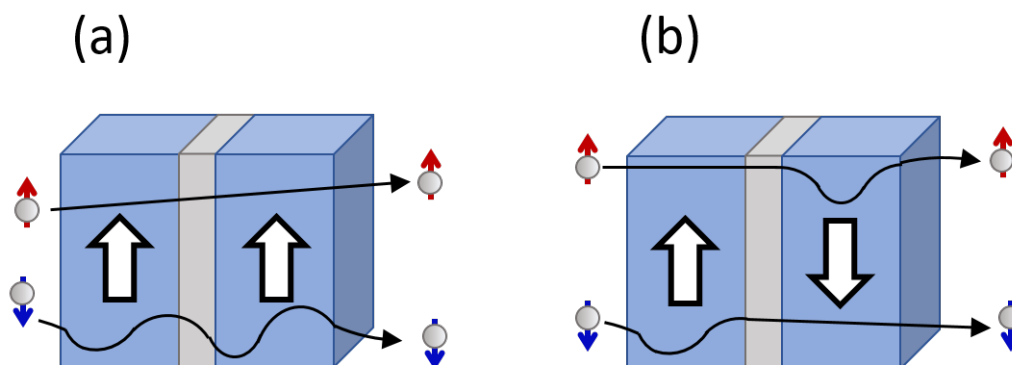


Figure 2.7: Representation of a simple SV device consisting of a FM (pinned)/NM/FM (free) structure in: (a) parallel configuration, where the scattering is minimized and hence, the device shows a low resistance; and (b) antiparallel configuration where the device shows a high resistance.

In MTJs the non magnetic spacer is replaced by an insulating barrier, such as Al_2O_3 or MgO . The spin dependent transport is then no longer diffusive but tunnelling. Using a simple model which neglects spin-flip events, Jullière derived the expression for the TMR ratio as a function of the spin polarisation of the two ferromagnetic layers, β'_1 and β'_2 [Jul75]:

$$\text{TMR} = \frac{2\beta'_1\beta'_2}{1 - \beta'_1\beta'_2} \quad (2.37)$$

where β'_1 and β'_2 is the spin polarization of each ferromagnetic layer as in eq. (2.26).

Experimentally, giant GMR ratios have been reported by Parkin and Yuasa independently [Par04; Yua04]. Accordingly, a TMR ratio as large as 604% has been achieved in a MTJ consisting of $\text{Co}_{0.2}\text{Fe}_{0.6}\text{B}_{0.2}(6\text{nm})/\text{MgO}(2.1\text{nm})/\text{Co}_{0.2}\text{Fe}_{0.6}\text{B}_{0.2}(4\text{nm})$ at room temperature [Ike08].

Another application of MTJs which constituted a major breakthrough was the experimental verification of the *spin transfer torque* (STT) [Tso98; Alb00], a concept first proposed by Slonczewski in 1996 [Slo96]. Essentially, if we think again of a FM/NM/FM structure as the SV in Fig. 2.7, at the contact with the free FM, the STT acts on the spin current to align it in the direction of the magnetisation. Simultaneously, a reaction torque \vec{T} is exerted on the magnetisation of the free layer (i.e. there is a transfer of spin angular momentum) causing

magnetisation reorientation [Slo02; RS08]. This torque can be described by adding to the LLG equation (2.20) a term of the form:

$$\vec{T} \propto \vec{m}_{free} \times (\vec{m}_{free} \times \vec{\mu}_s) \quad (2.38)$$

where \vec{m}_{free} is the magnetization of the free FM layer in the SV. The discovery of STT was very exciting as it offered a faster and more efficient switching mechanism without using large magnetic fields. Also, it enables addressing ferromagnetic elements individually in large arrays. Rapidly, STT combined with MTJ technology was implemented in data storage, giving rise to a new solid state magnetic random access memory, STT-MRAM [Eve].

2.4.1 Spin-orbit coupling effects and thermal effects in spintronics

The previously mentioned devices exploit spin-polarized currents. However, a second generation of spintronic devices seeks the use of pure spin currents. In this context, SOC effects such as the spin Hall effect (SHE) are of particular interest.

The Valet Fert model in § 2.3 excludes any interaction between charge and spin within the bulk, and it only allows interaction at the interface. To describe the SHE however, charge current and spin current must be coupled, enabling a spin to charge conversion. The origin of this coupling is the SOC and occurs via two different mechanisms. In the first mechanism, electrons with different spins are scattered in opposite directions by SO coupled impurities through side-jump and skew scattering mechanisms [Vig10]. This is known as the extrinsic SHE and was first described by Mott [MM33]. The second mechanism is the intrinsic SHE. In this case, the SO-coupled band structure of the metal or the SC leads to spin-dependent electron trajectories [KL54]. The equations that couple charge and spin current densities are [Dec18; Sin15; Dya07]:

$$j_i^c = \sigma E_i + |e|D \frac{\partial n}{\partial x_i} - |e|\theta_{SH}\epsilon_{ijk} \left[\mu' E_j s_k + D \frac{\partial s_k}{\partial x_j} \right] \quad (2.39)$$

$$j_{ij}^s = \frac{h}{2} \left\{ -\mu' E_i s_j - D \frac{\partial s_j}{\partial x_i} - \frac{\theta_{SH}}{|e|} \epsilon_{ijk} \left[\sigma E_k + |e|D \frac{\partial n}{\partial x_k} \right] \right\} \quad (2.40)$$

where μ' is the spin-independent electron mobility. θ_{SH} is the so-called spin Hall angle and ϵ_{ijk} is the Levi-Civita symbol. In equation (2.39) the third term corresponds to the anomalous Hall effect (AHE) whereby a transverse charge current is created from a spin polarized current. The fourth term accounts for the iSHE which converts a pure spin current into a perpendicular charge current. The distinction between these two terms have only risen historically due to the

difficulties of creating a pure spin current which only became possible recently. In the reciprocal effect, this distinction is not made and both third and fourth term in eq. (2.40) define SHE. In a heavy metal (HM) with high SOC such as Pt, a charge current flowing in the \hat{z} direction, $\vec{j}_c = j_c \hat{z}$, is converted into a spin current $\vec{j}_s = j_s(-\hat{x})$ within the HM (see Fig. 2.8) according to [Sin15]:

$$\vec{j}_s = \frac{\hbar}{2|e|} \theta_{SH} \vec{j}_c \times \vec{\sigma} \quad (2.41)$$

where $\vec{\sigma}$ is the spin polarization vector. The conversion efficiency is determined by the spin Hall angle, θ_{SH} .

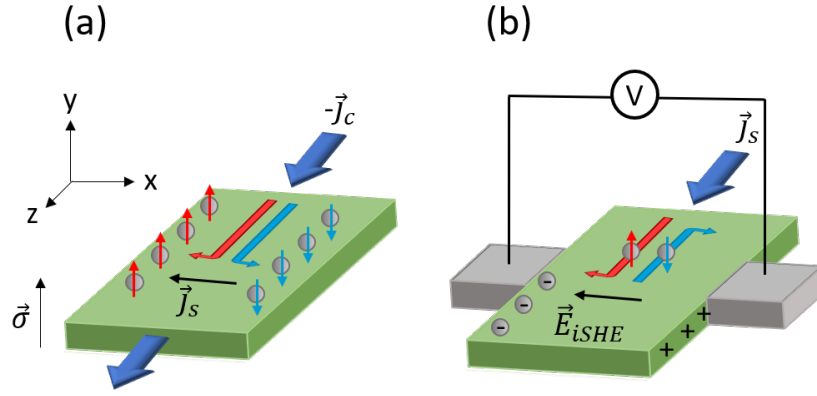


Figure 2.8: Representation of: (a) the SHE effect where a charge current leads to the generation of a transverse pure spin current in the NM with high SOC; and (b) the iSHE effect where the injection of a pure spin current gives rise to a charge accumulation and hence, a voltage across the NM.

If a FM is attached to the HM, the spin current leads to spin accumulation at the interface and part of it is diffused into the FM. At the FM, the component transverse to the magnetization is absorbed inducing a torque in the magnetization. In metals, devices have been demonstrated which replace the spin-filtering FM in a MTJ with a paramagnetic layer with large θ_{SH} [WAKA13; Roy14]. These devices have a major advantage over conventional MTJs in that the read paths and write paths are separate. Another recent and very promising application of the SHE relies on the inverse effect, iSHE for the generation of spin currents to be injected into SCs through the so-called *spin-pumping* process.

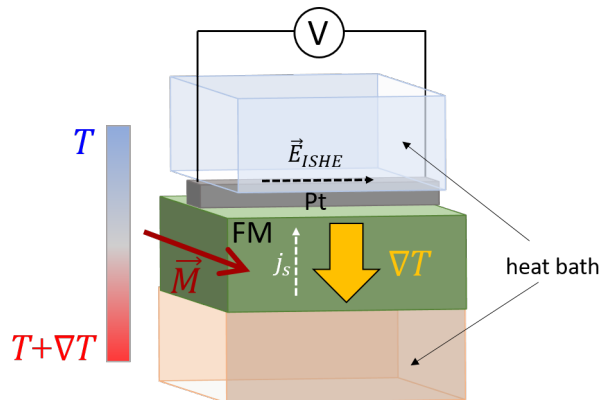


Figure 2.9: Typical geometry of a so-called longitudinal SSE experiment where a temperature gradient ∇T creates a spin current in the FM which is injected into the HM (Pt). The thermally induced spin accumulation is measured on the Pt as an inverse spin Hall signal, V_{iSHE} .

Thermal effects can also be used to inject a spin current into a NM. The spin equivalent of the well-known Seebeck effect, namely the spin Seebeck effect (SSE), was first observed in Permalloy by K. Uchida and co-workers [Uch08]. The Seebeck effect is the generation of an electric voltage when a temperature gradient (∇T) is applied across a conductor. Uchida *et al.* [Uch08] initially described SSE in terms of the spin accumulation μ_s created by ∇T by using the two conduction channel model in § 2.3, similarly to the conventional Seebeck effect. Their original explanation was that in a FM, spin-up and spin-down carriers have different scattering rates and densities and therefore, have different Seebeck coefficients⁵ $S_{\uparrow(\downarrow)}$. Thus, the FM can act itself as a thermocouple creating a spin voltage when a temperature gradient is applied. The geometry for a typical measurement of SSE can be seen in Fig. 2.9. Here, a temperature gradient is applied across a FM which generates a spin accumulation into the NM. If the NM has a high SOC, the injected spin current is converted into a charge current due to the iSHE, giving rise to an electric voltage that is proportional to ∇T . Later on, it was found that thermally generated iSHE signals could also be observed in ferromagnetic insulators [Gan17; Qu13] and thus, the SSE could not be explained by conduction electrons. The currently accepted picture of SSE [Xia10] is that it is actually a magnon-induced phenomenon.

2.5 Generation of spin currents

As we have seen throughout this chapter, there are several ways to generate spin currents in non-magnetic materials. These include electrical spin injection from a FM (desirable for large

⁵this effect would later be known as the spin-dependent Seebeck effect.

scale implementation) [JFVW01], optical spin injection [PM76], FMR-driven spin pumping [YH18; Sán13], SOC effects such as SHE [WAKA13; Roy14] and thermal effects such as SSE [Gan17; Qu13]. The efficiency of this spin current generation is critical for device application.

One of the most common methods for spin injection is to attach a FM to a NM through an ohmic contact or a tunnel barrier. Injection can be electric or via the aforementioned SOC effects. However, the interface between a FM and a NM for spin generation is limited due to the interfacial spin scattering which occurs with the presence of defects and contaminations. It is also important to eliminate any other effects, namely stray fields from the FM, which distort the estimation of the injection efficiency. By utilising highly spin-polarised FMs, such as half-metallic (HMF) Heusler alloys, the efficiency can be increased up to almost 30% to date.

For efficient spin injection, the conductance matching at the FM/ NM interfaces also plays a crucial role. Indeed, when boundary conditions are applied at the interface of a FM and a NM in equation (2.33), the solution represented as a function of z is shown in Figure 2.10[FJ01]:

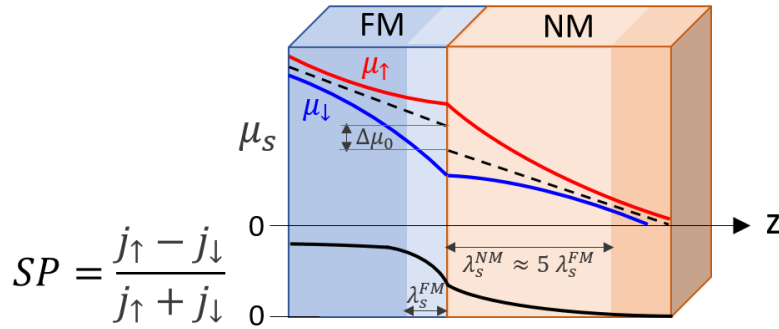


Figure 2.10: Spin accumulation μ_s and polarization of the spin-current SP in a FM/NM interface when the corresponding boundary conditions are introduced in eq. (2.33). As one can see, near the FM/NM interface, the polarization of the spin current is reduced nearly by half at the FM. This occurs due to the conductivity mismatch between the two materials. In a FM/SC interface the polarization is reduced even more, making spin-injection into the SC very inefficient.

The spin polarized current in the FM far from the interface ($\Delta\mu > 0$) is converted to a non-polarized current in the NM ($\Delta\mu \rightarrow 0$), also far from the interface. At the FM/NM interface, the ECP difference, $\Delta\mu_0 = \mu_s^{FM}(z=0) - \mu_s^{NM}(z=0)$, gives rise to a spin-coupled interface resistance [FJ01; Kri16]:

$$R_I = \frac{\Delta\mu_0}{eI} = \frac{\alpha_{FM}'^2 (\sigma_{NM}^{-1} \lambda_s^{NM}) (\sigma_{FM}^{-1} \lambda_s^{FM})}{\sigma_{FM}^{-1} \lambda_s^{FM} + (1 - \alpha_{FM}'^2) \sigma_{NM}^{-1} \lambda_s^{NM}} \quad (2.42)$$

In (2.42), $\sigma_{FM} = (\sigma_{\uparrow}^{FM} + \sigma_{\downarrow}^{FM})/2$, so that $\sigma_{\uparrow(\downarrow)}^{FM} = (1 (\pm) \alpha_{FM}') \sigma_{FM}$. The spin polarisation of the current at the interface $SP = (j_{\uparrow} - j_{\downarrow})/(j_{\uparrow} + j_{\downarrow})$ is then given by:

$$SP_I = \frac{\alpha'_{FM}}{1 + (1 - \alpha_{FM}^2) \cdot \frac{\rho_{NM}\lambda_s^{NM}}{\rho_{FM}\lambda_s^{FM}}} \quad (2.43)$$

where $\rho_{FM(NM)} = \sigma_{FM(NM)}^{-1}$. Therefore, the interface polarization is dominated by the ratio $\rho_{NM}\lambda_s^{NM}/\rho_{FM}\lambda_s^{FM}$. In most systems, this leads to a reduced spin injection because FMs have a lower spin resistance than NMs (i.e. $\rho_{NM}\lambda_s^{NM} > \rho_{FM}\lambda_s^{FM}$). We can think of a FM as a spin reservoir, where absorbed spins (diffused back from the NM) tend to flip to align with the magnetization of the FM. For a FM/SC interface the ratio is much larger and this effect is very drastic. The depolarisation occurs near the interface within the FM, preventing any spin-injection into the SC. This problem is known as a conductivity mismatch [Sch00; YF02].

One way to overcome the conductivity mismatch, is adding a thin insulating barrier which will act as an additional spin-dependent resistance at the interface [FJ01; Ras00]. Such spin-dependent resistance will create a discontinuity of the ECP difference at the interface. This in turn will make a balance between the spin flips, so that a comparable number of spin-flips occur in the SC and FM.

If one looks at equation (2.43), it can be seen that if the ferromagnet is 100% spin polarized (i.e. the injector is a HMF), $\alpha'_{FM} = 1$ and the conductivity mismatch can be avoided as $SP_I = 1$, achieving theoretically 100% spin polarized current at the SC. This has the additional advantage that no tunnel barrier is needed, which can make growth significantly harder.

2.6 Half-metals

For the most efficient spin-injection one needs the source to have almost 100% spin-polarization. This is the case of *half-metallic ferromagnets* (HMF). In Figure 2.11, a schematic representation of the conduction bands in a FM and a HMF are shown. As one can see, in addition to having an asymmetric DOS of spin-up and spin-down conduction electrons (as occurs in ferromagnetic materials), HMFs are characterized by a bandgap which splits the two spin conduction channels. Due to this bandgap, the flow of the electrons corresponding to one of the spin bands is prevented and therefore, such materials are 100% spin polarized at the Fermi level and are of great interest for spintronic devices. If one looks back at equations (2.37) and (2.43), half-metallicity can play a key role in both MTJs and hybrid devices. There are four major types of materials that exhibit half-metallic properties. These are diluted magnetic semiconductors (DMS), oxide compounds, perovskites and *Heusler alloys* (§ 2.7). The compounds studied in this thesis correspond to the latter category.

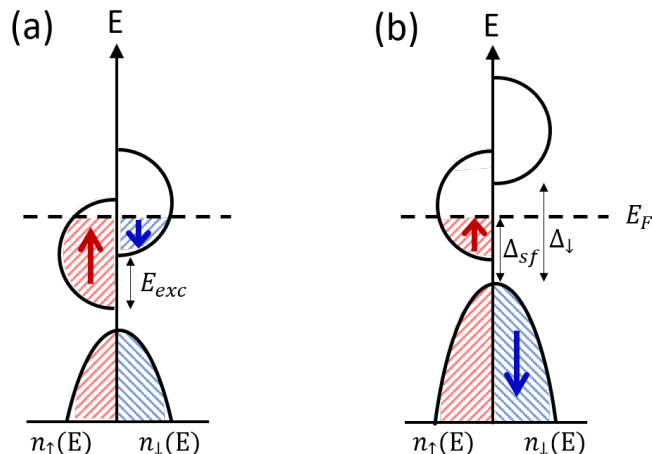


Figure 2.11: DOS of the d and s sub-bands of a FM (a) and a HMF (b) where the spin-up channel is conductive but the spin-down channel is insulating. Hence, the HMF is 100% spin-polarized at the Fermi level.

DMS are semiconductors doped with transition metal atoms such as Fe, Cr or Mn. Some of these materials, for example Mn-doped Ge are predicted to have 100% spin polarization at the Fermi level [Str03]. Experiments have also confirmed zinc-blend compounds such as (Ga,Mn)As [Mun89] and CrAs [AMS00] to have half-metallic properties. However, the Curie temperature (T_c) of these materials is below room temperature (RT), which hinders their integration in spintronic devices. Oxides such as rutile CrO_2 [Sou98] and spinel Fe_3O_4 [Gil16] are also half-metallic. A lot of research has been done in magnetite which has a very high T_c . The issue with Fe_3O_4 is that it only grows at a very specific range of oxygen pressure. Small deviations from the ideal growth conditions lead to variations of stoichiometry and formation of defects that are detrimental for its half-metallic behaviour. Some perovskite compounds also possess almost 100% spin polarization. For instance, this is the case of $\text{La}_{0.7}\text{Sr}_{0.3}\text{O}_3$ which was one of the first materials where half-metallicity was experimentally proven [Par98]. However, up to this date there is no experimental evidence of half-metallicity at RT in perovskites. Bulk Heusler alloys do exhibit half-metallicity at RT but there are no reports of half-metallicity in Heusler thin films yet. Even so, they are still the most promising candidates as spin injectors due to their high T_c and their lattice parameters matching that of technologically relevant substrates. Remarkably large GMR ratios of 82% have been achieved using the quaternary Heusler compound $\text{Co}_2\text{Fe}(\text{Ga}_{0.5}\text{Ge}_{0.5})$ (CFGG) at RT in CPP-GMR devices [Jun16].

2.7 Heusler compounds

Heusler compounds are an exceptional class of materials comprising more than 1500 members; a comprehensive review of these compounds is given in [GFP11] and [Fel15], from which most of the information in this section has been extracted. Half-Heusler compounds consist of three inter-penetrating fcc lattices with 1:1:1 stoichiometry (XYZ); whereas full-Heusler compounds are four inter-penetrating fcc lattices (see Fig. 2.12) with 2:1:1 composition (X_2YZ), and were discovered by Friedrich Heusler in 1903 [Heu03; HSH03]. A large majority are metallic (as is the case of Co_2FeSi), although a small group of semiconducting compounds (e.g. Fe_2VAl) also exists. In half- and full-Heusler alloys, X and Y are transition metal elements (Co, Fe, Ni, Cu...) and Z is a main group element (Si, Al, As, Sb...). The first discovered Heusler alloys, $CuMnSb$, Cu_2MnAl and Cu_2MnSn attracted a lot of attention because they display ferromagnetic properties while being formed from exclusively non-magnetic elements. Indeed, the appeal of this class of materials is the appearance of unexpected properties which can not be derived straightforwardly from their constituent elements giving rise to a vast range of (multi)functionalities including multiferroics, superconducting alloys and tunable topological insulators amongst others. Another of their properties can be half-metallicity.

The first Heusler alloy predicted to have half-metallic properties was $NiMnSb$ [DG83], although more recent experiments have shown that Mn segregation at the surface and/or interfaces reduces this half-metallic behaviour [Ris00]. Since then, many Heusler alloys have been investigated for their applicability in spintronics. Tetragonally distorted Mn-rich Heuslers are interesting for STT, SHE and permanent magnets due to their high SP, high MCA and high T_c but low Gilbert damping [Win12; Wol15]; whereas Co-based alloys (specially the Co_2YZ type), are particularly attractive as spin-injectors for CPP-GMR [Fur13; Jun16; Li18; Kub17] and TMR [Oka05; Sak06b; STT09; Tez06], as well as in lateral all-metallic SV devices [Ham12; Kim12; Oki13; Oki17], due to their high SP, high M_s , high T_c and low coercivity. Regarding spin injection/detection into SCs like GaAs, using Co_2FeSi injectors resulted in an improvement of the spin injection efficiency to slightly above 50% [Ram08] in comparison to the 40% or less achieved using conventional Fe injectors [Zhu01; Han02].

2.7.1 Atomic structure of Heusler alloys

The atomic structure of X_2YZ alloys is a cubic $L2_1$ structure or Cu_2MnAl with space group 225 ($Fm\bar{3}m$). As mentioned above, the unit cell consists of 4 interpenetrating fcc lattices. Two of these sublattices are populated by the X atom species, another sublattice by the Y species

and the last sublattice by the Z species. The shift vectors, in normalized units, between these 4 sublattices are given by:

$$\begin{aligned} 1^{\text{st}} \text{ X sublattice} &: (0, 0, 0) \\ 2^{\text{nd}} \text{ X sublattice} &: (1/2, 1/2, 1/2) \\ \text{Y sublattice} &: (1/4, 1/4, 1/4) \\ \text{Z sublattice} &: (3/4, 3/4, 3/4) \end{aligned}$$

Unlike in half-Heusler compounds, which only exhibit one magnetic sublattice, full-Heuslers have two distinct magnetic sublattices because the two X atoms in the unit cell occupy the tetrahedral sites, hence, allowing a magnetic interaction between the X atoms and the formation of a second, more delocalized magnetic sublattice on the Y sites. Due to the two different magnetic sublattices, full-Heusler compounds show all kinds of magnetic phenomena, such as ferro- or ferrimagnetism, half-metallic ferrimagnetism (Mn_2VAl , $\text{Cr}_2\text{MnSb}\dots$), and half-metallic ferromagnetism (Co_2FeSi , $\text{Co}_2\text{FeAl}\dots$). In this thesis, the Co_2FeSi (CFS) alloy will be investigated. In CFS, Fe corresponds to the Y species and Si corresponds to the Z species. The atomic structure of CFS has been represented in Fig. 2.12a.

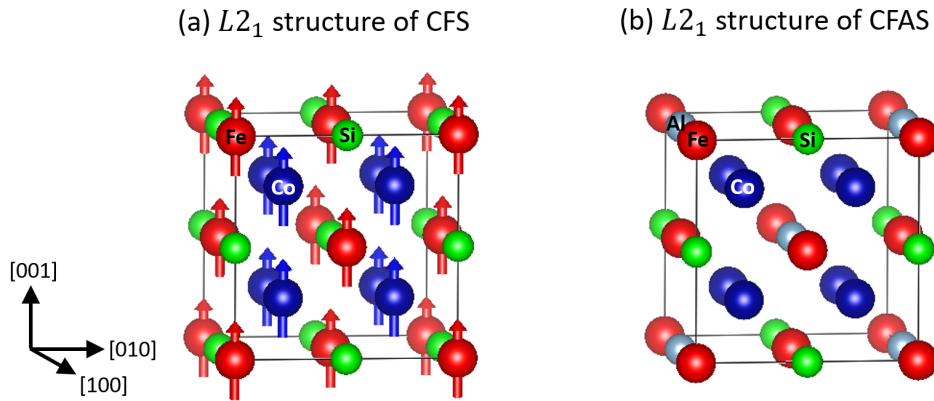


Figure 2.12: Structure of the fully $L2_1$ ordered CFS alloy (a) and CFAS alloy (b), with the blue, red, green and grey sites representing the location of the Co, Fe, Si and Al atomic species. This and the subsequent figures in this section have been drawn with VESTA.

Direct exchange between the Co-Co and Fe-Co pairs result in a parallel alignment of the spin moments. Figure 2.13 a and b (c and d) shows the atomic stacking for the $\vec{z} = [001]$ ($\vec{z} = [111]$) growth direction. Each stacking is shown along two orientations: along $[001]$ and $[1\bar{1}0]$ for $\vec{z} = [001]$; and along the two orthogonal directions $[1\bar{1}0]$ and $[11\bar{2}]$ for $\vec{z} = [111]$. These projections will be important when discussing cross-sectional (S)TEM (§ 4.2) studies later in

this thesis.

Co₂YZ Heusler compounds including CFS, follow the so-called Slater-Pauling curve, i.e. their total magnetic moment scales linearly with the number of valence electrons [KFF07]:

$$m = N_v - 24 \quad (2.44)$$

where N_v is the number of valence electrons. This behaviour is a sign of half-metallicity in that changing the number of valence band electrons changes the filling of the metallic spin polarized conduction band and consequently, the magnetic moment is increased/decreased proportionally to the number of valence band electrons. This is only true if the Fermi level is within the band gap. Like many other members of the Co₂YZ family, CFS is a soft ferromagnet with small MCA and high magnetization. Specifically, it has an M_s of ≈ 1100 emu/cc ($6\mu_B$ per formula unit) and has the highest T_c among all Heusler compounds, $T_c = 1120$ K [Wur06] (Tab. 2.2). With a lattice constant of 0.565 nm, CFS has a small lattice mismatch with technologically relevant substrates, 0.02% for Ge(001), 0.05% for GaAs(001), 4% for Si(001) and 4.9% for MgO(111); and it exhibits a magnetic damping constant of $\alpha \approx 8 \times 10^{-3}$ [Oog07; Haz19].

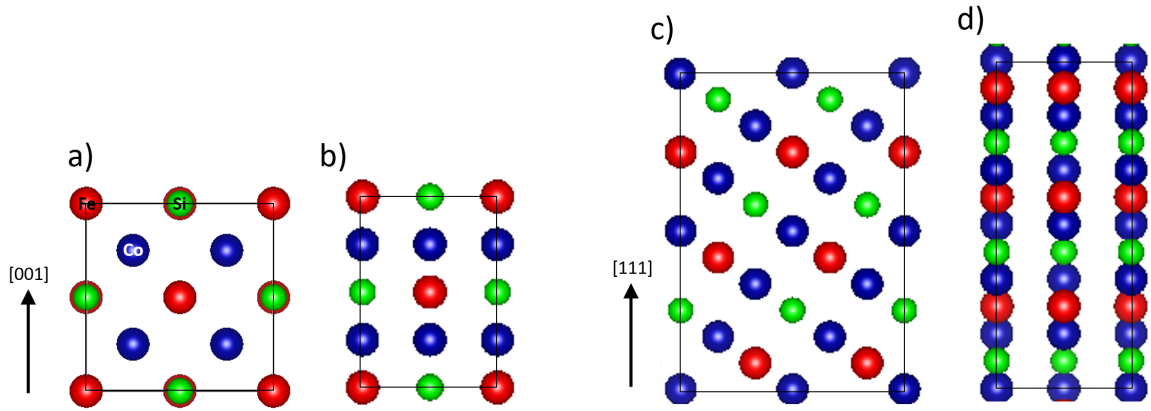


Figure 2.13: Repeat unit of CFS: (a) along the [001] growth direction and [100] projection; (b) along the [001] growth direction and $[1\bar{1}0]$ projection; (c) along the [111] growth direction and $[1\bar{1}0]$ projection; (d) along the [111] growth direction and $[11\bar{2}]$ projection. Colour coding is the same as in Fig. 2.12.

Co₂FeSi can be alloyed with another ternary compound, Co₂FeAl (CFA), to produce the Co₂FeAl_{0.5}Si_{0.5} (CFAS) quaternary Heusler compound which has some advantageous properties over its predecessors. In quaternary compounds, two atomic species can occupy the same sublattice. In the case of CFAS, the Z sublattice is occupied by both Si and Al with an equal concentration (see Fig. 2.12b). Another example is Co₂Fe_{0.5}Mn_{0.5}Si (CFMS) where Fe and Mn

share the Y sublattice.

2.7.2 Chemical disorder and half-metallicity in Heusler alloys

Even if Co-based Heuslers are ideal for spintronic applications, there are several factors which can affect their desired properties, particularly half-metallicity. These factors include stoichiometry, chemical and structural ordering and strain. For the inclusion of Heusler alloys in spintronic devices, they have to be grown as thin films. Therefore, the chemical and structural order must be preserved at the atomic level which constitutes a great challenge.

One of the most common defects in Co_2XY films is chemical disorder. If the Y and Z atomic species are evenly mixed (see Fig. 2.14a), the resulting structure is CsCl-like. As a consequence of this type of disorder, also known as B2-type, the symmetry is reduced and the resulting space group is $\text{Pm}\bar{3}\text{m}$ (refer to Tab. 2.1). If on the other hand, there is an exchange between X-Y (Fig. 2.14b) or X-Z (Fig. 2.14c) atoms, the disorder is DO_3 -type and leads to a BiF_3 structure. In the B32a disorder, the Co atoms in one of the X sublattices are mixed with the Y species, whereas the second Co sublattice is mixed with the Z. However, this type of disorder is very rare and has seldom been reported. Apart from all these partially disordered structures, if all the positions are equivalent in a tungsten-like bcc-lattice with reduced symmetry, this is known as A2 disorder. The types of atomic site disorder have been summarized in Table 2.1. Of course, most samples are not completely ordered or disordered; in most occasions, small amounts of disorder in an ordered compound or a low degree of order in a disordered structure is observed.

General formula	Strukturberichte	Structure type	Space group
X_2YZ	L2_1	Co_2MnAl	$\text{Fm}\bar{3}\text{m}$ (No.225)
XZ	B2	CsCl	$\text{Pm}\bar{3}\text{m}$ (No.221)
YZ_3	DO_3	BiF_3	$\text{Fm}\bar{3}\text{m}$ (No.216)
YZ	B32a	NaTl	$\text{Fd}\bar{3}\text{m}$ (No.227)
X	A2	W	$\text{Im}\bar{3}\text{m}$ (No.229)

Table 2.1: General formula and structures of differently ordered full-Heusler compounds.

As an example of how disorder can affect half-metallicity, ab-initio studies on CFMS films showed that the most detrimental types of disorder were X-Y and X-Z which led to a reduction or even complete destruction of the spin polarization [HSL13]. Fortunately, they also showed that these two types of disorder involving the Co atoms are more unlikely to happen, so that the half-metallicity can be preserved. Miura and co-workers arrived to the same conclusion for

the $\text{Co}_2(\text{Cr, Fe})\text{Al}$ alloy in [MNS04]. On the other hand, Co_2XY films often crystallize in a B2 structure, especially those compounds containing Al in the Z sites, such as CFA. In some compounds the B2 structure, though less desirable than the L2_1 , still preserves spin polarization at the Fermi level and hence, it is also sought-after. All in all, the crystallinity of the thin films plays a major role in their half-metallic properties which in turn, has a strong influence on device performance; for example in MTJs, where site disorder results in lower TMR values [Ino08].

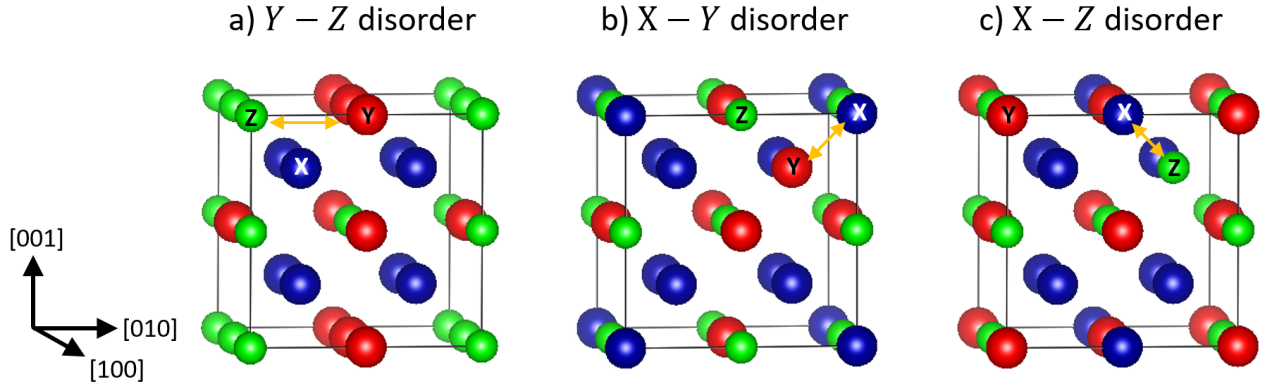


Figure 2.14: Possible disordered structures of the CFS alloy. (a) shows the Y-Z disorder, (b) shows the X-Y disorder and (c) shows the X-Z disorder. Colour coding follows the Fig. 2.12.

Even if the film were initially B2-ordered, the L2_1 structure can sometimes be achieved by annealing the film at temperatures $> 500^\circ\text{C}$ regaining its half-metallicity [TNS09; Kue18]. However, high temperature annealing is not ideal for CMOS processes and it can also result in detrimental interface effects, such as interfacial diffusion between the film and the substrate. In fact, many studies have reported issues related to interfacial intermixing or even the formation of secondary phases in Heusler/SC interfaces, where the atomic structure at the interface is different than in bulk. This in most cases works against an efficient spin injection from the Heusler electrode to the SC as was shown for the CFS/Si(111), CFAS/Si(111) and CFS/GaAs(001) interfaces in [Yam10], [Kue16] and [Has07] respectively. Even in MTJ metallic structures, the surface roughness and the interface morphology between the Heusler electrode and the insulating oxide barrier has a great influence on the TMR value [Oog06].

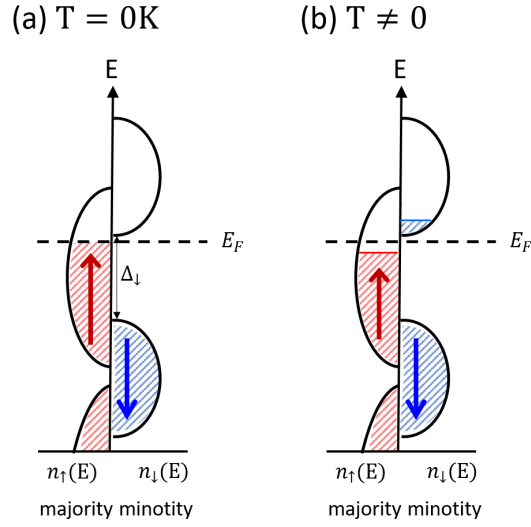


Figure 2.15: Schematic density of states of CFS with an energy gap Δ_\downarrow in the minority-spin band (\downarrow) and metallic band structure in the majority-spin band (\uparrow) when: (a) $T=0K$ and (b) $T \neq 0$. The Fermi-level is positioned very close to the bottom of the conduction band, which makes half-metallicity unstable against temperature increments.

In the table below, the magnetic properties of a few Co-based Heusler compounds have been summarized. In this thesis, a MBE system has been built for the growth of $\text{Co}_2\text{FeAl}_{1-x}\text{Si}_x$ thin films (Chapter 3). The motivation for building this system is precisely the combination of magnetic properties exhibited by the compounds belonging to this family, some of which have been listed⁶ in Tab. 2.2. All the Heusler alloys in the table have been predicted as 100% spin polarized at the Fermi level in the $L2_1$ structure [FF07], and in all of them this number decreases as the structural symmetry is reduced. CFA draws attention for being one of the Co-based compounds with smallest magnetic damping, a great quality for achieving a smaller switching current density in spin-transfer devices [Suk12; Wen12]. However, CFA films grow in a B2 structure and no trace of $L2_1$ ordering has been observed after annealing these films at elevated temperatures [Cui14; Suk12; Wen12]. On the contrary, $L2_1$ or mixed B2/ $L2_1$ -ordered CFS films have been reported numerous times [YWC13; Li18], occasionally even at low temperatures [Zan10]. Both CFA and CFS are however, very unstable HMFs because their Fermi level is situated at one of the edges of the energy band gap [FF07]. The advantage of CFAS is that, unlike CFS and CFA (refer to Fig. 2.15 to see the DOS of CFS), it has a mid-gap Fermi level, which makes its half-metallic properties more robust against temperature

⁶Note that improved annealing and growth techniques have allowed the reduction of α to even lower values than those listed in the table for some alloys. In any case, CFA is still the one showing the lowest α , with the smallest value reported in literature being $\alpha_{\text{CFA}} = 1 \times 10^{-3}$ ([Kum17]).

effects and small strain fields. Although CFAS is more prone to B2 disorder than CFS, the spin polarization of the B2 structure is preserved to a greater extent than in CFS (SP=0.9, 0.5 and 0.6 for B2-CFAS, B2-CFA and B2-CFS respectively at 5K) [Nak07] and hence, it is still one of the most promising candidates for spintronic applications with high saturated moment, high T_c and α values comparable to those of CFA.

Heusler compound	Crystal structure	Magnetic moment at 5K (μ_B /f.u)	T_c (K)	Gilbert damping parameter α
Co ₂ FeAl	L2 ₁ /B2	4.96 [BVEJ83]	1000 [Tru10]	2×10^{-3} [Cui14]
Co ₂ FeSi	L2 ₁ /B2	6 [Wur06]	1120 [Wur06]	8×10^{-3} [Oog07]
Co ₂ FeAl _{0.5} Si _{0.5}	L2 ₁ /B2	5.5 [Pet13]	1150 [Vah14]	2.5×10^{-3} [Loo14]
Co ₂ MnSi	L2 ₁ /B2	4.96 [Bro00]	985 [Bro00]	6×10^{-3} [Oog15]

Table 2.2: Magnetic properties of some Co₂XY Heusler alloys, including the compound studied in this thesis, CFS.

Chapter 3

Principles and design of a MBE system for the growth of Heusler alloys

3.1 Introduction

One of the main obstacles researchers faced when using Co-based Heusler films in MTJs was the strong dependence of TMR with temperature. For example, in [Sak06a] a remarkably high TMR ratio of 570% was achieved at 2K with $\text{Co}_2\text{MnSi}/\text{Al-O}$ stacking structures, but it decreased to only 70 % at RT. Such strong temperature dependence occurs because the half-metallicity of the Heusler electrodes is unstable against temperature fluctuations. The same occurs if the Co_2MnSi electrodes are replaced with CFA or CFS. In these compounds the Fermi-level is positioned very close to the top of the valence band and the bottom of the conduction band respectively (refer to fig.2.15). Although still predicted as 100% spin-polarized, they suffer a loss in spin polarization when the temperature increases and the electronic states near the boundaries of the band gap broaden. By adding Si to CFA, the Fermi level can be brought to the middle of the minority band gap with a Co:Fe:Al:Si=2:1:0.5:0.5 stoichiometry. This makes the half-metallicity of $\text{Co}_2\text{FeAl}_{0.5}\text{Si}_{0.5}$ (CFAS) more stable against temperature fluctuations. Using CFAS in MTJs improved the temperature dependence considerably [Tez06] and has also been used to achieve a highly efficient spin injection at RT into semiconductors [Fuj17].

Due to the thermal stability of CFAS, one of the main goals of this project has been the commissioning of a growth system for CFAS thin films for future spin-injection experiments. Equipped with Co, Fe, Al and Si evaporation sources, the system can also be used for the growth of CFA and CFS amongst others. Given the added difficulty of growing a quaternary alloy like CFAS, the system has been first optimized for the growth of CFS thin films as will be shown in chapters 5 and 6. The growth chamber has been designed by Dr. Barat Kuerbanjiang

and his help has been indispensable during the construction of the system.

Over the past 15 years, numerous studies have been performed on the synthesis of Co-based Heusler compounds. These studies have included different growth methods such as magnetron sputtering [MRK17; Haz19; Sch07], pulsed laser deposition (PLD) [Pat19] and molecular beam epitaxy (MBE) [Zan10; Ham16; Kud19]. However, the growth of good-quality Co_2YZ films is not straight forward. As explained in § 2.7.2, the preservation of the ideal physical or electronic properties of these films highly depends on characteristics such as the chemical/structural ordering [HSL13; MNS04] and the quality of the interface [Yam10; Kue16]. As a consequence, not all the growth methods have proven to be equally successful for the growth of highly-ordered Co_2YZ films. Amongst the different techniques, MBE stands out due to the UHV environment and the low deposition rates which allow a fine control of the growth process.

In [MRK17], three sets of CFS films were grown by DC-magnetron sputtering on GaAs(001), MgO(001) and Si(111) substrates. In that study, R.Mohankumar *et al.* observed that the films only showed the $L2_1$ ordered phase after they were annealed at a temperature of $\approx 700^\circ\text{C}$. On their part, Schneider *et al.* reported that for CFS films deposited by RF-sputtering on $\text{Al}_2\text{O}_3(11\bar{2}0)$ and MgO(001), post-annealing treatments above 700°C were also needed to find some evidence of $L2_1$ growth in the otherwise amorphous CFS films grown at RT [Sch07]. Regarding the PLD technique, none of the CFS films deposited by N. Patra *et al.* [Pat19] at various substrate temperatures, ranging from 150 to 600°C , showed any sign of either B2 or $L2_1$ crystallization. In fact, the existence of at least some partial $L2_1$ ordering in Heusler films grown at low temperatures has only been achieved by MBE [Zan10; Ham16; Kud19].

The first part of this chapter, comprising sections § 3.2, § 3.3 and § 3.4, will introduce general concepts about thin film growth and in particular, about MBE growth. Section § 3.5 will focus on the design and the technical specifications of the MBE system developed in this thesis. Two important analytical tools installed in the MBE chamber, QCM and RHEED, allow a preliminary assessment of the films and their working principle will be described in section § 3.6.

3.2 Vacuum generation

In order to grow high quality thin films, a precise control of the deposition rate, film thickness and stoichiometry is required. One of the most important characteristics of the different deposition methods is the pressure range at which the growth is carried out (see Fig. 3.1).

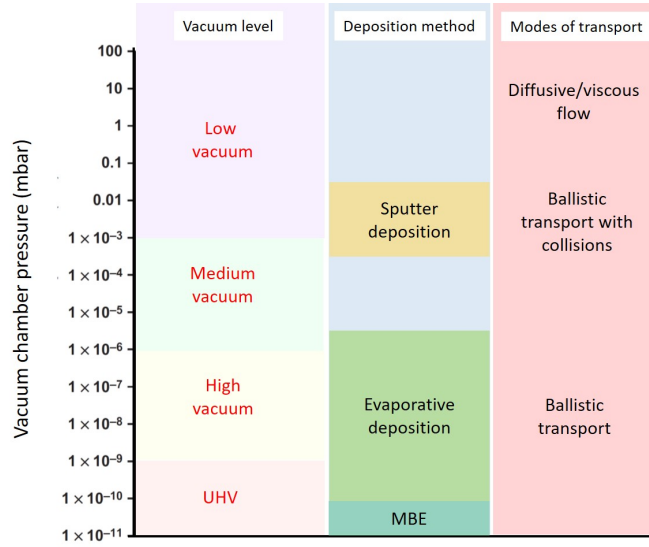


Figure 3.1: Diagram showing physical vapour deposition (PVD) methods to grow thin films based on the working pressure and the modes of material transport involved. Evaporation takes place at HV pressures whereas sputtering usually operates at 10^{-1} to 10^{-3} mbar because it requires a constant feed of Ar to activate the plasma required to sputter the materials from the source. MBE growth is an advanced form of evaporation deposition which operates at UHV. The figure has been adapted from [Cam15].

Although the boundaries are rather arbitrary, the level of vacuum can be categorized as low/rough vacuum ($1 - 10^{-3}$ mbar), medium vacuum ($10^{-3} - 10^{-6}$ mbar), high vacuum or HV ($10^{-6} - 10^{-9}$ mbar) and *ultra-high vacuum* or UHV ($< 10^{-9}$ mbar). In the low vacuum range, the mean free path of the gas molecules, equation (3.1), is much shorter than the characteristic size of the vessel that contains the gas and hence, there are frequent collisions between gas molecules that dominate over the interactions at the sample surface. On the contrary, the high vacuum range is sufficiently rarefied to allow free passage of particles and molecule-surface collisions dominate the gas behaviour. In this regime the gas flow is molecular and the transport mechanism is ballistic. MBE operates at even lower pressures ($10^{-10} - 10^{-11}$ mbar) to minimize contamination and to allow epitaxial growth.

$$\bar{\lambda} = \frac{k_B T}{\sqrt{2} \pi d_m^2 p} \quad (3.1)$$

In eq. (3.1), p is the vapour pressure of the gas (in Pascal), T is the absolute temperature (in K) and d_m is the diameter of the gas molecule. This and eq. (3.2) can be easily derived using the Maxwell–Boltzmann distribution of molecular speeds for an ideal gas. Taking the kinetic diameter for a typical residual gas like N_2 , $d_m^{N_2} = 3.64 \times 10^{-10}$ m, one finds that at ambient conditions the mean free path is in the order of nm, whereas under UHV conditions $\bar{\lambda}$

increases to several km:

$$\begin{aligned}\bar{\lambda} &\approx 68 \text{ nm for } p = 10^3 \text{ mbar} \\ &\approx 6.8 \text{ cm for } p = 10^{-3} \text{ mbar} \\ &\approx 68 \text{ km for } p = 10^{-9} \text{ mbar}\end{aligned}$$

Because the molecules of the more common gases are roughly comparable in size, the mean free paths will be of similar magnitude. A good textbook covering the fundamental physics about gases and vapors in the context of vacuum technology has been written by A. Chambers [Cha04].

A typical vacuum system for thin-film growth integrates a *vacuum chamber*, pumping units, process equipment (such as load-locks, manipulators, heaters, evaporators and gauges) and service equipment (controllers and power supplies). Vacuum pumps are crucial components that reduce the pressure inside the chamber by either removing the gas molecules out of the system and ejecting them into the atmosphere (*gas-transfer pumps*), or by bonding these gas particles to the walls of the chamber (*entrapment pumps*). Examples of gas transfer pumps are roughing pumps such as rotary pumps and scroll pumps, which typically reach pressures down to 10^{-3} mbar.

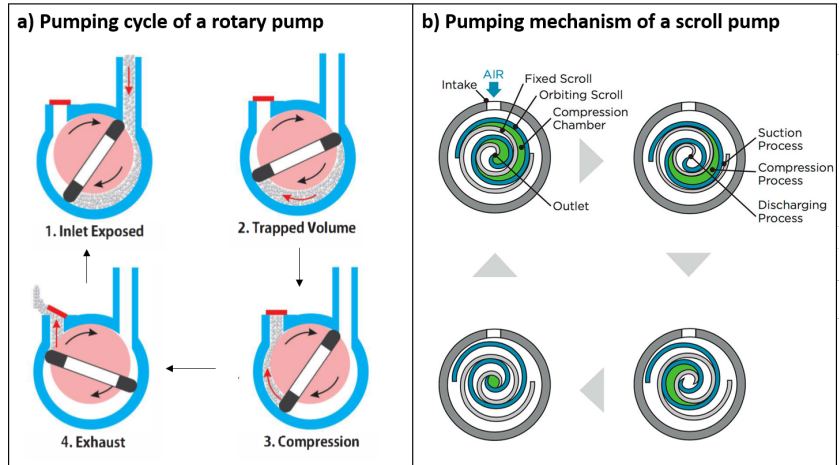


Figure 3.2: (a) Working principle of a rotary pump and (b) pumping mechanism of a scroll pump. One of the scrolls is fixed whereas the other orbits eccentrically trapping pockets of gas between them that are removed through the outlet. The figures were taken from [Hit] and [Ide] respectively.

A *rotary pump* consists of a vane mounted to a piston that turns eccentrically as shown in Fig. 3.2a. Springs move the vane in and out varying its length and allowing the vane slide

inside the housing. Gas entering through the inlet is pushed by the vane and is ejected from the pump through the exhaust. Oil is used for both sealing and lubrication which is not ideal as the oil can back-stream to the vacuum system leading to contamination. To increase efficiency and reduce backing line contamination, *scroll pumps* don't use any oil seals. Instead, a scroll pump uses two interleaving scrolls to pump the gas molecules out of the system, Fig. 3.2b.

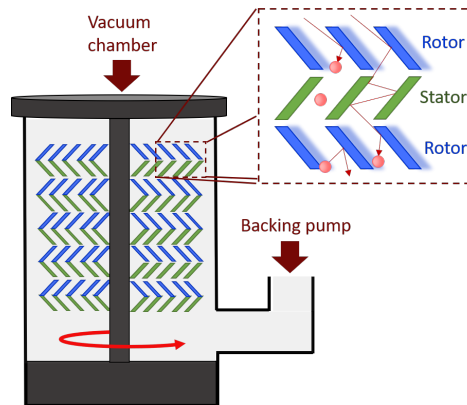


Figure 3.3: Representation of a turbomolecular pump that ejects the gas particles away using a set of rapidly moving rotors (in blue) interleaved with non-moving stators (in green).

In order to achieve pressures below 10^{-3} mbar, HV pumps such as turbomolecular pumps, must be used in combination with roughing pumps. A *turbomolecular pump* usually establishes a pressure of 10^{-7} mbar by spinning a series of blades called rotors interleaved with a set of non-moving blades called stators. The gas particles in the system impact with the rapidly moving surfaces of the rotor and are impulsed towards the outlet. The surfaces of the rotors form, with the stationary surfaces of the stators, intervening spaces in which the gas is transported to the backing port, Fig. 3.3.

To lower the pressure even further, the chamber itself, along with all bakeable components, has to be baked above 100°C to remove the water vapour from the walls. This enables a vacuum of $< 10^{-9}$ mbar which can be maintained with the aid of entrapment pumps like ion pumps and *titanium sublimation pumps* (TSPs). An ion pump consists of two negatively charged Ti or Ta plates and an array of circular anode cells, see Fig. 3.4a. A potential difference of $\approx 5 - 7$ keV between the cathodes and the anode array generates a large electrostatic field which pulls free electrons towards the anode. At the anode, the electrons get trapped in a circular motion around the magnetic field until they hit a gas molecule. This is represented in Fig. 3.4b for a O_2 molecule (in blue). From the collision a positively charged ion is formed O_2^+ (in red) which accelerates towards the Ti cathode at high velocity. When it hits the plate, Ti is sputtered into the anode walls. The original gas molecule then combines with the Ti (in orange) creating

TiO (in orange and yellow). Over the time, the anode assembly gets coated with Ti and Ti compounds reducing the pressure inside the chamber.

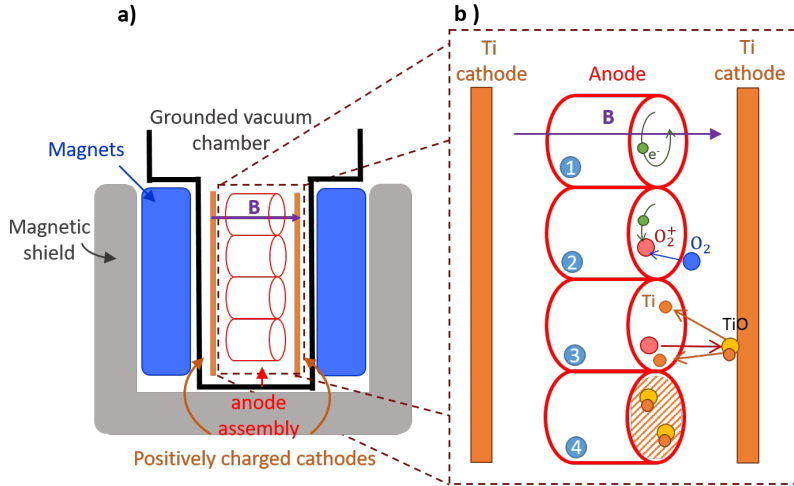


Figure 3.4: (a) Schematic diagram of a sputter ion pump and (b) its working principle.

A TSP works by running high current through a filament made of Ti and Mo alloy. The filament is heated to very high temperatures where the Ti atoms sublime. The Ti atoms make their way through the chamber until they land on a cooler surface, the chamber walls, where they solidify and form a film of pure Ti. As pure Ti is very reactive, it will react with the gas molecules in the system forming TiO or TiN molecules that will then condense at the walls. This way, the total amount of gas in the chamber decreases meaning a higher vacuum is reached. Eventually, all the Ti will have reacted and the filament will need to be heated again to create a new layer and start the process over. A turbomolecular pump working in combination with an ion pump and/or a TSP can easily establish pressures below 10^{-10} mbar in a well operated UHV system.

The pressure in the system is measured by pressure gauges, mainly pirani and ion gauges. The *pirani gauge* (Fig. 3.5) consists of a metal filament (usually a thin wire of Pt or W) suspended in a tube. Another filament, isolated from the vacuum system, is used as a reference. The filaments are heated by passing a constant electric current. The wire suspended in the gas will lose heat to the gas molecules that collide with the wire. If the gas pressure is reduced, less molecules will impact with the wire and the filament will lose heat more slowly. This change in the thermal conductivity results in a change in the resistance of the filament which provides a way to measure the pressure in the system. This type of gauge is sensitive to pressures between 1 mbar and 1×10^{-4} mbar. To measure lower pressures an ion(ization) gauge (IG), see Fig. 3.6, is needed. In an IG a heated filament, usually Ir or W, is used to emit electrons which

accelerate towards a grid. When the electrons pass into the space enclosed by the grid, they collide with the gas molecules that are in the system, producing positive ions. The ions are then collected by the ion collector which is at a negative voltage with respect to the grid. At a constant filament-to-grid voltage and electron emission current, the rate of formation of ions is directly proportional to the system pressure when the pressure lies between 10^{-5} and 10^{-11} mbar.

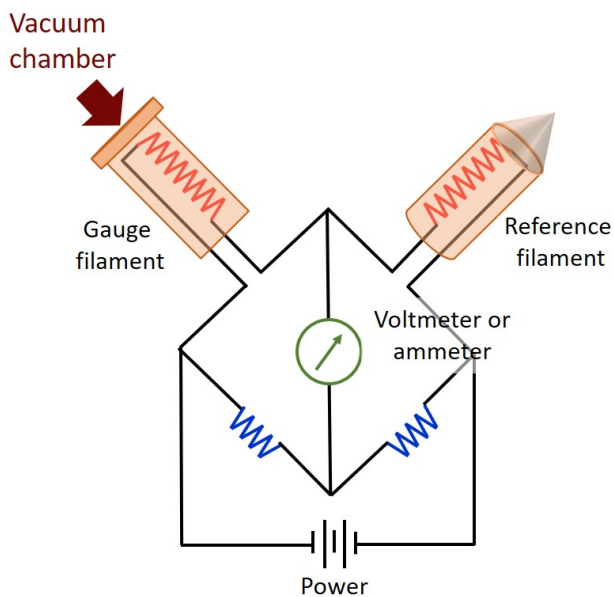


Figure 3.5: Circuitry of a Pirani Gauge.

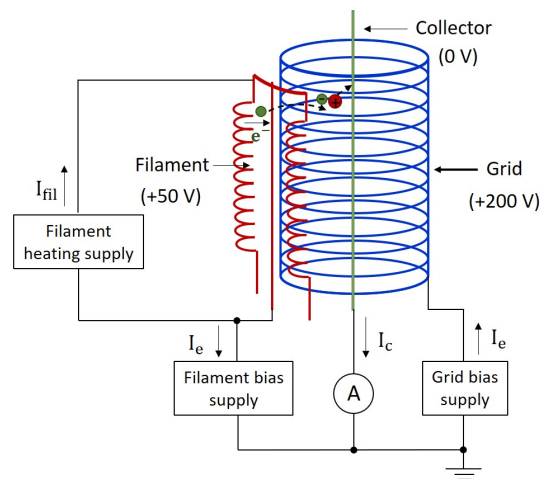


Figure 3.6: Illustration of an ion gauge.

Another component that allows to measure the vacuum in the system is the *mass spectrometer* or *residual gas analyzer* (RGA). In addition to measuring the total pressure, the mass spectrometer identifies the partial pressure of each gas in the chamber. As in the ion gauge, the mass spectrometer ionizes the gas molecules in the system through electron ionization. The ions are then accelerated to the same kinetic energy and subsequently deflected by a magnetic field according to their mass-to-charge ratio (m/e). The filtered ions are finally collected by a detector which can then quantify the abundance of each element in the system. The analysis of gases in a vacuum chamber is particularly useful to identify leaks from the system to the atmosphere. An example of the usefulness of the RGA is shown in Figure 3.7, where the RGA was used to test the Fe source (refer to § 3.5.2 for information on the evaporation sources).

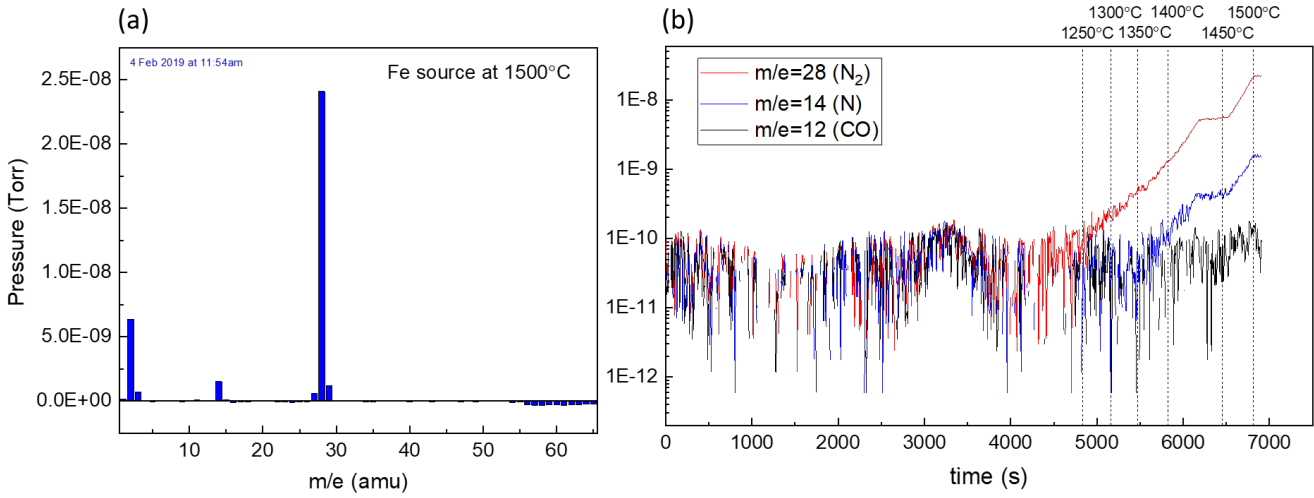


Figure 3.7: (a) Typical RGA scan taken during the outgassing procedure of the Fe source at 1500°C with an empty Al₂O₃ crucible (prior to loading the material). The scan shows high partial pressures at $m/e = 2, 14$ and 28 ; (b) time evolution of the $m/e = 12, 14$ and 28 partial pressures as the source was heated. The clear correlation between the pressure rise of $m/e = 14$ and $m/e = 28$ indicates release of N₂. This was eventually attributed to the decomposition of the PBN insulating rings caused by overheating of the crucible.

3.3 Growth modes

The exact characteristics of the grown film (roughness, composition, crystallinity...) depend crucially on the *mode of growth* which in turn is determined by the deposition parameters, such as chamber pressure, substrate temperature or vapour pressure of the deposited species. The individual atomic processes involved in the growth of the film are illustrated in Fig. 3.8.

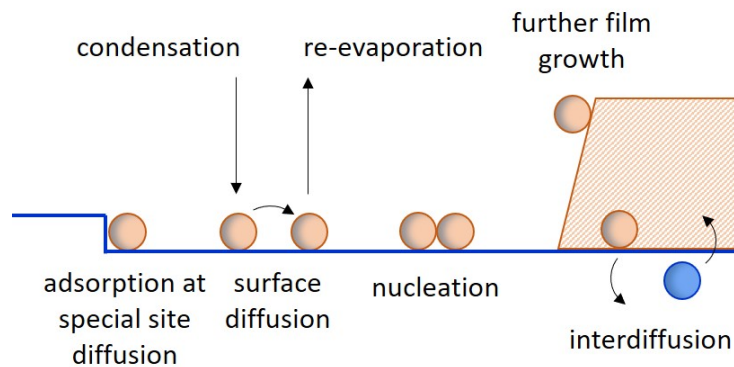


Figure 3.8: Schematic representation of elemental processes involved in film growth on a solid substrate. Adapted from [Lüt01].

Gas atoms impinge on unit area of surface at a rate [Cha04; Lüt01]:

$$\frac{dn}{dt} = \frac{pN_a}{\sqrt{2\pi k_B T M R_0}} \quad (3.2)$$

where n is the number of atoms/molecules in the unit volume and M is the molecular weight in kg/mol. N_a is the Avogadro's number and R_0 is the universal gas constant. In contact with the surface, and depending on the substrate temperature and the strength of the interface bonding, a particle can immediately re-evaporate or migrate across the surface to complete *dangling bonds* at special sites like edges. Besides *adsorption* at special sites, the atom can become a *nucleation* site for the adsorption of other atoms or it can bond with a previously formed island, further increasing its size. Interdiffusion between substrate and film atoms can also occur during the growth leading to washed out or smoothed interfaces. For this to happen a high mobility of the diffusing species is needed (i.e. high substrate temperatures).

Depending on the path taken through the various atomistic processes, the growth can be distinguished among layer-by-layer (or *Frank van der Merwe*, FVM) growth, island (or *Volmer-Weber*, VW) growth, and layer-plus-island (or *Stranski-Krastonov*, SK) growth. In the *layer-by-layer* growth (Fig. 3.8a) the film atoms are more strongly bounded to the substrate than to the neighbouring layer atoms. As a result, a new layer starts to grow only when the last one is completed. In the opposite case, the interaction between neighbouring film atoms is stronger than between the substrate and the growth of 3D *islands* occurs (Fig. 3.8b). The *layer plus island* growth is an intermediate case in which islands start to grow after the formation of one or several complete monolayers (Fig. 3.8c). For a more detailed description of these processes, refer to [Lüt01].

For low lattice mismatched substrates (see eq. (3.6)), vapour deposition can lead to planar, layer-by-layer growth. This produces the films with the highest quality, which is why good lattice matching is always desirable. However, for substrates with a greater lattice mismatch, the FVM mode is highly strained. After a critical thickness, the formation of islands relieves the strain at the expense of a greater interfacial area.

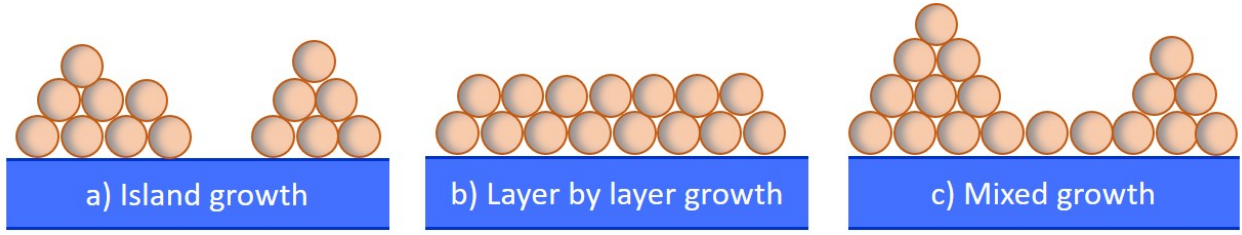


Figure 3.9: Depiction of the three possible growth modes: (a) island growth, (b) layer by layer growth and (c) mixed growth.

The condition for each of these growth modes to take place can be qualitatively described by the surface tension. If γ_S is the surface tension of the substrate/vacuum interface, γ_F is the surface tension between of the film/vacuum interface and γ_{SF} is the surface tension of the substrate/film interface, the force digram of a film island can be drawn as in Fig. 3.10. The equilibrium condition, also known as the *Young equation*, becomes [Lüt01]:

$$\gamma_S = \gamma_{SF} + \gamma_F \cos \varphi \quad (3.3)$$

where φ is the contact angle of the island with the surface. For layer by layer growth $\varphi = 0$, whereas for island growth $\varphi > 0$. Therefore the conditions become:

$$\gamma_S \geq \gamma_{SF} + \gamma_F \quad \text{layer by layer growth} \quad (3.4)$$

$$\gamma_S < \gamma_{SF} + \gamma_F \quad \text{island growth} \quad (3.5)$$

In this picture, the layer-plus-island growth can be understood as follows: at the initial stages of the growth, condition (3.4) is fulfilled and layers begin to grow. However, the formation of these layers alters the values of γ_S and γ_{SF} transitioning to condition (3.5) for island growth.

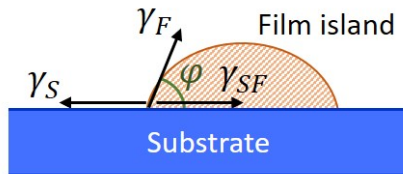


Figure 3.10: Diagram of the forces caused by the surface tension of a film island deposited in the substrate.

3.4 Molecular beam epitaxy (MBE)

A thin film is bounded by two interfaces, the film-substrate interface and its surface (film-vacuum interface). The properties of these two interfaces will mainly determine the properties of the film and thus, their analysis is essential in the study of thin films. Particularly important for modern technology are the interfaces formed by *epitaxial* thin films on single crystal substrates. Here, the film grows as a single crystal with a well-defined orientation with respect to the single crystal substrate.

When the substrate and the film are different (*heteroepitaxy*), there is a lattice mismatch between the two (eq. (3.6)). Only below a certain mismatch value will epitaxy occur, as the lattice constant of the film can adjust either by deformation of the lattice (inducing compressive or tensile strain) or by the formation of dislocations. The type of interface formed will actually depend on the lattice mismatch and the thickness of the film. Generally, for a bigger lattice mismatch, the formation of dislocations becomes more favourable than building up lattice strain in the whole layer without dislocations [Lüt01].

$$\text{mismatch} = \frac{a_{sub} - a_{film}}{a_{sub}} \times 100\% \quad (3.6)$$

with a_{sub} and a_{film} the lattice constants of the substrate and the film respectively.

The MBE growth process involves the control of molecular or atomic beams which are directed onto a substrate to achieve epitaxial growth. In order to minimize unintentional contamination from background gases, MBE operates at UHV ($< 10^{-10}$ mbar) which is translated into small growth rates of typically a few Å/min. In this way, the growth surface is kept clean by minimizing the arrival rate of background species. To put this into perspective, substituting the molecular weight of N_2 ($M \approx 28$ g/mol) into eq. (3.2), gives a gas arrival rate of $\approx 2.9 \times 10^{23}$ $\text{cm}^{-2}\text{s}^{-1}$ for a pressure of 10^3 mbar, $\approx 2.9 \times 10^{17}$ $\text{cm}^{-2}\text{s}^{-1}$ for $p = 10^{-3}$ mbar, and $\approx 2.9 \times 10^{11}$ $\text{cm}^{-2}\text{s}^{-1}$ for $p = 10^{-9}$ mbar at RT (293K). If one needs the impurities adsorbed in 1 hour to be less than a few percent of a monolayer, then pressures $< 10^{-10}$ mbar are required. This condition can be met if the surface is relatively unreactive with common background gases (e.g. the Si surface), and thus can be preserved in a clean state significantly longer.

As per eq. (3.1), in UHV the mean free path of the gas molecules and the atoms/molecules in the beams themselves is several orders of magnitude larger than the substrate-to-source distance ($< 0.2\text{m}$). Thus, reactions take mostly place at the substrate surface where solidification occurs and atoms are incorporated to the growing film. The stoichiometry of the film can be controlled both by the substrate temperature and the flow rates of the beams. Provided that the surface

has been properly cleaned and prepared, the film will then grow epitaxially on top. By a rapid actuation of the shutters, the molecular beams can be started or stopped in less than the time it takes to grow a monolayer of the film. This precise control over film stoichiometry, thickness, and doping concentrations is what makes MBE superior to other epitaxial technologies (see Table 3.1) and what makes it the preferred growth method for Heusler films, where the half-metallic property is conditioned by good chemical and structural ordering.

	Chemical processes		Physical processes
	Chemical Vapor Deposition (CVD)	Metal Organic CVD (MOCVD)	Molecular Beam Epitaxy (MBE)
Growth rate ($\text{\AA}/\text{min}$)	~ 1	~ 1	~ 0.1
Thickness control (\AA)	~ 250	~ 25	~ 5
Interface width (\AA)	< 65	< 10	< 5
Dopant range (cm^{-3})	$10^{13} - 10^{19}$	$10^{14} - 10^{19}$	$10^{14} - 10^{19}$

Table 3.1: Comparison of different epitaxial technologies from [KC01]. MOCVD is one of the most competitive alternatives to MBE. CVD techniques operate at high pressure and are more affordable and advantageous for mass-production. However, they are not as precise as MBE in controlling the composition and thickness of the films.

MBE uses resistive or e-beam heated sources to evaporate/sublimate the material to be deposited. The sources are key elements of the system and have to be carefully designed to provide the necessary uniformity and material purity [KC01]. Construction materials are refractory metals such as Ta and Mo and insulators like alumina or pyrolytic boron nitride (PBN). Depending on the application and the evaporant, there is a wide variety of evaporation sources; the standard sources for most MBE systems are the so-called *Knudsen or k-cells*. A typical k-cell consists of a heating element, a surrounding heat shield and a crucible-thermocouple assembly mounted on a port flange. The source evaporant is loaded into the crucible which fits into the furnace assembly. Crucible and material are then heated to evaporation temperatures by radiation from a resistively heated filament. The rate of the evaporation (or effusion flux) can be adjusted by changing the current passing through the filament, and depends on the k-cell temperature T_{eff} as:

$$\frac{dn_{eff}}{dt} = k_a A_{eff} (p_{ls} - p_{eq}) \frac{N_a}{\sqrt{2\pi k_B T_{eff} M R_0}} \quad (3.7)$$

That is, the effusion flux is the difference between the two opposing fluxes at the vapor-liquid (or vapor-solid) interface at the k-cell. p_{ls} is the pressure of the liquid (or solid) during

evaporation (or sublimation) and p_{eq} is the equilibrium pressure of the vapor/liquid (or vapor/solid) coexistence at T_{eff} . A_{eff} is the aperture area of the source and k_a is the sticking coefficient which can only take values between 0 and 1.

Another common type of sources are e-beam evaporators. Here the evaporant, either a rod or contained within a crucible, is bombarded with an electron beam from a charged W filament. This is done by holding the rod/crucible at a high voltage of 800-1000V, which draws the electrons from the hot filament into the tip of the rod/crucible (see Fig. 3.11). Using electron beams allows the evaporation of materials with very high melting temperatures such as Pt. The main problem of e-beam heating is that such localized heating can be detrimental for film uniformity and coverage. However, if used without a crucible it provides a very high purity flux as contamination from crucible outgassing is prevented.

Most of the sources used for the growth of CFS films in this project are k-cells and their specifications will be given in § 3.5.2.

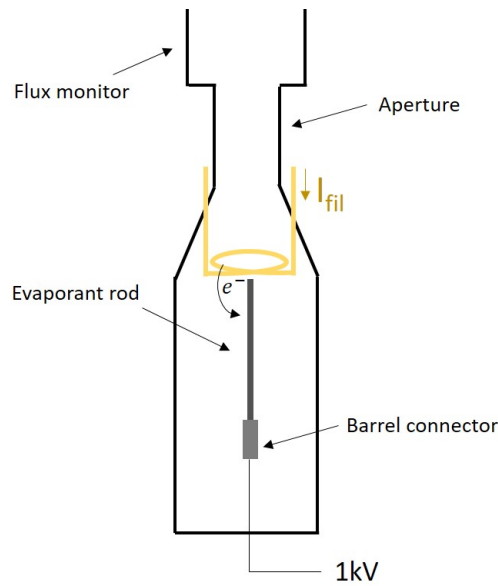


Figure 3.11: Illustration of an electron beam heated source.

3.5 Design of an MBE system for the growth of $\text{Co}_2\text{FeAl}_{1-x}\text{Si}_x$ films

The MBE system used for the growth of CFS alloys in this work was custom made. Like any MBE system, it comprises a *growth chamber* and a smaller load lock or *fast entry lock* (FEL) chamber to introduce and retrieve samples without exposing the main chamber to atmosphere.

Each chamber has an associated pumping line which consists of a turbomolecular pump backed by a scroll (rotary) pump for the main (FEL) chamber respectively. The chambers can be vented through N₂ venting lines to minimise air contamination. The two chambers are isolated from each other with a UHV *gate valve*. The Heusler growth chamber was eventually connected to a second UHV chamber (the so-called *oxide MBE chamber* in Fig. 3.13) through another gate valve for the growth of oxide/Heusler heterostructures.

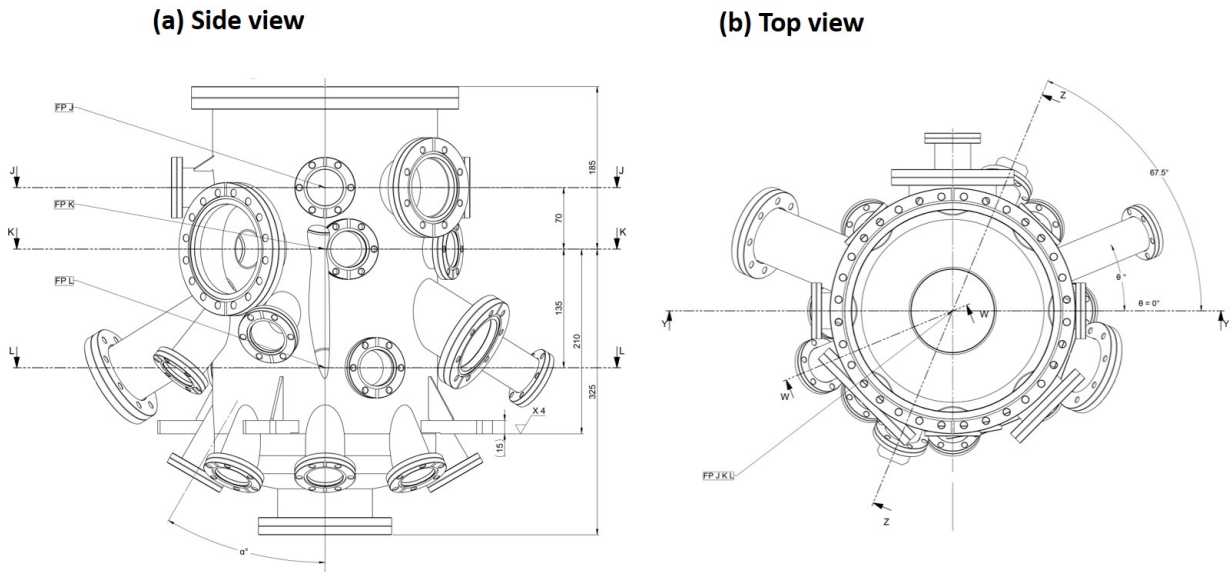


Figure 3.12: (a) side view and (b) top view blueprints of the MBE chamber designed for this thesis.

The design of the main chamber is shown in Figure 3.12. The main elements of the growth chamber are: *sample manipulator*, *evaporation sources*, a *quartz-crystal monitor* (QCM) and a RHEED system (§ 3.6); the last two components are used for in-situ monitoring of the growth. The chamber is also equipped with an IG to measure the base pressure, a TSP to maintain UHV, and an RGA for gas monitoring and leak testing. The water-cooling for the evaporators and the QCM is supplied by a closed-loop ThermoChill II chiller (Fisher Scientific) which can feed up to 10 cooling lines. The water flow in each of these lines can be tuned independently as required. Fig. 3.13 shows the custom designed MBE system, with all its different elements. Base pressures below 10^{-10} mbar were successfully reached when the main chamber and all its bakeable components were baked at 140 – 170°C for 24h – 72h. The only gas that could be detected with the RGA at those base pressures was H₂, as is shown in Fig. 3.18b. Hydrogen is indeed the most common background gas in a well-designed and well-baked UHV system. H₂ originates from the outgassing of the stainless steel chamber walls, and because it's a light and mobile molecule, it is also very difficult to pump.

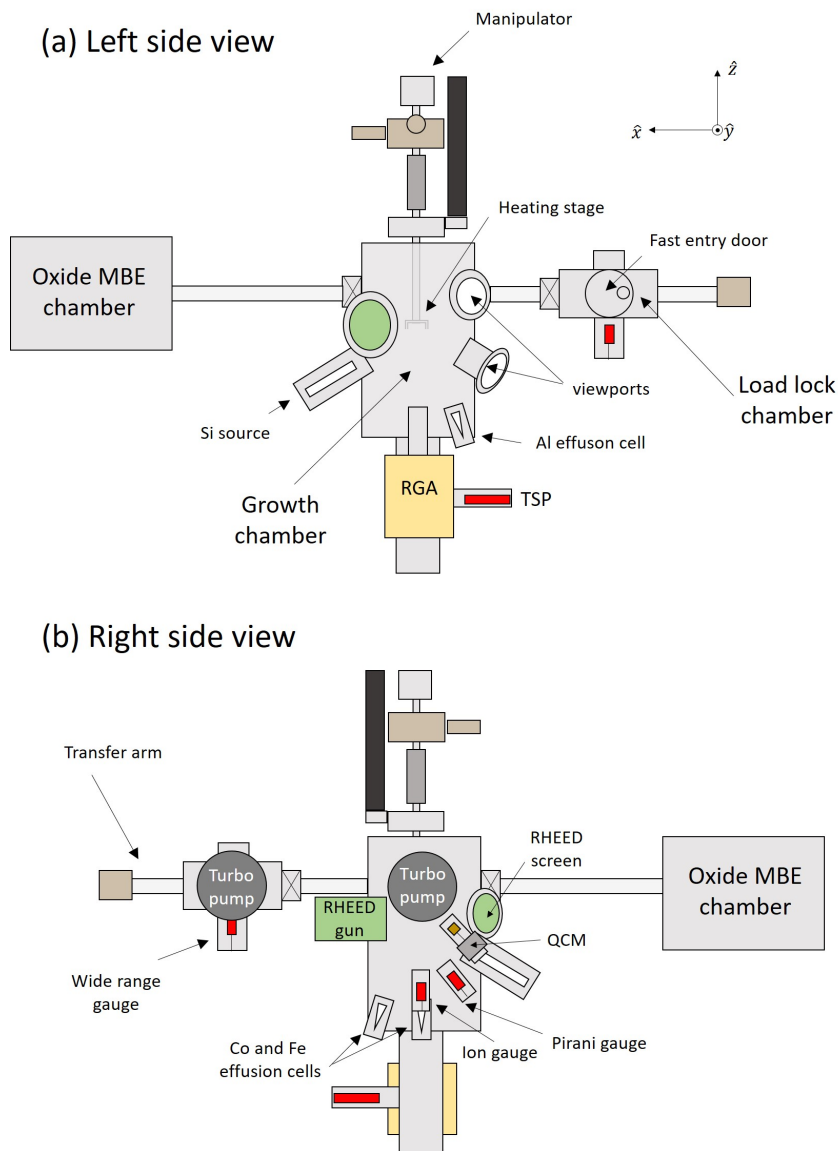


Figure 3.13: Left (a) and right (b) side views of the MBE system, including the growth chamber, the FEL chamber and the transfer arm. The working principle of all the main components in the growth chamber has been described throughout this chapter.

3.5.1 Sample manipulator and sample holder

The sample manipulator is one of the key components of the MBE system. In this case, it is a Vacgen HPT-WX manipulator and includes modules for X Y and Z motion (look at coordinate systems in Fig. 3.13a and Fig. 3.14c for reference), a XY rotation module, and a heating sample stage (see Fig. 3.14a). Electrical feedthroughs are connected to the heater supply and the corresponding tungsten-rhenium thermocouple. Among the future plans to upgrade the system is the integration of an electric motor to provide substrate rotation along \hat{z} (ϕ -rotation)

during growth, which will improve film uniformity.

Fig. 3.14b shows the manipulator elements that stay under vacuum. The heating stage (Fig. 3.14c) was custom made and all the electrical connections were made in the house. The sample stage is made of stainless steel and *inconel*, which makes it compatible with UHV and O₂ environment. Two inconel clamps are used to fix the sample which will be faced down during growth. With this heating stage, temperatures up to 1100°C can be achieved. The stage has a U-shaped opening in one of the sides, to enable the electrons from the RHEED gun hit on the substrate at grazing angles (§ 3.6).

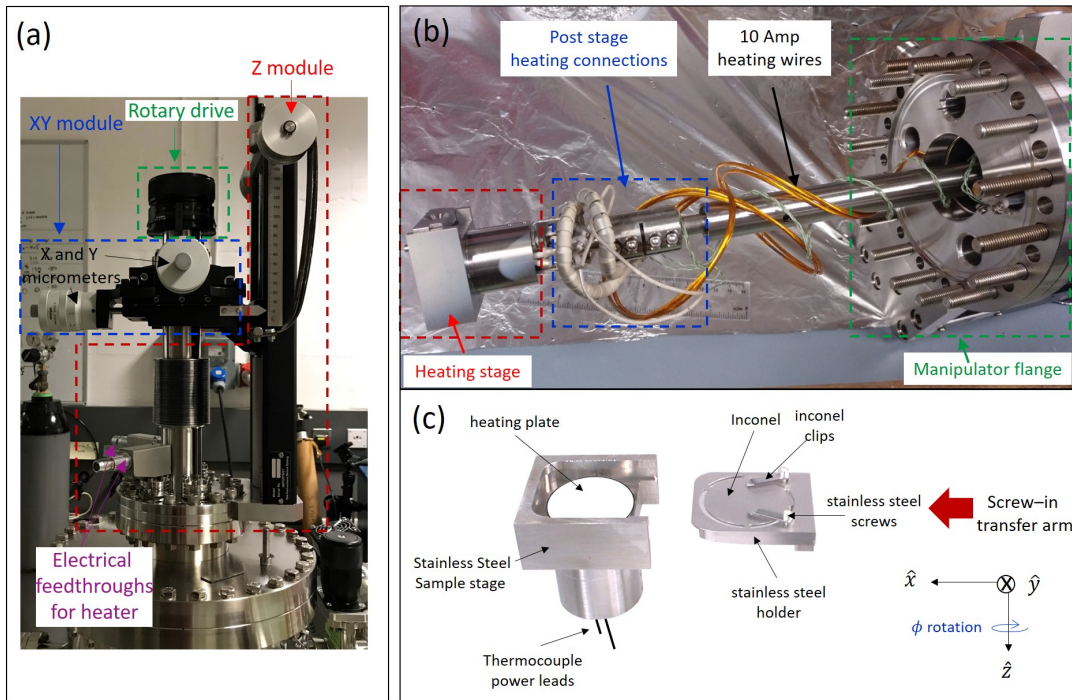


Figure 3.14: (a) Vacgen HPT-WX manipulator, (b) the different elements of the manipulator below the flange and (c) custom-made heating stage and sample holder which withstand substrate temperatures up to 1100°C.

To illustrate the performance of the heating stage, Fig. 3.15 shows the stage temperature T_B as a function of time during the cleaning of a Si(111) substrate before the growth of a CFS film (as per recipe in § 5.2). The heating process was controlled by a standard PID (proportional-integral-derivative) algorithm implemented in *Labview*. The difference between the setpoint (which is the desired temperature inputted into the program) and the values measured by the thermocouple serve as feedback for the control system which determines the current flowing through the heater.

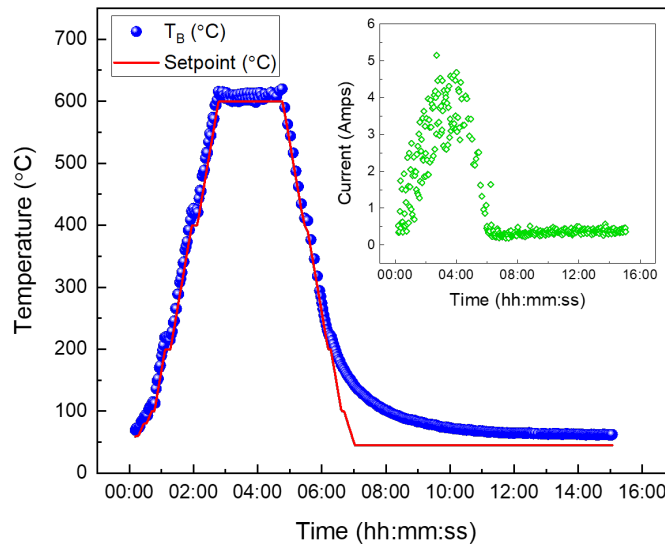


Figure 3.15: Temperature measured by the stage thermocouple (blue dots) and the setpoint temperature (red line) inputted into the labview program. In the inset, the output heating current has been plotted.

3.5.2 Evaporation sources

At the bottom of the chamber there are 4 ports destined to evaporation sources, 3 of which are now in use for the deposition of Co, Fe and Al. The evaporation sources are MBE-komponenten *effusion cells* or k-cells, already introduced in the previous section. A schematic representation of the standard k-cell (WEZ) chosen for the evaporation of Al is shown in Fig. 3.16a. This source has a Ta filament which can evenly heat the crucible containing the Al pellets up to 1500°C. On the other hand, the k-cells used for Co and Fe are high temperature cells (HTEZ) as the evaporation of these materials requires higher operating temperatures (because they have lower vapour pressure). Because elevated temperatures are needed, the heating wire consists in this case of a free standing W filament which is capable of reaching temperatures up to 2000°C. The crucible is made of Al_2O_3 and has the shape of a tapered cone which allows a big angular flux distribution of the evaporation while only using a small amount of material inside. All the effusion cells have integrated cooling shrouds and rotary shutters. A top view of the Fe source is shown in Fig. 3.16b.

For the deposition of Si a *Silicon Sublimation Source* (SUSI) was used, also from MBE-komponenten. The SUSI consists of a free standing high purity Si filament which is directly heated by electrical current. The filament is arch-shaped and all the shielding surrounding it

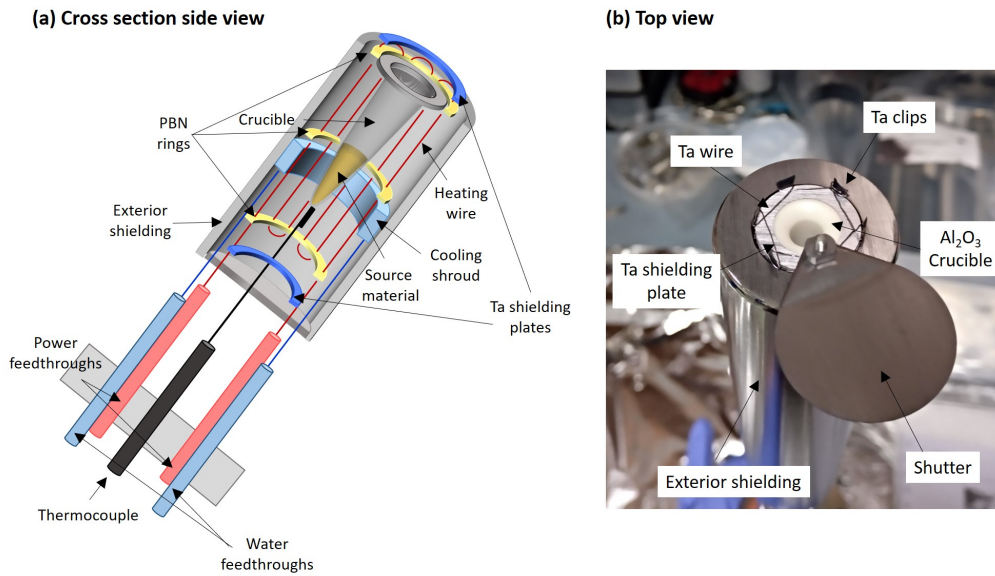


Figure 3.16: (a) Illustration of a effusion cell with a standard Ta heater. Insulating PBN ceramic parts are fully shielded by tantalum plates to prevent outgassing during operation. (b) Top view of the Fe HTEZ cell used in this project.

(the base plate, the shielding tube and the top plate) is also made of high purity monocrystalline Si. Hence, contamination is avoided and a very clean Si flux is achieved. This makes SUSI a better option compared to k-cells. A schematic representation of the Si source is shown in Fig. 3.17a. Extreme heating of metal and ceramic parts is prevented by a very effective water cooling of the electrical contacts. The SUSI is also a a good alternative to e-beam evaporators if flux stability and low flux rates are needed.

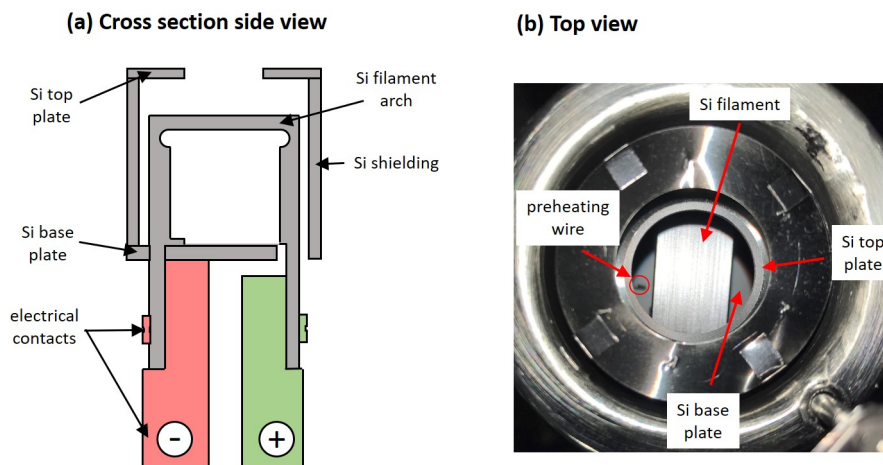


Figure 3.17: (a) Side view and (b) top view of the SUSI showing the different Si elements in the source.

Whenever the SUSI is exposed to air, the base plate will grow a thin layer of SiO_2 which will insulate the filament and therefore, heating won't be possible. The way to address this issue is by using the *preheat connection*. By applying a large enough voltage (between 70V and 200V) across the preheat pin, current can pass through the oxide layer, allowing heating of the filament. At temperatures around 500°C the filament becomes conductive and the preheat connection can be removed. Between frequent experiments, the Si source is kept at a standby temperature of 500°C to avoid it from insulating again. Fig. 3.17b is a top view of the source, where the Si top plate and the preheat pin can be seen.

The evaporation temperature of all the sources (Co, Fe, Al and Si) is controlled by a precision PID controller that adjusts the output power with a feedback-loop, and keeps the source at the input setpoint temperature within a $\pm 1^\circ\text{C}$ error. A photograph of the MBE system developed in this thesis is shown in Fig. 3.18a.

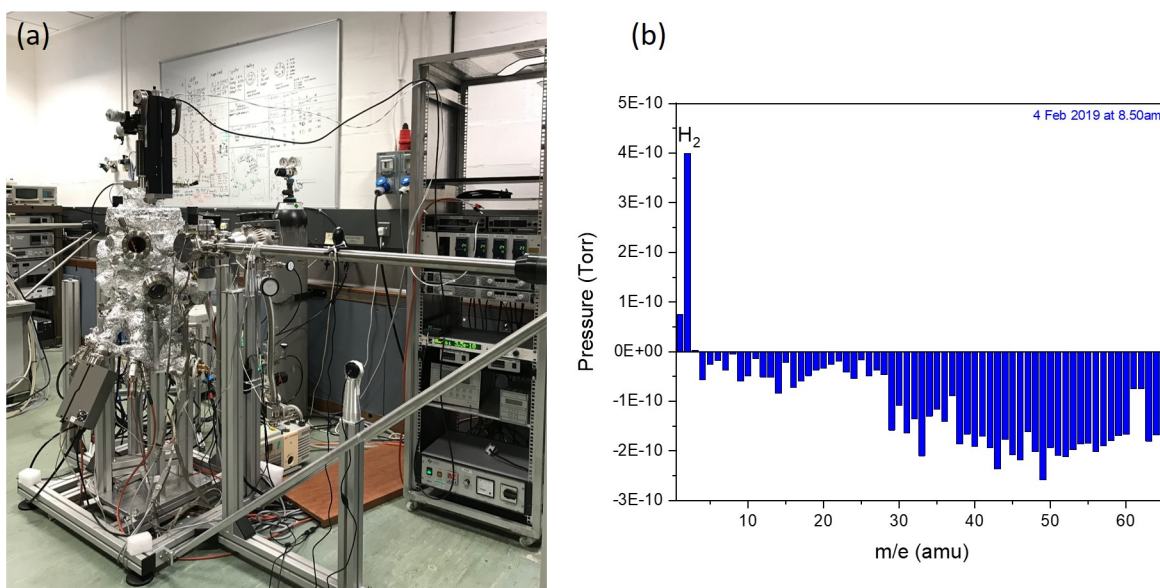


Figure 3.18: (a) Photograph of the metal MBE system built for the growth of $\text{Co}_2\text{FeAl}_{1-x}\text{Si}_x$ films and which was used to grow the CFS films in this project. Note that the photograph was taken before the system was connected to the oxide chamber. (b) RGA scan showing that H_2 is the only gas present in the chamber after baking; the IG was measuring 3×10^{-10} mbar when the scan was performed.

3.6 In-situ characterization. Rate monitors and RHEED

MBE benefits enormously from the incorporation of analytic tools that provide real time information on the growth process, such as QCM and RHEED.

3.6.1 Quartz crystal microbalance (QCM)

The *quartz crystal microbalance* (QCM) is a valuable technique to measure the deposition rate during growth. The QCM consists of a quartz crystal sandwiched between two electrodes, as shown in Fig. 3.19. When a voltage is applied across the electrodes, due to the piezoelectric properties of the quartz crystal, the quartz crystal is deformed. The deformation shears the disk in the thickness direction and if an alternating voltage is applied, the disk oscillates back and forth with the applied voltage.

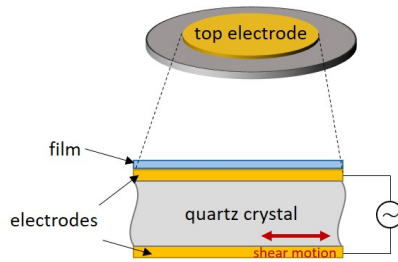


Figure 3.19: Illustration of the working principle of the quartz crystal microbalance.

The resonant frequency of the system is a function of the thickness of the crystal/electrode system. Therefore, changes in the fundamental frequency of the QCM are related to the change of mass at the electrode surface caused by deposition of a material. This relationship is given by the *Sauerbrey's equation* for uniform and rigid thin film deposits [Sau59]:

$$\Delta\nu = -C_q\Delta m \quad (3.8)$$

where C_q is the sensitivity factor, which is a fundamental property of the crystal:

$$C_q = \frac{2\nu_0^2 n}{\sqrt{\rho_q \mu_q}} \quad (3.9)$$

Here, ν_0 is the natural frequency of the fundamental mode, n is the harmonic number, ρ_q is the density of the quartz crystal and μ_q the shear modulus of the crystal. The thickness of the film can then be calculated as $t_f = \frac{\Delta m}{\rho_f}$, being t_f and ρ_f the thickness and density of the film respectively. As the thickness of the film increases, the Sauerbrey equation must be extended to incorporate the elasticity of the deposited film. This leads to the *Lu and Lewis equation* [LL72] which is widely used in current thin-film depositions:

$$t_f = \left(\frac{N_q \rho_q}{\pi \rho_f Z \nu_c} \right) \arctan \left[Z \tan \left(\frac{\pi(\nu_q - \nu_c)}{\nu_q} \right) \right] \quad (3.10)$$

Here, N_q is the frequency constant for AT-cut quartz crystal, ν_q is the frequency of the crystal prior to deposition, ν_f is the frequency of the loaded crystal and $Z = \sqrt{\frac{\rho_q \nu_q}{\rho_f \nu_f}}$ is the acoustic impedance of the film material. Film Z factors are usually very close to bulk factors and can be found in literature.

3.6.2 Reflection High Energy Electron Diffraction (RHEED)

As well as characterizing the structure of bulk crystals and interfaces, electron diffraction can also be used to study atomic arrangements in surfaces. MBE systems are often equipped with electron diffraction based analysis instrumentation such as LEED or RHEED for in-situ characterization. In RHEED experiments an electron gun emits high energy electrons, with energies between 10 and 100 kV, at grazing angles onto the sample surface. Electrons are coherently scattered according to Bragg's law (4.1) and form interference patterns at similar detection angles which are observed in a fluorescent screen. In this grazing geometry, with typical incident angles between 3° and 5° , the electrons only penetrate a few atomic layers and thus, the surface is probed [Lüt01].

A schematic representation of the RHEED set up in the MBE system in this work is shown in Fig. 3.20, with the gun and sample axes perpendicular to each other. The electron gun, from *StaiB instruments*, consists of a W filament which is heated and emits electrons at 15 kV via thermionic emission. The electron beam is focused with a *Wehnelt cylinder* and acquires a beam diameter of 1 mm at the surface. The fluorescence screen is coated onto the inside of one of the windows in the UHV chamber along with a transparent conductive film to prevent charging.

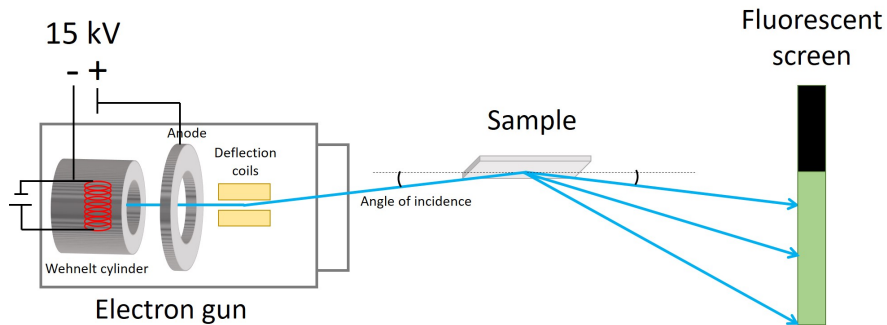


Figure 3.20: Schematic representation of the RHEED set-up in the MBE system designed for $\text{Co}_2\text{FeAl}_{1-x}\text{Si}_x$ growth. Due to the relatively large distance between the electron gun and the sample, and between the sample and the screen, RHEED is very flexible in relation to sample conditions and experiments can be performed in-situ during sample growth.

Ideally, if the optics are perfect, the surface is illuminated by a plane wave. However, in reality there is always an angular distribution (2β) and an energy distribution (ΔE) of the primary beam, which in our case is determined by the Wehnelt cylinder. These deviations give rise to the so-called *coherence length*, Δr_c . Atoms in the surface separated distances longer than Δr_c are not illuminated by a plane wave and therefore, scatter incoherently and can't form diffracted beams (the phase of the diffracted beams is no longer correlated and they can't interfere constructively). The correlation length is given by:

$$\Delta r_c = \frac{\lambda}{2\beta \left(1 + \left(\frac{\Delta E}{2E}\right)^2\right)} \quad (3.11)$$

For RHEED the coherence length is ≈ 100 nm which limits the scales that can be probed.

RHEED is a key tool for surface characterization. A RHEED pattern is essentially a 2D projection of the reciprocal lattice and can therefore be used to identify surface reconstructions. In RHEED conditions, the Ewald sphere (refer to section § 4.1) has a very large diameter and cuts the lattice rods in the reciprocal space at grazing angles (see Fig. 3.22a). Both the Ewald sphere and the lattice rods have a finite thickness due to limitations of the electron gun and imperfections of the surface respectively. As a consequence, a RHEED pattern is usually formed by streaks of certain thickness (Fig. 3.22b). Only when the surface is extremely flat and very good instrumentation is used, can very sharp diffraction spots be seen.

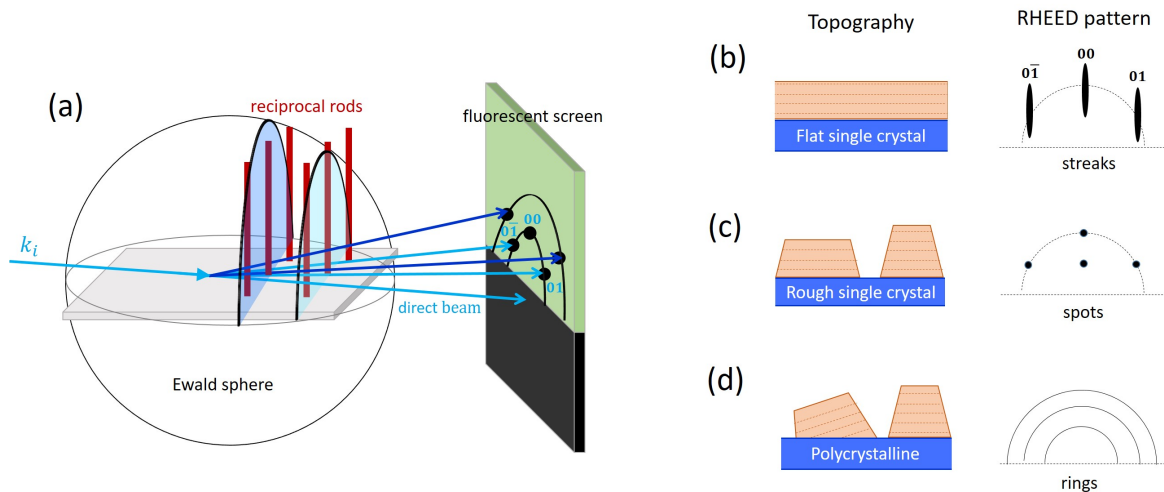


Figure 3.21: (a) Working principle of RHEED, a diffraction spot is formed when a rods of the reciprocal lattice intersects the Ewald sphere; Schematic RHEED patterns for (b) a flat single-crystal surface, (c) a rough single-crystal surface and (d) a polycrystalline surface.

At an appropriate incident electron beam energy, the RHEED intensity oscillates during

growth and each peak value represents the completion of a new monolayer. This is another powerful tool to monitor the MBE growth rate in situ. If there are crystalline islands at the surface (characteristic of the VW and SK growth modes, § 3.3), bulk scattering of the primary beam can result in spots rather than streaks in the diffraction pattern (Fig. 3.22c). If the surface is rough, the RHEED pattern will look spotty and sometimes show rings (Fig. 3.22d). In this work, RHEED will mainly be used to assess the quality of the substrate surface prior to the growth of CFS films.

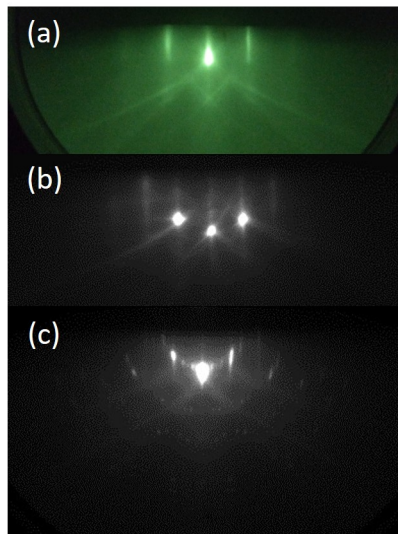


Figure 3.22: Experimental RHEED patterns from (a) a MgO(001) surface along $[010]$, (b) a Si(111) surface along $[11\bar{2}]$ and (c) a STO(001) surface along $[010]$ after cleaning.

Chapter 4

Ex-situ characterization techniques

The CFS films grown by the MBE technique developed in Chapter 3 were characterized ex-situ using well-established experimental techniques. The first two sections in this chapter will introduce the two main techniques used to study the structure of the films, namely x-ray diffraction (XRD) and reflectivity (XRR) (§ 4.1), and transmission electron microscopy (TEM) (§ 4.2). The last section (§ 4.3), will focus on the magnetic characterization techniques used in this work, i.e. ferromagnetic resonance spectroscopy (FMR) and vibrating sample magnetometry (VSM).

4.1 X-ray diffraction. Bragg's law and Laue formulation

X-ray diffraction (XRD) is a powerful non destructive technique to characterize crystalline materials. It provides information about structures, phases, preferred crystal orientations and other structural parameters, such as crystallinity and strain. In a XRD set-up, an incident beam of x-rays is diffracted by the atomic planes of a crystal as depicted in Fig. 4.1. Due to the periodicity of the lattice, the scattered rays preserve their phase and interfere constructively in a few scattering directions forming diffracted beams. The resulting diffraction pattern (DP) reflects the symmetry of atomic ordering in the crystalline sample. The first part of this section will cover the basic theory on x-ray diffraction and at the end of the section the use of this tool in the analysis of thin films will be discussed. For a more extended study on the topic refer to [Cul56].

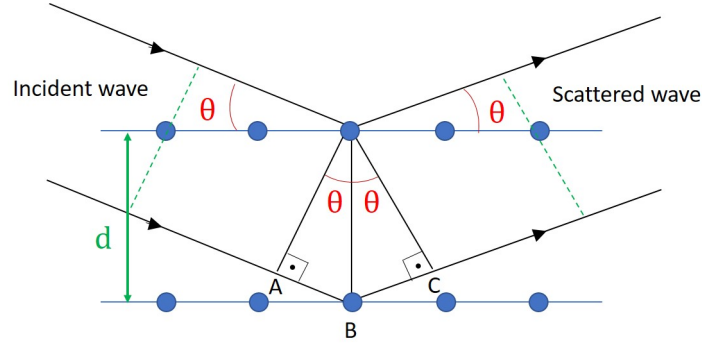


Figure 4.1: X-ray diffraction by a periodic lattice of atoms spaced a distance d apart when an x-ray beam impinges at an angle $\theta_{in} = \theta$.

The conditions under which the incident beam will constructively interfere after being elastically scattered by the crystal is described by *Bragg's law*. When a beam of perfectly parallel monochromatic x-rays of wavelength λ impinges on the crystal at an angle θ_{in} with respect to the scattering planes (hkl) , the scattered beams will be in phase and reinforce each other when:

$$2d_{hkl} \sin \theta_B = m\lambda \quad (4.1)$$

where d_{hkl} is the distance between the (hkl) planes. Equation (4.1) can be easily understood if one looks at Fig. 4.1 and calculates the extra length travelled by the lower beam as $\overline{AB} + \overline{BC} = 2 \times d_{hkl} \sin \theta$. Under Bragg's condition, a diffracted beam appears in the direction θ_B called the Bragg angle. m is the *order of diffraction* and is equal to the number of wavelengths in the path difference between the x-rays scattered by adjacent planes. For a cubic crystal structure with lattice parameters $a = b = c$, the interplanar spacing is given by:

$$\frac{1}{d_{hkl}^2} = \frac{h^2 + k^2 + l^2}{c^2} \quad (4.2)$$

In thin films, a and b usually denote the in-plane lattice constants, whereas c refers to the lattice constant along the direction perpendicular to the film. Combining eq. (4.1) and eq. (4.2), x-ray diffraction allows the extraction of lattice parameters in a single crystal thin film provided that its crystal structure is known. If the crystal is tetragonally distorted, with axes a and c , the corresponding general equation is:

$$\sin^2 \theta_B = \frac{\lambda^2}{4} \left(\frac{h^2 + k^2}{a^2} + \frac{l^2}{c^2} \right) \quad (4.3)$$

As can be observed from eq. (4.3), the directions (or Bragg angles) at which the x-ray beam of wavelength λ is scattered, are only determined by the crystal system (cubic, tetragonal,

monoclinic etc.) and the dimensions of the unit cell. However, the intensity of these reflections depends on the position of the atoms in the lattice, or in other words, on its basis. For example, in a non-primitive unit cell like fcc or bcc, the relative phases of different points in the unit cell can lead to destructive interferences which reduce the intensity of certain diffracted beams to 0, even though they were predicted by Bragg's law.

The symmetry of the lattice, i.e. the *space group*, determines which reflections are forbidden (*systematic absences*) and which are allowed based on the so-called selection rules. For instance, the $L2_1$ structure of CFS (Fig. 2.12a) is f-centred cubic with $m\bar{3}m$ point group. The selection rules for allowed reflections then state that h, k, l must be all odd or even. Therefore, reflections $hkl=111, 200, 220\dots$ are allowed, whereas $hkl=100, 110, 210, 211\dots$ are forbidden. If the disorder in the lattice increases, e.g. the B2 structure in Fig. 2.14a, the lattice has a lower symmetry (refer to Table 2.1 for the space group of the different structures) and hence, more reflections are forbidden. This allows to identify between A2, B2 and $L2_1$ structures using x-ray diffraction. The list of allowed reflections for each possible structural phase of CFS has been summarized in Tab. 5.2.

Although Bragg's law is very useful for numerical purposes, crystals are in general 3-dimensional and hence, for greatest generality the equations to describe the directions of the diffracted beams should be expressed in terms of vectors. The von Laue formulation differs from Bragg's approach in that no particular sectioning of the crystal is singled out and that no assumption about specular reflection is imposed. The von Laue approach is extensively used both in x-ray and electron diffraction as will be seen in § 4.2.2. To derive the Laue equation consider two scatterers placed at the sites \vec{R} of a Bravais lattice that can reradiate the incident beam in all directions [AM76].

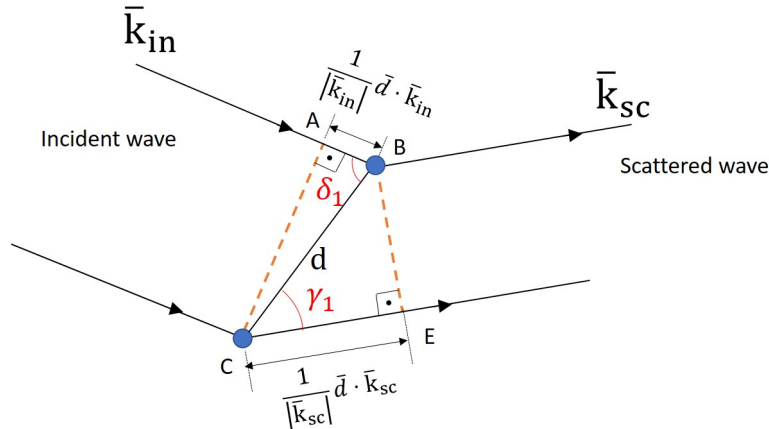


Figure 4.2: Path difference between beams scattered by two scatterers separated by \vec{d} .

From Fig. 4.2, the condition for constructive interference is given by the path difference

$\overline{CE} - \overline{AB}$ such that:

$$\vec{d}(\cos \gamma_1 - \cos \delta_1) = \vec{d} \cdot \frac{(\vec{k}_{sc} - \vec{k}_{in})}{(2\pi/\lambda)} = m\lambda \rightarrow \vec{d} \cdot (\vec{k}_{sc} - \vec{k}_{in}) = 2\pi m \quad (4.4)$$

By applying the same procedure to a three dimensional network of scatterers at the sites of a lattice with primitive vectors $\vec{a}, \vec{b}, \vec{c}$, (with lattice spacings a, b and c respectively):

$$\vec{G} \cdot \vec{R} = 2\pi m \quad (4.5)$$

where $\vec{G} = \vec{k}_{sc} - \vec{k}_{in}$ is called the *scattering vector* and it is the difference between the scattered beam and the incident beam. \vec{R} is the direct lattice vector defined by the set of three primitive vectors of the unit cell of the crystal:

$$\vec{R} = p\vec{a} + q\vec{b} + r\vec{c} \quad (4.6)$$

with p, q and r integers. Equation (4.5) implies that the scattering vector is indeed a reciprocal lattice vector \vec{g}_{hkl} .

$$\vec{G} = \vec{g}_{hkl} = h\vec{a}^* + k\vec{b}^* + l\vec{c}^* \quad (4.7)$$

where

$$\vec{a}^* = (2\pi/V_c)(\vec{b} \times \vec{c}), \quad \vec{b}^* = (2\pi/V_c)(\vec{c} \times \vec{a}), \quad \vec{c}^* = (2\pi/V_c)(\vec{a} \times \vec{b}) \quad (4.8)$$

are the primitive vectors of the reciprocal lattice, being V_c the volume of the unit cell in real/direct space. The equivalence between Bragg's law and Laue's equation can be easily demonstrated when one works out that:

$$|\vec{G}| = \frac{2\pi}{d_{hkl}} \quad (4.9)$$

with \vec{g}_{hkl} representing the vector normal to the (hkl) planes. Thus, the reciprocal lattice of a crystal consists of all possible Bragg reflections and can be conveniently used to describe diffraction.

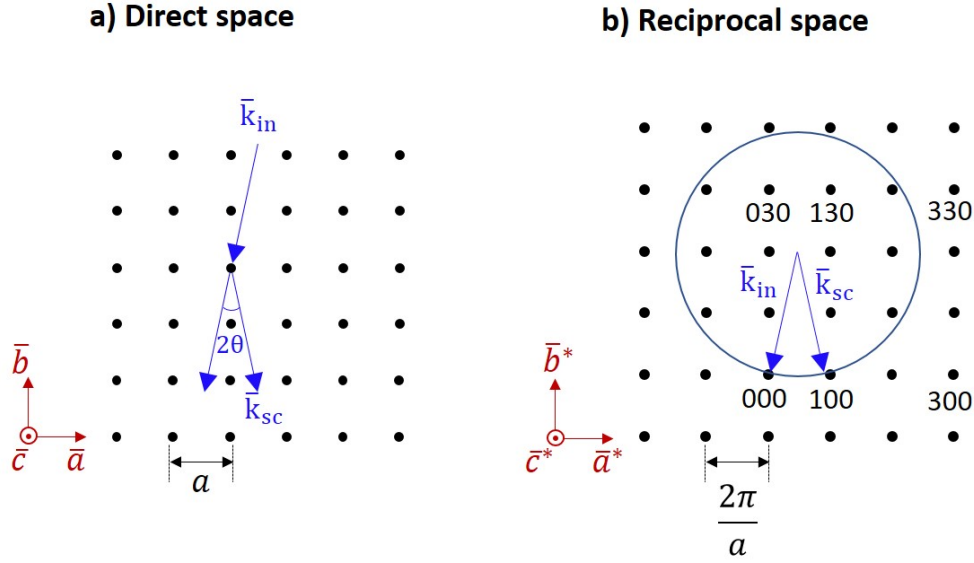


Figure 4.3: (a) Direct lattice and (b) reciprocal lattice of a simple cubic crystal. The Ewald sphere is shown for an incident radiation \vec{k}_{in} with wavelength λ . The orientation of the incident beam is such that the (100) diffraction occurs and the reciprocal lattice point 100 is intersected by the Ewald sphere.

The conditions for diffraction can be represented graphically in reciprocal space using the *Ewald sphere* construction. The first step in plotting the Ewald sphere is to construct the reciprocal lattice in question. Next, one plots \vec{k}_{in} parallel to the incident beam direction with length $2\pi/\lambda$ (\AA^{-1}) and terminating it at the origin of the reciprocal lattice. The sphere centered at the origin of vector \vec{k}_{in} and with radius $2\pi/\lambda$ is the Ewald sphere. This has been shown for a cubic crystal in Fig. 4.3. In order for diffraction to be observed, \vec{k}_{sc} and hence, \vec{G} must end on a reciprocal lattice point. When the Ewald sphere intersects a reciprocal lattice point g_{hkl} , the diffraction from the (hkl) planes is observed¹.

4.1.1 2θ - ω scans

The most widely used XRD measurement is undoubtedly the $2\theta - \omega$ scan. In this particular geometry, the x-ray tube and the detector move simultaneously over the angular range ω and θ respectively. In a symmetric scan, depicted in Fig. 4.4, the x-ray tube and the detector move at the same velocity, $\omega = \theta$, so that the angle between the incident beam and the detector equals 2θ to meet Bragg's condition (4.1). Then, along the angular range of interest, (hkl) diffraction peaks are observed at specific θ (or 2θ) angles every time eq. (4.3) is satisfied. If $\chi = 0^\circ$, i.e.

¹Note that in crystallography it is customary to define the reciprocal lattice by removing the 2π factors in eq. (4.8) and the radius of the Ewald sphere is then taken as $1/\lambda$ as it appears in many textbooks.

the sample sits horizontal, then only those planes parallel to the surface of the film can be probed and the out-of-plane constant can be extracted from the position of the film peaks. In such a scan, the $(00l)$ reflections would be revealed for a cubic single-crystal film with (001) surface; whereas for a (111) surface, the (hhh) family would be observed. In order to access other reflections, the goniometer can be tilted around \hat{y} ($\chi \neq 0^\circ$) and rotated around \hat{z} by an angle ϕ . ϕ scans have also been used in this thesis to study the relative orientation between the epitaxial film and the substrate.

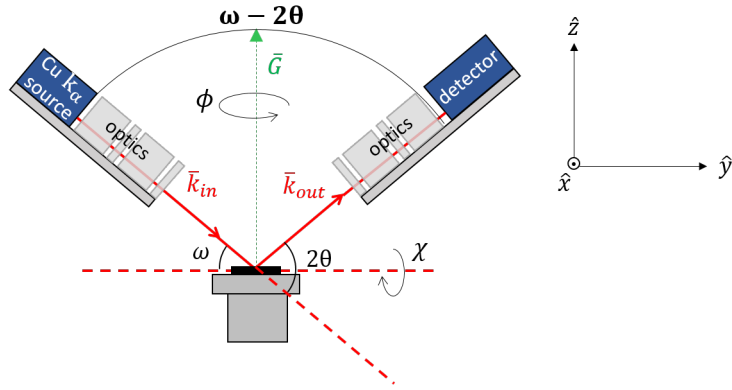


Figure 4.4: Geometry of a symmetric 2θ - ω scan used to measure the out of plane momentum transfer, \vec{G} in the CFS films. The measurements were performed with a Rigaku SmartLab diffractometer using a $\text{Cu } K_\alpha$ source.

In perfect cubic structures without strain, the out-of plane lattice constant gives access to the other lattice constants as $a = b = c$; however, if tetragonal distortions are present the in-plane constants will suffer small deviations. In order to measure the in-plane lattice constants, a different geometry has to be used, where the incident radiation impinges the sample at grazing incidence.

In this work, conventional out-of plane $2\theta - \omega$ measurements as the one illustrated in Fig. 4.4 have been performed in the CFS films. As explained before, the presence/absence of certain reflections allows to identify the ordering phases present in these films (A2, B2 or $L2_1$). The absolute intensities of the peaks depend on many factors including instrumental factors, the already mentioned structure factor, the accelerating voltage and so on and hence, it is difficult to extract any useful information from them. Fortunately, the relative intensities of the peaks and the relative differences in their integrated intensity (the area under the peak) are of major interest. The relative intensities can be used to estimate the relative proportions of phases in the film as will be explained in Chapter 5.

On the other hand, the width of an individual peak, often defined as the full width at half the maximum height (FWHM), can be an indicator of the quality of the thin film. Indeed, peak

widths are sensitive to the presence of lattice distortions (strain) and defect density. Narrower peaks arise from more coherent structures of higher quality; whereas poor crystal quality leads to peak broadening by defects like misalignment between grains, known as mosaicity, and other effects such as dislocations, sample curvature and strain. In the case of mosaicity, slightly mis-oriented grains result in small shifts of the Bragg angle, which collectively give rise to a broader diffraction peak. While the exact values of FWHM are not useful in isolation, comparing the FWHM allows a relative comparison of their structural quality. However, one should be careful to rule out that changes in the FWHM do not originate from changes in the instrumental broadening (which depends on the optical conditions used such as the configuration of slits or a misalignment of the diffractometer among others) as these two contributions, instrumental and intrinsic broadening, cannot always be easily isolated in the analysis. In a $2\theta - \omega$ geometry, the peak width also depends on film thickness.

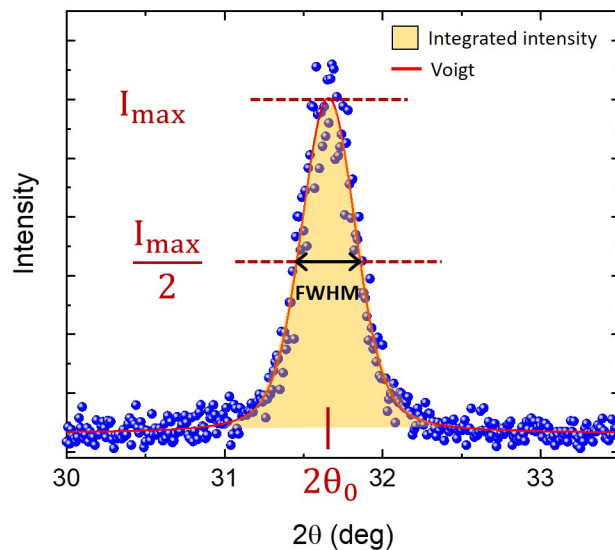


Figure 4.5: Basic features of a XRD peak fitted by a Voigt distribution, which is the convolution of a Gaussian and a Lorentzian distribution with linewidths Δ_G and Δ_L , respectively. Δ_G is related to the instrumental broadening, whereas Δ_L has to do with the intrinsic broadening.

All of the XRD data presented in this thesis was recorded using a Rigaku Smartlab x-ray diffractometer with a Cu K_α x-ray source with $\lambda = 1.5406\text{\AA}$. A 2-bounce Ge(220)x2 monochromator was installed in order to eliminate additional K_β and L_α reflections.

4.1.2 X-ray reflectivity (XRR)

The utilization of x-rays is not limited to diffractometry. *Specular x-ray reflectivity* (XRR) is another powerful technique in the study of thin films and can be used to gain information on the film thickness and interfacial roughness. Even though it does not evaluate diffraction phenomena, XRR measurements can be performed with the same optics and set-up used for XRD (Fig. 4.4). The measurement is indeed just a symmetric $2\theta - \omega$ scan that is performed at low angles, with 2θ values typically between 0.1 and 10 degrees (i.e. close to the critical angle for total reflection).

When x-rays are incident below a critical angle (the incident angle being that between the surface of the sample and the incident beam), θ_c , they are totally reflected by the surface of the sample. The most widely used x-rays in XRR measurements have a wavelength of $\lambda \sim 0.1$ nm and consequently, the interaction of these x-rays with matter can be well described by a refractive index n . $n = n(\rho_e, \lambda)$ determines the change of direction of the x-rays when they are transmitted from air into a material according to *Snell's law*, and depends on the electron density of the material (ρ_e) and the x-ray wavelength (λ). The exact mathematical expression that links n , ρ_e and λ can be found in [GH00].

For x-rays, n is slightly less than 1 and hence, total reflection can occur at small enough incident angles ($\theta_{in} < \theta_c$). θ_c depends on the refractive index as:

$$n = \cos \theta_c \quad (4.10)$$

Because n is close to 1, θ_c is very small and can be approximated using the Taylor expansion for the cosine function. Using the relation of dependence of n with ρ_e and λ , this yields:

$$\theta_c^2 = \frac{r_e \lambda^2}{\pi} \rho_e \quad (4.11)$$

where $r_e = 2.813 \times 10^{-6}$ nm is the classical radius of the electron and θ_c is in radians.

As θ_{in} increases above θ_c , the reflectivity rapidly decreases as the x-rays start penetrating into the material. Interference fringes are then formed due to the phase difference between the x-rays reflected from each interface in the layered structure. If the surface of the reflecting material is flat, the reflected intensity will be confined in a direction symmetric from the incident one (known as *specular*) which is probed by the $2\theta - \omega$ scan. If a simple 1-layer system is considered, a thin film on a substrate, x-rays reflected from the surface and the film-substrate interface interfere. The reflectivity, which is defined as the normalized intensity of the reflected beam, $R(\theta) = \frac{I(\theta)}{I_0}$ (where I_0 is the intensity of the incident beam), can then be calculated by

solving the Helmholtz equation with the appropriate boundary conditions at the two interfaces. The solution to this problem is:

$$R = \left| \frac{r_{0,1} + r_{1,2}e^{-2ik_{z,1}t_1}}{1 + r_{0,1}r_{1,2}e^{-2ik_{z,1}t_1}} \right|^2 = \frac{r_{0,1}^2 + r_{1,2}^2 + 2r_{0,1}r_{1,2} \cos(2k_{z,1}t_1)}{1 + r_{0,1}^2r_{1,2}^2 + 2r_{0,1}r_{1,2} \cos(2k_{z,1}t_1)} \quad (4.12)$$

Here the numbers 0, 1 and 2 refer to the different layers following the nomenclature in Fig. 4.7; that is, 0 is air, 1 is the thin film and $N = 2$ is the substrate. $r_{0,1}$ and $r_{1,2}$ are the so-called *Fresnel coefficients* of reflection at the air/film and film/substrate interface respectively, $k_{z,1}$ is the z-component of the wavevector in the 1st medium (eq. (4.13)), and t_1 is the thickness of the film.

$$k_{z,1} = |k| \sqrt{n_1^2 - \cos^2 \theta_{in,1}} = \frac{2\pi}{\lambda} \sqrt{\cos^2 \theta_{c,1} - \cos^2 \theta_{in,1}} \quad (4.13)$$

For a step-by-step derivation of eq. (4.12), refer to [GH00]. The presence of the cosine terms in (4.12) point to an oscillatory pattern of reflectivity. These oscillations are called *Kiessig fringes*, and they can be observed in Fig. 4.6a in blue for a Fe film simulated with *GenX*. The period of the oscillations is inversely proportional to the thickness of the film, and therefore, the oscillations are brought closer together as the thickness of the film increases. This is illustrated in Fig. 4.6b for the blue and red lines which correspond to the reflectivity of a 20 nm-thick and a 40 nm-thick Fe film respectively. Clearly, the frequency of the Kiessig fringes of the 40nm-thick film is twice the frequency of the oscillations of the thinnest film. Samples thicker than a few hundred nanometres suppress this reflectivity as the fringes become so close that they become indistinguishable. At the same time, the increasing thickness of the film leads to the attenuation of the reflection from the film/substrate interface, impeding the interference behaviour.

Eq. (4.12) implies that the reflectivity will show maxima when: $\cos(2k_{z,1}t_1) = 1 \rightarrow k_{z,1}t_1 = m\pi$ with $m \in \mathbb{N}$. By substituting (4.13) in (4.12), one can see that these maxima occur at incident angles where the path difference is an integer multiple of the x-ray wavelength:

$$m\lambda = 2t_1 \sqrt{(\cos^2 \theta_{c,1} - \cos^2 \theta_{in,1})} \xrightarrow{\theta_{in,1} \ll 1} (m\lambda)^2 \approx 4t_1^2 (\theta_{in,1}^2 - \theta_{c,1}^2) \quad (4.14)$$

The film thickness and critical angle can then be extracted from the slope of a line fitted to the squares of the angular values of the reflectivity maxima (in radians) versus the square of their order m , while the intercept of such a line will yield $\theta_{c,1}$, from which the density of the film can be computed (eq. (4.11)).

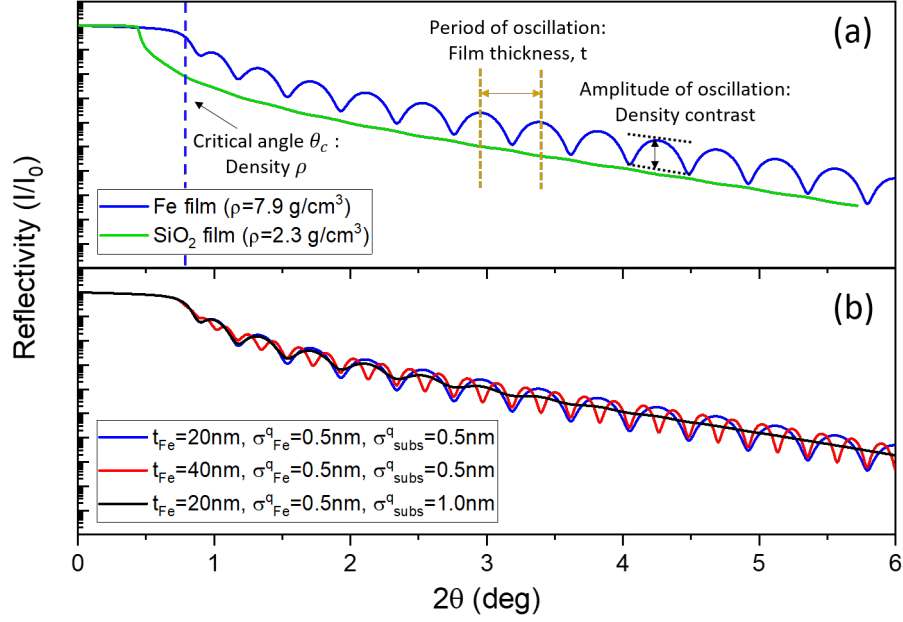


Figure 4.6: Reflectivity profiles simulated with GenX for (a): a 20nm-thick Fe film in blue and a 20nm-thick SiO_2 film in green; and (b) Fe films with: $t=20\text{nm}$ and $\sigma_{\text{subs}}^q = 0.5\text{nm}$ in blue, $t=40\text{nm}$ and $\sigma_{\text{subs}}^q = 0.5\text{nm}$ in red, and $t=20\text{nm}$ and $\sigma_{\text{subs}}^q = 1.0\text{nm}$ in black.

If one more layer is added to the system ($N = 3$), the analytical expression of the reflectivity becomes tedious. The reflectivity can in these cases be calculated using the Parratt recursion equation derived from a different formalism [Yas10]:

$$R_{j,j+1} = \frac{R_{j+1,j+2} + r_{j,j+1}}{R_{j+1,j+2} r_{j,j+1} + 1} a_j^4 \quad (4.15)$$

$$a_j = e^{\frac{-ik_{z,j}}{2} t_j}$$

where $r_{j,j+1}$ is again the Fresnel coefficient at the $j/j+1$ interface. To obtain the reflectivity of the system, $R_{0,1}$ is calculated by solving eq. (4.15) starting from the substrate, that is $j = N$. For a 1-layer system ($N = 2$), eq. (4.12) is retrieved taking into account that $R_{2,3} = 0$ and $a_0 = 1$:

$$R_{1,2} = \frac{r_{1,2}}{r_{1,2} + 1} a_1^4 \quad (4.16)$$

$$R_{0,1} = \frac{r_{1,2}a_1^4 + r_{0,1}}{r_{1,2}r_{0,1}a_1^4 + 1} a_0^4 = \frac{r_{1,2}a_1^4 + r_{0,1}}{r_{1,2}r_{0,1}a_1^4 + 1} \quad (4.17)$$

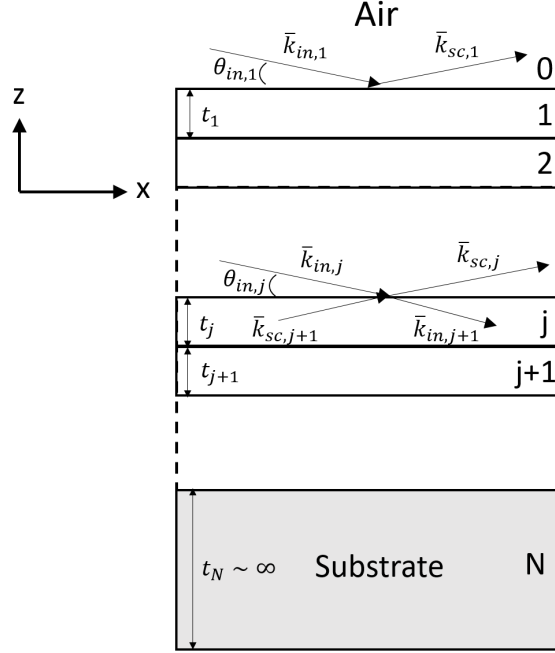


Figure 4.7: Schematic of a layered material and nomenclature used in this section.

If the layers are not ideally flat, the reflectivity profile decays more rapidly. To take into account the influence of interface/surface roughness (σ_q), the Fresnel coefficients are substituted by the modified Fresnel coefficients $r_{j,j+1} \rightarrow \tilde{r}_{j,j+1}$:

$$\tilde{r}_{j,j+1} = r_{j,j+1} e^{(-2k_{z,j}k_{z,j+1}\sigma_q^2)} \quad (4.18)$$

In fitting software packages like the one used in this thesis, GenX, the reflectivity profile of the model is calculated using Parratt's recursion equation. GenX then uses a least squares fitting method to look for the optimal values for the density, roughness and thickness parameters of the layers in the structure. Although the reflectivity profile can be very complex, for the 1-layer system mentioned before (see Figs. 4.6a and b) the following dependencies are observed: the amplitude of the fringes is proportional to the density contrast between the film and the substrate, the width of the fringes is inversely proportional to the thickness of the film and the oscillation decay rate is proportional to the surface roughness. The intensity decay rate increases with both the surface and interface roughness.

Because the amplitude of the Kiessig fringes increases with the difference in densities be-

tween the film and the substrate, Kiessig fringes are very difficult (or impossible) to observe in homoepitaxial structures. If one looks at Fig. 4.6a, the green curve corresponds to the reflectivity of a SiO₂ film on a Si substrate. One can see two clear differences compared to the reflectivity curve of the Fe film in blue; one is θ_c , and the other is the lack of fringes in SiO₂. This happens because the density of SiO₂ ($\rho_{\text{SiO}_2} = 2.30\text{g/cm}^3$) is very close to the density of Si ($\rho_{\text{Si}} = 2.33\text{g/cm}^3$).

4.2 Electron microscopy

Electrons are easier to focus than x-rays and can be used to characterize materials at the atomic scale with *electron microscopy*. The main advantage of electron microscopes over conventional optical microscopes is that the wavelength of highly energetic electrons can be up to 10⁵ times shorter than the wavelength of photons, which gives the electron microscopes much higher resolution. The wavelength of the accelerated electrons is given by the well known *de Broglie* formula:

$$\lambda = \frac{h}{p} = \frac{h}{\left[2m_0eV \left(1 + \frac{eV}{2m_0c^2}\right)\right]^{1/2}} \quad (4.19)$$

where V is the accelerating voltage, m_0 is the electron rest mass and e is the electron charge. Here, the factor $\left(1 + \frac{eV}{2m_0c^2}\right)$ reflects the relativistic nature of the electrons, which at typical energies of $> 100\text{keV}$ acquire velocities of the same order of magnitude as the speed of light. At these energies, λ is of the order of several picometers, giving the electrons the capability of imaging specimens with atomic resolution (assuming no aberrations).

In an electron microscope, the specimen interacts with the incident electrons giving rise to different exit signals (Fig. 4.8) which are collected and analysed. The *scanning electron microscope* (SEM) and the *transmission electron microscope* (TEM) are the two main types of electron microscopes. While the most important signals for a SEM are the secondary and backscattered electrons, TEM uses the direct beam and the transmitted elastically scattered electrons to form images with the aid of (electro)magnetic lenses. As a result, TEM offers invaluable information on the inner structure of the sample such as crystal structure, morphology, and stress state information. However, only if the specimen is thin enough, can the electrons be forward scattered and hence, sample preparation for TEM is much more tedious and requires experience in methods like mechanical polishing and focused ion beam milling (FIB). Besides diffraction and spatial imaging, the high-energy electrons cause electronic excitations

in the atoms of the specimen which analytical electron microscopy uses to obtain chemical information. The two types of spectroscopies in a TEM are *energy dispersive x-ray spectrometry* (EDS) and *electron energy-loss spectrometry* (EELS). By combining imaging, diffraction and spectroscopy, many questions about the microstructure and chemistry of the sample can be tackled during a TEM session.

Due to its high spatial resolution (in aberration corrected TEMs, images with spatial resolution of < 50 pm have been reported, in contrast to the ~ 0.5 nm resolution of a SEM) TEM is considered to be the most popular technique in characterizing nanomaterials in electron microscopy. However, operating the instrument involves intensive training and the results can be very difficult to interpret. Among the numerous books that teach about TEM, [CW16] and [FH12] were the main sources of this section and are recommended as introductory readings. After looking at the optics of a TEM (§ 4.2.1), the attention will be fixed on the main techniques used in this thesis (§ 4.2.2 to § 4.2.4). Finally, the preparation procedure for TEM samples will be explained in § 4.2.5.

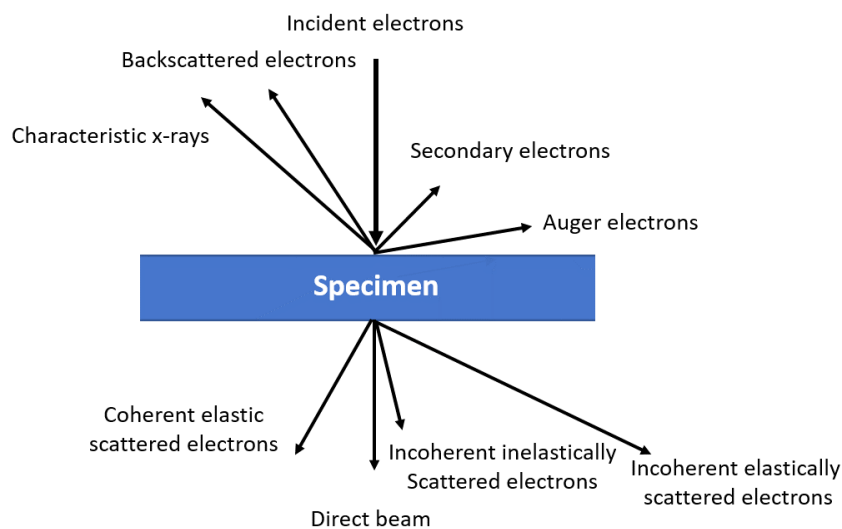


Figure 4.8: The different signals that can take place after an incident beam of electrons has interacted with the specimen. The thinner the specimen, the more electrons will pass through it.

4.2.1 Optics and lenses in TEM

A transmission electron microscope consists of an electron gun and a complex assembly of electromagnetic lenses, apertures, a sample holder and an image viewing/recording system. The gun generates high energy electrons which are deflected and focused many times inside the

microscope column before finally being detected by a charge-coupled-device (CCD) camera or a fluorescent viewing screen. The system of lenses between the electron gun and the specimen is called illumination system. These lenses collect the electrons coming out of the gun and focus them on the specimen as a parallel beam (or a convergent beam in the case of scanning TEM § 4.2.3). Once the electrons have interacted with the specimen, another complex system of lenses is used to magnify and record either an image or a diffraction pattern. These sets of lenses are the objective, intermediate and projector lenses. A schematic representation of the components of a TEM is shown in Fig. 4.9a.

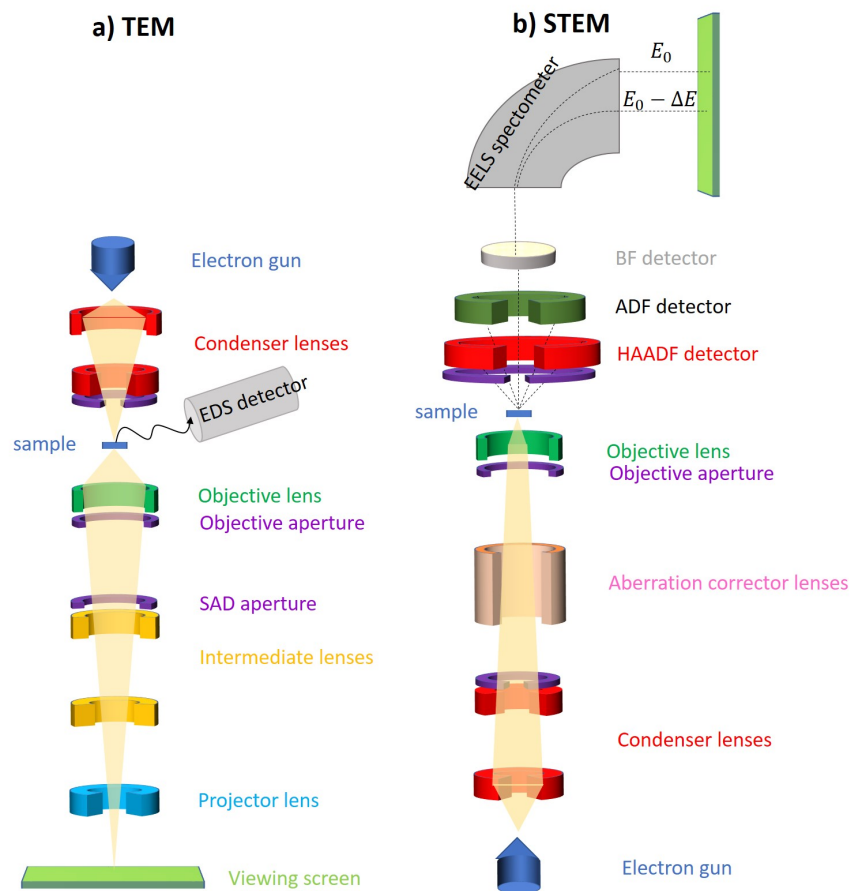


Figure 4.9: Schematic representation of the electromagnetic lenses, apertures and detectors in (a) TEM and (b) STEM mode.

The lenses in an electron microscope are completely different from conventional optical lenses in which light is focused by refraction. In contrast, in a magnetic lens, electrons are focused via strong magnetic fields created by Cu-coils that are surrounded by soft Fe pole pieces. The strength of the lens is varied by varying the current flowing through the coils. Electrons that pass through the lenses are then deflected by the Lorentz force and their trajectories can be modified:

$$\vec{F}_{Lorentz} = -e(\vec{E} + \vec{v} \times \vec{B}) \quad (4.20)$$

where \vec{v} is the velocity of the electron and \vec{E} and \vec{B} are the external electric and magnetic fields respectively. Due to the normal and parallel components of the electron velocity, the electrons follow spiral trajectories as they travel along the lens. Although the magnetic fields within the lens provide a control mechanism over the electron trajectories, magnetic lenses are far from perfect. The spherical aberration, chromatic aberration and astigmatism are some of the most important lens imperfections that limit the resolution of the microscope and hence, minimizing them is important.

The *spherical aberration* comes from the inability of the lens to behave the same way for paraxial electrons (electrons travelling near the optic axis) and electrons travelling off-axis. Indeed, the further the electron is to the optic axis, the more strongly it is bent back towards it. Hence, a point object is imaged as a disk of finite size as illustrated in Fig. 4.10. The spherical aberration of the objective lens is the most limiting defect in TEM and hence, many modern microscopes nowadays incorporate C_s correctors. These correctors have significantly improved spatial resolution, with some of them reaching values $< 1\text{\AA}$.

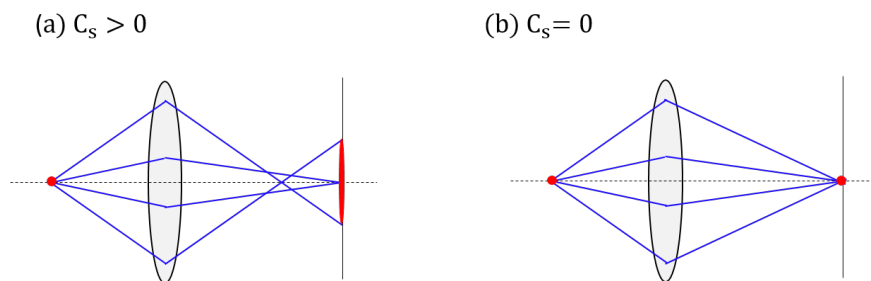


Figure 4.10: (a) Effect of the spherical aberration in an electron lens, where electrons at different angles to the optic axis are brought to a focus at different points; (b) The effect of correcting the spherical aberration which brings all electrons into focus at the same point. Here C_s is the spherical aberration constant which relates to the radius of the disk and so, the smaller C_s is the better.

Chromatic aberration is related to electrons with different wavelengths which arise from the energy spread of the electron gun. Electron guns do not emit ideally monochromatic beams but they all have an energy spread that can vary from $\sim 0.3\text{eV}$ to $\sim 1.0\text{eV}$. Electrons with lower energies will be deflected more and they will have shorter focal lengths than the more energetic electrons. As a consequence, this will create a blurred disk at the imaging plane rather than a point, similarly to the spherical aberration. If the microscope is C_s -corrected, chromatic aberration is the next persistent imperfection that limits its resolution. Cold cathode

field emission guns reduce the energy spread to $\sim 0.3\text{eV}$, which can be further improved to $\sim 0.015\text{eV}$ using monochromators.

Finally, *astigmatism* relates to inhomogeneities of the magnetic field in the lens. Astigmatism can be corrected using octapoles that generate small compensating magnetic fields, which can be manually controlled by the operator of the microscope.

4.2.2 Imaging and diffraction in TEM

A simplified ray diagram of the microscope in diffraction and imaging modes is shown in Fig. 4.11. When the intermediate lens is focused on the image plane of the objective lens, all transmitted and diffracted beams leaving the specimen are combined to form an image. In this imaging mode, the specimen shows a generic *mass-thickness contrast*. Mass-thickness contrast originates from elastic scattering when the incident electrons are deflected due to Coulomb interactions as they pass through an atom. The probability of scattering depends on the strength of the Coulomb interaction, and increases with the atomic number Z and the thickness of the specimen. If the thickness is homogeneous, areas with heavy atoms appear darker and areas with light atoms appear brighter.

However, if no objective aperture is used, mass-thickness contrast is weak. Looking at Fig. 4.11a, one can see that not all the transmitted and scattered beams are required to form an image. A full image can also be formed by using only the beams that pass through one point in the back focal plane. What distinguishes the points located in the back focal plane is that all the beams entering a given point have been scattered at the same angle. Thus, the back focal plane contains the diffraction pattern of the area illuminated by the electron beam. By inserting the objective aperture at a specific position in the back focal plane, one can form an image with only those electrons that have been diffracted by a specific angle. This defines two imaging modes. When the aperture is positioned to select the transmitted beam, a *bright-field* (BF) image is taken. When the aperture is positioned to select the electrons diffracted by an angle, a *dark-field* (DF) image is taken. The contrast in BF and DF images is called *diffraction contrast* and it is used to enhance the otherwise little contrast shown by an apertureless image. BF and DF imaging modes are particularly useful to image structural defects such as dislocations and interfaces or to look at crystal grains.

Unlike BF and DF imaging modes, *high-resolution TEM* (HRTEM) uses both the transmitted beam and several diffracted beams which interfere coherently to form *phase contrast* images. In theory, the larger the range of Δk of diffracted electrons, the better is the spatial resolution of the image. However, conspiring against this precision is the spherical aberration of

the objective lens. Thus, in reality one needs to optimize the range of angles for which entering rays suffer acceptable phase distortions.

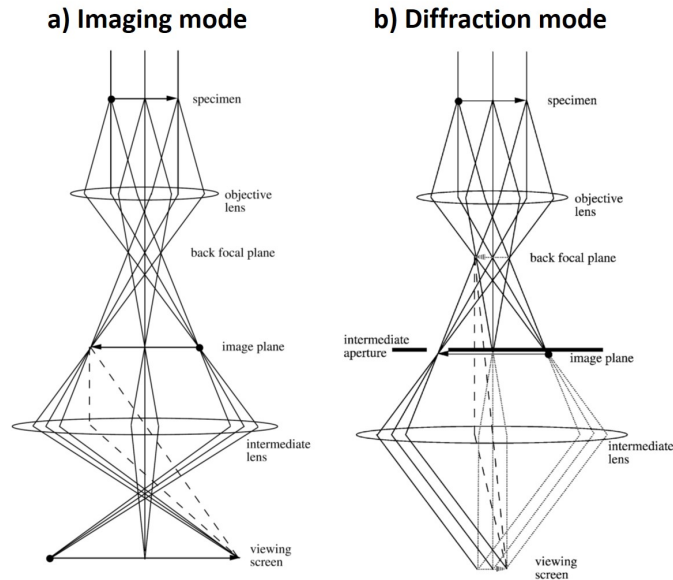


Figure 4.11: Simplified ray diagrams of a TEM in (a) imaging and (b) diffraction mode. Taken from [FH12].

If only the forward beam and one diffracted beam (\vec{g}) are taken, when the amplitudes of the two beams are added together, a contrast known as *lattice fringes* arises. These fringes lie perpendicular to \vec{g} , and have the same periodicity as the spacing of the scattering planes, $2\pi/\vec{g}$. If several diffracted beams are selected, intersecting sets of fringes are obtained in the image, producing sets of black or white spots, identified as *atomic columns*. With HRTEM, interfaces can be studied at the atomic level. All the mentioned imaging modes have been depicted in Fig. 4.12.

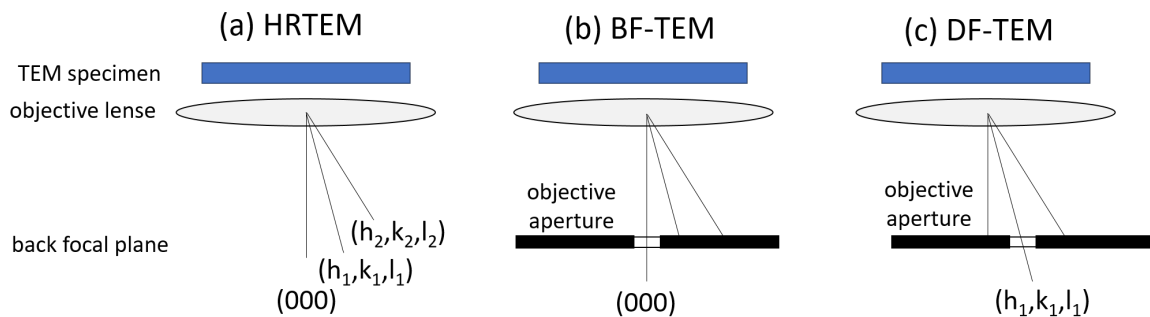


Figure 4.12: Different imaging modes in a conventional TEM; the user can switch between the modes by changing the position of the objective aperture at the back focal plane.

Diffraction patterns can be viewed in a TEM when the intermediate lens is focused on the

back focal plane of the objective lens (Fig. 4.11b). This can be done by changing the strength of the intermediate lens so that it takes the back focal plane of the objective lens as its object. In crystalline samples, the diffraction pattern is a group of sharp spots formed when the electrons are elastically scattered by the different sets of atomic planes in the specimen. In order to select the area from which the diffraction pattern is taken, a selected area aperture can be inserted in the first intermediate image plane. An image recorded this way receives the name of *selected area diffraction* (SAED) pattern.

When the angle between the incident wavefront and the scattering planes meets Bragg's condition, constructive interference occurs and a diffraction spot is observed in the viewing screen of the TEM. Each set of (hkl) planes yields a fundamental reflection, g_{hkl} , and a set of high order reflections g_{nhnknl} . For high energy electrons, with wavelenegths of 2 – 4pm, the surface of the Ewald sphere is very flat (refer to Fig. 4.3) and therefore, many diffraction spots can be measured at the same time in contrast to x-rays where a big angular range is required. Also, because a TEM specimen is thin, i.e. the dimension is confined in one direction, the points in the Ewald sphere elongate in one direction, forming rods instead of points. Thus, even when the Bragg condition is not perfectly satisfied, the diffraction spots can still be seen in the DP. In TEM it is sufficient to tilt the specimen to a high symmetry *Zone axis* [UVW] direction, which is common to all the planes of the zone, to obtain the information needed about the crystallinity of the sample.

4.2.3 STEM high angle annular dark field imaging (STEM-HAADF)

In the previous section, SEM and TEM were introduced as the main electron microscopy techniques. Actually, there is one more technique to mention which is a combination of TEM and SEM called *scanning transmission electron microscopy* (STEM). It can be applied to both systems, but its full capabilities are revealed when applied to a TEM tool. Most modern TEMs can be switched to *STEM mode*, and the user only needs to alter their alignment procedure. In STEM mode, the beam is finely focused and scans the sample area (as SEM does), while the image is generated by the transmitted electrons (like in TEM).

A schematic representation of STEM imaging is shown in Fig. 4.9b. In this configuration, a narrow ($\approx 1\text{--}10 \text{ \AA}$) focused beam of electrons is scanned across the surface of the specimen. The condenser and objective lenses above the specimen create a convergent beam which is focused to a sub-angstrom probe. The size of the probe, limited by the aberrations of the objective lens, determines the resolution of the image. By rastering the probe across the surface, local information of the structure can be gained on the angstrom scale. The fundamental difference

between the STEM mode and the TEM mode is the position of the lenses. In STEM there are no lenses below the specimen to magnify and construct the image. Instead, STEM uses detectors positioned at different angles to collect the electrons for each pixel of the scanning frame. The magnification of the image is given by the size of the pixels. The angular ranges of the detectors in STEM mode have been illustrated in Fig. 4.13.

When the electrons interact with the specimen they scatter under different angles. Using the different collection angles three types of images can be formed. The low angle electrons (up to 10 mrad) form so called bright field (BF)-STEM images while the electrons scattered at very high angles (from 70 to 200 mrad) form the *high angle annular dark field* (HAADF)-STEM images. The rest of the electrons which scatter in the mid-range are detected by the annular dark field (ADF) detector and form ADF-STEM images.

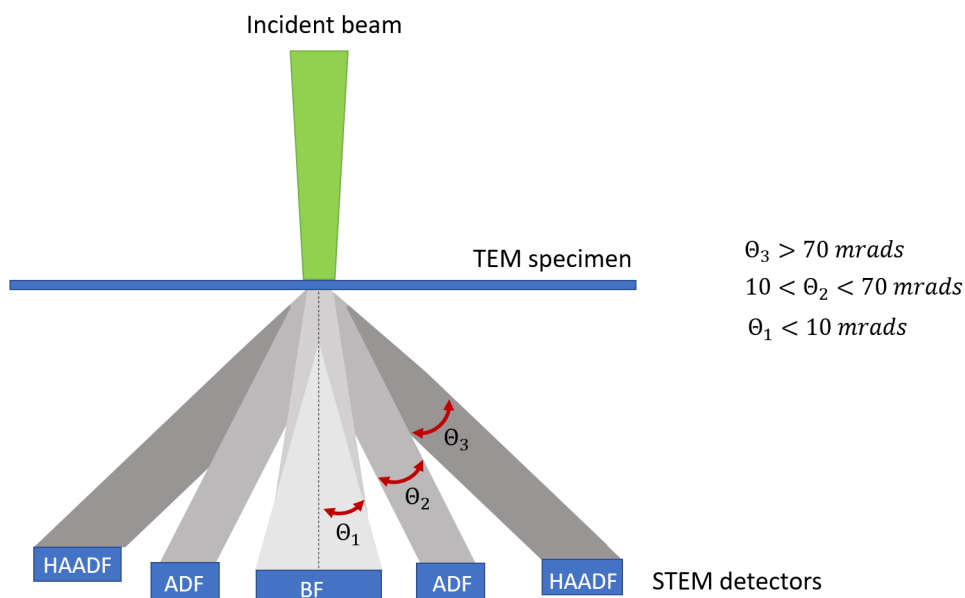


Figure 4.13: Angular range of the forward scattered electrons which are collected by the different detectors in STEM.

HAADF imaging (also called *Z contrast imaging*) is a very well established high-resolution imaging technique. Unlike HRTEM images, HAADF images are formed from incoherent elastically scattered electrons which experience Rutherford scattering proportional to the atomic number as $\approx Z^2$. Because they scatter incoherently, phase differences and interferences that were central issues for HRTEM imaging are irrelevant for HAADF imaging. Each atomic column can then be considered as an independent scatterer because there is no constructive or destructive interference between the phases of the wavefunctions coming from each column. Thus, the intensity recorded by the HAADF detector can be expressed as a sum of all scat-

tering intensities coming from the scattering centres which have interacted with the probe. If the probe size is in the sub-angstrom region, this allows us to visit several pixels in-between two neighbouring atomic columns at high magnification. As a consequence, the signals coming from two neighbouring atomic columns are practically independent and can be resolved. The atomic columns that contain elements with higher Z appear brighter, whereas those containing lighter atoms appear darker. This has been the most useful imaging technique for the CFS films studied in this thesis. Indeed, HAADF images are easier to interpret than HRTEM and they make it possible to distinguish between $L2_1$ -ordered grains and B2-ordered regions in the mixed-phased films² as will be seen in Chapter 5.

4.2.4 STEM spectroscopy: EELS and EDS

A major advantage of STEM is that it can be coupled with spectroscopy measurements like *electron energy loss spectroscopy* (EELS) and *energy-dispersive x-ray spectroscopy* (EDS) to reveal the local chemistry of the specimen.

Some of the electrons that traverse the TEM specimen will lose energy to plasmons or core excitations as illustrated in Fig. 4.14a. Then, jumps in spectral intensity called *absorption edges* occur at the threshold energies required to excite the core electrons of the atoms in the material. The intensities of these absorption edges are used to identify and quantify all the elements in the periodic table. In modern STEMs, EELS acquisition can be made simultaneously with HAADF-STEM imaging. While the electrons scattered elastically are collected at high angles by the HAADF detector, those scattered inelastically travel under a very small angle and go through the hole of the HAADF detector. These electrons are then directed to the EELS spectrometer which can spatially separate them into different channels according to their energy (see Fig. 4.9b). In addition to elemental identification, the low-loss processes detected by EELS give a tremendous amount of information about the chemistry and the electronic structure of the specimen atoms such as their bonding/valence state, the nearest-neighbour atomic structure, the free electron density and more. The main drawback of EELS is that it can be a challenging experimental technique; it requires very thin specimens to get the best information, and understanding and processing the spectra requires more of a physics background than EDS.

In contrast to EELS where the primary process is measured (i.e. the energy loss), in EDS the secondary process is detected. That is, after the core electron has been excited, the remaining

²To be precise, HAADF images allow the distinction between the B2 phase and the $L2_1/DO_3$ phases. However, it cannot differentiate the $L2_1$ structure from the DO_3 type of disorder which is highly detrimental for half-metallicity. Nonetheless, as will be discussed in Chapter 5, the correlation between structural and magnetic properties of the films shown in this work points to the presence of $L2_1$, rather than to the disordered DO_3 .

core hole decays by the emission of an x-ray (Fig. 4.14b) which is collected by the EDS detector. Solid state EDS detectors are usually reverse biased p-i-n Si(Li) diodes with metallic contacts at their ends. Most of the semiconducting detector is intrinsic but the regions adjacent to the contacts are n-type and p-type, configuring a p-i-n junction. When the detector absorbs the incoming x-ray, the energy is transferred to an electron which in turn, is transferred from the valence band into the conduction band of the intrinsic SC, and accordingly a hole in the valence band is created. Due to the much higher energy of the x-rays ($\sim keV$) compared to the energy required to create an electron-hole pair ($\sim eV$), one incoming x-ray typically generates thousands of such pairs. The charge is collected on the electrodes by generating a pulse of current through the p-i-n junction, and is finally converted into a voltage signal. The detected voltage is proportional to the energy of the x-ray, and hence elemental identification is possible. The EDS detector processes the x-rays one by one as they enter the detector, and generates the spectrum of energies. Although EDS does not offer as much information as EELS (and its spatial resolution is also lower), it is an easier experiment to perform and can be implemented in all SEM, TEM and STEM microscopes. Also, it does not require samples to be so thin. In this work, EDS has been used to find the elemental composition of the CFS films, both in planar-view SEM-EDS and in cross-sectional STEM-EDS.

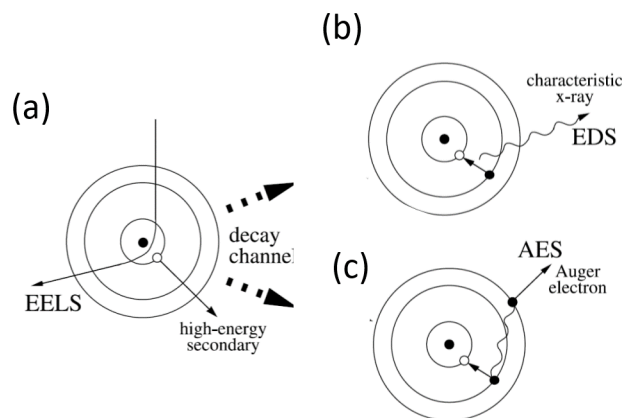


Figure 4.14: Some of the interaction processes between a high energy electron and an atom that generate x-rays for spectroscopy. Taken from [FH12].

To quantify the chemical concentrations from an EDS spectrum, the background (which mainly originates from *bremstrahlung* radiation) is first subtracted. The isolated intensities are then compared for the different elements in the sample, and are finally converted into absolute concentrations. If the sample under study is a thin film ($< 10\text{nm}$), the concentration ratio of two elements A and B (C_A/C_B) can be approximated to:

$$\frac{C_A}{C_B} \approx k_{AB} \frac{I_A}{I_B} \quad (4.21)$$

where I_A and I_B are the characteristic x-ray intensities of elements A and B respectively, and k_{AB} is the so-called *Cliff-Lorimer* factor that depends on the accelerating voltage and the specific EDS spectrometer. For thicker samples, *ZAF* corrections³ must be introduced in the calculation. In this thesis, the AZtecLive software and the NSS software have been used for the quantitative analysis of the SEM-EDS and STEM-EDS spectra respectively. A typical SEM-EDS spectrum is shown in Fig. 4.15 for a CFS/MgO(001) sample. At energies below $< 2\text{keV}$, the L_α lines of Fe and Co and the K_α line of Si can be observed; for energies between 6 and 8 keV the K_α lines of Fe and Co appear. The atomic concentrations extracted with AZtecLive reveal a film composition of: at% of Co, Fe and Si=46%, 26% and 28% respectively.

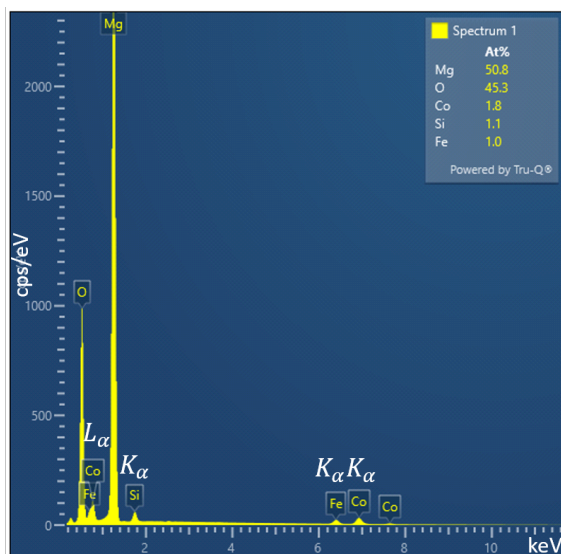


Figure 4.15: Plan-view EDS spectrum taken for a CFS/MgO(001) sample. The spectrum was taken for an accelerating voltage of 15kV and a 3nA probe current in the JEOL-7800 SEM system. The atomic concentration of the substrate elements (Mg and O) and the film elements (Fe, Co and Si) are shown in the light-blue box on the top-right corner.

³ZAF corrections take into account the influence on the intensity of emitted x-rays by: the atomic number, which affects the penetration of incident electrons into the material (Z); the absorption of x-rays in the specimen (A); and the fluorescence caused by other x-rays generated in the specimen (F).

4.2.5 Focused Ion Beam (FIB) for cross-sectional specimen preparation

4.2.5.1 Introduction

In this thesis, a *focused ion beam* (FIB) system has been used to create the lamellas for cross-sectional (S)TEM. Good reviews on this topic can be found in [GS99] and [SJ16]. A FIB instrument is usually a dual-beam system that combines a high resolution SEM column and a FIB column in a vacuum chamber. The combination of the two is especially useful for cross-sectional specimen preparation where the electron beam is used to monitor the cross-sectional face as the ion beam mills perpendicular to the surface of the specimen. The SEM column is perpendicular to the sample stage and the ion column typically forms a 52° angle with the SEM. A schematic diagram of a typical FIB configuration is shown in Fig. 4.16a. To its right, Fig. 4.16b, the FEI Nova dual system used in this thesis.

The most important component in the FIB column is the ion source. This is usually a *liquid metal ion source* (LMIS) which uses liquid Gallium (Ga^+) to generate a very stable flux of ions. The main reasons for using Ga^+ ions are the low melting point, low vapour pressure and good vacuum properties of the material. A typical LMIS contains a tungsten (W) needle attached to the Ga^+ reservoir. When a voltage is applied to the LMIS, the Gallium melts and flows towards the tip of the needle. Here, two forces compete with each other. One is force created by the electric field generated by a couple of extractor electrodes which pulls the Ga^+ ions out of the needle. The other is the surface tension of the liquid Gallium which attracts the molecules to the end of the tip. When the two forces balance out, the so-called *Taylor cone* is formed, which has a typical radius smaller than 10 nm. At this point, if the current is slightly increased, the Ga^+ ions start to come out from the end of the cone generating a highly controlled Ga^+ flux. The Ga^+ beam is then collimated and reaches the sample surface after passing through the various lenses, apertures and deflectors in the ion column. By controlling the strength of the electrostatic lenses and adjusting the effective aperture sizes, the ion current and hence the beam diameter, can be altered from 1 pA to almost 50 nA. On impact with the surface, atomic sputtering occurs removing material from the surface. In addition to sputtering, other phenomena can take place, such as implantation of Ga^+ ions. The bombardment of ions also results in the emission of secondary electrons which allows imaging the sample.

The main drawback of using FIB over other mechanical methods is the irradiation damage from the exposure to the beam. In fact, irradiation with the Ga^+ beam can lead to undesired changes of the physical and chemical properties of the material. The Ga^+ implantation for example, can change the coercivity and anisotropy in magnetic films [Gup05; OL02]. In order

to minimize the ion damage, in addition to using lower currents, protective layers are deposited prior to the milling using *ion beam assisted vapour deposition*. Here, a *gas injection system* (GIS) containing a metalorganic material such as platinum, $(\text{CH}_3)_3\text{Pt}(\text{CpCH}_3)$, is used. The GIS consists of a retractable needle tube which is used to direct the gas to the sample surface. During deposition, the gas is heated and injected into the surface through the needle tube. Then, the electrons coming from the SEM column or the ions coming from the FIB column break the chemical bonds in the gas and deposit the desired molecule onto the surface.

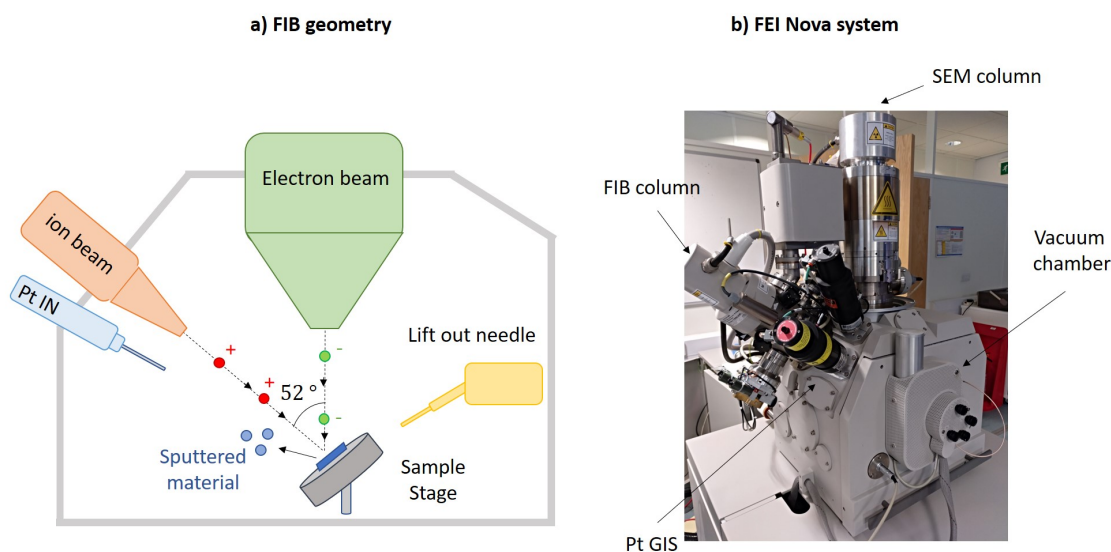


Figure 4.16: (a) Schematics of a combined FIB-SEM system and (b) FEI Nova 200 NanoLab system used for the preparation of lamellas in this thesis.

4.2.5.2 Procedure for TEM sample preparation

In order to be able to screen a specimen with the TEM, the specimen must be very thin so that electrons can be transmitted through the sample. For this to happen, thicknesses below 100 nm are needed. One of the methods to create these so-called *lamellas* is using the FIB. The procedure to make a TEM lamella for cross section experiments can be divided in three steps: the *mill out*, the *lift out* and the *thinning*.

Prior to loading the sample into the vacuum chamber, the sample is coated with a thin layer of carbon followed by a 5-10 nm layer of a highly conductive metal such as Au or a PtPd alloy. This, in addition to protecting the surface of the sample, also prevents it from charging. Electric charging happens when the electrons bombarding the sample accumulate in the surface which then repel the successive electrons coming from the SEM column. If there is no conducting path for electrons to flow from the surface to ground (when the sample is poorly conductive), typically the sample holder, imaging becomes very challenging causing all sorts

of problems such as drift, blur and low contrast. Once the sample is ready, it is loaded in the chamber which is pumped down to pressures typically between 10^{-3} and 10^{-4} Torr.

During the *mill out* the actual lamella is produced. Before the milling is begun, two layers of Pt with a total thickness of $\approx 3\mu\text{m}$ are deposited over an area with typical dimensions of $\approx 2\mu\text{m} \times 18\mu\text{m}$, which marks the region of interest (ROI) and the desired crystal orientation (Fig. 4.17a). The first layer of Pt has a thickness of 300 nm – 500 nm and it is deposited using the e-beam. This is followed by a second thicker layer of $2.5\mu\text{m} - 3\mu\text{m}$ deposited with the ion beam. Milling is then started. Large trenches of material are sputtered on three sides (two long and one short) of the ROI using Ga^+ currents of 3 nA (Fig. 4.17b). The trenches are milled with a *staircase pattern* so that more material is sputtered closer to the ROI. The width of the patterns for milling the channels is typically $5\mu\text{m}$ with which a $\approx 1.5\mu\text{m} - 1.8\mu\text{m}$ deep lamella will be obtained. A margin of about $1\mu\text{m}$ is left between the trenches and the ROI. That area is subsequently milled with lower Ga^+ currents (1 nA) and with a ± 2 degree tilt with respect to the ion column. In order to cut the lamella out, a U-shaped cut is performed at one of the long sides of the specimen at a 45° angle with respect to the FIB column (i.e with the stage tilted at 7°). A second wedge is then milled at the other long side of the specimen by rotating the stage by 180 degrees (Fig. 4.17c). The mill out step finishes leaving a small bridge of material at one of the short sides of the lamella, which holds it in place until it is lifted out.

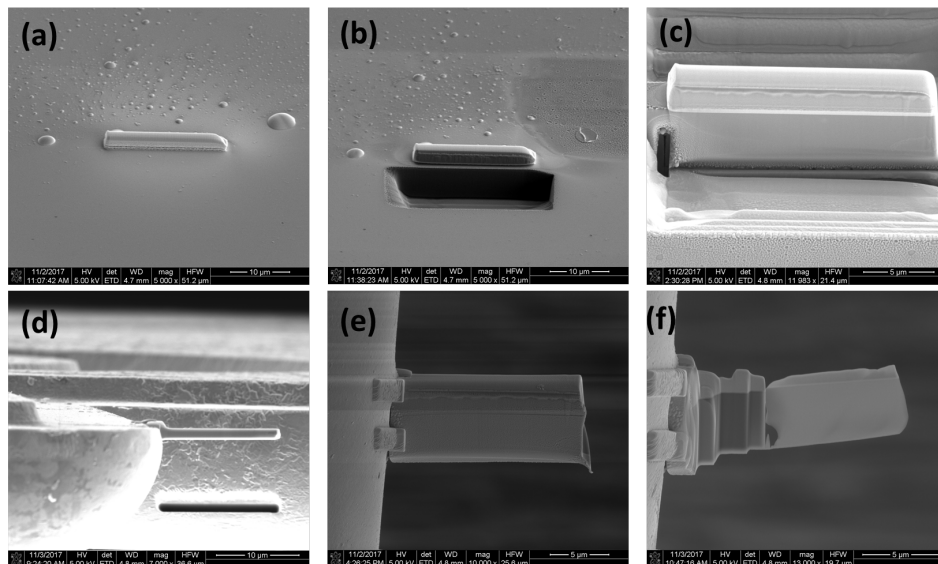


Figure 4.17: Images taken during the preparation of a FIB-lamella for cross-sectional TEM.

The next step is to *lift out* the lamella. The stage is tilted back to 0 degrees, that is, the ion gun forms a 52° angle with the surface of the sample. An Omniprobe lift-out needle is then inserted and moved towards the short side of the ROI that was freed during the cut out.

The needle is brought into contact with the lamella and a bridge is created by depositing a ≈ 400 nm layer of e-Pt across the contact which is reinforced by an additional ≈ 300 nm layer of Ga⁺-Pt. Note that at this point, the stage cannot longer be rotated as any rotation will break the contact between the lift out needle and the lamella. The lamella can now be cut free with a 1nA Ga⁺ current that hits the bridge joining the specimen and the bulk at a 52° angle (0° respect to the SEM column). When the specimen has been detached, the lamella is lifted out by lowering the sample stage, and it is then driven to the Cu grid by moving the stage underneath the needle. When the lamella is positioned at the desired post in the grid, lamella and post are attached together by depositing a couple of Pt layers with both the e-beam and the i-beam. The lamella is finally freed from the needle using Ga⁺ currents of 1nA and the needle is withdrawn (Figs. 4.17d and e).

To finish the cross-sectional specimen preparation, the lamella has to be thinned to electron transparent thicknesses ideally < 50 nm. To do so, the stage is tilted to 52° where the ion beam is parallel to the sides of the lamella. Each side is then consecutively thinned in several steps. In each step, the angle between the cross-sectional face and the ion beam is decreased, starting with a relative angle of $\pm 4^\circ$ (i.e with stage tilts of 56° and 48°) and finishing with $\pm 0.5^\circ$ in the last step. For each step, the thinning length becomes smaller and smaller to avoid bending the lamella. As the lamella becomes thinner, the Ga⁺ current must be decreased to avoid over-milling and contamination of the specimen. For the very last steps, the energy of the ion beam is also reduced to 10 kV and 5 kV. A typical thinning recipe used for the samples in this thesis is shown in Tab. 4.1. When the lamella has been thinned to $\approx 60 - 70$ nm, a final milling is performed with the stage tilted at 42° using a Ga⁺ beam of 5 kV and 29 pA. This final step serves to clean the lamella and thin it slightly further. An image of a finished TEM lamella is shown in Fig. 4.17f.

Step	Stage tilt (°)	Stage rotation	Voltage (kV)	Current (pA)	final thickness of lamella (nm)
1	56	0	30	500	3000
2	48	0	30	300	2000
3	54	0	30	300	1400
4	50	0	30	100	850
5	53	0	30	100	500
6	51	0	10	50	300
7	53	0	10	50	200
8	51.5	0	5	70	100
9	52.5	0	5	70	< 100
10	42	0	5	29	—
11	42	180	5	29	—

Table 4.1: Steps used to thin the lamella to electron transparent thickness. Typical stage angles and the Ga^+ voltage and current used for each angle are shown. The thickness of the lamella after the thinning step is also shown in the last column.

4.3 Magnetic characterization

4.3.1 Ferromagnetic resonance spectroscopy (FMR)

Ferromagnetic resonance (FMR) occurs when a magnetic sample is exposed to a large static field (\vec{H}) and a small RF field (\vec{h}) applied perpendicular to \vec{H} and whose frequency ω is tuned to the Larmor frequency of the system. When the bias field is applied, the magnetic moments in the sample will start precessing around \vec{H} with the characteristic Larmor frequency $\omega = \gamma H$ until they eventually align with the field. The magnetic moments then act as a macrospin that can be driven to precession when an RF field is applied as illustrated in Fig. 4.18. When the frequency of the RF field matches the natural frequency ω , the amplitude of the precession is maximum and the macrospin can precess resonantly about the equilibrium direction. FMR is a well-established method in magnetism to study magnetic excitations, magnetization dynamics and damping mechanisms in thin films [Far98].

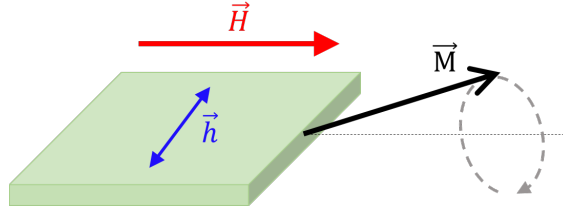


Figure 4.18: Illustration of the FMR effect where a magnetic sample is subjected to a bias field \vec{H} and a transverse RF perturbation \vec{h} .

In the classical picture, the resonance phenomenon can be described by the LLG equation (eq. (2.20)) as a Larmor-like precession about the following effective field [Kit51]:

$$\vec{H}^{eff} = \vec{H} + \vec{h} + \vec{H}_{anis} \quad (4.22)$$

where $\vec{H}_{anis} = -\frac{1}{\mu_0 M_s} \frac{\partial U_{ani}}{\partial \vec{m}}$ is the so-called anisotropy field. Among the energy contributions derived for a FM system in Chapter 2, the sources of anisotropy in the films studied in this thesis are the shape anisotropy (§ 2.1.3) and the magnetocrystalline anisotropy⁴ (§ 2.1.2). On top of these two, two more contributions have been included in the form of uniaxial anisotropies, U_{\perp} and U_{\parallel}^u , which are defined as:

$$U_{\perp} = -K_{\perp} \cos^2 \theta_M \quad (4.23)$$

$$U_{\parallel}^u = -K_u (\vec{m} \cdot \hat{n}_U)^2 = -K_u \sin^2 \theta_M \cos^2 (\phi_M - \phi_U) \quad (4.24)$$

U_{\perp} takes into account tetragonal distortions and favours the magnetization to point out-of-plane competing against the shape anisotropy. On the other hand, U_{\parallel}^u accounts for a two-fold in-plane anisotropy commonly observed in thin films due to interfacial and surface effects. The total anisotropy energy is then:

$$U_{anis} = U_{can} + U_{ms} + U_{\perp} + U_{\parallel}^u \quad (4.25)$$

To find the resonance condition, one has to solve eq. (2.20) for the effective field in eq. (4.22) with $h \ll H$. This can be done by decomposing the magnetization into a static and a dynamic part as done in [Bil07]. Another approach is to solve the Smit-Beljers equation⁵ [Smi55]:

⁴The exchange interaction is not considered here because it is isotropic and does not contribute to the angular dependence of FMR. The magnetoelastic energy is also ignored as there is no strain being applied to the system.

⁵Note that this equation neglects damping effects, which will add a small correction to the resonant frequency.

$$\left(\frac{\omega}{\gamma}\right)^2 = \frac{1}{M_s^2 \sin^2 \theta_M} \left[\frac{\partial^2 U}{\partial \theta_M^2} \frac{\partial^2 U}{\partial \phi_M^2} - \left(\frac{\partial^2 U}{\partial \theta_M \partial \phi_M} \right)^2 \right] \quad (4.26)$$

where ω is the angular resonant frequency. Here, the energy density is the sum of the internal anisotropy energy (U_{anis}) and the Zeeman energy (U_z) for the static field \vec{H} . In in-plane FMR, the bias field is applied parallel to the sample (Fig. 4.20) and hence, the expression for the Zeeman energy, eq. (2.15), is simplified to the case where $\theta_H = 90^\circ$ (eq. (2.16)). The energy density is then:

$$U_{z+anis}^{001} = -HM_s \sin \theta_M \cos(\phi_M - \phi_H) + K_c \sin^2 \theta_M \left[\frac{1}{4} \sin^2 \theta_M \sin^2(2\phi_M) + \cos^2 \theta_M \right] \quad (4.27)$$

$$+ 2\pi M_s^2 \cos^2 \theta_M - K_\perp \cos^2 \theta_M - K_u \sin^2 \theta_M \cos^2(\phi_M - \phi_U)$$

Note that eq. (4.27) has been written in cgs units, so M_s is in emu/cm³ and K_c, K_u and K_\perp are given in erg/cm³. Solving eq. (4.26) for $U = U_{z+anis}^{001}$ and making the substitution $\theta_M \rightarrow 90^\circ$ for in-plane magnetization, leads to:

$$\left(\frac{\omega}{\gamma}\right)_{001}^2 = \left[H \cos(\phi_M - \phi_H) + 4\pi M_{eff} + \tilde{K}_c [2 - \sin^2(2\phi_M)] \right. \\ \left. - 2\tilde{K}_u \cos^2(\phi_M - \phi_U) \right] \cdot \left[H \cos(\phi_M - \phi_H) + 2\tilde{K}_c \cos^2(4\phi_M) - 2\tilde{K}_u \cos[2(\phi_M - \phi_U)] \right] \quad (4.28)$$

where the anisotropy constants have been expressed as: $\tilde{K}_c = \frac{K_c}{M_s}$, $\tilde{K}_u = \frac{K_u}{M_s}$ and $\tilde{K}_\perp = \frac{K_\perp}{M_s}$, and M_{eff} is the so-called effective magnetization in emu/cm³:

$$4\pi M_{eff} = 4\pi M_s - 2\tilde{K}_\perp \quad (4.29)$$

At high enough frequencies, where the magnetization completely aligns to the field, $\phi_M \rightarrow \phi_H = \phi$ and the expression can be further simplified to:

$$\left(\frac{\omega}{\gamma}\right)_{001}^2 = \left[H + 4\pi M_{eff} + \tilde{K}_c [2 - \sin^2(2\phi)] - 2\tilde{K}_u \cos^2(\phi - \phi_U) \right] \cdot \left[H + 2\tilde{K}_c \cos^2(4\phi) \right. \\ \left. - 2\tilde{K}_u \cos[2(\phi - \phi_U)] \right] \quad (4.30)$$

For the (111)-oriented CFS films, the same procedure is followed, but in this case the

expression of the energy density (U_{z+anis}^{111}) is written in terms of the spherical coordinates of the new coordinate system (Fig. 2.2), where the CAN is now given by eq. (2.7):

$$\begin{aligned}
 U_{z+anis}^{111} = & -HM_s \sin \theta_M \cos(\phi_M - \phi_H) + K_c \left[\frac{1}{3} \cos^4 \theta_M + \frac{1}{4} \sin^4 \theta_M - \frac{\sqrt{2}}{3} \sin^3 \theta_M \cos \theta_M \sin(3\phi_M) \right] \\
 & + 2\pi M_s^2 \cos^2 \theta_M - K_{\perp} \cos^2 \theta_M - K_u \sin^2 \theta_M \cos^2(\phi_M - \phi_U)
 \end{aligned}
 \tag{4.31}$$

also in cgs units. The solution for the in-plane configuration is in this case:

$$\begin{aligned}
 \left(\frac{\omega}{\gamma} \right)_{111}^2 = & \left[H \cos(\phi_M - \phi_H) + 4\pi M_{eff} - \tilde{K}_c - 2\tilde{K}_u \cos^2(\phi_M - \phi_U) \right] \cdot \left[H \cos(\phi_M - \phi_H) \right. \\
 & \left. - 2\tilde{K}_u \cos[2(\phi_M - \phi_U)] \right] - 2\tilde{K}_c^2 \cos^2(3\phi_M)
 \end{aligned}
 \tag{4.32}$$

And in the limit where $\phi_M \rightarrow \phi_H = \phi$:

$$\left(\frac{\omega}{\gamma} \right)_{111}^2 = \left[H + 4\pi M_{eff} - \tilde{K}_c - 2\tilde{K}_u \cos^2(\phi - \phi_U) \right] \cdot \left[H - 2\tilde{K}_u \cos[2(\phi - \phi_U)] \right] - 2\tilde{K}_c^2 \cos^2(3\phi)
 \tag{4.33}$$

Equations (4.30) and (4.33) give the dependence of the resonant frequency with the azimuthal angle ϕ and the bias field, H . Hence, plotting ω as a function of the bias field H allows the anisotropy of the sample to be investigated and a number of useful magnetic properties, such as M_{eff} , the gyromagnetic ratio γ and the anisotropy constants can be probed.

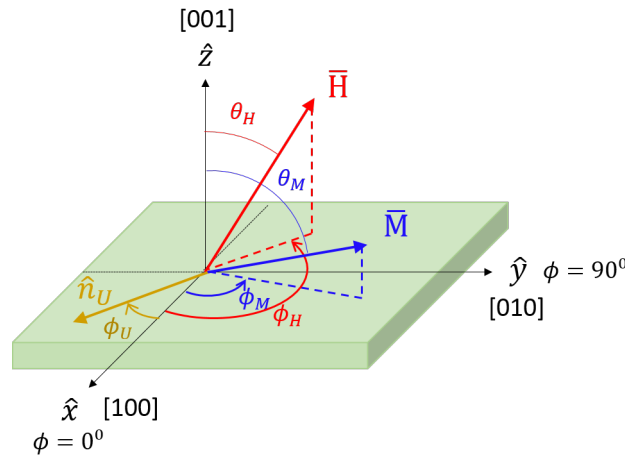


Figure 4.19: Representation of the magnetization and the magnetic field in spherical coordinates.

Apart from studying the magnetic anisotropy, another relevant parameter that can be extracted from FMR spectroscopy is the *Gilbert damping parameter* (α) introduced in § 2.2 which plays a very important role in the magnetization dynamics. In fact, materials with high damping need large excitations to drive resonant precession and thus, the manipulation of these spins is inefficient. On the contrary, weakly damped systems are better candidates for device applications as their magnetization can be switched more easily. The damping mechanism can be *intrinsic* if it arises from interactions in the lattice or *extrinsic* if it arises from structural or magnetic defects. The intrinsic damping α is the one known as Gilbert damping [Gil04; HM09] and is related to the ferromagnetic resonance linewidth ΔH as:

$$\Delta H(\omega) = \Delta H(0) + \alpha \frac{\omega}{\gamma} + \Delta H^{2m}(\omega) \quad (4.34)$$

in cgs units. If only intrinsic damping mechanisms are present, ΔH is linearly related to ω . $\Delta H(0)$ and $\Delta H^{2m}(\omega)$ are contributions from extrinsic damping mechanisms. The latter term introduces a non linear factor with ω and it is due to two magnon scattering processes [AM99].

In the FMR experiments performed in this thesis, a sample is placed on a 50Ω coplanar waveguide (CPW) which sits in the centre of two large Helmholtz coils as illustrated in Fig. 4.20. A Vector Network Analyser (VNA) is used to induce a high frequency magnetic field which oscillates perpendicular to the stripline. The RF field excites the magnetization in the sample, while the DC magnetic field applied between the electromagnets (up to 2T) allows to change the natural frequency of the system. When the precessional frequency coincides with that of the RF field, the sample undergoes FMR.

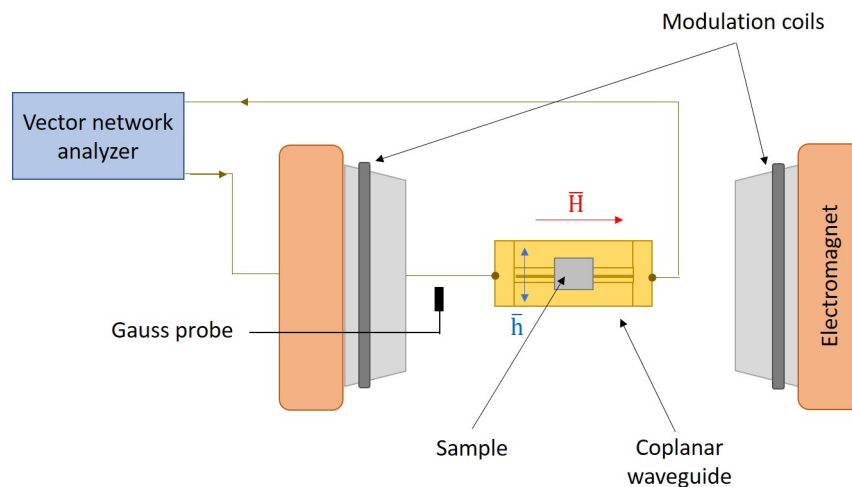


Figure 4.20: FMR set-up using a VNA to measure the RF absorption through a coplanar waveguide.

At resonance, absorption of the microwave power causes an attenuation of the RF current passing through the CPW. This attenuation is observed in the VNA trace as a dip in the microwave transmission coefficient from the input port (port 1) to the output port (port 2), ΔS_{21} , for a fixed RF frequency. Fig. 4.21 shows an example of a VNA-FMR ΔS_{21} spectrum of a CFS film in this work. The spectrum can be fitted to an asymmetric Lorentzian function which accounts for the small mixing of the real and imaginary parts of the susceptibility, allowing the resonant frequency and the linewidth of the resonance to be extracted:

$$\chi'' \cos \delta + \chi' \sin \delta = A \frac{\Delta H \cos \delta + (H - H_r) \sin \delta}{\Delta H^2 + (H - H_r)^2} + B \quad (4.35)$$

Here, χ'' are the χ' are the real and imaginary components of the AC susceptibility respectively and δ is the mixing angle between the absorptive and dispersive components of the FMR; A and B are constants.

By changing the value of the magnetic field and repeating the frequency sweep or vice versa, it is possible to construct a map of the attenuation intensity as a function of the applied RF frequency and H . The frequency-field map will display the distinctive Kittel curve given by eqs. (4.30) and (4.33) for the (001) and (111)-oriented films respectively, allowing the anisotropy constants, M_{eff} and γ to be obtained. The behaviour of the resonance linewidth with ω also allows the quantification of the Gilbert damping according to eq. (4.34).

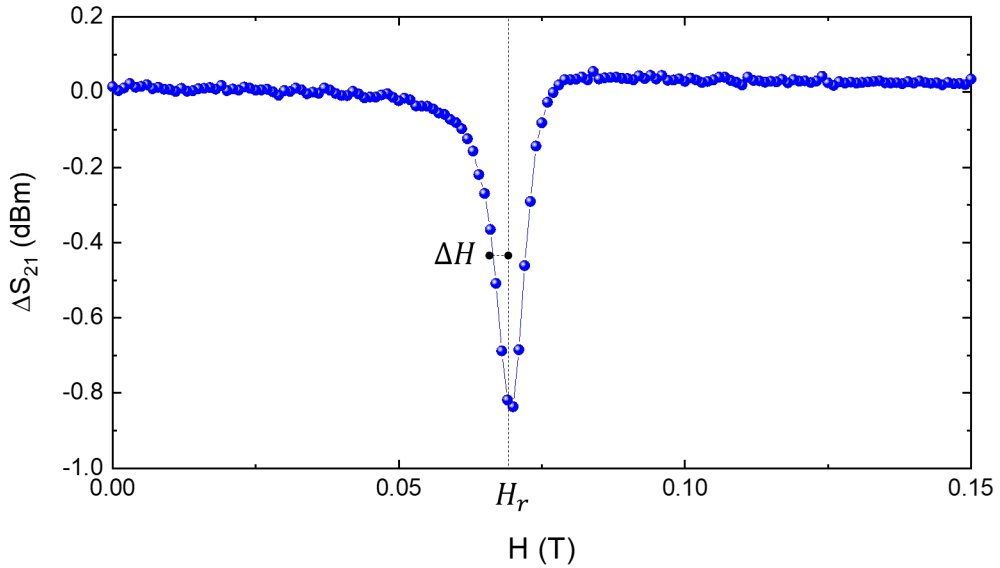


Figure 4.21: ΔS_{21} signal for a CFS film measured at an RF frequency of 10GHz; the ferromagnetic resonance is characterized by the resonant field H_r and the linewidth ΔH .

4.3.2 Vibrating sample magnetometry (VSM)

In order to understand the magnetization reversal mechanism in thin films, it is important to characterize their static magnetic properties. Vibrating sample magnetometry (VSM) is a versatile technique for measuring the magnetization, \vec{M} , of a sample when it is vibrated perpendicularly to a uniform magnetic field, \vec{H}_0 . Changes as small as 10^{-5} to 10^{-6} emu can be detected with this method [Fon59]. In the measurement setup, a magnetic sample moves in the proximity of four pickup coils as shown in Fig. 4.22a. The sample is fixed to the sample rod and vibrates vertically with a frequency ω and amplitude A :

$$\hat{z} = z_0 + A \cos(\omega t) \quad (4.36)$$

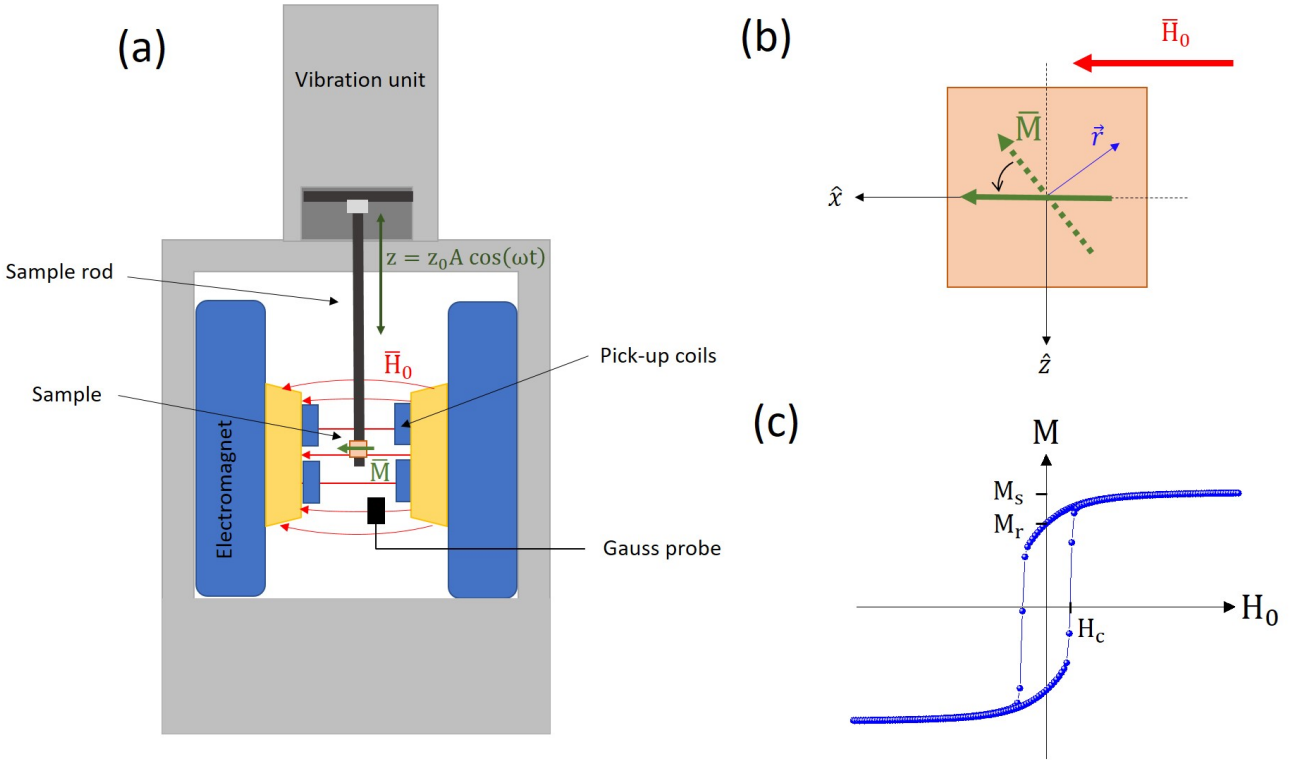


Figure 4.22: (a) Schematic representation of a VSM measurement, (b) sample geometry in in-plane configuration and (c) magnetic hysteresis loop showing the saturation magnetization M_s , the remanent magnetization M_r and the coercive field H_c .

The sample is centered between the two pole pieces of an electromagnet which generates a magnetic field, \vec{H}_0 , of high homogeneity. \vec{H}_0 magnetizes the sample along the direction of the field, inducing a magnetic moment in the \hat{x} direction (Fig. 4.22b). The magnetic centre of the

sample coincides with the symmetric centre of the 4 pick up coils mounted at the electromagnet.

According to Faraday's law, an electromagnetic force is generated in a coil when there is a change in the magnetic flux through the coil. For a number n_c of pick-up coils with n_w winding turns, the voltage induced in the coils is:

$$U = \sum_{n_c} \sum_{n_w} \int_S \frac{\partial \vec{B}(\vec{r})}{\partial t} \cdot d\vec{S} \quad (4.37)$$

The magnetic moment of the sample, induced by \vec{H}_0 , generates a magnetic field $\vec{B}(\vec{r})$ according to eq. (2.9). Therefore, when the sample moves along \hat{z} , the magnetic field that passes through the pick up coils changes. This results in a change of flux and induces an AC voltage in the pick up coils. The amplitude of this AC voltage is proportional to $M = M_x$, that is, to the component of the magnetization along \vec{H}_0 .

Fig. 4.22c shows a typical ferromagnetic *hysteresis loop* measured in this thesis. If the sample is magnetized to the saturation magnetization M_s by an applied field, then when the applied field is reduced to 0, the magnetization reduces to the remanent magnetization, M_r . A magnetic field equal to the coercive field, H_c , is needed to switch the magnetization into the opposite direction. M_r and H_c are used to characterize the response of the ferromagnet to the external field.

Chapter 5

Growth and characterization of CFS films on Si(111)

5.1 Introduction

Following the construction of the MBE (Chapter 3), all the components in the system were tested and calibrated, including all four evaporators and the substrate heater. After the sample position was optimized, Fe, Co and Si films were grown using different source temperatures to calculate the growth rates for each element. Once the growth rates were known, $\text{Co}_x\text{Fe}_{1-x}$ alloys were deposited to find the optimum Co and Fe rates to achieve a 2:1 Co to Fe ratio, and finally moved on to the synthesis of high quality Co_2FeSi alloys. Although its half-metallicity is not as robust compared to CFAS, CFS is still in the spotlight due to its incredibly high T_c (Tab. 2.2), and it has been successfully used to inject pure spin currents into Cu [Oki17] and to achieve large electrical spin-injection efficiencies into GaAs [Ram08].

For the first set of CFS films, the substrate of choice was Si(111) due to its good lattice match with CFS and its wide availability. The growth of CFS films on Si(111) also allowed to compare the characteristics of the grown-in-the-house films with the high quality epitaxial $\text{Co}_2\text{FeAl}_{1-x}\text{Si}_x/\text{Si}(111)$ samples grown by the more experienced Dr. Kohei Hamaya's group at Osaka University [Kue16; Ned16a]. The first challenge was to control the film stoichiometry. Despite the predicted ideal properties of half-metallic Co-based Heusler alloys, the preservation of these properties requires the exact chemical composition, structural ordering and the absence of defects (refer to § 2.7.2). Indeed, chemical disorder can drastically change the spin polarisation in Heusler films [HSL13; MNS04], rendering them inefficient for device applications. It has also been observed that the existence of disordered phases can worsen the magnetic properties of the alloys, such as an increase of the Gilbert damping parameter [Cui14; Kue18].

In order to improve the spin-electronic properties, annealing at elevated temperatures of 500°C – 700°C [TNS09; Kue18], is the common method to obtain the desired L2₁-ordered Heusler films. However, this occurs in detriment of a sharp interface which in turn has a negative effect on the spin polarization at the interface, as well as on the magnetization of the films [Kue18; Has07]. For growth on Si substrates, extensive intermixing occurs even at low temperatures [Yam10; Kue16]. Hence, it is of utmost importance to optimize the growth conditions at low temperatures to minimize the formation of defects and secondary phases while achieving the best possible magnetic and structural properties. In this chapter, the focus will be on the growth and optimization of CFS thin films grown on Si(111) at < 130°C, and it will be shown that good quality Heusler films can be grown using the newly developed MBE technique. The CFS films will be characterized using XRD (§ 5.3.1), TEM and STEM-HAADF (§ 5.3.2), VSM (§ 5.4.1) and FMR (§ 5.4.2) and the effects of stoichiometry and chemical ordering on their structural and magnetic properties will be investigated.

5.2 MBE growth of CFS films

In order to grow Co₂FeSi films, the Co, Fe and Si evaporators were calibrated by growth of Co, Fe and Si films at different evaporation temperatures. The thickness of each film was measured by XRR and the growth rates were subsequently calculated. The Co and Fe films were grown on standard p-type Si(111) substrates; whereas the Si films were grown on Ge(111) as a substrate with a different density to that of the film was needed to produce the Kiessig fringes (refer to § 4.1.2). The XRR measurements for these films are shown in Fig. 5.1a. The red curves correspond to the fitted curves extracted using the software package GenX. From the fitted curves the thickness of the films was obtained, which together with the deposition times were used to calculate the growth rate for each evaporation temperature. The rates as a function of the source temperature are shown in Fig. 5.1b for Co (blue squares), Fe (red triangles) and Si (black dots). Over the range of temperatures considered, the evaporation rate is mostly linear with temperature. The linear fits are also shown in the figure.

These initial single-element films were also used to calibrate the QCM (§ 3.6.1) by calculating the tooling factor, $Q^{\text{Fe,Co,Si}}$, for each element. $Q^{\text{Fe,Co,Si}}$ is a geometric factor that accounts for the distance between the QCM and the Fe, Co and Si evaporators respectively. If this distance is reduced, the atoms will reach the QCM more rapidly, increasing the rates measured by the QCM. Because the tooling factor depends on the evaporator-QCM distance, the calibration is performed with the QCM positioned as close to the sample position as possible. The ideal sample position is the point in the chamber where the fluxes coming from the three evaporators

intersect. Here, the rates are maximized and the films are most uniform. For each element, $Q^{\text{Fe,Co,Si}}$ is calculated iteratively after each growth until the error between subsequent iterations is $< 10\%$:

$$Q_n^{\text{Fe,Co,Si}} = Q_{n-1}^{\text{Fe,Co,Si}} \times t_{\text{XRR}}^{\text{Fe,Co,Si}} / t_{\text{QCM}}^{\text{Fe,Co,Si}} \quad (5.1)$$

Here, $Q_{n-1}^{\text{Fe,Co,Si}}$ is the tooling factor measured for the previous film, $t_{\text{XRR}}^{\text{Fe,Co,Si}}$ is the film thickness measured by XRR, and $t_{\text{QCM}}^{\text{Fe,Co,Si}}$ is the film thickness measured by the QCM. $t_{\text{QCM}}^{\text{Fe,Co,Si}}$ is calculated through eq. (3.10).

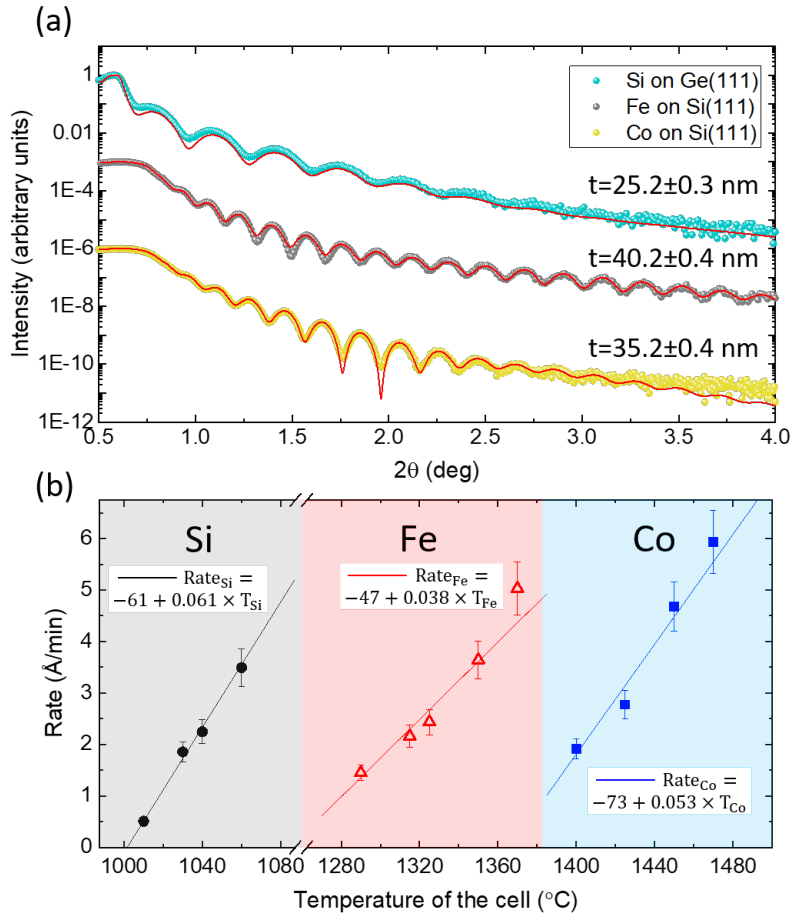


Figure 5.1: (a) X-ray reflectivity curves for a Si, Fe and Co films; and (b) rates as a function of the source temperature for the Si, Fe and Co evaporators.

As described in § 2.7.2 achieving the right chemistry in the growth of Co_2FeSi is fundamental to obtain the desired L2_1 ordered phase of the alloy. As a first approach, a series of 30-40 nm-thick $\text{Co}_x\text{Fe}_{1-x}$ binary alloys was grown, estimating x from the Fe and Co growth rates in Fig. 5.1b.

The composition of the films was studied by measuring the saturation magnetization of the samples in the VSM (§ 4.3.2), as M_s depends on the composition of the alloy. By plotting M_s against x , the trend observed is known as the Slater-Pauling curve where the magnetization reaches a maximum when $x = 0.25$ and subsequently decreases as the concentration of Co increases. The theoretical Slater-Pauling curve for bulk $\text{Co}_x\text{Fe}_{1-x}$ is the dashed line in Fig. 5.2b and the experimental M_s values are the blue squares. The experimental values differ significantly from the theoretical curve, although this could be related to the crystallinity of the films which was not investigated. The M_s measured for pure Fe ($x = 0$), $M_s = 1580 \pm 100$ emu/cc, and for pure Co ($x = 1$), 1365 ± 100 emu/cc, are close to their bulk values at RT, $M_s = 1700$ emu/cc and $M_s = 1400$ emu/cc respectively. However, the chemistry of the alloys between $x = 0.25$ and $x = 0.7$ is impossible to assess because in this range M_s is constant within error. Hence, a chemical analysis had to be performed by SEM-EDS (§ 4.2.4). The values acquired by EDS are shown in Tab. 5.1 and agree with the nominal values in the first column within a $< 10\%$ error.

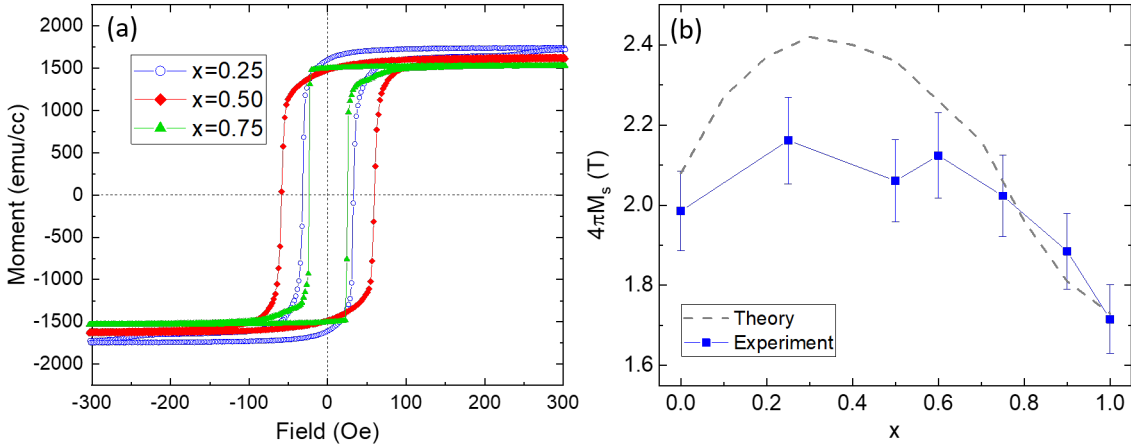


Figure 5.2: (a) Ferromagnetic hysteresis loops for the MBE-grown $\text{Co}_x\text{Fe}_{1-x}$ films measured by VSM. (b) M_s values extracted as a function of the concentration of Co, x ; the dashed grey line is the Slater-Pauling curve for bulk $\text{Co}_x\text{Fe}_{1-x}$ alloys shown as a reference from [Boz93].

According to Tab. 5.1, a Co:Fe 2:1 ratio corresponds to a Co and Fe growth rate of ≈ 5.6 Å/min and 3.8 Å/min respectively. By fixing the sources to these rates, it was similarly proceeded to the growth of ternary Co_2FeSi films with varying concentrations of Si (i.e. varying the temperature of the Si source, T_{Si}). The thickness of the films was kept constant. For these series, a commercial Si(111) substrate was chosen due to the small lattice mismatch of 4% between the Co_2FeSi lattice ($a_{\text{CFS}} = 5.65$ Å) and Si ($a_{\text{Si}} = 5.43$ Å). The Si(111) substrates were

cleaned using the following procedure:

- 5 min in acetone (ACE) in sonic bath
- 5 min in ethanol in sonic bath
- 2 min in $\text{NH}_3:\text{H}_2\text{O}_2:\text{DI}$ (1:5:8) in sonic bath at 65°C
- 5 min in deionized (DI) water in sonic bath
- 6 min in 1% hydrofluoric acid (HF)
- rinse in DI water

The piranha solution, $\text{NH}_3:\text{H}_2\text{O}_2:\text{DI}$ (1:5:8), removes the organic impurities and the HF removes the native oxide from the substrates. When the substrate was loaded into the MBE chamber, the Si(111) surface was additionally outgassed at $\approx 500^\circ\text{C}$ in UHV to avoid any contamination during growth. The base pressure of the chamber was in the 10^{-11} mbar range. The pressure during growth was $< 3 \times 10^{-8}$ mbar and all the samples were grown using rates of $\approx 5\text{-}6 \text{ \AA}/\text{min}$. Although no current was passed through the heater, the temperature of the substrate was $\approx 70^\circ\text{C}$ in the beginning of the growth and steadily increased to $\approx 130^\circ\text{C}$ at the end of the growth due to the heat generated by the evaporators.

Nominal composition	at% of Co	at% of Fe	Co rate ($\text{\AA}/\text{min}$)	Fe rate ($\text{\AA}/\text{min}$)	Growth rate ($\text{\AA}/\text{min}$)
$\text{Co}_{25}\text{Fe}_{75}$	25.5 ± 0.2	74.5 ± 0.2	1.9 ± 0.1	5.2 ± 0.3	9.3 ± 0.6
$\text{Co}_{50}\text{Fe}_{50}$	53.7 ± 0.8	47 ± 1	5.2 ± 0.3	4.7 ± 0.3	13 ± 0.9
$\text{Co}_{66.6}\text{Fe}_{33.3}$	67.5 ± 0.5	32.5 ± 0.6	5.6 ± 0.4	3.8 ± 0.3	11.4 ± 0.8
$\text{Co}_{75}\text{Fe}_{25}$	72.9 ± 0.6	27.1 ± 0.6	5.1 ± 0.3	2.3 ± 0.2	8.0 ± 0.6

Table 5.1: Co and Fe concentrations in at% measured by EDS in the $\text{Co}_x\text{Fe}_{1-x}$ alloy films, and the rates used for their growth.

5.3 Structural properties of CFS films grown on Si(111)

Fig. 5.3a shows the RHEED pattern of a clean Si(111) surface taken before the growth of the CFS film. The incident electrons are parallel to the $[11\bar{2}]$ direction of the Si surface. After the cleaning procedure detailed above, the Si(111) shows the characteristic reciprocal lattice rods of an oxide-free surface. Fig. 5.3b shows the RHEED pattern after the growth of the CFS film. As described in § 3.6.2, the appearance of symmetrical streaks are indicative of single crystal growth and a flat surface (refer to Fig. 3.22) and so, suggests epitaxial growth. Similar patterns are observed in all the samples. It should be noted that due to the twinning between

the film and the substrate (see Fig. 5.5b in § 5.3.1), the sample stage was rotated in order to take the second pattern due to the sample holder obstructing the diffraction in this geometry.

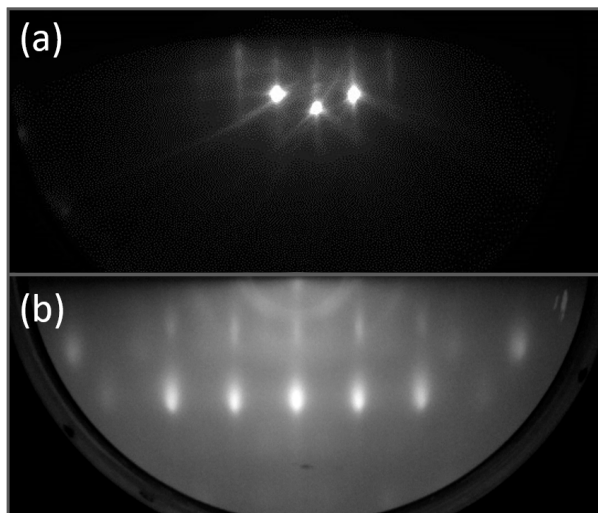


Figure 5.3: RHEED patterns of (a) the Si(111) surface and (b) the CFS(111) surface taken along the $[11\bar{2}]$ azimuth; suggesting epitaxial growth of CFS on Si(111).

5.3.1 X-ray diffraction and reflectivity measurements

The main XRD technique used to characterize the CFS films was symmetric $2\theta - \omega$ scans in parallel-beam (PB) geometry. As explained in section § 4.1.1, the different phases of the CFS alloy (§ 2.7.1) lead to different structure factors and hence, certain reflections that are present in the fully-ordered $L2_1$ phase are not observed in the B2 phase or A2 phase [Wij91]. Specifically, in the $L2_1$ ordered structure, the (200) and (111) superlattice reflections are expected, whereas only the CFS(200) family of diffraction peaks is observable in the B2 phase. Because the atoms are completely disordered across the lattice in the A2 structure, non of these reflections occur in the latter. The list of allowed reflections for each phase is summarized in Table 5.2.

Ordered structure	Allowed reflections	Examples
$L2_1$, fully-ordered	h,k,l are all odd numbers $h+k+l=4n+2$	111, 311 200,222
B2	$h+k+l=4n+2$	200,222
A2, fully disordered	$h+k+l=4n$ with h,k,l even	220, 400, 444

Table 5.2: List of allowed reflections for each possible structural phase of CFS.

As for the substrate, Si(200) is a basis-forbidden reflection and hence, is not present in any

of the measurements shown here.

Although x-ray diffraction is a handy technique to identify and quantify the structural phases in CFS films, one should be aware that XRD analysis with an ordinary Cu K_α source (as the one used in this work) has a big limitation, it cannot distinguish between the fully-ordered $L2_1$ structure and the DO_3 -type of disorder involving an exchange between Fe and Co atoms. This happens because the atomic scattering factor of Fe is almost the same as that of Co for the Cu K_α source and consequently, both structures give rise to the same superlattice reflections. This is similarly an issue in the performed STEM experiments (§ 5.3.2) where Z-contrast imaging cannot tell the Fe ($Z = 26$) and Co ($Z = 27$) atomic columns apart due to their very similar atomic numbers. Generally, detection of the DO_3 or *hidden* disorder requires special measurement set-ups such as neutron diffraction [ZW74a], synchrotron XRD [Rav02; Bas09] and nuclear magnetic resonance [Ino08]. However, as explained in § 2.7.2 the most common type of disorder in CFS films is B2. This and the fact that the films showing stronger (111) diffraction peaks in this analysis are the ones displaying improved magnetic properties, justifies the attribution of the observed (111) superlattice reflection to $L2_1$.

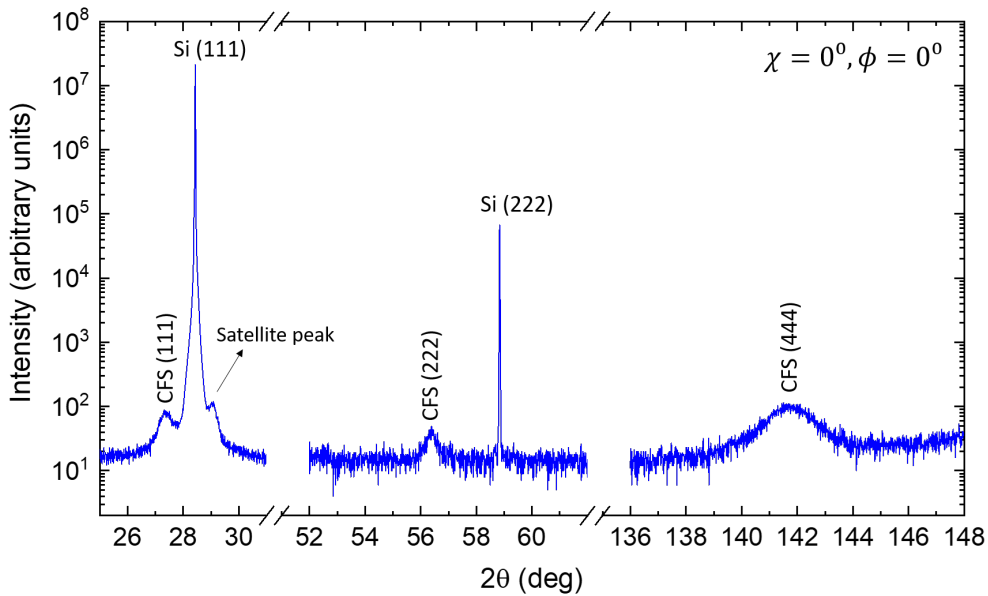


Figure 5.4: Out of plane $2\theta - \omega$ scan for the $T_{Si} = 1040^\circ\text{C}$ sample with $\chi = 0^\circ$; which reveals the CFS(hhh) reflections with $h = 1, 2$ and 4.

Figure 5.4 shows a typical symmetric $2\theta - \omega$ scan of one of our Co_2FeSi films ($T_{Si} = 1040^\circ\text{C}$) aligned to Si(111), i.e. with the goniometer at $\chi = 0^\circ$ and $\phi = 0^\circ$. Three characteristic reflections are found at $2\theta \approx 142$, $2\theta \approx 56.5$ and $2\theta \approx 27.5$ degrees, which correspond to CFS(444), CFS(222) and CFS(111) respectively. This indicates the out-of-plane (111) textured

growth of the CFS layers. According to Tab. 5.2, CFS(444) is a fundamental reflection always present independent of the ordered structure; whereas CFS(222) only appears if there is some structural ordering (either the B2 or the L2₁ phase) and the CFS(111) is exclusive to the L2₁ phase. Hence, it can be said that this film is at least partially L2₁-ordered. The fits to these peaks and the corresponding analysis, will be shown later in this section (Figs. 5.9 and 5.10) for all the CFS/Si(111) samples. In any case, at this stage it is worth mentioning that although the CFS(444) peak appears significantly wider than the other two reflections, this simply originates from the non-linearity of the sine function in Bragg's law. Ideally, one should work in reciprocal space units and show the data as a function of the modulus of the momentum transfer vector instead of 2θ to avoid this artefact. Usually for small angular ranges, this is not noticeable but because in this case the structural peak is at a very high angle ($> 140^\circ$), the effect becomes apparent.

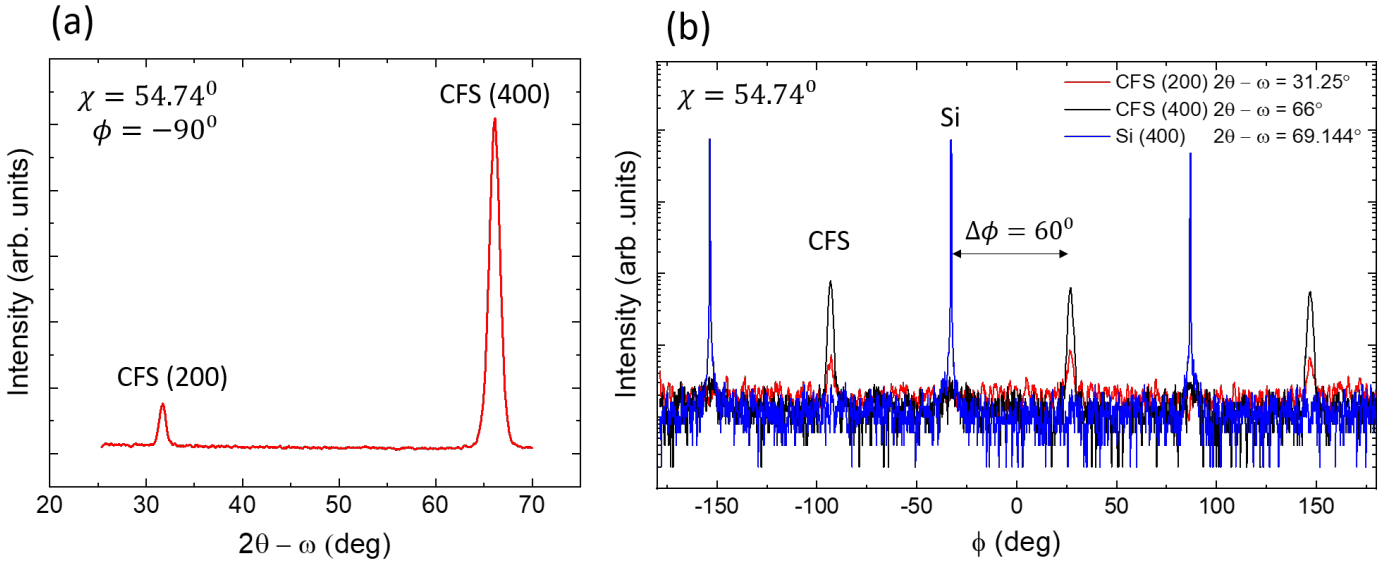


Figure 5.5: (a) $2\theta - \omega$ scan for $T_{Si} = 1040^\circ\text{C}$ aligned to the CFS(200) peak, with the goniometer at $\chi = 54.74^\circ$ and $\phi = 90^\circ$; (b) ϕ scan aligned to CFS(200) (in red), CFS(400) (in black) and Si(400) (in blue) showing the twinning of the film.

By tilting the stage to $\chi = 54.74^\circ$ and $\phi = 90^\circ$, one can align the sample to the Si(400) reflection, and a $2\theta - \omega$ scan then reveals the CFS(200) and the CFS(400) peaks (Fig. 5.5a). The fact that the Si(400) is not observed shows that there is some in-plane rotation of the film respect to the substrate. By performing a ϕ scan (Fig. 5.5b), the three CFS $\langle 200 \rangle$ diffraction peaks and the also three-fold symmetric Si $\langle 400 \rangle$ reflections spaced 120 degrees apart are measured. This confirms the epitaxial growth of CFS on the Si substrate. It is also observed that the CFS peak is separated from the substrate peak by 60 degrees which gives the following epitaxial

relationship between the film and the substrate: $\text{CFS}(\bar{1}\bar{1}0)||\text{Si}(\bar{1}10)$ and $\text{CFS}(111)||\text{Si}(111)$. This agrees with previous findings on CFAS/Si(111) films [Ned16b]. Given that the CFS(111) is difficult to observe due to its proximity to the substrate peak, an additional scan was also performed aligning the sample to another accessible reflection of the $\langle 111 \rangle$ family, specifically to the CFS($\bar{1}\bar{1}1$) peak at $\chi = 70.53^\circ$ and $\phi = 90^\circ$, shown in Fig. 5.6. Due to the twinning effect, this removes the substrate peak and isolates the CFS($\bar{1}\bar{1}1$), showing without any doubt the presence of the fully-ordered phase in the film.

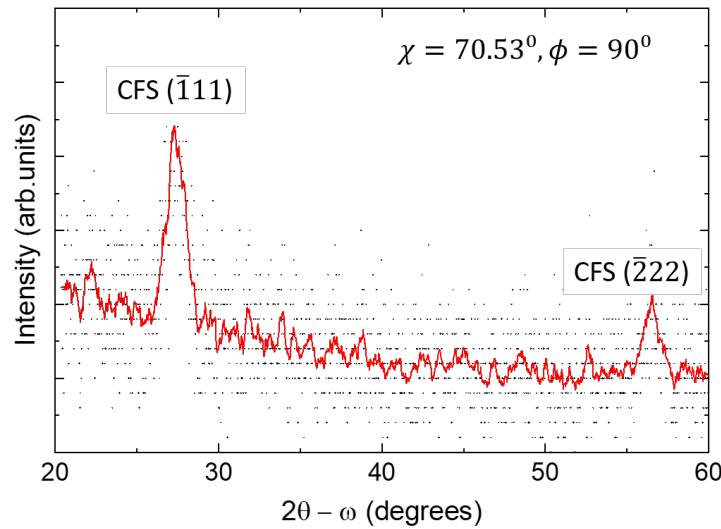


Figure 5.6: $2\theta - \omega$ scan aligned to CFS($\bar{1}\bar{1}1$) for $T_{\text{Si}} = 1040^\circ\text{C}$.

Any changes in the chemistry of the film will change the structural ordering of the alloy, which in turn will be reflected in the diffraction pattern. Thus, similar XRD measurements were performed for all the $\text{Co}_2\text{FeSi}/\text{Si}(111)$ films with varying Si concentrations (T_{Si}) to study the ordering as a function of chemistry. All the films have a thickness of 26–29 nm as confirmed by the reflectivity curves shown in Fig. 5.7a. The curves were fitted using GenX and the model used to fit the data is the three layer structure depicted in Fig. 5.7d. An oxide layer (CoFe_2O_4) was included to account for the oxidation of the uncapped metallic layer, as well as a silicide phase at the CFS/Si interface. The presence of a very thin silicide layer was already observed in similar films [Ned16a] but more importantly, a layer with the same crystal structure of CFS is being introduced (starting from Fig. 2.12, one just needs to remove one of the two Co-sublattices and replace the Fe sublattice by Si to form CoSi_2) but with a lower density. Hence, this will also effectively describe any out-diffusion of Si from the substrate. The density of the oxide layer and the substrate were constant and the density of the CFS layer was allowed to vary around its bulk value, $\rho_{\text{CFS}} = 0.0222 \text{ f.u./\AA}^3$. The figure of merit (FOM) from the fits is

shown in the inset of Fig. 5.7a, which is a numerical value assigned to the quality of the fit. The further away the fit is from the data, the higher this number. All the fits show a FOM below 0.1, between 6×10^{-2} and 9×10^{-2} indicating good fits to the proposed model.

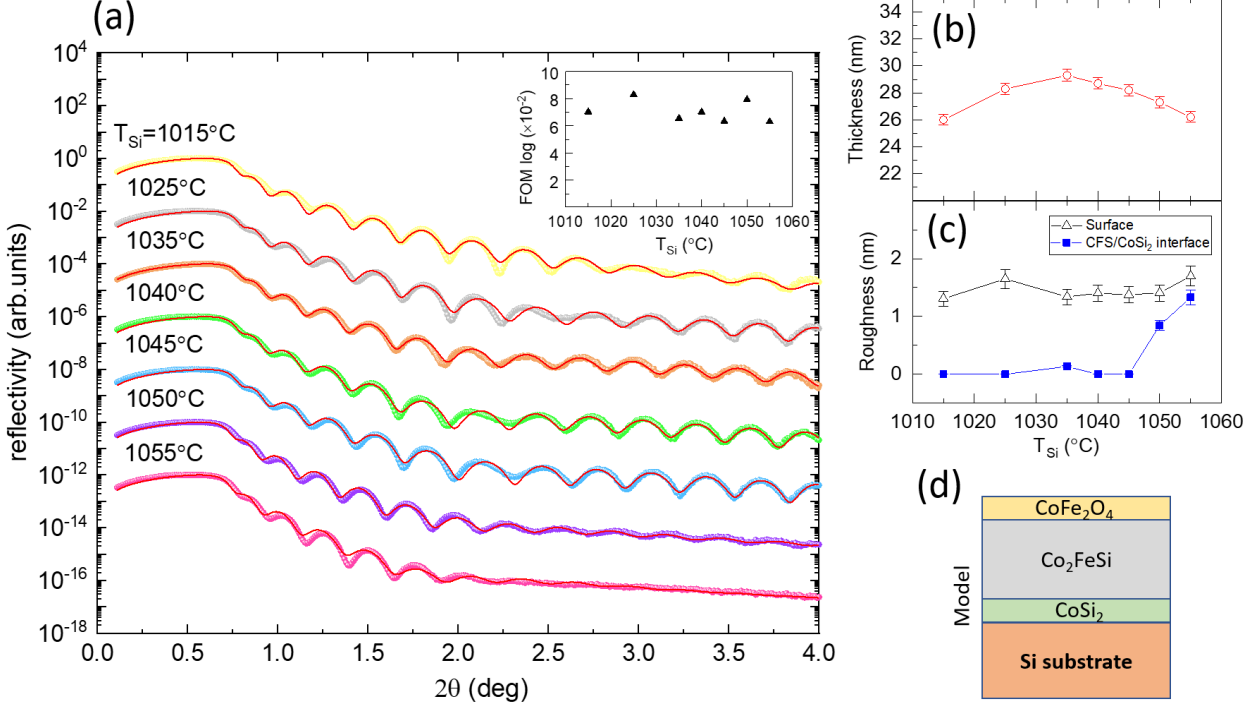


Figure 5.7: (a) x-ray reflectivity measurements (coloured dots) and fits (red lines) for the CFS/Si(111) samples with varying T_{Si} ; (b) thickness of the CFS layers extracted from the fits; (c) surface (black triangles) and interface (blue squares) roughness; and (d) the three-layer model used to fit the data. The density of CoFe_2O_4 and the substrate were set to $\rho_{\text{CoFe}_2\text{O}_4} = 0.0137 \text{ f.u./\AA}^3$ and $\rho_{\text{Si}} = 0.050 \text{ f.u./\AA}^3$ respectively.

The thickness of the CFS layers extracted from the fitted curves are shown in Fig. 5.7b. The thickness of the films fluctuates from $26.0 \pm 0.3 \text{ nm}$ to $29.3 \pm 0.3 \text{ nm}$, i.e. 4.0% to 17.0%-off the nominal value of 25 nm. This fluctuation in thickness is attributed to the accuracy of the QCM. In fact, apart from the error intrinsic to the measurement of the frequency of the crystal, the calculation of the thickness (eq. (3.10)) depends on the foreknown Z-factor and density of the deposited material. However, in these films the chemistry varies and hence, there are changes to the density that were not taken into account and resulted in a larger error in the thickness of the layers. On the other hand, the roughness of the CFS/CoSi₂ interface and the surface roughness, which comes from the top CoFe₂O₄ layer, have been plotted in Fig. 5.7c. As can be seen, the roughness of the bottom interface for low Si concentrations is small ($< 1.5 \text{ \AA}$) and

increases rapidly when $T_{Si} > 1045^\circ\text{C}$, reaching a roughness of 1.3 ± 0.2 nm for the CFS with the highest Si content. This is evidenced by how the Kiessig fringes die out at much lower angles at these source temperatures. The surface roughness is constant within error (1.3 ± 0.2 nm for $T_{Si} = 1015^\circ\text{C}$ and 1.7 ± 0.2 nm for $T_{Si} = 1055^\circ\text{C}$) for all the samples.

Figure 5.8 shows the values for the densities of the CFS layer in Fig. 5.7c extracted from GenX in formula units (f.u.) per volume. Although the variations are small, the trend is consistent and shows that the density of the film decreases with the increase of Si in the layer. This is logical as the heavier Fe and Co atoms are being substituted for the lighter Si. The blue squares correspond to a first set of fits where the density of the CoSi_2 layer was fixed, and the red circles were extracted from a second set of fits where the density of CoSi_2 was allowed to vary. The thickness of the CoSi_2 layer retrieved from the fits is below 3 nm in all the samples, although it does not follow any clear trend. Thus, no conclusions could be extracted about the presence of this phase or about the amount of Si outdiffusion as a function of T_{Si} .

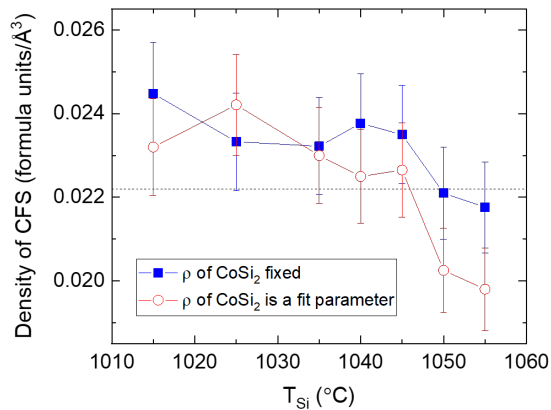


Figure 5.8: Densities of the CFS layer extracted from the fits with: (blue squares) the density of the CoSi_2 layer fixed, and (red circles) the density of the CoSi_2 layer as a fit parameter. The dashed line corresponds to the density of bulk CFS, $\rho_{\text{CFS}} = 0.0222$ f.u./ \AA^3 .

Fig. 5.9a shows the out of plane $2\theta - \omega$ scans for this series of samples close to the fundamental CFS(444) peak. The data was fitted to a Voigt distribution (the red lines in the figure) with parameters $2\theta_0$ and A_{hkl} , which represent the centre of the peak and the area below the peak, also known as the integrated intensity, respectively (refer to Fig. 4.5). From $2\theta_0$, the out of plane lattice constant $c = d_{444}$ was extracted using equation (4.3). Plotted against T_{Si} , c follows the trend shown in Figure 5.9b. As the Si content increases, the lattice shrinks, because the ionic radius of the Si is smaller than that of Fe and Co. Taking into account the lattice constant of Si, the structure with the lowest c is hence, the one with the biggest mismatch

with respect to the substrate. The value in literature for the lattice constant of bulk CFS, $a = 5.65\text{\AA}$, would fall in the range of $1025^\circ\text{C} < T_{\text{Si}} < 1045^\circ\text{C}$.

Finally, Fig. 5.9c shows the full width at half maximum (FWHM) of the diffraction peak. From $T_{\text{Si}} = 1015^\circ\text{C}$ to $T_{\text{Si}} = 1035^\circ\text{C}$, FWHM does not suffer big variations; at $T_{\text{Si}} > 1035^\circ\text{C}$ it starts increasing, and at $T_{\text{Si}} > 1045^\circ\text{C}$ it jumps until at $T_{\text{Si}} = 1055^\circ\text{C}$ the FWHM has increased by a $\approx 50\%$ respect to its initial value. The trend is the exact opposite to that of the lattice constant shown on top. Hence, one would think that the increase in FWHM is not due to an intrinsic property of the film, but simply a consequence of the peak moving to higher angles. As mentioned earlier, when discussing the big difference in widths between the CFS(444) and the CFS(222) and CFS(111) peaks, the width (if measured in degrees) is bigger as the sine function fans out with θ . Hence, the shifts of the peak due to the change of the lattice constant also result in the increase of the FWHM which at high angles dominates over any other intrinsic effect.

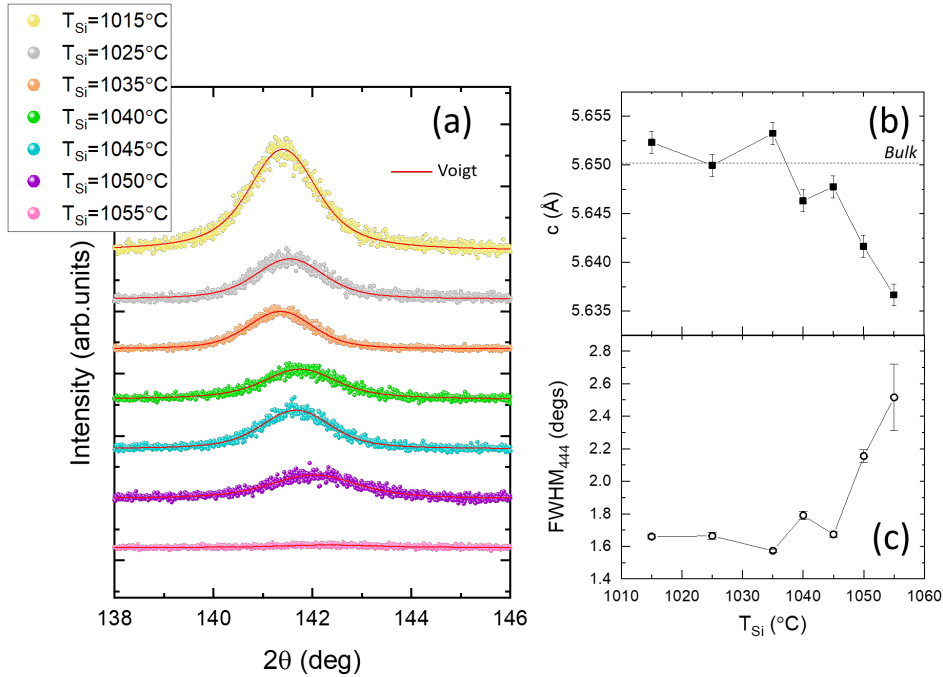


Figure 5.9: (a) $2\theta - \omega$ scans (coloured dots) and fits (red lines) around the CFS(444) reflection for the CFS/Si(111) samples with varying T_{Si} ; (b) the out of plane lattice constant calculated from the fits using Bragg's law; and (c) the FWHM of the CFS(444) peak.

In order to compare between samples, the degree of B2 and $L2_1$ ordering in the films has to be quantified. For Heusler alloys, the parameters of chemical ordering degree S_{B2} and S_{L21} can be evaluated by the relative peak intensities according to the extended Webster model [TNS09;

ZW74b] through the following equations [Kud19]:

$$S_{B2} = \sqrt{\frac{A_{002}/A_{004}}{A_{002}^R/A_{004}^R}} \quad (5.2)$$

$$S_{L21} = \frac{2}{3 - S_{B2}} \sqrt{\frac{A_{111}/A_{202}}{A_{111}^R/A_{202}^R}} \quad (5.3)$$

Here, A_{hkl} is the integrated intensity of the CFS hkl plane and A_{hkl}^R is the theoretically calculated intensity for the B2 ordered structure in (5.2) and for the L2₁ structure in (5.3). As can be seen from these equations, the intensity ratios A_{002}/A_{004} and A_{111}/A_{202} represent a measure of degree of B2 and L2₁ phase respectively. Although due to the scan geometry in Fig. 5.4, the (002) and (202) cannot be measured, one can still estimate the degree of B2/L2₁ order by studying the (222) and (111) superlattice reflections respect to the (444) structural peak. That is, by studying the A_{222}/A_{444} and A_{111}/A_{444} ratios one can compare the degree of B2 and L2₁ ordering between the films with different T_{Si} .

Figures 5.10a and 5.10b show the fits of the CFS(222) and CFS(111) peaks respectively. Note that even though the curves and fits have been represented one on top of the other for clarity, the intensities were calculated with a common zero-baseline for all the films. In Fig. 5.10c the integrated intensities extracted from the fits are plotted as a function of T_{Si} . Finally, in Fig. 5.10d the ratios of the integrated intensities for the CFS(222) in blue and the CFS(111) in red have been plotted. The integrated intensities of the fundamental peak are displayed in the inset. It should be noted that the big error bars for A_{111} at $T_{Si} = 1050^\circ\text{C}$ arise because the CFS(111) diffraction peak is too small to be fitted to a Voigt function (purple dots in Fig. 5.10a). At $T_{Si} = 1055^\circ\text{C}$ the peak is no longer observed, which in the graph corresponds to $A_{111} = 0$ with no error bars.

As can be seen from Fig. 5.10d, A_{111}/A_{444} increases with T_{Si} and reaches its maximum at $T_{Si} = 1045^\circ\text{C}$; after which it decreases until at $T_{Si} = 1050^\circ\text{C}$, the L2₁ diffraction peak can barely be observed. On the contrary, the A_{222}/A_{444} ratio monotonically rises with the Si content. The biggest increase occurs between $T_{Si} = 1050^\circ\text{C}$ and $T_{Si} = 1055^\circ\text{C}$. However, turning to Fig. 5.10c, one notices that the absolute intensity of the B2 reflection A_{222} actually goes down at temperatures above $T_{Si} = 1045^\circ\text{C}$, and so does A_{111} . This happens because for $T_{Si} > 1050^\circ\text{C}$, the intensity of the fundamental reflection (in the inset of Fig. 5.10d) goes to 0, and hence, the A_{222}/A_{444} ratio increases. This means that even though at $T_{Si} > 1050^\circ\text{C}$ the degree of B2 ordering measured is the highest, the small values for A_{444} imply that for these films the amount of Si is too high and the CFS structure is lost. Hence, the data indicates that

the optimal Si content is achieved for $T_{Si} \approx 1045^\circ\text{C}$, where the degree of $L2_1$ ordering reaches its maximum. This agrees with the temperature range where the lattice constant measured previously (Fig. 5.9b) meets the value in literature.

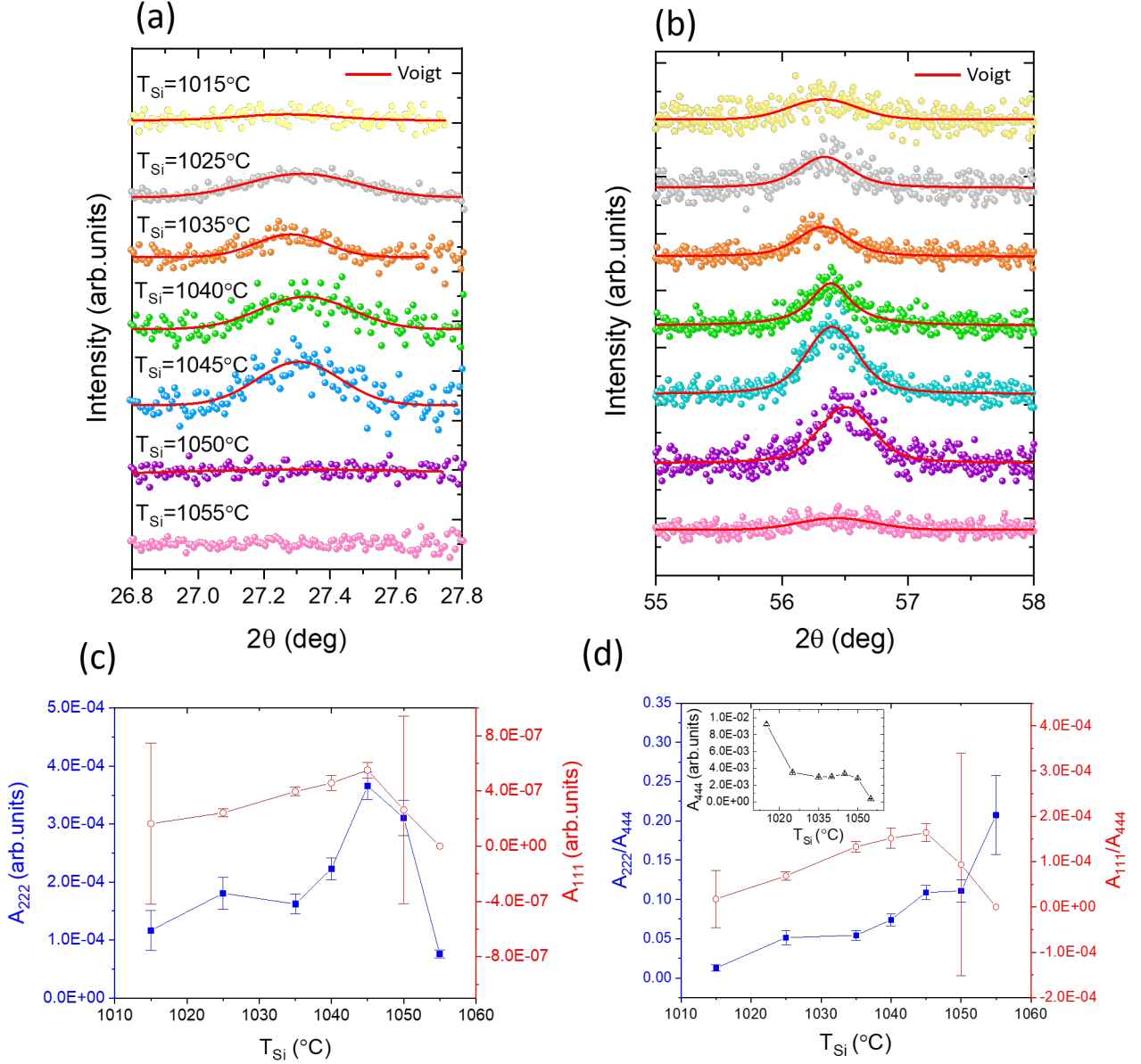


Figure 5.10: $2\theta - \omega$ scans (coloured dots) and fits to a Voigt function (red lines) of (a) the CFS (111) reflection and (b) the CFS (222) reflection; (c) the integrated intensities extracted from the fits in a and b; (d) ratios of the integrated intensities representative of the B2 ordering in blue, and the $L2_1$ ordering in red. The inset shows the integrated intensities of the structural peak from the fits in Fig. 5.9a.

The FWHM of the superlattice reflections was also analysed and it is shown in Fig. 5.11a. The trend shown by the CFS(222) peak is clearly far from the one observed for the CFS(444)

in Fig. 5.9c. Because the superlattice reflections occur at lower angles the effect of the sine function does no longer mask true changes in broadening related to sample imperfection. The Voigt distribution is a convolution of a Gaussian distribution and a Lorentzian distribution; hence the FWHM of the Voigt profile ($\text{FWHM} = 0.5346\Delta_L + \sqrt{0.2166\Delta_L^2 + \Delta_G^2}$) is a function of the Gaussian width, Δ_G , and the Lorentzian width, Δ_L which are fitting parameters that are retrieved from the fits.

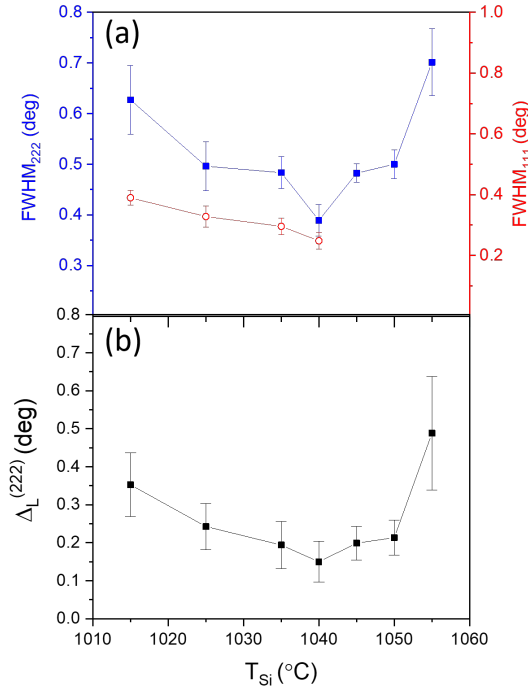


Figure 5.11: (a) FWHM of the CFS(222) (blue squares) and CFS(111) (red circles) diffraction peaks and (b) Lorentzian linewidth of CFS(222).

Although it can be difficult to separate the instrumental broadening from the broadening related to imperfections in the sample, the narrowest peaks agree with the source temperatures ($T_{Si} = 1040^\circ\text{C} - 1045^\circ\text{C}$) where the integrated intensities are the highest (compare with Fig. 5.10c), hence they more likely point to an improvement of crystallinity rather than to instrumental factors. Moreover, all the samples in this series were measured using the exact same optics and slits after a careful sample alignment. Hence, there is no reason to think that the instrumental broadening will change from sample to sample. A second fit was also performed for CFS(222) for each sample keeping the Gaussian linewidth constant ($\Delta_G = 0.36^\circ$), as this is more frequently related to instrumental broadening. Similar values for R^2 were obtained for these new fits. In Fig. 5.11b, Δ_L has been plotted and shows a similar behaviour, albeit less pronounced, to FWHM. The FWHM of the CFS(111) follows a decreasing trend up to

$T_{Si} = 1040^{\circ}\text{C}$, but due to the difficulty of extracting the FWHM of the $T_{Si} > 1040^{\circ}\text{C}$ samples within reasonable error, it is impossible to say what the trend is at the highest source temperatures.

5.3.2 Cross-sectional TEM and STEM measurements

Although XRD is a good indicator of the structural phases existing in the CFS films, it can only give averaged information over the mm length scale. In order to get a further insight on how these phases are distributed throughout the film, one needs to work with much smaller beam sizes, such as those of electron microscopes. Initial specimen checks were carried out in an aberration-corrected JEOL 2200 FS microscope at the JEOL Nanocentre in York. Atomic level imaging was performed on a Nion UltraSTEM 100 microscope operated at 100kV at the SuperSTEM facility by the hands of Dr. Kepaptsoglou. All the specimens were prepared in the house with the FEI Nova 200 NanoLab dual system (§ 4.2.5.2) along the $[1\bar{1}0]$ direction of CFS. The last thinning steps were performed by Argon ion milling in a PIPS II polisher. Specimens were prepared for $T_{Si} = 1025^{\circ}\text{C}$, $T_{Si} = 1035^{\circ}\text{C}$, $T_{Si} = 1040^{\circ}\text{C}$ and $T_{Si} = 1045^{\circ}\text{C}$, and the results will be shown in this section.

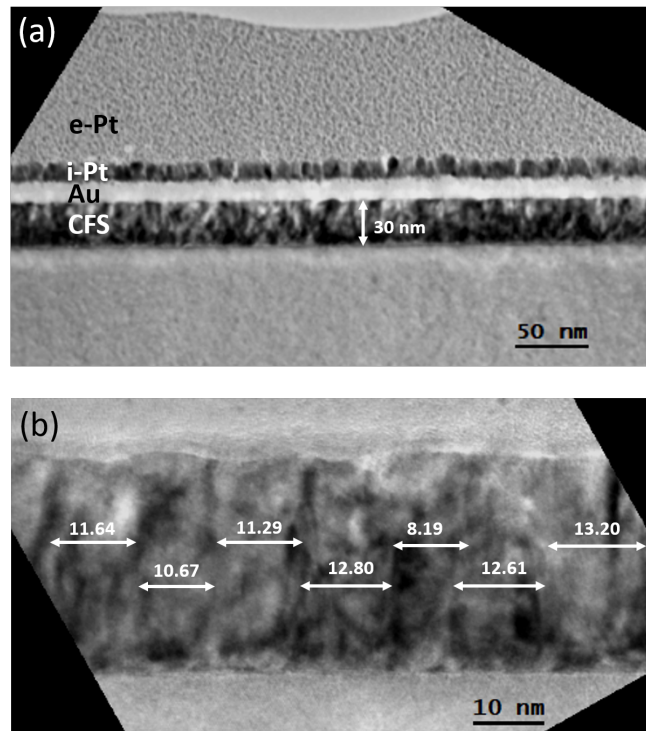


Figure 5.12: Micrographs showing the cross-section of $T_{Si} = 1035^{\circ}\text{C}$ prepared along $[1\bar{1}0]$. (a) is an overview of the lamella showing its different layers and (b) reveals the granular nature of the CFS.

Fig. 5.12a shows a low magnification BF image of the $T_{Si} = 1035^\circ\text{C}$ specimen. One can clearly identify the ≈ 30 nm-thick Co_2FeSi film capped with a 10 nm conducting Au layer sputtered prior to cross-sectional specimen preparation. The two topmost layers are the protective Pt layers deposited locally with the FIB using the electron beam (e-Pt) and the ion beam (i-Pt). The film shows an overall roughness of ≈ 1 nm, in agreement with the surface roughness measured by XRR (Fig. 5.7c). Fig. 5.12b is a higher magnification TEM image of the CFS layer, which shows 10 – 15 nm wide crystallographic grains in the film. A similar grain distribution was observed in all the specimens. The SAED pattern in Fig. 5.13a was taken with the JEOL-2011 TEM microscope from an area of this lamella containing both CFS and substrate. This figure demonstrates the presence of the $L2_1$ phase in this film, as well as the epitaxial relationship with the substrate. Indeed, the 111 family of diffraction spots can be observed in the DP, in accordance with the (111) diffraction peak measured with the XRD for this sample. Figs. 5.13b and 5.13c are the DPs simulated for CFS $[\bar{1}\bar{1}0]$ and Si $[\bar{1}\bar{1}0]$ respectively. The disposition of the spots confirms the twinned epitaxial relationship deduced from the XRD measurements: CFS $(1\bar{1}0) \parallel \text{Si}(\bar{1}\bar{1}0)$ and CFS $(111) \parallel \text{Si}(111)$. The blue arrow indicates the growth direction. The same epitaxial relationship between film and substrate was confirmed in all the other specimens, namely $T_{Si} = 1025^\circ\text{C}$, $T_{Si} = 1040^\circ\text{C}$ and $T_{Si} = 1045^\circ\text{C}$.

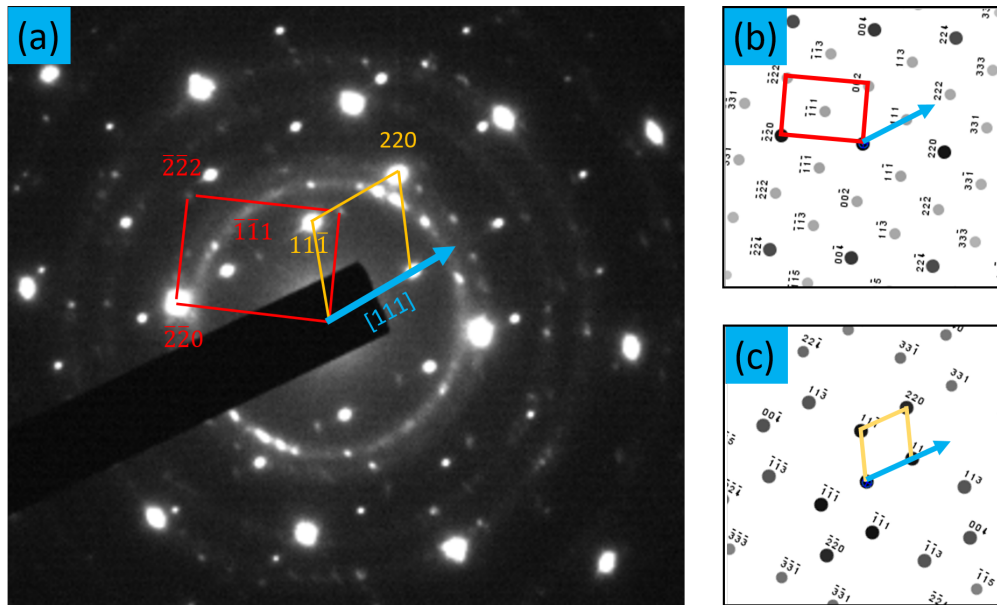


Figure 5.13: (a) Selected-area-diffraction pattern showing the diffraction spots for CFS and Si; (b) and (c) are the diffraction patterns of CFS $[\bar{1}\bar{1}0]$ and Si $[\bar{1}\bar{1}0]$ simulated using the software Jems. the DPs perfectly match our observations. The repeating unit of the CFS DP is the red rectangle and the repeating unit of the Si DP is the gold rhombus.

The presence of the $L2_1$ phase in the CFS film was further supported by atomic level

imaging. Figs. 5.14a and 5.14d are HAADF-STEM images of two small regions of the CFS layer also taken for $T_{Si} = 1035^\circ\text{C}$. The HAADF-STEM imaging was performed with an inner detector angle of 76 mrad. As explained in § 4.2.3, Z-contrast imaging allows the distinction between heavy elements, which exhibit bright contrast, and light elements, which are imaged dark. One can infer from this that in Fig. 5.14a each bright spot corresponds to either Fe or Co, whereas each dark spot represents a Si atomic column. At the right side of the image, Fig. 5.14b, the intensity profile extracted from the box outlined in blue is shown (averaged over the thickness of the box), highlighting the bright, bright, bright, dark, ... pattern of the atomic stacking along the [100] direction. This pattern agrees with the intensity profile that one would expect at this zone axis for the atomic stacking of the $L2_1$ structure. This has been depicted in Fig. 5.14c, where the atomic columns go as Co, Fe, Co, Si, ... As mentioned before, one has to be careful with the interpretation of this data because there is no difference in the contrast shown by Co and Fe and hence, the same intensity profile could also be the fingerprint of the DO_3 disorder. However, as explained before, the magnetic properties measured in these films most likely correlate with the fully-ordered $L2_1$ phase rather than DO_3 .

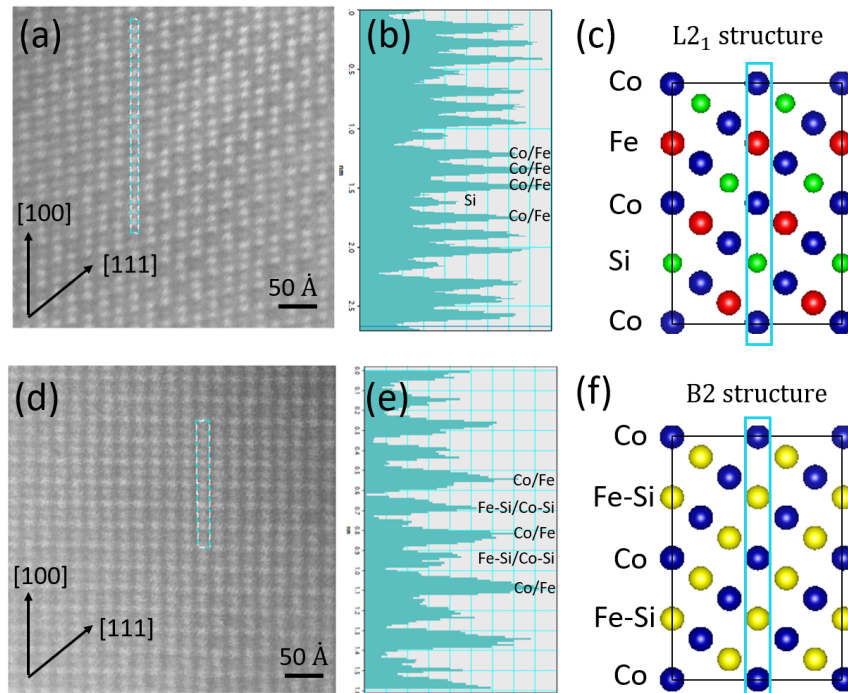


Figure 5.14: Atomic level HAADF-STEM images displaying the atomic stackings characteristic of (a) the $L2_1$ structure and (d) the B2 structure; (b) and (e) are the intensity profiles of the boxed areas in a and d respectively. The structural models are shown in (c) for $L2_1$ and (f) for B2. The specimen preparation along the $[1-10]$ axis allows the distinction between the structures very clearly. These images were taken from $T_{Si} = 1035^\circ\text{C}$.

On the other hand, the atomic stacking in Fig. 5.14d is obviously different from Fig. 5.14a. The intensity profile in Fig. 5.14e is now bright, medium, bright, medium, ..., where "medium" is used to indicate that the intensity lies somewhere between the bright contrast shown by Co/Fe and the dark contrast shown by Si. This profile here matches the B2 ordered structure in Fig. 5.14f where the Fe and Si sublattices are mixed (Co, Fe-Si, Co, Fe-Si, ...). The uncertainty regarding Fe and Co, has once again been taken into account when labelling the intensity peaks. Note also that the images were rotated to show the [100] direction along the vertical, so that the growth direction [111] is now at an angle.

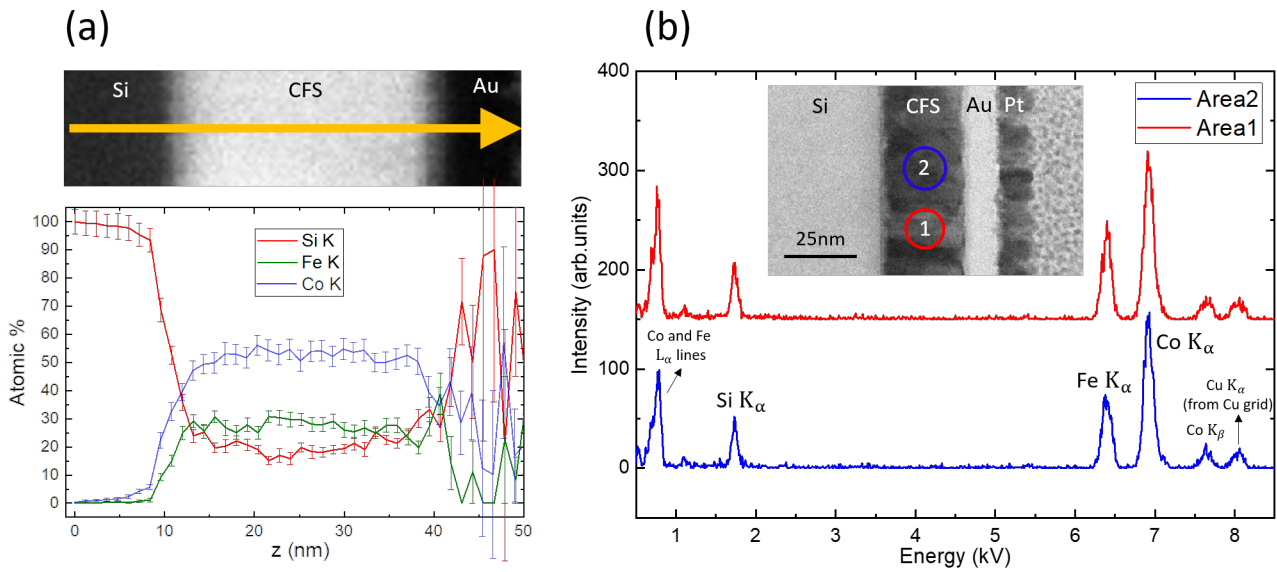


Figure 5.15: (a) EDS linescan taken across the CFS for $T_{Si} = 1035^\circ\text{C}$ with a spatial resolution of $< 1\text{nm}$; and (b) EDS spectra from two different areas in the same specimen. The micrographs in (a) and (b) are HAADF and TEM images of the regions from which the linescan and the spectra were taken respectively.

An EDS line scan taken across the CFS layer is shown in Fig. 5.15a for $T_{Si} = 1035^\circ\text{C}$. The area from which the line scan was taken has been specified by the yellow arrow on the micrograph on top. The chemical analysis (first row in Table 5.3) shows an average composition of $20 \pm 3\%$ Si, $28 \pm 2\%$ Fe and $53 \pm 2\%$ Co in at%. This is close to the desired ratios, but the Si content is on the low side. This result agrees with the higher lattice constant measured by XRD (Fig. 5.9b) and, as will be shown next, the higher saturation magnetization measured for this sample (refer to Fig. 5.21). The chemical composition is uniform across the film for Fe and Co to within a 5%, with small variations observed for Si. Fig. 5.15b displays two EDS spectra for the same specimen, the red (blue) spectrum taken from area 1(2) marked in the

micrograph. The two regions show a variation of contrast, the area labelled as 1 in the TEM image appears brighter than the area labelled as 2. The contrast could arise from thickness variations, compositional variations or slightly different diffraction conditions. However, the chemical composition extracted from the spectra (2nd and 3rd rows in Tab. 5.3) is the same for both regions within error. Hence, the contrast is more likely related to different diffraction conditions between grains.

atomic %	Co K	Fe K	Si K
Linescan in Fig. 5.15a	53±2	28±2	20±3
Area 1 in Fig. 5.15b	54±3	29±2	17±2
Area 2 in Fig. 5.15b	53±3	29±2	18±2

Table 5.3: Co, Fe and Si concentrations in at% measured by EDS in the Co_2FeSi film extracted from the linescan in Fig. 5.15a (first row) and the spectra in Fig. 5.15b (second and third rows).

Traces of both the $L2_1$ and the B2 order were found in all $T_{Si} = 1025^\circ\text{C}$ to $T_{Si} = 1045^\circ\text{C}$ specimens. The image in Fig. 5.16 for instance was taken for the most Si-rich $T_{Si} = 1045^\circ\text{C}$ specimen, which in two different areas exhibits the distinctive pattern of the $L2_1$ ordering (outlined in blue), and that of the B2 order (outlined in red). The same characteristic patterns are observed in the least Si-rich $T_{Si} = 1025^\circ\text{C}$ specimen in Fig. 5.17a.

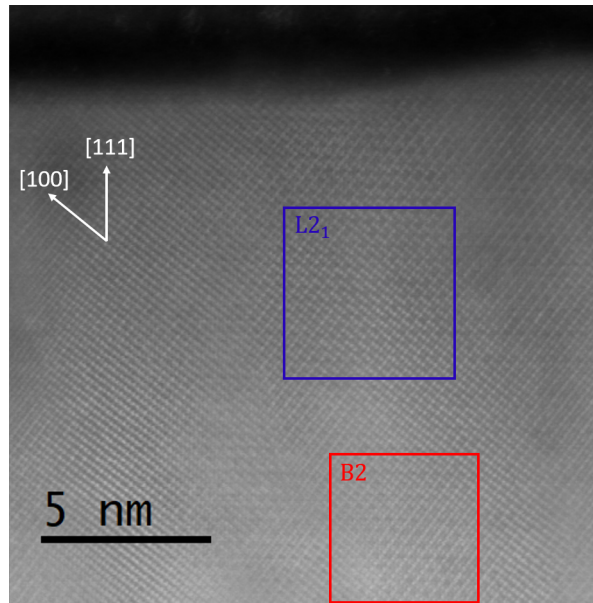


Figure 5.16: Cross-section of the CFS film for $T_{Si} = 1045^\circ\text{C}$ revealing the two types of ordered structures within the film, the $L2_1$ order in blue and the B2 order in red.

It is evident that the films in this section consist of a combination of B2 and L2₁-ordered grains. The fact that only small areas of ordering were highlighted in blue and red in Figs. 5.16 and 5.17a, does not mean that the remaining area in the images has a different structure, but that there is an overlap between slightly misoriented grains across the thickness of the lamella. In fact, if one looks at the diffraction space of the L2₁ and B2 areas in Figs. 5.17a, b and c respectively, one sees that even in the B2 structure there is some intensity of the 111 diffraction spots related to L2₁. These spots, although weaker than in Fig. 5.17b (marked with the white arrows), show how L2₁ is also present in this area, despite this did not seem to be the case initially. The same occurs in any other part of the specimen.

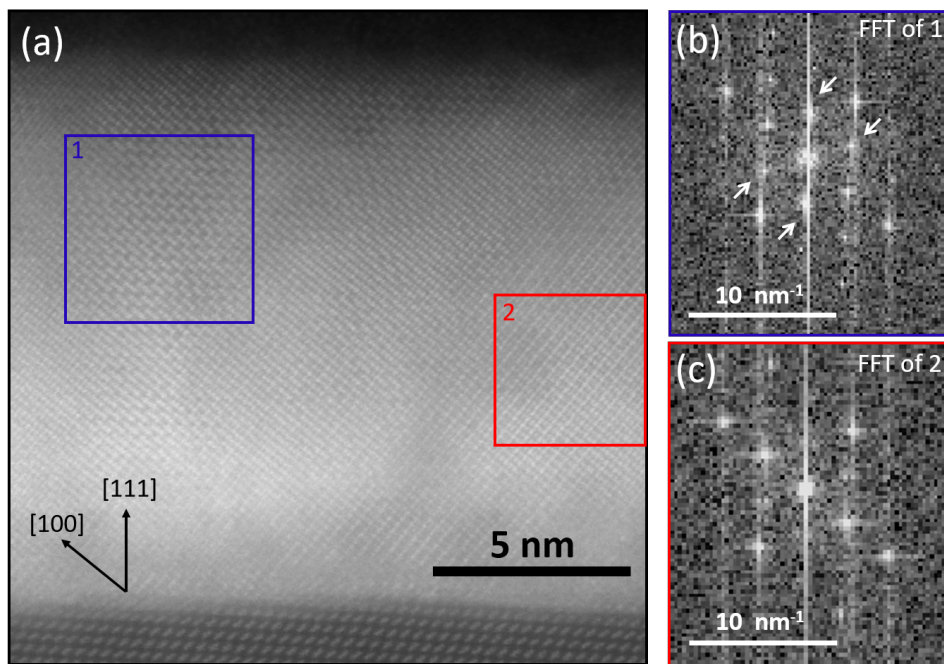


Figure 5.17: (a) HAADF-STEM micrograph of $T_{Si} = 1025^{\circ}\text{C}$, also showing the two types of ordering; (b) and (c) are the FFT-s of the areas marked in blue and red respectively, which match the diffraction patterns of a L2₁ and a B2 structure respectively. The FFTs were performed with the Digital Micrograph software.

To quantify the degree of L2₁ and B2 order, one should study the intensities of the 111 and 002 diffraction spots in each individual grain. However, in order to do so, the specimen has to be perfectly aligned to the zone axis of each individual grain. If a grain is misoriented, the specimen tilt has to be adjusted to find the new zone axis of this grain before measuring the intensities of the DP. Because the grains in these films are relatively small, high resolution HAADF is not reliable to quantify the L2₁ and B2 phases. Ideally, one would like to have a single grain along the thickness of the lamella, which in this case means preparing a ≈ 10 nm-thick lamella. However, reaching this thickness can be challenging, particularly with the FEI-Nova

system used in this project and the specimen can also be damaged in the process. Thus, the best alternative is performing 4D-STEM, where a full 2D diffraction pattern can be recorded at each pixel position in a STEM map. Correlated EDS and 4D-STEM experiments are currently under way for all 4 specimens to quantify the phase ordering and see if there are any compositional variations between grains with different structure.

Finally, the focus wants to be put on the CFS/Si interface. Fig. 5.18a shows the interface region for $T_{Si} = 1025^\circ\text{C}$. In this specimen, the atomic steps of Si are clearly visible, one of which has been marked with the yellow dashed line. Fig.5.18b shows the area delimited by the blue box enlarged. Here, the characteristic Si dumbbell pattern can be spotted in the substrate, as well as the atomic columns in the CFS. The intensity profile of one of the CFS atomic columns along $[100]$ has been illustrated in Fig. 5.18c for clarity.

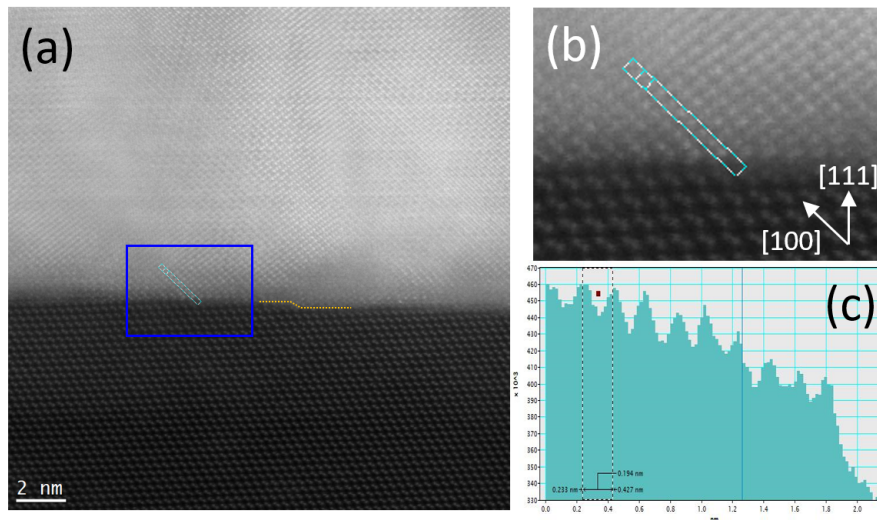
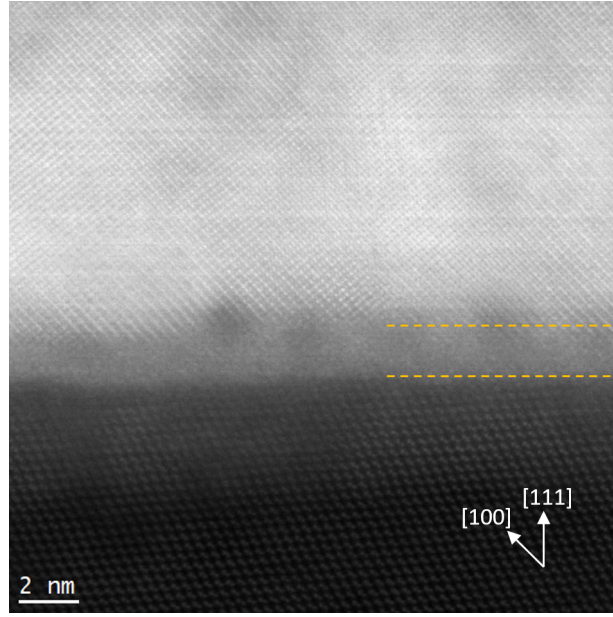


Figure 5.18: (a) $[1\bar{1}0]$ view of the CFS/Si interface for $T_{Si} = 1025^\circ\text{C}$, and (b) the enlarged image of the region of interest in a; (c) is the intensity profile along the line in (b).

In comparison, Fig. 5.19 shows a HAADF image of the interface for the film with $T_{Si} = 1040^\circ\text{C}$. As can be seen, the interface in this specimen looks "messier" and the atomic steps in the Si surface can no longer be easily spotted. The change in this interface would correlate with a larger Si out-diffusion at higher temperatures; or the formation of silicide phases from the reaction of Co and Si (such as CoSi_2), promoted by both the increased growth temperature and the increased Si content in the film. Something similar is observed in the $T_{Si} = 1045^\circ\text{C}$ sample. However, these changes in the interface could also be due to the specimen thinning process and so, EELS measurements are required to confirm this possibility.

Figure 5.19: CFS/Si interface of $T_{Si} = 1040^\circ\text{C}$.

5.4 Magnetic properties of CFS films grown on Si(111)

The static magnetic properties of the CFS films were studied with a LakeShore 8600 series VSM (§ 4.3.2). The dynamic magnetization characteristics were probed with the coplanar waveguide VNA-FMR technique described in § 4.3.1.

5.4.1 VSM measurements

In Figure 5.20 the magnetic hysteresis loops taken with an in-plane magnetic field applied along the $[1\bar{1}0]$ (in blue) and the $[11\bar{2}]$ (in red) crystallographic orientations of the CFS film can be seen. Fig. 5.20a (f) corresponds to the film with lowest (highest) Si content. For $[1\bar{1}0]$ and $[11\bar{2}]$ the loops have a different shape and hence, indicate the presence of an in-plane magnetic anisotropy. For $T_{Si} = 1015^\circ\text{C}$ (Fig. 5.20a), a square loop is observed along $[11\bar{2}]$ showing one step switching, characteristic of an easy axis. The loop measured along $[1\bar{1}0]$ shows hard axis behaviour.

As T_{Si} increases, the remanence decreases until at $T_{Si} = 1040^\circ\text{C}$ (Fig. 5.20d), the remanence goes to $M_r = 960 \pm 50 \text{ emu/cc}$ with a change in the EA direction. Above $T_{Si} = 1040^\circ\text{C}$, one can clearly identify the $[1\bar{1}0]$ direction with the easy axis and $[11\bar{2}]$ with the hard axis of the magnetization. The 90 degree angle between the EA and the HA points to a twofold uniaxial anisotropy. Although a weak 6-fold anisotropy is expected for a (111)-oriented CFS film, this

behaviour has already been observed for Heusler alloy films which exhibit two contributions to the in-plane anisotropy, a strong uniaxial contribution and a weaker cubic component [Haz19; Haz20]. The anisotropy exhibited by these films will be studied in more detail with the FMR in § 5.4.2.

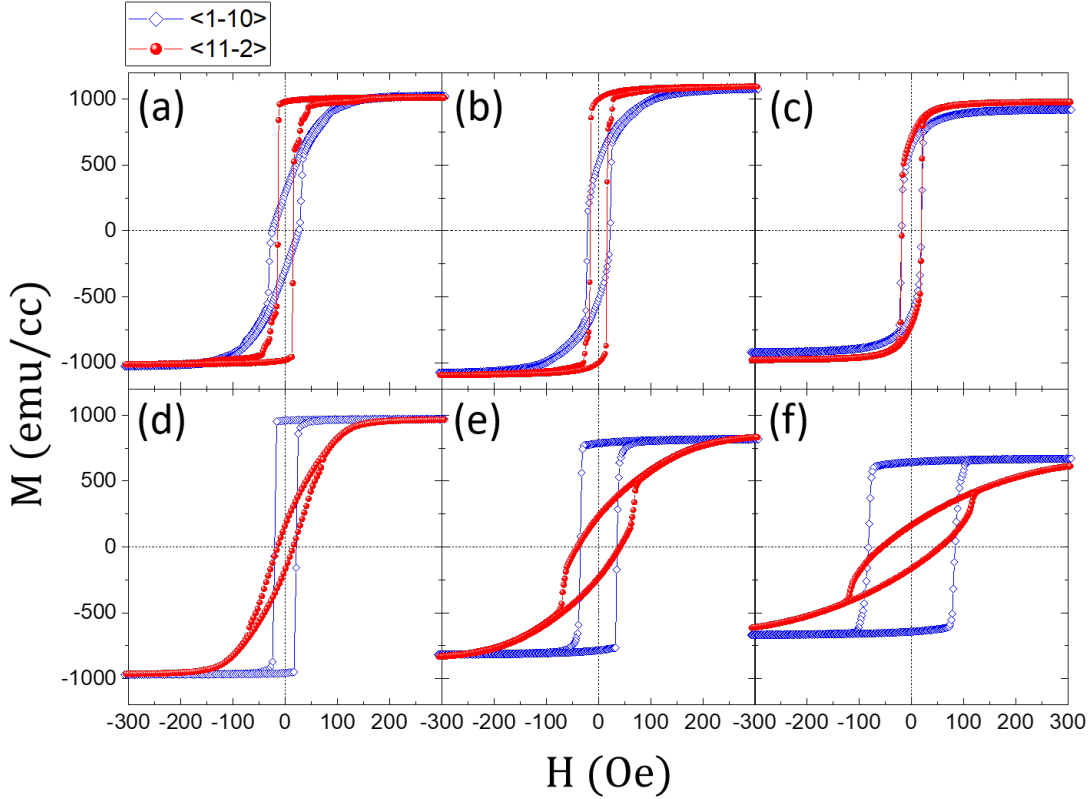


Figure 5.20: Magnetic hysteresis loops along the $[1\bar{1}0]$ (empty blue rhombus) and $[11\bar{2}]$ (red dots) for the CFS films with increasing Si content: (a) $T_{Si} = 1015^\circ\text{C}$, (b) $T_{Si} = 1025^\circ\text{C}$, (c) $T_{Si} = 1035^\circ\text{C}$, (d) $T_{Si} = 1040^\circ\text{C}$, (e) $T_{Si} = 1045^\circ\text{C}$ and (f) $T_{Si} = 1050^\circ\text{C}$.

The saturation magnetization M_s and the coercive field H_c have been derived from the EA hysteresis loops and are plotted in Fig. 5.21 as a function of the temperature of the Si source, T_{Si} . M_s and H_c follow different trends. M_s decreases with the increase of Si due to the reduction of the magnetic species Fe and Co. For temperatures above $T_{Si} = 1025^\circ\text{C}$, the values for M_s are lower than the ideal bulk value for the fully-ordered CFS ($M_s \approx 1100$ emu/cc) [Wur06]; although for $T_{Si} = 1040^\circ\text{C}$ ($M_s = 900 \pm 90$ emu/cc) and $T_{Si} = 1045^\circ\text{C}$ (800 ± 90 emu/cc), the values are still close to bulk. The coercivity of the films is low as expected from a soft ferromagnet. The coercive field stays below 20 Oe for $T_{Si} < 1045^\circ\text{C}$ but it is somewhat bigger than the values of ≈ 10 Oe reported for similar films [Kue18]. Above $T_{Si} = 1045^\circ\text{C}$, the coercivity jumps to 85 ± 5 Oe. This might be related with an increase in the number of grains

in the film and with changes in the interface (due to Si out-diffusion or an interfacial layer) as suggested by the STEM images.

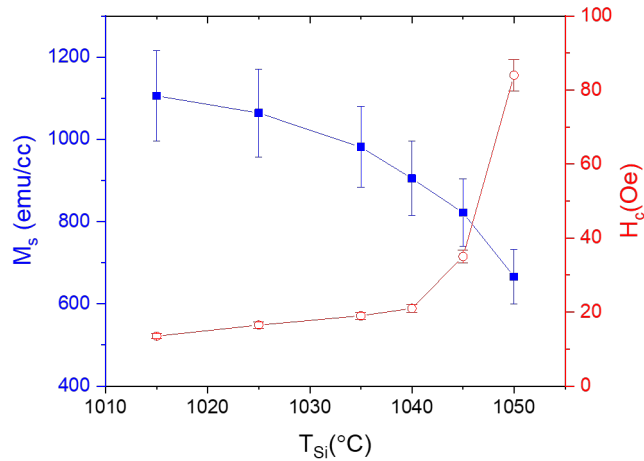


Figure 5.21: M_s (blue squares) and H_c (red circles) extracted from the hysteresis loops in Fig. 5.20.

5.4.2 FMR measurements

In order to study the magnetic anisotropy and other dynamic properties, VNA-FMR measurements were performed using the set-up in Fig. 4.20. The VNA-FMR linescans were performed over a field range between 0T to 0.35T in steps of 2mT. For each magnetic field, the RF frequency was swept from 100 kHz to 20 GHz in 1601 equally spaced steps, constructing the frequency-field maps shown in Fig. 5.22. The maps in Fig. 5.22 were measured along the easy axis for the various CFS/Si(111) samples, and reveal the characteristic Kittel curves in dark blue¹. Without further analysis, one can already sense how the resonance broadens as the source temperature increases. In Fig. 5.22e is intriguing to see the presence of two additional weaker resonances which have been highlighted in red. The origin of these other resonances was also investigated and attributed to lateral inhomogeneities in this particular film arising from the shadowing effect caused by the clamps that hold the sample to the stage during growth, as will be detailed later on.

¹Notice that the maps shown here are the ones taken along $\phi = +60^\circ$ for $T_{Si} < 1040^\circ\text{C}$ and $\phi = 0^\circ$ for $T_{Si} \geq 1040^\circ\text{C}$ in accordance with the two easy axes, $[10\bar{1}]$ and $[\bar{1}10]$ respectively, revealed by the polar plots in Fig. 5.24.

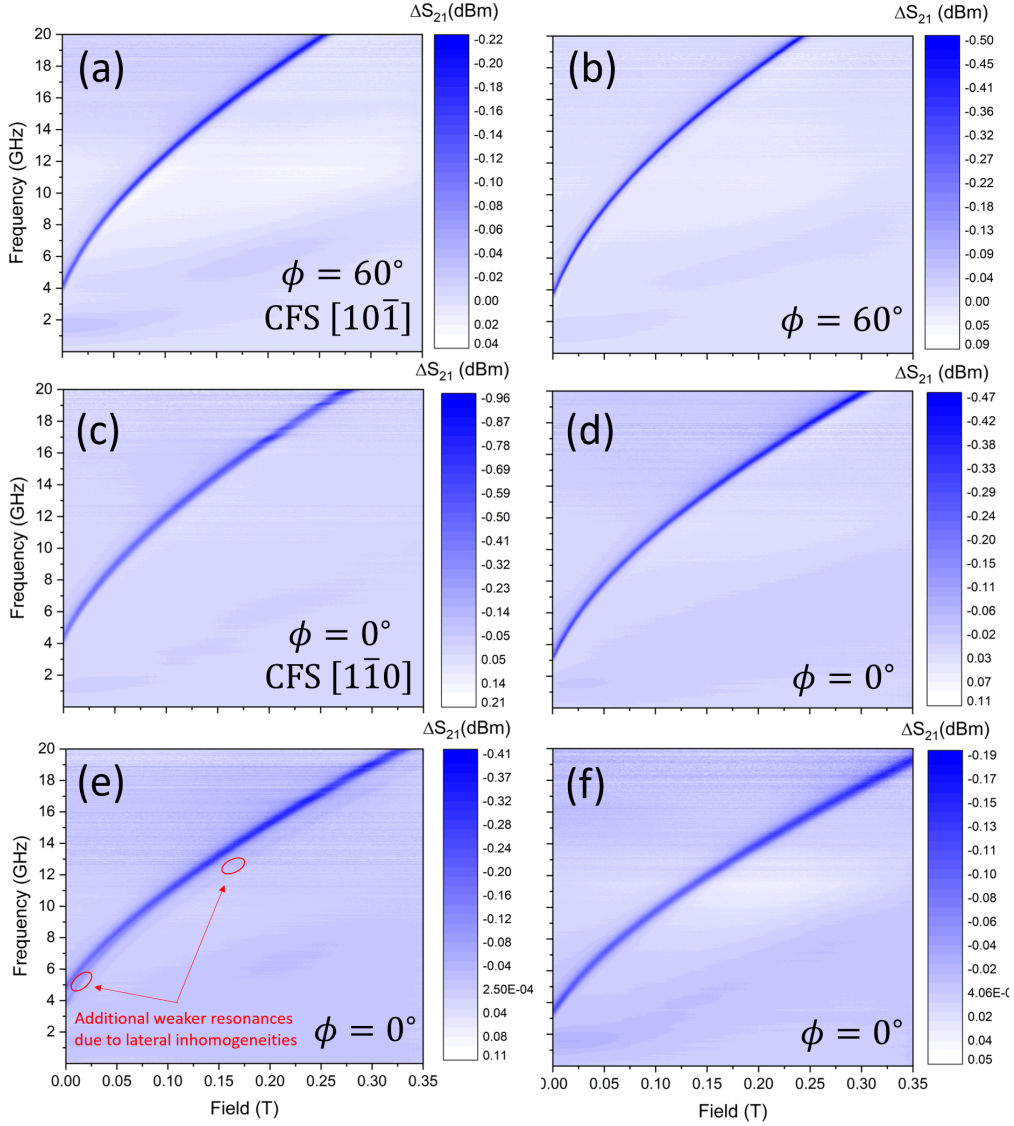


Figure 5.22: FMR frequency-field maps for: (a) $T_{Si} = 1015^\circ\text{C}$, (b) $T_{Si} = 1025^\circ\text{C}$, (c) $T_{Si} = 1040^\circ\text{C}$, (d) $T_{Si} = 1045^\circ\text{C}$, (e) $T_{Si} = 1050^\circ\text{C}$ and (f) $T_{Si} = 1055^\circ\text{C}$.

Similar maps were also taken for azimuthal angles between $\phi = -90^\circ$ and $\phi = +90^\circ$, rotating the electromagnets in steps of $\Delta\phi = 5^\circ$ degrees around $\phi = 0^\circ$. Fig. 5.23a shows the horizontal line scan taken through the frequency-field map in Fig. 5.22b at a frequency of 10 GHz, representing the field swept FMR for $T_{Si} = 1025^\circ\text{C}$. The equivalent signals measured for $\phi = 0^\circ$ and $\phi = -60^\circ$ are illustrated in Fig. 5.23b and Fig. 5.23c respectively for the same sample. Judging by the shift of H_r there is some in-plane anisotropy present in the film. Before extracting any parameters from the linescans, the background noise was subtracted using a spline interpolation. The resulting curves were then fitted to the asymmetric Lorentzian

function (eq. (4.35)) as described in § 4.3.1. From the fitted curves, shown in red, the resonant frequency (H_r) and the resonance linewidth (ΔH) could be obtained as a function of the azimuthal angle. It should be noted that for larger azimuthal angles ($|\Delta H| > 60^\circ$), the precession amplitude is reduced and thus, the data is subjected to larger errors. As a result, in the cases where the data was no longer reliable, the measurements were repeated at $\phi = 0^\circ$ by rotating the sample itself by 90° and performing a second angular sweep. By combining these two data sets, the whole picture of the in-plane anisotropy could be achieved.

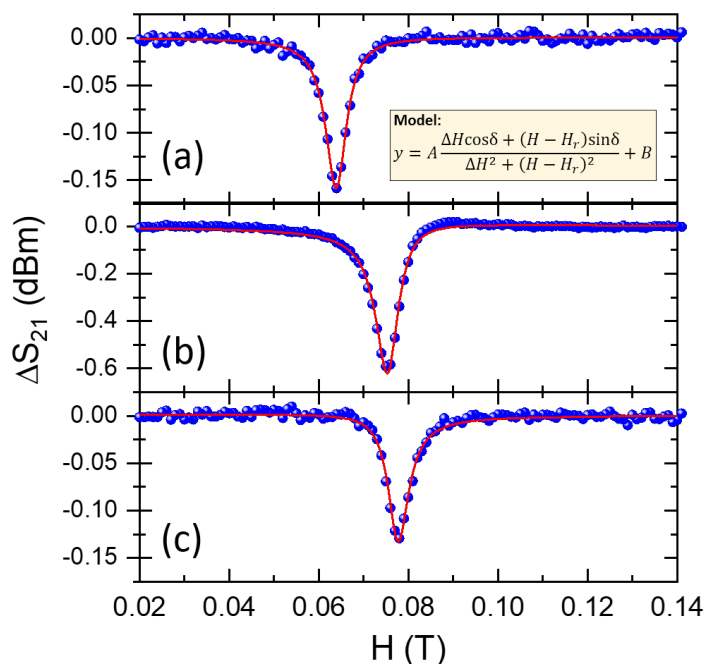


Figure 5.23: FMR linescans (blue dots) for $T_{Si} = 1025^\circ\text{C}$ for (a) $\phi = +60^\circ$, (b) $\phi = 0^\circ$ and (c) $\phi = -60^\circ$; and corresponding fits (red lines) to an asymmetric Lorentzian, allowing the extraction of H_r as a function of ϕ .

In Fig. 5.24, $H_r(\phi)$ azimuthal plots are shown for the CFS films with varying Si content. The easy axis is identified as the direction at which the resonance field is minimum, whereas along the hard axis, H_r is maximized. As discussed in § 2.1.2, the magnetocrystalline anisotropy in CFS is cubic and brings the easy axes along the $\langle 100 \rangle$ directions when $K_c > 0$. In a (111)-oriented film, the projection onto the (111)-plane results in a weak 6-fold in-plane anisotropy if the shape anisotropy is small in the film plane. Contrary to such expectations, a two-fold anisotropy is observed in all the $\text{Co}_2\text{FeSi}/\text{Si}(111)$ films grown in this work. Although its origin is still unclear, many authors have observed a similar uniaxial character of the anisotropy in cubic Heusler films [Yam10; Haz19; Tru10]. Uniaxial anisotropies in thin films are often related to interface, surface or strain effects and do not arise from the bulk structure. In the case of

CFS/Si(111) films, some authors have attributed it to shape effects that arise from the step edges on the surface of the substrate (the presence of such step edges was indeed observed in our films in the STEM, Fig. 5.18a) as it occurs for Fe ultrathin films on Si(111) [Ye13]. Other authors have claimed that the uniaxial anisotropy is the result of a non-isotropic deposition process during growth at an oblique angle [Oza83]. The latter is unlikely to be our case because the flux is coming from multiple directions during growth. Also, this would not explain the change in the direction of the anisotropy that is observed at $T_{Si} = 1040^\circ\text{C}$ and which will be subsequently discussed.

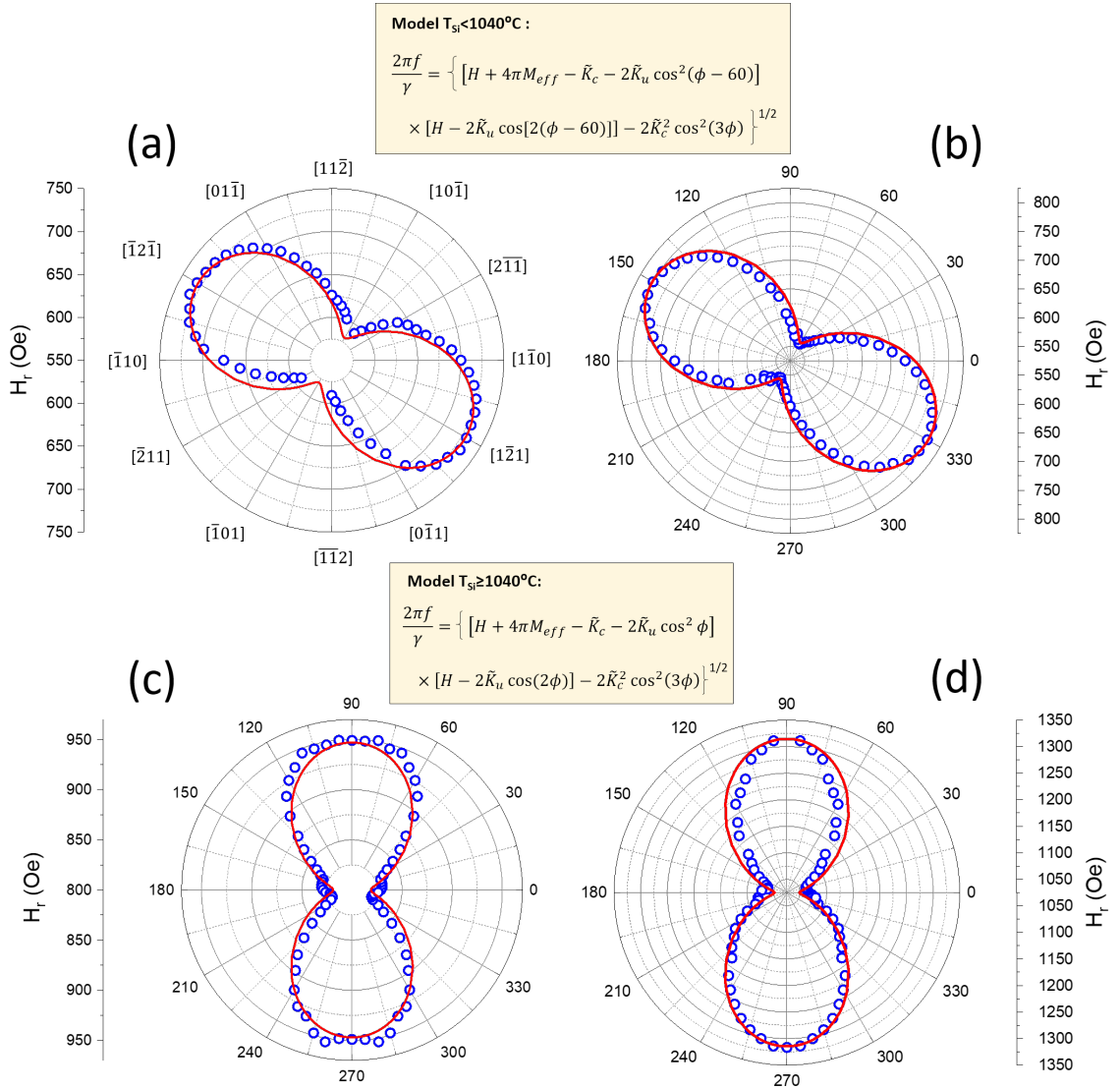


Figure 5.24: Azimuthal H_r plots for (a) $T_{Si} = 1015^\circ\text{C}$, (b) $T_{Si} = 1035^\circ\text{C}$, (c) $T_{Si} = 1045^\circ\text{C}$ and (d) $T_{Si} = 1055^\circ\text{C}$; $\phi = 0^\circ$ corresponds to $[1\bar{1}0]$ and $\phi = 90^\circ$ to the $[11\bar{2}]$ direction.

For $T_{Si} < 1040^\circ\text{C}$, the easy axis lies along $\phi = +60^\circ$ which corresponds to the $[10\bar{1}]$

crystallographic direction of CFS (Figs. 5.24a and 5.24b). However, at $T_{Si} = 1040^\circ\text{C}$, the uniaxial anisotropy switches by an angle of 60 degrees, i.e. the easy axis now points along $[1\bar{1}0]$. This agrees with the observations from the VSM measurements. The directions that were being probed in Figs. 5.20a-c were actually not the easy and hard axes of the film, which is why the two loops in Fig. 5.20c look equivalent. For Figs. 5.20d-f, the easy and hard axes were indeed the $[1\bar{1}0]$ and $[11\bar{2}]$ directions respectively. The change of the uniaxial anisotropy axis was reproduced in a second batch of CFS films grown under the same growth conditions at $T_{Si} = 1035, 1040, 1045$ and 1050°C .

The change in anisotropy seems to occur as the Si content of the film is increased. In the MBE system, growing at higher Si rates implies a rise of the deposition temperature due to the radiation emanating from the sources. In order to rule out that the effect was due to a change in the chemistry of the films, and instead a temperature related phenomenon, one last CFS film was grown using a lower Si rate but with a higher growth temperature by running some current through the substrate heater. In such sample, the easy axis lay along $[1\bar{1}0]$ and hence, confirmed that the switch in anisotropy is independent of the amount of Si in the film. Because it is unrelated to the Si content, the effect can't be a result of differences in the structural order of the CFS. The switching occurs at relatively low growth temperatures of $\approx 130^\circ\text{C}$, far from the annealing temperatures ($\approx 500^\circ\text{C}$) used to prepare the substrate; and thus, it is also unlikely that it happens due to a change on the step edges of the Si surface. This switching of the anisotropy was already observed by other authors when the growth temperature was increased above 100°C [Yam10]. However, it might arise because of another interface effect. As the growth temperature increases, more Si atoms will out-diffuse into the CFS layer leading to changes in the interface that could affect the properties of the films. However, a much more detailed study is needed to find this correlation.

In order to fit the angular dependent data shown in Fig. 5.24, one should solve the quadratic equation (4.33) for the magnetic field, H . Because this is too laborious of a task, it results more effective to fit the Kittel curves taken for a fixed ϕ angle instead. Taking sample $T_{Si} = 1015^\circ\text{C}$ as an example, one could substitute $\phi \rightarrow 60^\circ$ in eq. (4.33), and fit the Kittel curve measured along this direction (the EA) to obtain M_{eff}, K_u, K_c and γ . However, when one tries to do this, the values obtained for the fitting parameters are very unrealistic and dependent on their initial values; hence, unreliable. The issue is undoubtedly to do with the multiparameter fitting. In order to improve the fitting, several Kittel curves taken along different ϕ were simultaneously fitted with shared parameters, M_{eff}, K_u, K_c and γ . As γ and M_{eff} are not easily decoupled during the fit, γ was set to the electron gyromagnetic ratio as first approximation, that is, $\gamma = 1.76 \times 10^7 \text{ rad s}^{-1} \text{ Oe}^{-1}$ (i.e. $g_e = 2.0$) which coincides with other reported data [Haz19].

An example of the fitting is shown in Fig. 5.25 for $T_{Si} = 1015^\circ\text{C}$. Although only two curves ($\phi = 60^\circ$ and $\phi = 330^\circ$) are shown in the graph, the global fit was performed on three different curves, namely $\phi = 0^\circ$ (IA), $\phi = 60^\circ$ (EA) and $\phi = 330^\circ$ (HA). The first curve ($\phi = 0^\circ$) is not shown here for clarity as the data overlaps the other curves, but the quality of the fit was similar with an R-squared of 0.99847. The same procedure was followed for all the CFS/Si(111) samples. The direction of the uniaxial anisotropy in eq. (4.33) was set to $\phi_u = 60^\circ$ for $T_{Si} < 1040^\circ\text{C}$, and $\phi_u = 0$ for $T_{Si} \geq 1040^\circ\text{C}$ according to the switching phenomenon observed. Before moving forward, it should be noted that at low frequencies, $\omega \approx 4 \times 10^{-10} \text{ rad/s}^{-1}$ (refer to Fig. 5.25 one more time), the model is not able to reproduce the data, especially along the HA. This happens because the approximation made in eq. (4.33), $\phi_M = \phi_H$, i.e. that the magnetization aligns with the field, does not apply at low RF frequencies. Here, the resonant field is lower than the saturation field required to align the magnetization and thus, the magnetization forms a small angle with H and the data deviates from the model. However, because the angular data in Fig. 5.24 was taken above this low frequency range (at 10 GHz), the values extracted in this manner can be effectively used to describe the behaviour of the in-plane anisotropy observed at this frequency. The values for the resulting M_{eff} , K_u , K_c and γ were substituted in eq. (4.33) and the model has been plotted along the angular sweep in Fig. 5.24.

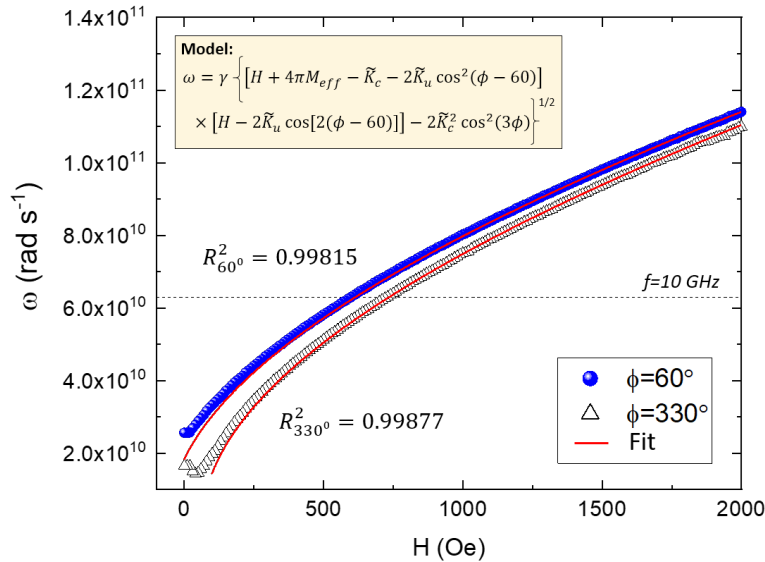


Figure 5.25: Kittel curves measured at the easy axis, $\phi = 60^\circ$ (blue dots), and the hard axis, $\phi = 330^\circ$ (black triangles), for $T_{Si} = 1015^\circ\text{C}$. The red lines are the fits to eq. (4.33) with shared parameters M_{eff} , K_u , K_c and γ .

The various parameters extracted from these fits are shown in Fig. 5.26. K_c was in all cases equal to 0 and hence, it is not shown here. The uniaxial anisotropy in these films clearly dominates and completely masks any underlying cubic magnetocrystalline anisotropy of CFS. M_{eff} and K_u are shown in Fig. 5.26a and Fig. 5.26b respectively as a function of T_{Si} . The grey dashed line in Fig. 5.26a represents the M_s values obtained from the VSM which, in the absence of tetragonal distortions, should match M_{eff} . As can be observed, the discrepancy between the two values at low T_{Si} is large. Unlike the values for M_s obtained from magnetometry measurements, where the magnetic volume has to be known, M_{eff} is in emu/cm^3 units and hence, any errors arising from the calculation of the magnetic volume are omitted in FMR measurements. Errors in the calculation of the magnetic volume arise mainly from the $\approx 10\%$ error in the film thickness measured by XRR. The discrepancies observed here are evidently bigger than this, and follow a clear trend with T_{Si} . Therefore, this behaviour is more likely explained as a consequence of lattice distortion at low T_{Si} . As revealed by the XRD measurements, the inclusion of more Si to the lattice results in a smaller unit cell and therefore, a decreasing out-of plane lattice parameter is measured in Fig. 5.9b. Because Si has a lattice constant $\approx 4\%$ smaller than that of bulk stoichiometric CFS, the lattice mismatch is bigger for Si-poor films, which are hence more likely to be subjected to a compressive strain that distorts the lattice. In Si-rich films, the mismatch decreases reducing the strain. Such strain induced anisotropy is reflected in the perpendicular anisotropy constant, $K_{\perp} = 2\pi M_s(M_s - M_{eff})$, which has been plotted in the inset of Fig. 5.26a.

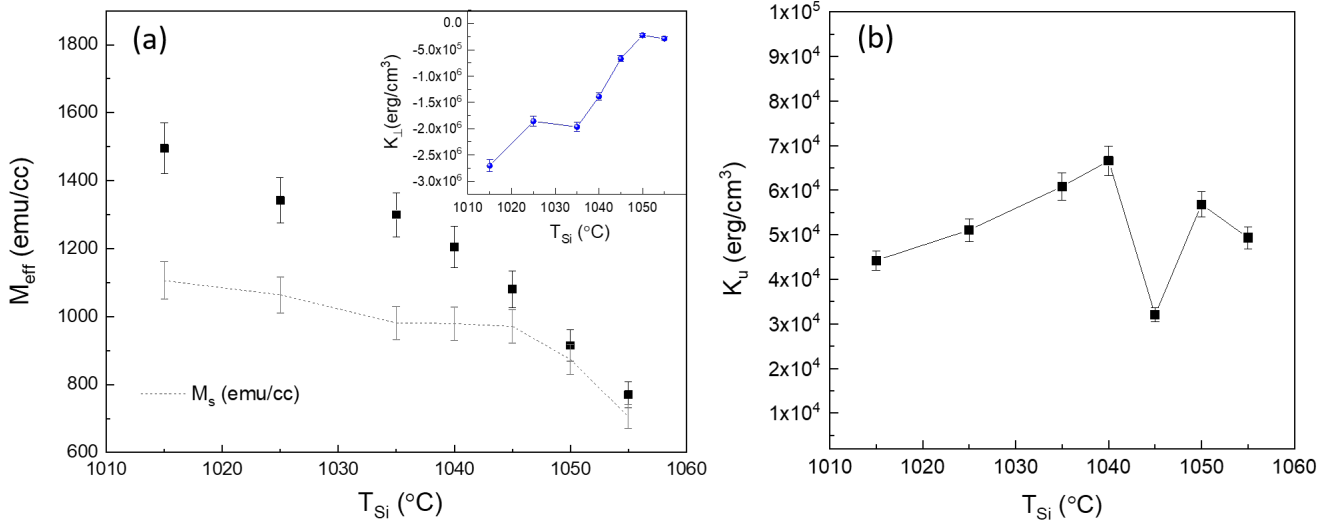


Figure 5.26: (a) Fitting parameter M_{eff} extracted from the Kittel curves (black squares) compared to the M_s values measured with the VSM (grey dashed line); perpendicular anisotropy constant K_{\perp} , proportional to the difference of M_s and M_{eff} , is shown in the inset. (b) Uniaxial anisotropy constant K_u as a function of T_{Si} .

For T_{Si} between 1045°C and 1050°C, M_{eff} and M_s agree within error and have values very close to bulk (1100 emu/cc). For $T_{Si} > 1050^\circ\text{C}$, the magnetization decreases down to ≈ 700 emu/cm³ which correlates with the detriment of the crystallinity of the film observed in the XRD measurements.

As for the uniaxial anisotropy constant² in Fig. 5.26b, K_u monotonically increases from $4.4 \pm 0.2 \times 10^4$ at 1015°C to $6.7 \pm 0.3 \times 10^4$ erg/cc at $T_{Si} = 1040^\circ\text{C}$. Above 1050°C, the anisotropy field starts decreasing towards its initial value. However, the most striking feature of this figure is that at $T_{Si} = 1045^\circ\text{C}$, K_u suddenly drops to $3.2 \pm 0.2 \times 10^4$ erg/cc deviating from this trend. The interest on this outlier wouldn't be as high if it weren't for the fact that this sample also shows a drop in the damping parameter as will be shown next. The reason for such decrease in the uniaxial anisotropy field is unknown. The substrate preparation and growth conditions for all the films in this series was the same and given that the nature of the uniaxial anisotropy is more likely due to interfacial effects, it unlikely originates from the higher crystallinity shown by this film.

²In some papers, it is common to talk about the anisotropy field, rather than anisotropy constant. The way the anisotropy constants were defined in this thesis, the uniaxial and cubic anisotropy fields can be estimated as $H_u = 2M_s K_u$ (Oe) and $H_c = M_s K_c$ (Oe) respectively, for the sake of comparison.

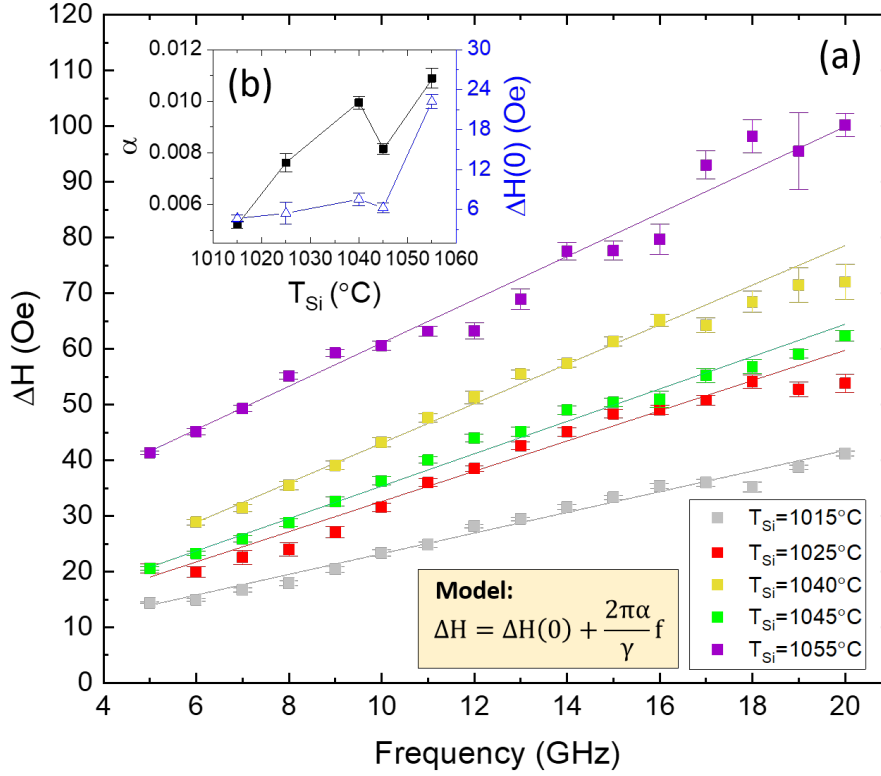


Figure 5.27: (a) ΔH as a function of the RF frequency and the corresponding linear fits for $T_{Si} = 1015^\circ\text{C}$ (grey), $T_{Si} = 1025^\circ\text{C}$ (red), $T_{Si} = 1040^\circ\text{C}$ (yellow), $T_{Si} = 1045^\circ\text{C}$ (green) and $T_{Si} = 1055^\circ\text{C}$ (purple); (b) Gilbert damping parameter and $\Delta H(0)$ extracted from the linear fits in (a).

Finally, the magnetic damping was extracted from the FMR for the CFS films. At the easy axis of each film, the field linescans for RF frequencies between 5GHz to 20GHz (in steps of 1GHz) were fitted to eq. (4.35). Fig. 5.27 shows the resonance linewidth, ΔH , extracted from those fits as a function of the driving frequency for the different samples. Note that the results for $T_{Si} = 1050^\circ\text{C}$ have been omitted because the presence of a second weak resonance close to the main resonance (illustrated in Fig. 5.22e), didn't allow to achieve good fits for this sample. The presence of this second resonance was due to a non-uniform coverage in this film, confirmed by the almost disappearance of such resonance when the sample was cut into a smaller piece and remeasured. When the two-magnon scattering is not present, the slope of this curves is related to the Gilbert parameter α through eq. (4.34). Although the effect of the two-magnon scattering cannot be completely ruled out in these samples, the dependency of ΔH with frequency is almost linear and hence, α can be extracted from the linear fits shown in the figure. The Gilbert damping parameter has been plotted in the inset.

The linewidth increases with T_{Si} and so does the slope of the curves, which is related to

α . The steeper slopes are translated into an increase of the Gilbert damping that goes from $(5.2 \pm 0.1) \times 10^{-3}$ at $T_{Si} = 1015^\circ\text{C}$ to $(11.0 \pm 0.2) \times 10^{-3}$ at $T_{Si} = 1055^\circ\text{C}$, and reflects how the changes in the stoichiometry of the film lead to significant changes in the dynamic properties of the magnetization. Between $T_{Si} = 1035^\circ\text{C}$ and $T_{Si} = 1045^\circ\text{C}$ (where all the measurements suggest that the chemical composition is closed to the ideal Co:Fe:Si=2:1:1 and the ordering is maximized), the intrinsic damping takes values from $(7.6 \pm 0.4) \times 10^{-3}$ to $(9.9 \pm 0.3) \times 10^{-3}$. These values are of the order of magnitude to those found in literature for non-annealed CFS films, $\alpha \approx 7 \times 10^{-3}$ in [Oog07; Haz19]. Interestingly, at $T_{Si} = 1045^\circ\text{C}$, α drops to $(8.1 \pm 0.2) \times 10^{-3}$. This could either be a consequence of the structural order being improved in this film, or be related to the lower uniaxial anisotropy measured in this film (Fig. 5.26b) which is in turn attributed to an interface effect. $\Delta H(0)$ has also been illustrated in the inset plot and it is related to extrinsic damping mechanisms. $\Delta H(0)$ increases with T_{Si} in the same way α does, but the biggest change occurs from $T_{Si} = 1045^\circ\text{C}$ to $T_{Si} = 1055^\circ\text{C}$ where $\Delta H(0)$ jumps from 6.3 ± 0.7 Oe to 22 ± 1 Oe. This reflects an increase of magnetic impurities or inhomogeneities in the Si-rich film which is most likely the cause of the high coercivity exhibited by this film (Fig. 5.21).

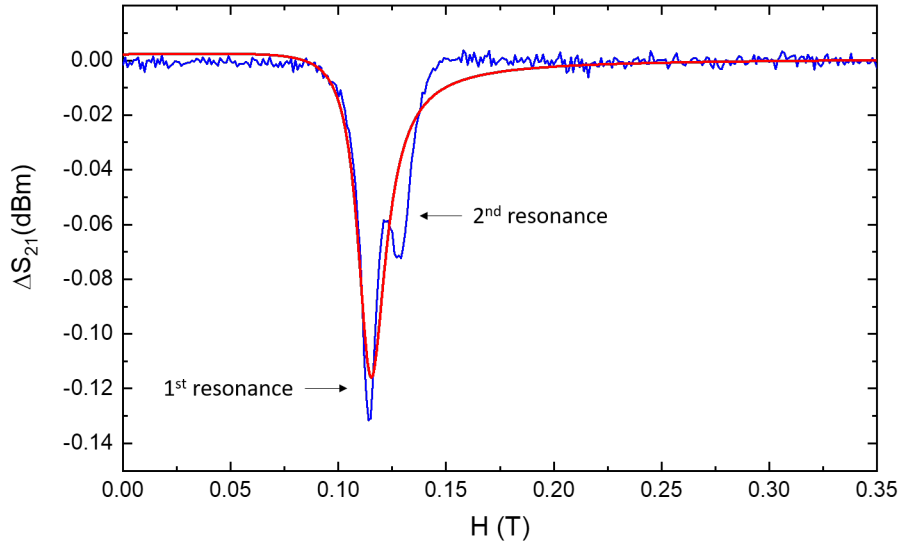


Figure 5.28: FMR linescan measured for $T_{Si} = 1050^\circ$ (in blue) showing the two resonances present in this sample. The red line is the fit to the asymmetric Lorentzian which returns a bigger value for ΔH due to the proximity of the second adsorption dip. This effect was worst at low RF frequencies preventing the extraction of reliable linewidths where the behaviour is most linear.

5.5 Summary and conclusions

In this chapter, it is demonstrated that high quality CFS Heusler films can be grown with the MBE system commissioned in this work. A set of non-annealed Co_2FeSi films with varying Si content were grown on Si(111) and were subsequently characterized. The structural properties of the samples were measured by XRD and suggest the presence of both B2 and L2_1 phases in the films. The XRD analysis also indicates that the degree of L2_1 ordering reaches a maximum at $T_{Si} = 1045^\circ\text{C}$. The coexistence of grains crystallized in a B2 and L2_1 structure was confirmed by STEM-HAADF imaging but more work is needed to quantify the degree of structural ordering and correlate it with the XRD analysis.

The magnetic properties of the films were measured by VSM and FMR. The M_s measured via both techniques, provides clear evidence of the changes on the chemical composition of the films, which also correlates with the out-of-plane lattice parameters extracted from the XRD measurements. M_s decreases as the Si rates are risen due to the reduction of the magnetic species (Fe and Co) in the film; the lattice constant c also goes down because atoms with smaller ionic radius (Si) are replacing those with larger radius (Fe and Co). All the samples show an in-plane uniaxial anisotropy which agrees with the observations of other authors [Haz19; Haz20]. However, the most interesting finding is the 60 degree rotation of the uniaxial anisotropy upon the slight increase of the growth temperature at $\approx 130^\circ\text{C}$. This rotation is independent of the Si content in the films but the result of an increase of the sample temperature during growth. The mechanism why this happens is still unclear. It could be due to an interfacial effect like the Si out-diffusion that increases with temperature, although a follow up is required to investigate this further.

The intrinsic damping parameters measured by FMR ($\approx 7.6 \times 10^{-3} - 9.9 \times 10^{-3}$) are of the order of magnitude, although somewhat higher, than those found in literature for CFS films [Oog07; Haz19]. Interestingly, the trend for α is to increase with T_{Si} but at $T_{Si} = 1045^\circ\text{C}$, α suddenly drops to $\approx 8.0 \times 10^{-3}$ along with the uniaxial anisotropy constant K_u that reaches its minimum value at this Si rate. This could indicate a change in the structure of this film where the L2_1 order is the highest and stresses the influence of the chemical composition on the magnetic properties of CFS alloys.

Chapter 6

Growth and characterization of CFS films on MgO(001)

6.1 Introduction

As described in § 2.5, a novel way to inject a highly-spin polarized current in the otherwise inefficient FM/SC interface is the use of a spin-dependent insulating barrier. In this context, the combination of HMFs with important single-crystalline oxides such as MgO, SrTiO₃ (STO) and AlO_x provides an attractive platform for designing electronic interfaces.

Following the observation of a large TMR ratio at RT in a MTJ consisting of a Co₂(Cr_{0.6}Fe_{0.4})Al (CCFA) electrode and an amorphous alumina barrier [Ino03], experiments with Co₂YZ/AlO_x MTJs were triggered involving Co₂MnAl [Sak06b], Co₂FeAl [Oka05] and Co₂MnSi [Sak06a] etc. In particular, a MTJ with a L2₁-Co₂MnSi film showed a very large TMR ratio of 570% at 2K, although it rapidly reduces to 68% at RT [Sak06a]. MTJs fabricated with an oriented MgO barrier gathered a lot of attention after a TMR ratio as high as 6000% was predicted in Fe/MgO/Fe(001) MTJs [But01; MU01]. Afterwards, TMR ratios of 220% were obtained at RT in CoFe/MgO/CoFe(001) structures, which were increased up to 500% using CoFeB electrodes. Despite such achievements at RT, these MTJs would require lower resistance to reach ultrahigh speed and high density for future spintronic applications. A way to achieve this, is the use of HMF electrodes with an MgO barrier. The TMR ratio of MTJs composed of a MgO barrier and a full Co-based Heusler has steadily improved [Tez06; MY07; Ish08]. In [Tez06] for instance, a TMR ratio of 175% was achieved using CFAS electrodes and a MgO barrier at RT. However, disordered phases especially near the barrier interface, have been shown to have a detrimental effect on the spin polarized electron transport [Hir13].

In the work by M. Ramsteiner *et al.* [Ram08], although a highly spin-polarized current was

successfully injected from the MBE-grown CFS electrodes into GaAs, it was also observed that the epitaxial growth of CFS on top of GaAs suffers from Fe and Co diffusing into the GaAs which leads to a deterioration of spintronic functionalities [Has07]. More recently, it has been demonstrated that this undesirable interdiffusion at the HMF/SC interface can be eliminated by MgO interlayers [HHR19]; but the CFS/MgO/SC tunnel contacts might still be affected by HMF and oxygen intermixing at the new HMF/MgO interface. There is also a lot of work on $\text{Co}_2\text{MnSi}/\text{GaAs}$ and other half-metals showing mixing between the film and the substrate [Rat18]. Thus, the synthesis of low temperature fully-ordered $\text{Co}_2\text{FeAl}_{1-x}\text{Si}_x$ on MgO becomes crucial too. As such, this chapter will focus on the growth of CFS/MgO(001) films. In § 6.2 the effects of stoichiometry on the structural and magnetic properties will be studied and compared to those of CFS/Si(111) films in Chapter 5. In § 6.3, the impact of growth temperature on the structure of the CFS films will be investigated.

Antiferromagnetic order has traditionally played an important supporting role in ferromagnetic spintronics. For example, as described in § 2.4, in GMR and TMR stacks the reference FM layer is pinned by means of the interlayer exchange bias with an adjacent AFM layer. Recently, AFMs and antiferromagnetic insulators (AFIs) have also emerged as active spintronic elements. In this context, the study of AFM/HMF and AFI/HMF structures is important. After optimising the growth on MgO(001), the growth of NiO as an overlayer on CFS has been explored. NiO has the same isostructure, i.e. the same space group, and very close lattice matching (0.1% mismatch) with MgO. Also, NiO is one of the prototype G-type AFI materials, which is extensively used in combination with other ferromagnetic layers such as $\text{Y}_3\text{Fe}_5\text{O}_{12}$ (YIG). In fact, the insertion of NiO in Pt/NiO/YIG heterostructures, enhances the spin mixing conductance due to magnon and spin fluctuation in the NiO layer [Lin16; LC17]. In section § 6.4 the structural quality of NiO grown on CFS, as well as the effect of NiO on the magnetic properties (such as MCA) and the structural properties of CFS, has been investigated.

6.2 Optimization of the chemical composition of CFS films on MgO(001)

After the successful growth of CFS films on Si(111), the growth was optimized for the second substrate of interest, that is, single-crystal MgO(001). MgO has a rock-salt type structure, i.e. an fcc array of Mg^{2+} cations with an interpenetrating lattice of O^{2-} anions, with a lattice constant of 4.17\AA . This means that a cubic crystal like CFS with $a = 5.65\text{\AA}$ (§ 2.7.1), grows 45 degrees rotated in-plane with respect to the (001) surface (see Fig. 6.20e). The lattice

mismatch is then $\approx 4.9\%$, that is, around 1% bigger than the mismatch with Si. Before loading them into the MBE chamber, the MgO substrates were cleaned using the following recipe:

- 15 min in ethanol in sonic bath
- 15 min in DI water in sonic bath
- annealing in air at $900^\circ\text{C} - 1000^\circ\text{C}$ for 1 hour

The annealing in air was done in a MILA-5000 furnace with an infrared lamp using a $100^\circ\text{C}/\text{minute}$ ramp rate; with this procedure a flat MgO surface was achieved, as confirmed by RHEED. Once the substrates were loaded into the MBE, they were further outgassed in UHV at 250°C to remove any water molecules adsorbed by the surface and restore good epitaxial order. It was observed that annealing the substrates at higher temperatures ($> 400^\circ\text{C}$) in vacuum (i.e. in the absence of oxygen) prior to growth subsequently led to films with poorer crystallinity. This can possibly be attributed to the segregation of Mg to the surface of the substrate (whose onset occurs around 670K) which changes its morphology [And97]. All the films were grown at pressures of $< 1.5 \times 10^{-8}$ mbar and rates of $\approx 5\text{-}6 \text{ \AA}/\text{min}$. The predominant gas detected during growth, upon rising the temperature of the sources, was H_2 , with a partial pressure of $\approx 1 \times 10^{-8}$ mbar. A small amount of N_2 was also detected but with a much lower partial pressure below 1×10^{-9} mbar. To optimize the chemical composition of the films, a first set of 25 nm-thick CFS films were grown fixing the Fe and Co rates to the optimal values found in § 5.2, and varying the concentration of Si (that is, following the same procedure as in Chapter 5).

The XRR measurements for the first set of CFS/MgO(001) samples are shown in Fig. 6.1a, for Si rates corresponding to $T_{\text{Si}} = 1035^\circ\text{C}, 1040^\circ\text{C}, 1045^\circ\text{C}$ and 1050°C . This is the range of evaporation temperatures within which the optimal Si evaporation rate ($T_{\text{Si}} = 1045 \pm 5^\circ\text{C}$) was found for the CFS films grown on Si in the previous chapter; hence, one expects this to be close to the optimal T_{Si} value for CFS/MgO(001) as well. Nevertheless, it is worth to go through this procedure again, albeit in less detail, for a few reasons. First, even if the Si rates were the same, the sticking coefficient, eq. (3.7), depends on the growth surface and thus, different substrates might require different evaporation rates to achieve the same film stoichiometry. Although this is also true for Fe and Co, the concentration of these two elements in the film can be easily compared to those found in the CFS/Si(111) samples doing quick planar SEM-EDS measurements. However, this was obviously not feasible for Si due to its presence in the substrate for the films grown on Si. Second, because out-diffusion of Si is expected in CFS/Si, the Si rates required in the case of MgO might be slightly reduced.

The reflectivity curves were fitted to the structural model in Fig. 6.1d and the resulting fits are the red lines displayed in Fig. 6.1a. Once again, the CoFe_2O_4 oxide capping layer was

included in the model. This time, though, the silicide phase at the bottom interface (refer to Fig. 5.7d) was omitted because no lower density phases originating from out-diffusion are expected to form on MgO at low growth temperatures. The density of the capping layer and the substrate were set to $\rho_{\text{CoFe}_2\text{O}_4} = 0.0137 \text{ f.u./\AA}^3$ and $\rho_{\text{MgO}} = 0.054 \text{ f.u./\AA}^3$ respectively, according to the values found in literature. Although many different oxide compounds can be expected from the oxidation of CFS, an oxide containing Co was chosen because this is the most abundant element in CFS. Also, note that CoFe_2O_4 has a very similar density and scattering factor to other well-known common oxides such as Co_3O_4 and Fe_3O_4 . Hence, all these oxides give the same results when fitting the XRR curves, which gave low FOM values for both CFS/Si(111) and CFS/MgO(001). The density of the CFS layer was introduced as a fit parameter to account for the variation of the Si content among the films, and was allowed to vary by 18% from its bulk stoichiometric value, $\rho_{\text{CFS}} = 0.0222 \text{ f.u./\AA}^3$ (i.e. from 0.018 to 0.027 f.u./ \AA^3). This model is able to represent the data accurately with FOM values < 0.1 . The standard GenX log FOM function was used to optimize the fit, see [Gen] for a more detailed description of the fitting procedure.

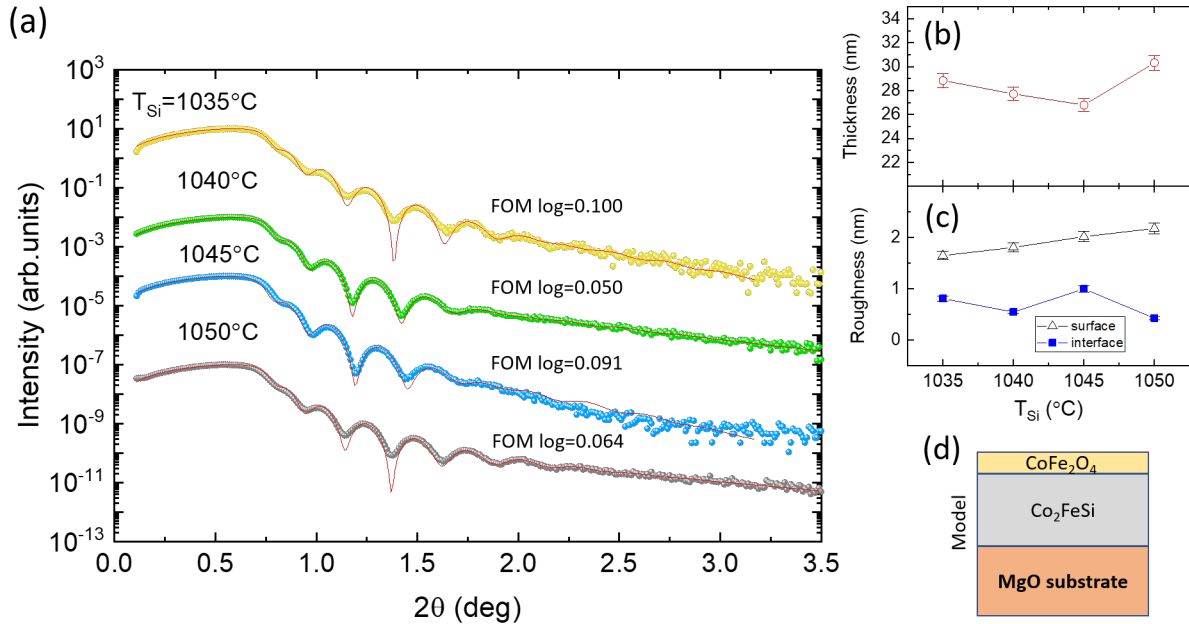


Figure 6.1: (a) XRR measurements on the CFS/MgO(001) samples for $T_{\text{Si}} = 1035^\circ\text{C}$ (yellow), $T_{\text{Si}} = 1040^\circ\text{C}$ (green), $T_{\text{Si}} = 1045^\circ\text{C}$ (blue) and $T_{\text{Si}} = 1050^\circ\text{C}$ (grey), and the corresponding fits in red; (b) thickness of the CFS layers extracted from the GenX fits in (a); (c) roughness of the oxide layer (i.e. the surface) (black triangles) and roughness of the bottom CFS/MgO interface (blue squares); (d) 2-layer model to which the data was fitted.

The values extracted for the thickness of the CFS layers and the roughness of the top and

bottom interfaces have been plotted in Figs. 6.1b and c respectively. The thickness of CFS oscillates between 27 ± 1 nm and 30 ± 1 nm, i.e. between 8% and 20%-off the nominal value, which is once again due to errors related to the QCM. The roughness of the top surface and the bottom CFS/MgO interface have been represented in Fig. 6.1c as black triangles and blue squares respectively. As can be seen, the surface roughness increases monotonically with T_{Si} from 1.65 ± 0.08 nm to 2.2 ± 0.1 nm. The surface is approximately 15% rougher than that of the CFS films grown on Si(111), whose roughness was $\approx 1.5 \pm 0.2$ nm (refer to Fig. 5.7c). The increased surface roughness seems at least partially a consequence of the increased roughness at the CFS/MgO interface, which in the case of MgO does not fall below 0.4 nm regardless of T_{Si} . Such interfacial roughness is indeed the responsible for the lack of Kiessig fringes above $2\theta \approx 2^\circ$ for CFS/MgO(001).

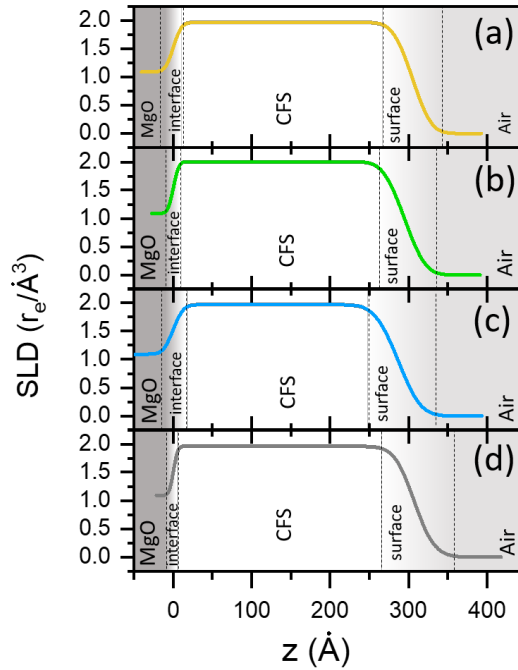


Figure 6.2: X-ray scattering length density profile of CFS/MgO(001) for $T_{Si} = 1035^\circ\text{C}$ (a), $T_{Si} = 1040^\circ\text{C}$ (b), $T_{Si} = 1045^\circ\text{C}$ (c) and $T_{Si} = 1050^\circ\text{C}$ (d). The greyed areas define bulk-like MgO and air regions, whereas the gradient areas represent the CFS/MgO interface and the air/CFS surface.

In order to compare more easily the structural parameters obtained by fitting the XRR data, the profiles of the x-ray scattering length density (SLD) with depth (that is, with thickness) have been illustrated in Fig. 6.2. The SLD is a combination of the density and the sum of the atomic scattering factors for each element in the layer (which in turn, is related to the

refractive index), where the interfaces are modelled according to the corresponding roughness representation. Thus, the Kiessig fringes change if the SLD is modified. In GenX, a built-in SLD simulation tool is used. For instance, in Fig. 6.2 one can see that the rougher CFS/MgO interfaces at $T_{Si} = 1035^\circ\text{C}$ and 1045°C , result in longer tails at the *interface* region in Figs. 6.2a and c in comparison to $T_{Si} = 1040^\circ\text{C}$ (Fig. 6.2b) and 1050°C (Fig. 6.2d).

To conclude the XRR analysis, in Fig. 6.3, the density of the CFS layers as a function of T_{Si} has been illustrated. The thick grey dashed line represents the densities of the CFS films for the CFS/Si(111) samples (Fig. 5.8) shown for comparison. The density in the CFS/MgO(001) samples is constant within error and their values just overlap with those found for CFS/Si(111). The values obtained for the density agree with the theoretical value of $\rho_{\text{CFS}} = 0.222 \text{ f.u./\AA}^3$ for CFS (black dotted line in Fig. 6.3). Therefore, no correlation could be found between the chemical composition of the films and the densities measured with XRR.

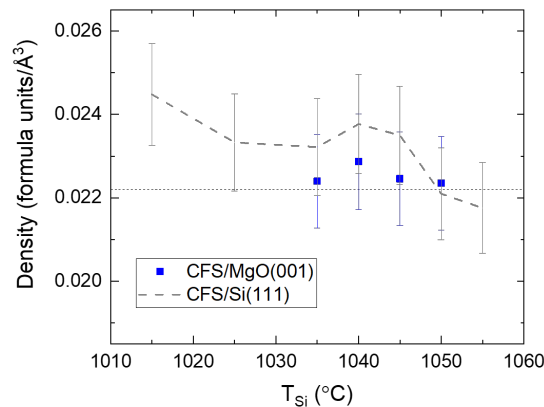


Figure 6.3: Density of the CFS layers extracted from the fits in Fig. 6.1a versus T_{Si} for the CFS/MgO(001) samples (blue squares) and the CFS/Si(111) samples (grey dashed line).

The symmetric $2\theta - \omega$ scans for the CFS/MgO(001) samples are shown in Fig. 6.4 for $T_{Si} = 1035^\circ\text{C}$ (yellow), $T_{Si} = 1040^\circ\text{C}$ (green), $T_{Si} = 1045^\circ\text{C}$ (blue) and $T_{Si} = 1050^\circ\text{C}$ (grey). In all the films the CFS(004) reflection is observed at $2\theta \approx 66^\circ$, together with the MgO(002) substrate peak at $2\theta \approx 42.5^\circ$. Hence, as expected, the CFS layers grow along the out-of-plane [001] direction. Looking back at Tab. 5.2 of allowed reflections for CFS, the CFS(004) is a fundamental reflection and although it is present in all the films, it is clearly much weaker in the sample with the lowest Si concentration ($T_{Si} = 1035^\circ\text{C}$), which is translated into the lowest integrated intensity A_{004} (see Fig. 6.6c). The CFS(002) peak is seen in samples $T_{Si} = 1040^\circ\text{C}$ to $T_{Si} = 1050^\circ\text{C}$ and is characteristic of the B2 and the $L2_1$ structure. The intensity of these peaks are weaker than those measured for CFS/Si(111) because the multiplicity of the ($h00$)

reflections (which have a multiplicity of 6) is lower than that of the (hhh) reflections (which have a multiplicity of 8).

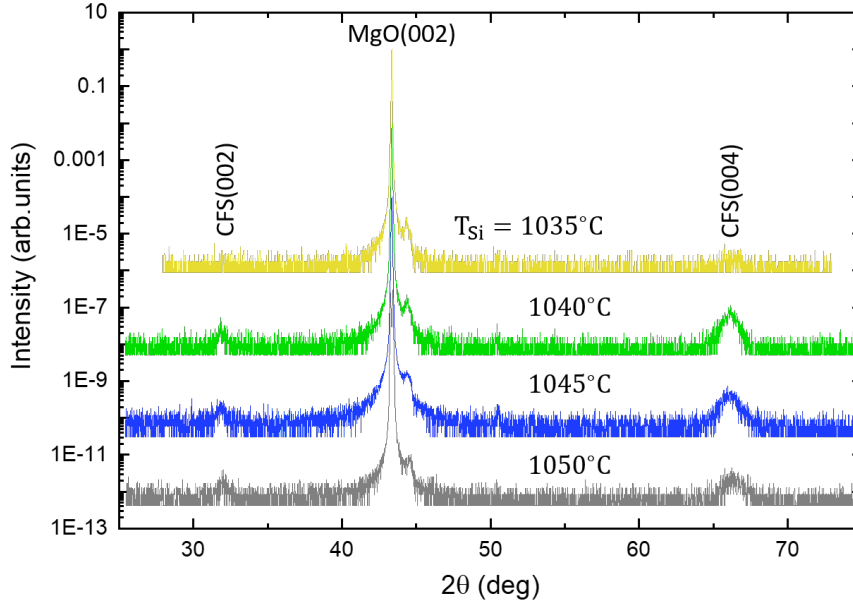


Figure 6.4: $2\theta-\omega$ measurements for $T_{Si} = 1035^\circ\text{C}$ (yellow), $T_{Si} = 1040^\circ\text{C}$ (green), $T_{Si} = 1045^\circ\text{C}$ (blue) and $T_{Si} = 1050^\circ\text{C}$ (grey), aligned to MgO(002).

No trace of the CFS(111) superlattice reflection was measured for any of these films grown at $< 130^\circ\text{C}$, so there is no indication of the presence of $L2_1$ ordering. The CFS(002) peak was therefore mainly attributed to the B2 phase. In order to quantify the degree of B2 ordering in these samples, the diffraction patterns were analysed as in Chapter 5. The raw intensities were first normalized to the intensity of the substrate, MgO(002) in this case, and the background offset was subtracted. The diffraction peaks were then fitted to a Voigt distribution in linear scale with the following fit parameters: $2\theta_0$ (the position of the peak), Δ_G (the Gaussian linewidth), Δ_L (the Lorentzian linewidth), y_0 (the intensity offset) and A_{hkl} (the integrated intensity). The fits are shown in Figures 6.5a-d and Figs. 6.5e-h for CFS(004) and CFS(002) respectively for the various Si rates.

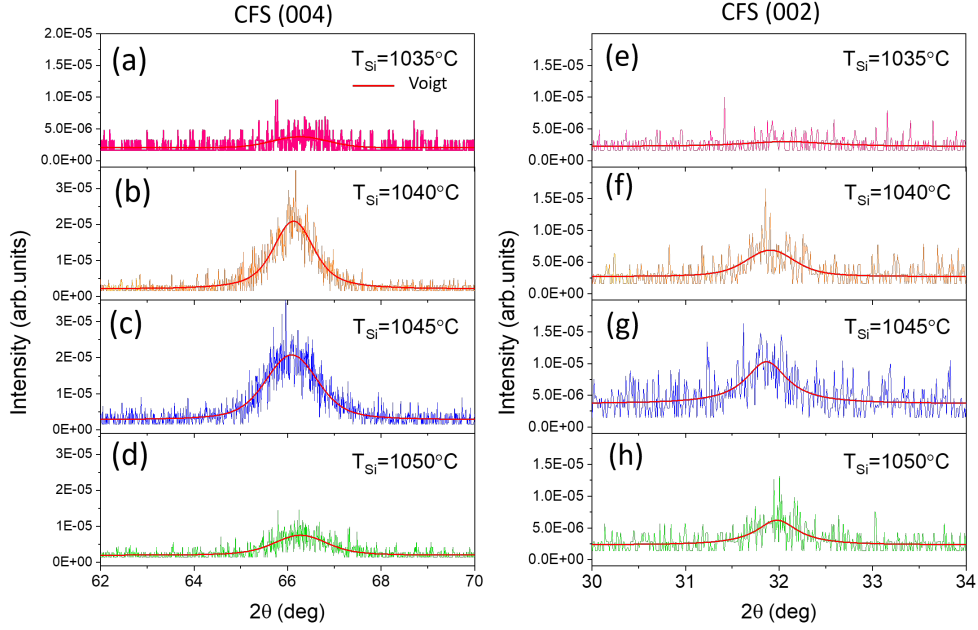


Figure 6.5: Voigt fits of: (a-d) the CFS(004) peak, and (e-h) the CFS(002) peak for $T_{Si} = 1035^{\circ}\text{C}$ (pink), $T_{Si} = 1040^{\circ}\text{C}$ (orange), $T_{Si} = 1045^{\circ}\text{C}$ (blue) and $T_{Si} = 1050^{\circ}\text{C}$ (green).

The integrated intensities extracted from those fits are shown in Fig. 6.6a for the CFS(002) peak (blue) and the CFS(004) peak (red). The integrated intensities of both reflections follow a very similar trend and reach their maximum value at $T_{Si} = 1045^{\circ}\text{C}$. This agrees with our initial estimations for the optimal evaporation rate of Si. The absence of the CFS(111) reflection together with spottier patterns in RHEED and the larger interfacial roughness measured by XRR, suggests that the growth of CFS on MgO(001) is more challenging than on the Si(111) surface. This is possibly because the lattice mismatch between CFS and MgO is larger than with Si; and because the out-diffusion of Si atoms from the substrate in CFS/Si(111) can help the formation of buffer layers (such as the aforementioned CoSi_2) that reduce the strain at the interface. However, the intensities of the XRD peaks between the (001) and (111)-oriented CFS films are not directly comparable because of their different multiplicity. The Lorentzian linewidth of the CFS(002) superlattice reflection is shown in Fig. 6.6c. The values measured for 1040°C and 1045°C are $0.5 \pm 0.1^{\circ}$ and $0.6 \pm 0.1^{\circ}$ respectively, bigger than those measured for the CFS/Si(111) samples (refer to Fig. 5.11), pointing once more to a lower crystallinity. However, one needs to be careful because in this geometry, peak width also depends on film thickness. Obtaining a value for $\Delta_L^{(002)}$ with reasonable error bars for $T_{Si} = 1035^{\circ}\text{C}$ and $T_{Si} = 1050^{\circ}\text{C}$, was however impossible due to the low intensity of these peaks. Hence, one cannot comment on the dependence of peak width with the Si concentration in the film.

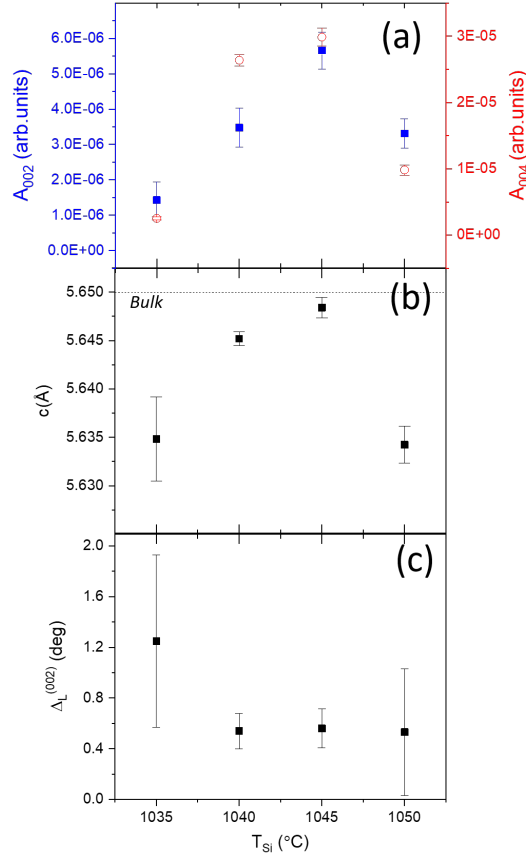


Figure 6.6: (a) Integrated intensities extracted from the Voigt fits in Fig. 6.5 for CFS(002) (blue squares) and CFS(004) (red circles); (b) out-of plane lattice constants extracted from the CFS(004) reflection; and (c) Lorentzian width of CFS(002).

The out of plane lattice constant, $c = d_{004}$ for these films is shown in Fig. 6.6b. In this case the lattice parameter increases for medium temperatures, 1040°C and 1045°C (where the measured value matches to the one found in literature) and drops at 1035°C and 1050°C. In CFS/Si(111) samples the trend was clear, showing how the lattice shrinks in Si-rich samples. Hence, one would expect to observe once more a decrease in the unstrained lattice constant as T_{Si} increases, which is not the case. The reason for such discrepancy most likely arises from a wrong interpretation of the chemical composition as revealed by the planar SEM-EDS measurements summarized in Tab. 6.1. Several EDS spectra were taken at different areas in the film with the JEOL-7800F microscope at 15kV; the elemental compositions retrieved from the AZtecLive software for each spectrum were then averaged. This average and its standard error are the numbers shown in the table. Although the absolute numbers measured with EDS may be subjected to errors from the quantitative analysis § 4.2.4, it serves for comparison between samples. As one can see, the at% of Si in samples $T_{Si} = 1035^\circ\text{C}$ and $T_{Si} = 1050^\circ\text{C}$ are constant

within error, hence the same lattice constant measured in XRD. This means that the Si rates at $T_{Si} = 1035^\circ\text{C}$ are actually bigger than the expected. This was attributed to instability of the Si flux in this sample. As Si is grown, the Si filament (§ 3.5.2) gets thinner and the evaporation rates for a given T_{Si} increase. If the filament is new, the rates are mostly constant from growth to growth and calibrating the fluxes every ≈ 10 growths is sufficient. However, when the Si filament gets closer to the end of its life, the Si flux starts becoming more unstable and the rates can suffer significant changes between two subsequent growths. This is precisely what happened for sample $T_{Si} = 1035^\circ\text{C}$ and the Si filament was indeed replaced shortly after.

$T_{Si}(\text{°C})$	at% of Co	at% of Fe	at% of Si
1035	45 ± 2	25.4 ± 0.3	29 ± 1
1045	47 ± 2	26.0 ± 0.5	27.2 ± 0.8
1050	46 ± 1	24.2 ± 0.3	30 ± 1

Table 6.1: Co Fe and Si concentrations in at% measured by EDS in the CFS/MgO(001) samples for different T_{Si} .

Also, note how the seemingly small compositional changes measured with the EDS (at $T_{Si} = 1035^\circ\text{C}$, the at% of Co and the at% of Si are 4% and 8%-off their values measured for $T_{Si} = 1045^\circ\text{C}$), have a great impact on the crystallinity of the films as per Figs. 6.5 and 6.6; and hence the importance of achieving the exact chemical composition in Co_2FeSi films. The lattice constant is closer to that of bulk CFS at $T_{Si} = 1045^\circ\text{C}$, where the at% of Si measured by EDS is also the closest to the stoichiometric value of 25%. Therefore, the key message of this section is that $T_{Si} = 1045^\circ\text{C}$ gives the best quality CFS/MgO(001) film.

6.3 MBE growth of CFS films at different growth temperatures

Contrary to CFS/Si(111), achieving some degree of $L2_1$ ordering at low temperatures ($< 130^\circ\text{C}$) for CFS films grown on MgO(001) has proven to be difficult, possibly due to a larger strain at the interface between the two lattices. Hence, to further promote structural ordering, two more samples were grown fixing the Si rate at 1045°C and increasing the growth temperature to 350°C and 550°C . In this section, the results on these two samples will be shown and compared to a CFS/MgO(001) film grown at $T_B < 130^\circ\text{C}$. Here, T_B is the temperature of the sample stage measured with the K-type thermocouple. From now on, the sample grown at $T_B < 130^\circ\text{C}$

will also be refer to as grown at "RT" because the sample stage was not purposefully heated in this case. As explained earlier, the temperature of the substrate inevitably rises during growth due to the radiation from the sources. In all the plots shown here, this sample corresponds to $T_B = 120^\circ\text{C}$ because this was the highest temperature recorded during its growth, but keep in mind that the temperature of the stage at the beginning of the evaporation was $\approx 70^\circ\text{C}$. The two high temperature films were grown at $< 3 \times 10^{-8}$ mbar and with a growth rate of $\approx 5 \text{ \AA}/\text{min}$. At this growth rate, 25 nm-thick layers were obtained after 45-50 minutes of deposition under annealing conditions. The MgO surfaces were prepared following the same cleaning procedure in § 6.2.

6.3.1 Structural characterization of CFS/MgO(001) grown at different temperatures

RHEED patterns were acquired in-situ before and after the growth of the CFS films. In Fig. 6.7a the RHEED image of one of the cleaned substrates is shown, taken with the e-beam along [010]. The three main (00), (0-1) and (01) streaks are observed along with the X-like feature formed by the Kikuchi lines which arise from diffuse scattering processes. The sharp streaks are indicative of a flat surface which favours subsequent epitaxial growth.

The RHEED patterns taken after the growth of a 25nm-thick CFS layer are shown in Figs. 6.7b, c and d for $T_B < 130^\circ\text{C}$, $T_B = 350^\circ\text{C}$, and $T_B = 550^\circ\text{C}$ respectively. The film grown at RT (Fig. 6.7b) displays a spotty pattern indicative of a 3D film growth (refer to Fig. 3.22 for the depiction of the distinctive features of a RHEED pattern). As the growth temperature is increased, Fig. 6.7c, the spots become sharper and new features start appearing between the original rows of spots. At $T_B = 550^\circ\text{C}$ (Fig. 6.7c), the spots are sharp and weak streaks are visible suggesting an improvement of the crystallinity of the film. However, the lack of broader streaks (such as the ones observed for CFS/Si(111) in Fig. 5.3) points to a relatively rough surface.

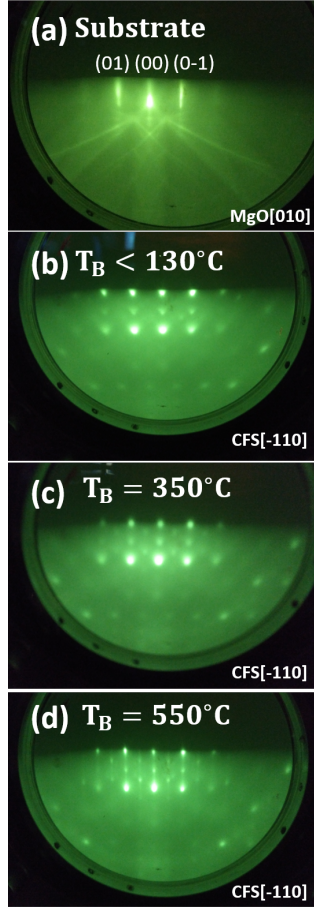


Figure 6.7: RHEED images for: (a) the MgO(001) surface along the $[010]$ direction before the growth at RT of CFS; the CFS(001) surface after the growth at (b) $T_B < 130^\circ\text{C}$, (c) $T_B = 350^\circ\text{C}$ and (d) $T_B = 550^\circ\text{C}$ along the $[\bar{1}10]$ azimuth.

6.3.1.1 X-Ray diffraction and reflectivity measurements

The XRR scans for CFS/MgO(001) grown at different temperatures are shown in Fig. 6.8a. The data was fitted to the same model as in section § 6.2 (Fig. 6.8d) and the thickness of the CFS layers and the roughness of the top and bottom interfaces were similarly extracted. These have been plotted in Figs. 6.8b and c respectively. As can be observed, the thickness of the CFS films does not change between samples (27 ± 1 nm, 28 ± 1 nm and 28 ± 1 nm for $T_B = \text{RT}$, 350°C and 550°C respectively). The surface roughness (the black triangles in Fig. 6.8c) however, increases with the growth temperature. At a substrate temperature of $T_B < 130^\circ\text{C}$, a roughness of 1.9 ± 0.1 nm was measured in agreement with the RT-grown samples in § 6.2. However, as T_B is increased, the roughness also increases to 2.4 ± 0.1 nm at $T_B = 350^\circ\text{C}$ and 2.8 ± 0.1 nm at $T_B = 550^\circ\text{C}$. Such increase in surface roughness with the substrate temperature was also observed by Mohankumar *et al.* for Co_2FeSi films deposited via DC magnetron sputtering on Si(111) and MgO(001) [MRK17]. In our case, the roughness of the

CFS/MgO interface is constant for the three films and so, rougher films at higher T_B might be related to a change in the grain size of the films due to the change of the interfacial reactions of the substrate atoms with CFS.

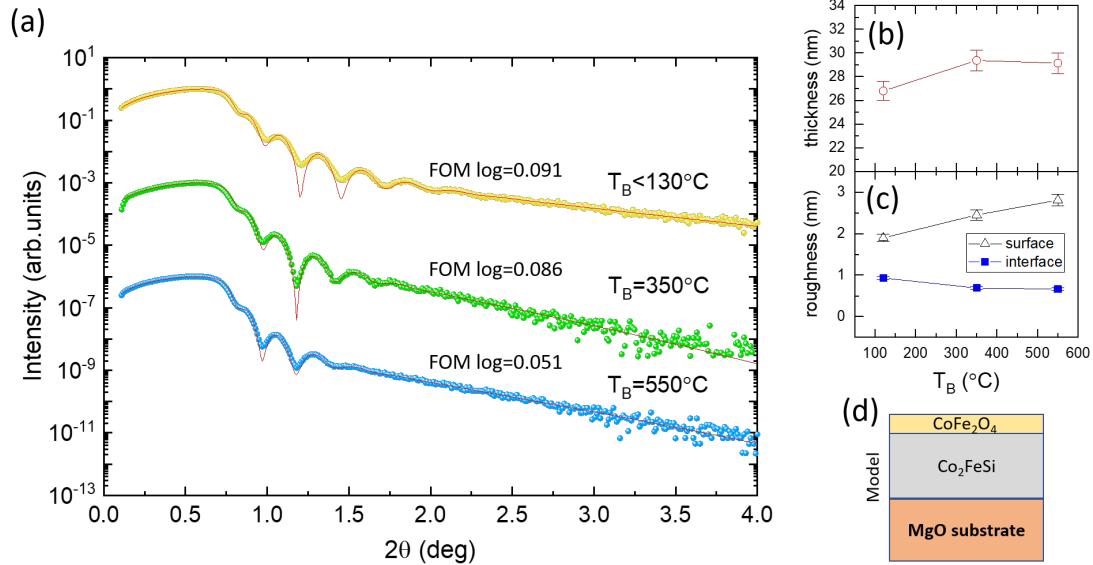


Figure 6.8: (a) XRR scans for the CFS/MgO(001) samples grown at RT (yellow), $T_B = 350^\circ\text{C}$ (green) and $T_B = 550^\circ\text{C}$ (blue); (b) thickness of the CFS layers extracted from the fits to the XRR curves; (c) roughness of the surface (black triangles) and the CFS/MgO interface (blue squares); (d) 2-layer model used to fit the data with GenX.

A comparison of the SLD extracted from the three XRR fits in Fig. 6.8a is shown in Fig. 6.9. The dark grey region corresponds to MgO and the light grey region to air, whereas the gradient regions correspond to the bottom CFS/MgO interface and the top air/CoFe₂O₄ surface. No big differences can be observed among the three films grown at different temperatures. The tail at the top surface region is expected from the oxidation of the surface. On the contrary, the CFS/MgO interface is quite sharp, which seems to rule out the presence of secondary interfacial phases or mixing regardless of the growth temperature. XRR fitting can however be an art and greatly depends on making the correct assumptions when constructing the model. Thus, the deductions about the CFS/MgO interface have to be backed up with other experimental techniques such as electron microscopy.

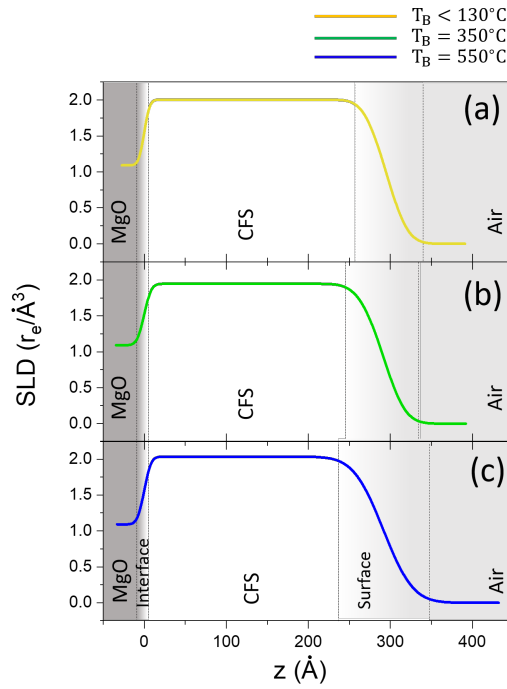


Figure 6.9: X-ray scattering length density profile of CFS/MgO(001) grown at (a) $T_B < 130^\circ\text{C}$, (b) $T_B = 350^\circ\text{C}$ and (c) $T_B = 550^\circ\text{C}$. The greyed areas define bulk-like MgO and air regions, and the gradient areas represent the CFS/MgO interface and the air/CoFe₂O₄ surface.

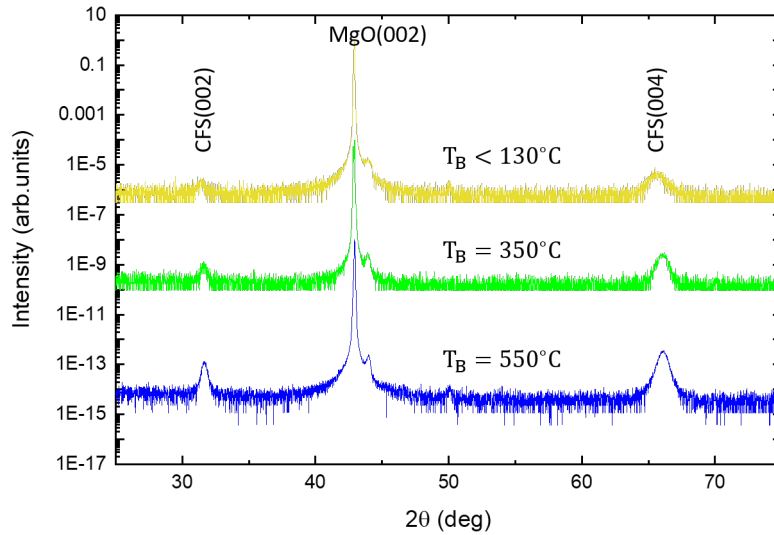


Figure 6.10: Out-of-plane $2\theta - \omega$ scans for $T_B < 130^\circ\text{C}$ (yellow), $T_B = 350^\circ\text{C}$ (green) and $T_B = 550^\circ\text{C}$ (blue).

The $2\theta - \omega$ scans for these samples are shown in Fig. 6.10, revealing the CFS(002) and the CFS(004) diffraction peaks observed previously while no secondary phases could be detected.

Clearly, without the need of any quantitative analysis, one can already see that the intensity of both reflections increases with growth temperature. The Voigt fits are shown in Fig. 6.11a for CFS(002) and Fig. 6.11b for CFS(004).

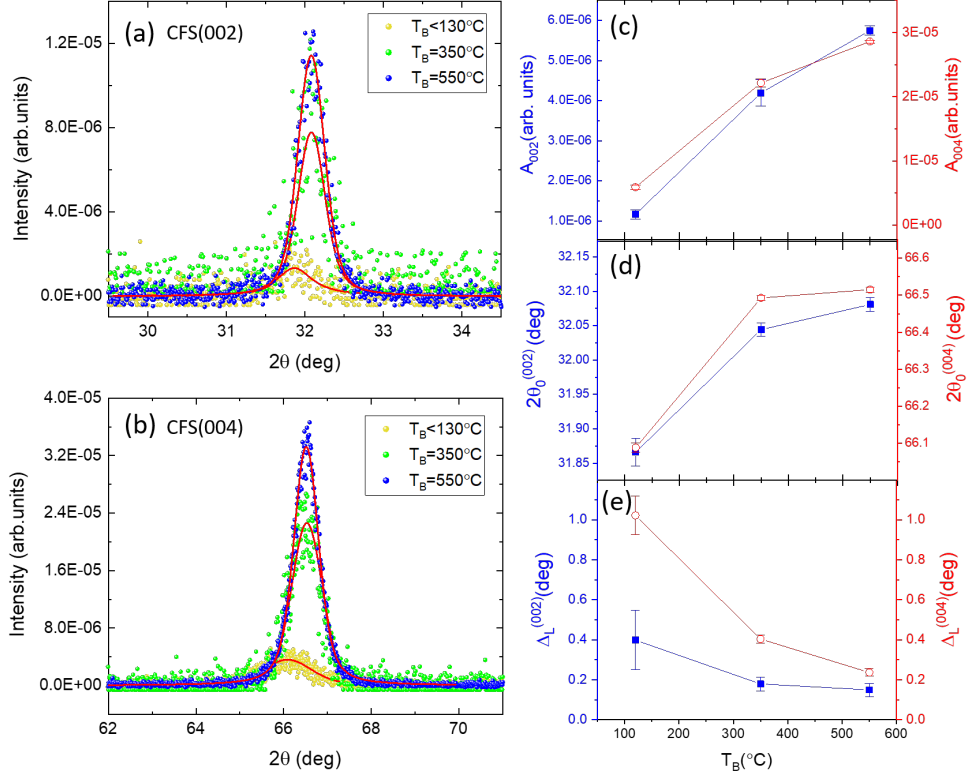


Figure 6.11: (a) CFS(002) and (b) CFS(004) diffraction peaks and the corresponding Voigt fits for the three growth temperatures using the same colour coding in Fig. 6.10; integrated intensities (c), peak positions (d), and Lorentzian linewidth for CFS(002) (blue squares) and CFS(004) (red circles) respectively.

The integrated intensities (A_{hkl}) extracted from the fits can be seen in Fig. 6.11c. A_{004} increases from $5.9 \pm 0.4 \times 10^{-6}$ at RT to $28.6 \pm 0.3 \times 10^{-6}$ at $T_B = 550^\circ\text{C}$. The integrated intensity of the (002) reflection also increases a fivefold from $1.2 \pm 0.1 \times 10^{-6}$ at RT to $5.7 \pm 0.1 \times 10^{-6}$ at $T_B = 550^\circ\text{C}$, indicating improved B2 ordering. This occurs along with a reduction of the peak width of the fundamental and superlattice reflections, Fig. 6.11e, which confirms the improvement of the structure of the film with T_B . A lattice parameter of $5.648 \pm 0.002 \text{ \AA}$ for the RT film is obtained from the diffraction data, consistent with that reported previously for CFS. In addition, the position of the peak ($2\theta_0$) can be seen to move to higher angles with growth temperature corresponding to a reduction in the lattice constant. The ratio of the relative intensities (A_{002}/A_{004}) which is, as was explained in the previous chapter, a measure of

the degree of B2 ordering of CFS, is constant within error for the three films with a value of $A_{002}/A_{004} = 0.20 \pm 0.02$.

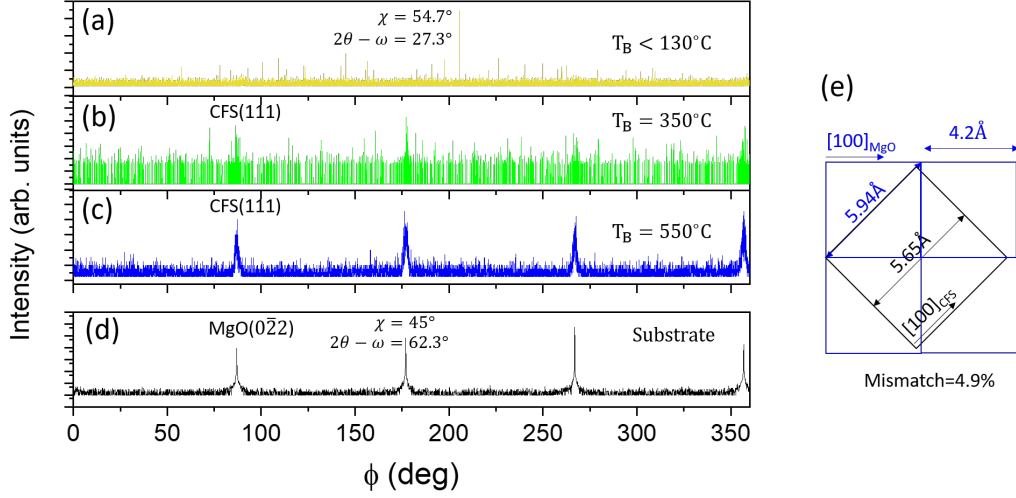


Figure 6.12: ϕ scans aligned to CFS(111) for $T_B < 130^\circ\text{C}$ (a), $T_B = 350^\circ\text{C}$ (b) and $T_B = 550^\circ\text{C}$ (c) revealing an enhancement of the $L2_1$ ordering in (b) and (c); (d) ϕ scan aligned to MgO($0\bar{2}2$) verifying the CFS($1\bar{1}0$)||MgO(100) epitaxial relationship; and (e) illustration of the 45° rotation of the film with respect to the substrate, with a mismatch between the lattice constant of CFS (5.65\AA) and the diagonal length of the lattice constant of MgO ($\sqrt{2} \times 4.2\text{ nm} = 5.9\text{\AA}$) of $\approx 5\%$.

Finally, the goniometer was tilted to $\chi = 54.7^\circ$ and the x-ray source and detector were oriented to fulfil the Bragg conditions for the CFS(111) reflection at $2\theta = 27.32^\circ$. In this geometry, ϕ scans were performed for $T_B < 130^\circ\text{C}$ (Fig. 6.12a), $T_B = 350^\circ\text{C}$ (Fig. 6.12b) and $T_B = 550^\circ\text{C}$ (Fig. 6.12c). At $T_B < 130^\circ\text{C}$ no diffraction peaks are observed, that is, no indication of $L2_1$ ordering was found for the film grown at low temperature, as it occurred for all the CFS/MgO samples in § 6.2. For growth temperatures $\geq 350^\circ\text{C}$, the 4 peaks are found at $\phi \approx 90^\circ, 180^\circ, 270^\circ$ and 360° . The 4-fold symmetry is characteristic of the (001) texture and demonstrates epitaxial growth of the CFS films on the MgO substrate. The $L2_1$ ordering peaks are weak for $T_B = 350^\circ\text{C}$ and their presence becomes evident at 550°C , demonstrating the improvement of the $L2_1$ ordering as the substrate temperature increases. In Fig. 6.12d, the ϕ scan was taken with the diffraction conditions tuned to the MgO($0\bar{2}2$) peak. The 4 peaks appear at the same ϕ angles as the CFS(111) reflections above and hence, reveals the following epitaxial relationship between the films and the substrate: CFS($1\bar{1}0$)||MgO(100) and CFS(001)||MgO(001). That is, as expected, the film is rotated in-plane by 45° . This ro-

tation between the two lattices has been schematically represented in Fig. 6.12e. An additional $2\theta - \omega$ scan was also performed aligning the sample to CFS(111) at $\chi = 54.7^\circ$ and $\phi = 90^\circ$, which is shown in Fig. 6.13 for $T_B = 350^\circ\text{C}$. The presence of the fully-ordered phase in this sample is confirmed by the CFS(111) and CFS(222) reflections revealed in the scan. However, the intensity of the (111) peak cannot be compared with the CFS/Si(111) superlattice reflection either, because the diffraction conditions are different in these two orientations.

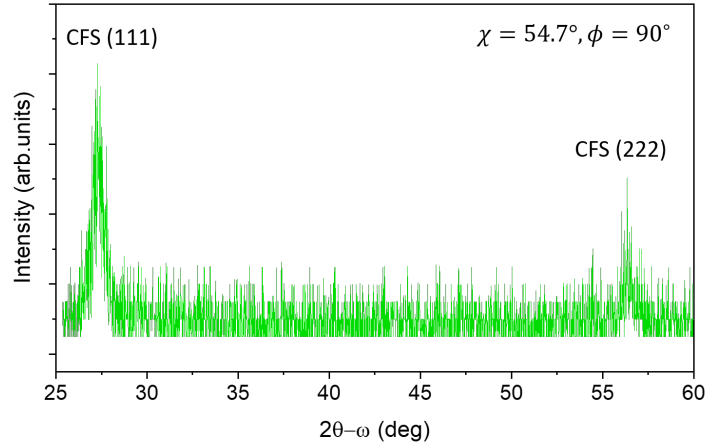


Figure 6.13: $2\theta - \omega$ scan aligned to CFS(111) for $T_B = 350^\circ\text{C}$.

6.3.1.2 Cross-sectional TEM and STEM measurements

A cross-sectional specimen was prepared for $T_B = 350^\circ\text{C}$. The specimen was lifted-out following the FIB technique detailed in § 4.2.5.2 with the $[\bar{1}\bar{1}0]$ direction of CFS along the thickness of the lamella (that is, the lamella was cut with the long edge aligned to one of the edges of the MgO substrate). The sample had been previously capped with a 10 nm-thick $\text{Pt}_{80}\text{Pd}_{20}$ conductive layer, sputtered with a Cressington sputter coater. The images shown in this section were taken at 200kV with the JEOL-2200FS microscope equipped with imaging and probe aberration correctors.

Fig. 6.14a shows a $200k\times$ magnification image of the specimen. The CFS film is granular and displays grains that are 15-20 nm wide in the $[\bar{1}\bar{1}0]$ direction throughout the entire lamella. These grains are larger than those observed for the CFS/Si(111) specimen in Fig. 5.12b and correlates with the smaller FWHM and Δ_L of the superlattice peak measured for the CFS/MgO film with XRD. The CFS layer shows an overall roughness of ≈ 3 nm, close to the surface roughness of 2.5 ± 0.1 nm obtained from the XRR measurements (see Fig. 6.8c) and ≈ 2 nm larger than the roughness shown by the cross-sectional CFS/Si(111) specimens. The rougher CFS/MgO films could, as mentioned before, be due to the larger lattice mismatch between

the film and the substrate, which might also be related to changes in the grain size. The MgO surface, though flat, seems somewhat rougher in comparison to Si which means that the cleaning procedure for MgO might still be improved, although it could also be an artefact from the specimen preparation process. Fig. 6.14b displays a higher magnification HRTEM image of the CFS/MgO interface for the same specimen. One can see that the CFS is crystalline but the lamella is still too thick to be able to resolve the atomic columns in HAADF-imaging. Thus, the specimen needs to be further thinned by Ar ion milling. In any case, this is not an obstacle to do diffraction measurements with 4D-STEM which are currently in process to quantify the structural ordering of the film in the same way as with CFS/Si(111).

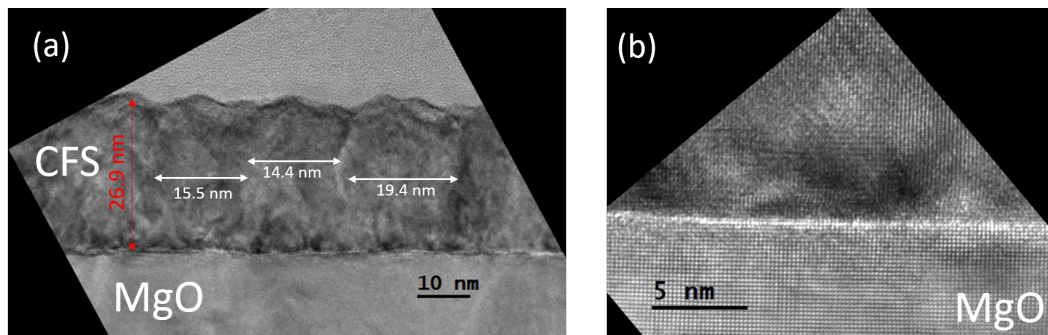


Figure 6.14: (a) TEM image of the CFS/MgO(001) specimen grown at $T_B = 350^\circ\text{C}$ and (b) CFS/MgO interface of the same specimen.

Two FFTs have been taken in Fig. 6.15a from an area within the film and an area within the substrate, which can be seen in Figs. 6.15b and c respectively. The FFT in Fig. 6.15b clearly matches the diffraction pattern of the fully-ordered CFS structure, shown in Fig. 6.15d as a reference. All the diffraction spots characteristic of the $L2_1$ structure have been captured by the FFT, in particular the 111 spot which is exclusive of the $L2_1$ phase and is absent in all the disordered phases, as well as the CFS 002 and 220 spots. All the low-index spots have been labelled in the figure. This is enough to prove that the CFS film grown at 350°C is partially $L2_1$ ordered, as was also observed in the XRD measurements. The XRD and STEM measurements combined, point clearly to a mixed $L2_1/B2$ structure where some of the crystallographic grains in Fig. 6.14 are arranged in a B2 structure, whereas others have an $L2_1$ structure. The DP motifs have been labelled with the red rectangle for the film and yellow solid square for the MgO substrate. The MgO DP is also the expected for a single-crystal MgO taken along the $\langle 100 \rangle$ zone axis. Taken into account the growth direction, this confirms the epitaxial relationship deduced from XRD, namely: $\text{CFS}(1\bar{1}0) \parallel \text{MgO}(100)$ and $\text{CFS}(001) \parallel \text{MgO}(001)$.

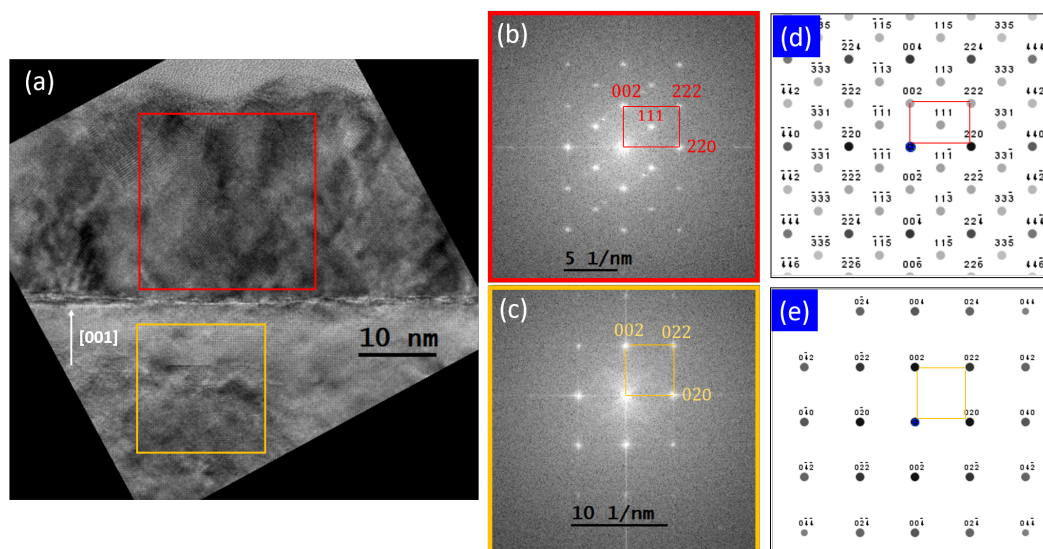


Figure 6.15: (a) TEM image of the CFS/MgO(001) film for $T_B = 350^\circ\text{C}$; (b) and (c) FFTs of the images enclosed by the red square (film) and yellow square (substrate) respectively; and (d) and (e) simulated diffraction patterns for CFS[1-10] and MgO[100] respectively.

Finally, the EDS maps shown in Fig. 6.16 demonstrate that there is no mixing between the film and the substrate at $T_B = 350^\circ\text{C}$, and give an overall composition of: $\text{at}\% \text{Co} = 47 \pm 7$, $\text{at}\% \text{Fe} = 29 \pm 5$ and $\text{at}\% \text{Si} = 24 \pm 5$. The errors for the chemical composition in this measurement are however too large to discuss the stoichiometry of this film. The reason for such big errors could arise from compositional variations throughout the film and hence, local chemical analysis might be required. Cross-sectional specimens for the low temperature and the 550°C sample are being prepared for a full characterisation of the three samples.

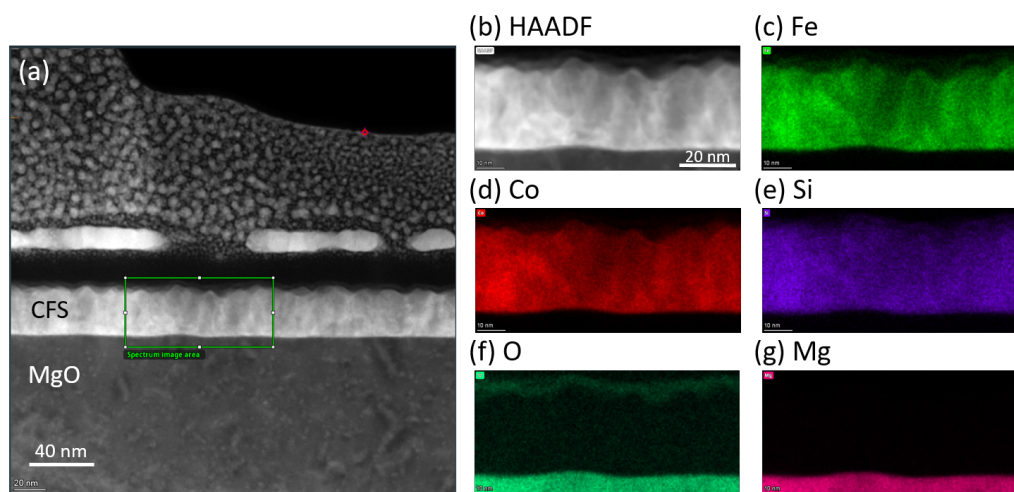


Figure 6.16: (a) Specimen overview; and (c)-(g) EDS net intensity maps, after background subtraction of the scan area in (b).

6.3.2 Magnetic characterization of CFS/MgO(001) grown at different temperatures

6.3.2.1 VSM measurements

The magnetic hysteresis loops taken with the in-plane magnetic field applied along the [010] direction of MgO (that is, along the $[\bar{1}10]$ crystallographic orientation of CFS) are displayed in Figs. 6.17a, b and c for $T_B < 130^\circ\text{C}$, $T_B = 350^\circ\text{C}$ and $T_B = 550^\circ\text{C}$ respectively. The loops have the shape of a HA, in accordance with the FMR measurements in § 6.3.2.2. Unfortunately, due to some technical difficulties, the hysteresis loops along the EA (which as will be shown in § 6.3.2.2 lies along the [010] direction of CFS) were not measured. The measurements along the EA are currently on their way.

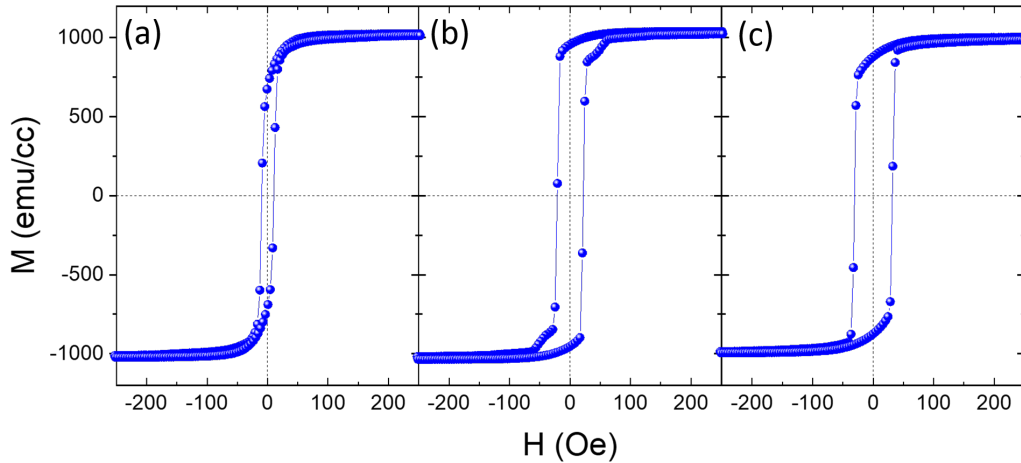


Figure 6.17: Magnetic hysteresis loops along CFS $[\bar{1}10]$ for: (a) $T_B < 130^\circ\text{C}$, (b) $T_B = 350^\circ\text{C}$ and (c) $T_B = 550^\circ\text{C}$.

The coercive field and the saturation magnetization have been represented as a function of the growth temperature in Fig. 6.18. M_s is constant within error and has a value of $1000 \pm 50 \text{ emu/cc}$, which is very close to the ideal bulk value of fully-ordered CFS ($M_s = 1100 \text{ emu/cc}$) [Wur06] and is a good sign that the chemical composition of the alloy films is correct. H_c follows a linear relationship with T_B . At $T_B < 130^\circ\text{C}$, the coercive field is 10.0 ± 0.5 Oe and increases linearly to 30.0 ± 1 at $T_B = 550^\circ\text{C}$. The increase of coercivity with growth temperature is different to the findings in [Kue18] for CFAS/Si(111) films where H_c remained stable and below 10 Oe up to 500°C , but it agrees with the observations of Mohankumar *et al.* in [MRK17]. In that study, the increase of coercivity was explained as an increase in the number of grains and thus, as an increase in the number of grain boundaries that act as pinning

sites. However, in our case this seems to contradict the behaviour of Δ_L in Fig. 6.11c which points to an increasing grain size (and hence, to a reduction of the number of grains) with T_B . Therefore, the change in H_c has to arise from other structural changes or defects in the high temperature films. However, finding the cause is difficult as H_c can be related to a number of things. The small H_c value of ≈ 10 Oe measured for the low temperature film is also in good agreement with the values found in literature [Kue18; MRK17], although it is not strictly comparable to literature because the loops were not taken along the EA.

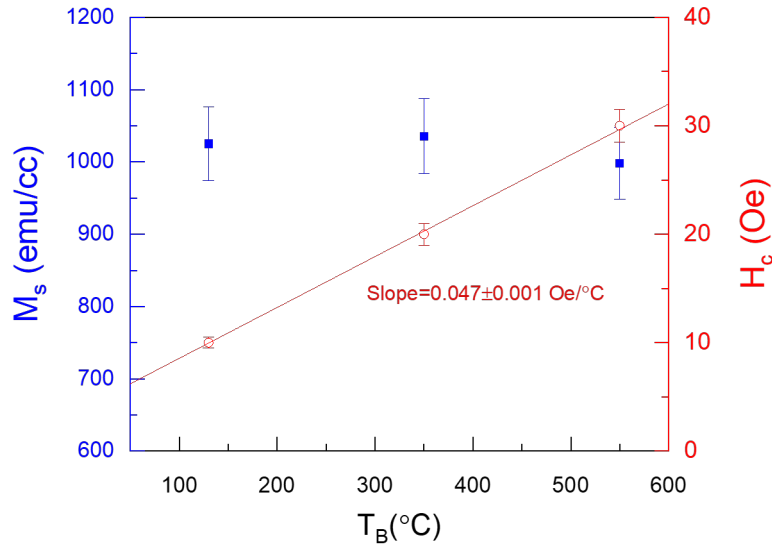


Figure 6.18: M_s (blue squares) and H_c (red circles) extracted from the hysteresis loops in Fig. 6.17 plotted against T_B .

6.3.2.2 FMR measurements

VNA-FMR measurements were performed to investigate the changes in the dynamic magnetic properties of the films as a function of the growth temperature. VNA-FMR linescans were taken over a field range between 0T to 0.38T in steps of 1mT, and for each magnetic field, the driving frequency was swept from 100 kHz to 20 GHz. The measurements were repeated for each azimuthal angle ranging from $\phi = -80^\circ$ to $\phi = +80^\circ$ with $\Delta\phi = 5^\circ$. To obtain reliable data at large ϕ , two sweeps were performed for each sample as discussed in Chapter 5; the first sweep with the MgO[100] edge of the sample mounted parallel to the waveguide transmission line at 0° , and the second sweep with the MgO[010] aligned to $\phi = 0^\circ$. In this manner, it was possible to construct the 360° maps of the resonant frequency that will be shown this section (Fig. 6.20). The Kittel curves recorded along the EA can be observed in the frequency-field maps shown in Fig. 6.19. It is evident that the resonance undergoes certain changes when

the growth temperature is increased. In particular, the linewidth of the resonance is reduced at $T_B = 350^\circ\text{C}$, whereas at $T_B = 550^\circ\text{C}$ the resonance widens significantly and a very weak second resonance starts to appear at its left hand side (i.e. at smaller magnetic fields). As will be found at the end of the chapter, this is a consequence of the increase of both the intrinsic and extrinsic damping in this sample.

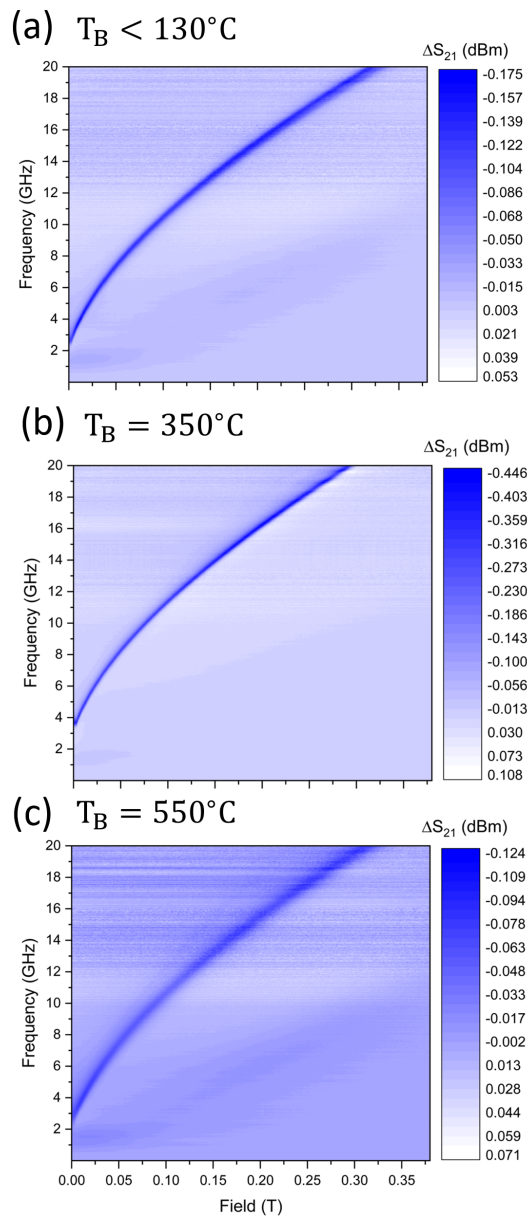


Figure 6.19: Frequency-field maps for fields between $0 < H < 0.38\text{T}$ and frequencies between 100kHz and 20GHz for: (a) $T_B < 130^\circ\text{C}$, (b) $T_B = 350^\circ\text{C}$ and (c) $T_B = 550^\circ\text{C}$, taken along the EA (i.e. along CFS[100]).

In order to explore the in-plane anisotropy of the films, the FMR signals measured along the various azimuthal angles at the same RF frequency of 10GHz were processed and fitted to eq. (4.35). The extracted values for the resonant frequency are shown in Figs. 6.20a to 6.20c for $T_B < 130^\circ\text{C}$ to $T_B = 550^\circ\text{C}$ respectively. For the sake of clarity, the crystallographic directions in Fig. 6.20a have been labelled with CFS as a reference. That is, in Fig. 6.20, the 0° angle corresponds to the $[100]$ direction of CFS and hence, to the $[\bar{1}\bar{1}0]$ direction of MgO due to the 45 degree angle existing between the two lattices (as per Fig. 6.12e). Thus, if up to here ϕ was defined as the angle between the MgO $[100]$ edge and the externally applied field H , the azimuthal angle has now been redefined as $\phi \rightarrow \phi + 45^\circ$. In order to avoid any confusion, the label has also been changed to ϕ_{CFS} and will be used from now on instead of ϕ . The profile of the anisotropy is noticeably different from the one observed previously in the (111)-oriented CFS films. The symmetry of H_r in this case is fourfold agreeing with the signature of the cubic magnetocrystalline anisotropy expected for CFS. The EA is along $[100]$ and hence, corresponds to a cubic MCA with $K_c > 0$. If only MCA was present, the two EAs ($[100]$ and $[010]$) as well as the two HAs ($[\bar{1}10]$ and $[\bar{1}\bar{1}0]$) would be equivalent. Clearly, this is not true due to the existence of a uniaxial anisotropy along $[\bar{1}\bar{1}0]$ which makes the $[\bar{1}10]$ direction *harder* than $[\bar{1}\bar{1}0]$.

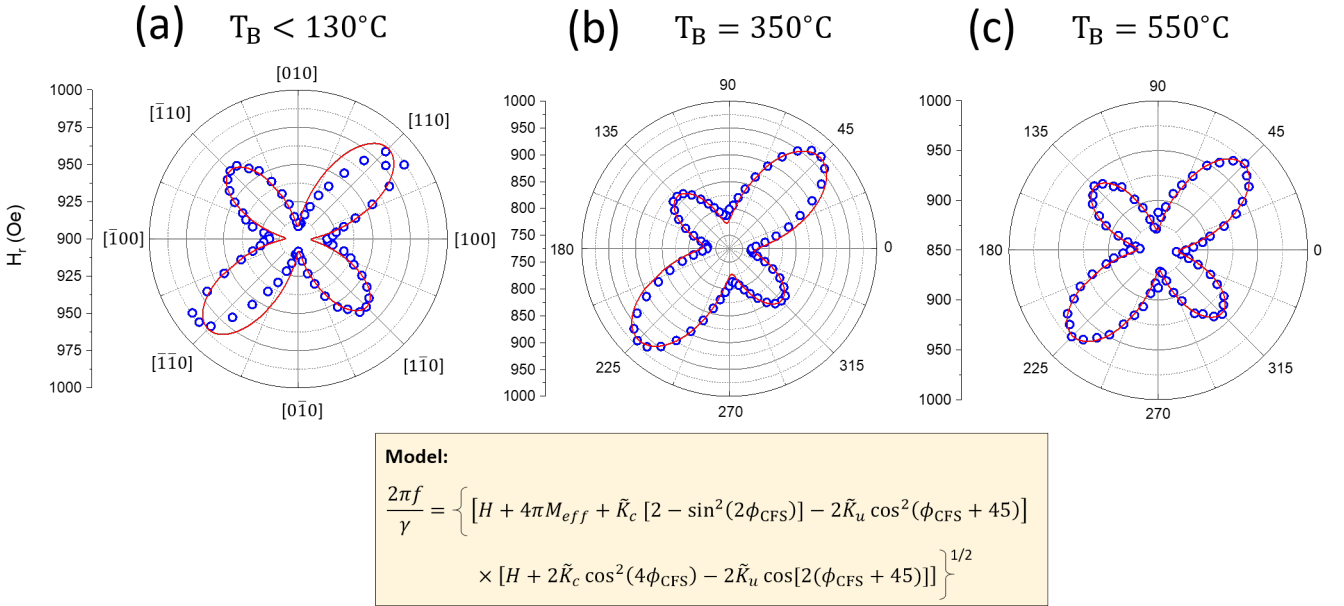


Figure 6.20: $H_r(\phi_{CFS})$ azimuthal graphs at 10GHz for (a) $T_B < 130^\circ\text{C}$, (b) $T_B = 350^\circ\text{C}$ and (c) $T_B = 550^\circ\text{C}$. The orientations specified in (a) are the crystallographic directions of CFS.

The presence of a uniaxial anisotropy superimposed on the cubic MCA has been reported very often in similar Co-based Heusler films [AKP00a; AKP00b; Wan05a]; and although there have been many theoretical efforts to explain its origin, it still remains an open question. When

grown on semiconductors of the zinc-blende structure like GaAs(001), several explanations have been put forward, including: surface reconstruction of the GaAs substrate, the formation of an interface alloy and the most likely anisotropy of the dangling covalent bonds at the surface of GaAs(001). However, the occurrence of the twofold anisotropy is not as easily understood when the films are grown on MgO(001). For instance, the uniaxial anisotropy was almost unaffected whether $\text{Co}_2\text{Cr}_{0.6}\text{Fe}_{0.4}\text{Al}$ was grown on GaAs(001) with or without a 1.5nm MgO buffer [Uem07b; Uem07a]; whereas if the MgO buffer thickness was increased to 3.0 nm for Co_2MnSi on GaAs(001), the anisotropy was markedly reduced [Uem08]. However, using a MgO-buffered MgO substrate does not eliminate this particular anisotropy, as similar (albeit less pronounced) magnetization switching features (namely a two-step M-H loop along the EA, $[110]_{\text{CFAS}}$, and a HA along $[100]_{\text{CFAS}}$) were observed for $\text{Co}_2\text{FeAl}_{0.5}\text{Si}_{0.5}$ grown on MgO(001) [Wan08]. In this study, Wang *et al.* proposed that the uniaxial anisotropy may be due to the lattice misfit between CFAS and MgO. To fully understand its origin, though, further systematic studies are necessary.

In order to extract the anisotropy constants K_c and K_u , Kittel curves along various ϕ_{CFS} were globally fitted to eq. (4.30) in the same way it was done in § 5.4.2. In eq. (4.30) ϕ_u was set to -45° in accordance to the uniaxial anisotropy that is observed along the $[\bar{1}10]$ direction of CFS. Typically, three curves were used for this purpose, the one along the EA ($\phi_{\text{CFS}} = 0^\circ$), the one along the first HA ($\phi_{\text{CFS}} = +45^\circ$) and the one along the second, inequivalent HA ($\phi_{\text{CFS}} = +315^\circ$); these are shown in Fig. 6.21a for $T_B = 350^\circ\text{C}$. The effective magnetization retrieved from the fits has been plotted in Fig. 6.21b against T_B . The values for M_{eff} agree within a 10% of the M_s values recorded from the VSM. Both values match at $T_B < 130^\circ\text{C}$ and $T_B = 550^\circ\text{C}$, while there is a small discrepancy of $\approx 7\%$ at $T_B = 350^\circ\text{C}$. The discrepancy however is small and could be due to instrumental errors or errors arising from the calculation of the magnetic volume as explained earlier.

K_c and K_u have been represented in Fig. 6.21c. $K_c = 1.80 \pm 0.09 \times 10^4 \text{ erg/cm}^3$ for the sample grown at $< 130^\circ\text{C}$, which matches with the value of $1.8 \times 10^4 \text{ erg/cm}^3$ measured in [Has05] for a stoichiometric 18.5 nm-thick CFS film grown on GaAs(001) at 100°C . K_u is of the same order of magnitude as K_c and somewhat lower than in the CFS/Si(111) films in Chapter 5 (refer to Fig. 5.26b). At the lowest substrate temperature of $T_B < 130^\circ\text{C}$, K_u ($0.56 \pm 0.02 \times 10^4 \text{ erg/cm}^3$) is one order of magnitude smaller than that measured by Hashimoto *et al.* in [Has05] ($6.3 \times 10^4 \text{ erg/cm}^3$), although because those films were grown on GaAs, the two values are not directly comparable. Values for K_u on $\text{Co}_2\text{FeAl}_{1-x}\text{Si}_x$ films grown on MgO(001) could not be found in literature.

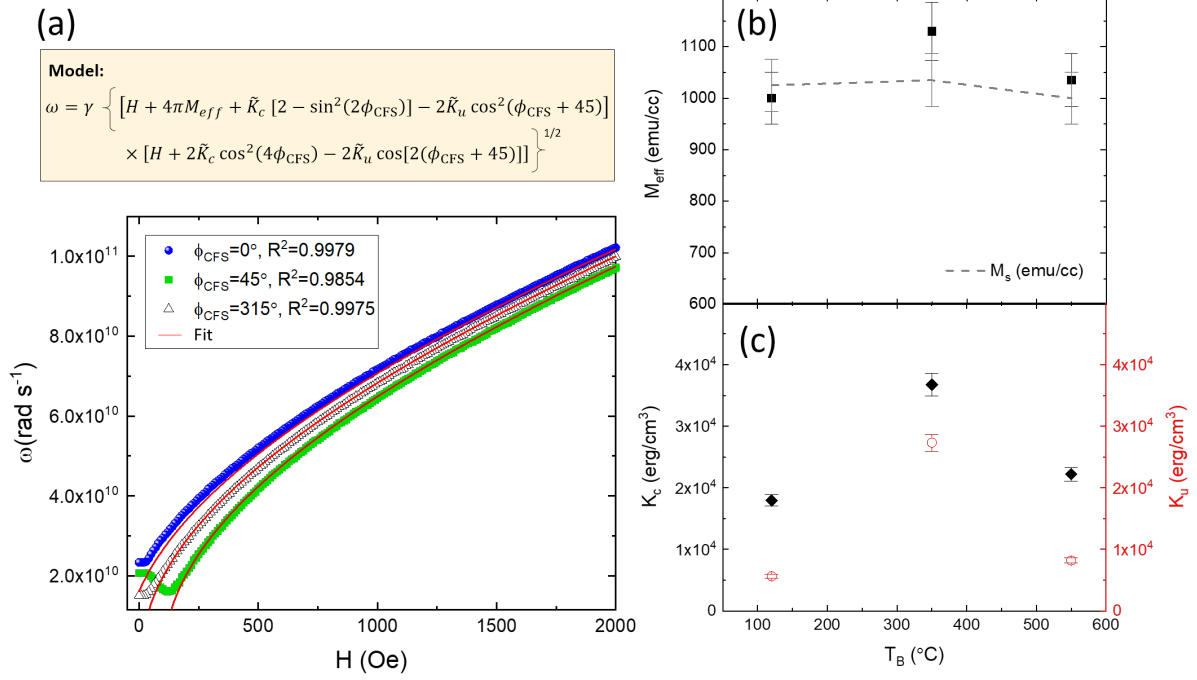


Figure 6.21: (a) Kittel curves along the EA (blue dots), the HA (green squares) and the *less hard* HA (empty black triangles) fitted to eq. (4.30) (red lines); (b) M_{eff} values (black squares) extracted from the fits in (a), and M_s values (grey dashed line) measured with the VSM shown in comparison; (c) cubic (black rhombus) and uniaxial (red circles) anisotropy constants extracted from the fits.

K_c increases by twofold at 350°C. The reason for this is most likely the improvement of the structural order in this sample as deduced from the appearance of a weak CFS(111) reflection in XRD (refer to Fig. 6.12). Although XRD pointed to an ever further increase of the ordering at $T_B = 550^\circ\text{C}$, it is common that at a certain threshold temperature, the magnetic properties start to worsen (albeit an increased structural order) due to the deterioration of the interface as elements from the substrate start out-diffusing into the film. This is likely happening at $T_B = 550^\circ\text{C}$ because the segregation of Mg atoms starts occurring at $\approx 400^\circ\text{C}$. If Mg has out-diffused far enough into the lattice, it is possible that it has an effect on bulk properties such as K_c as well. On the other hand, K_u seems to follow the same trend as K_c , it increases up to $2.73 \pm 0.01 \times 10^4 \text{erg/cm}^3$ at $T_B = 350^\circ\text{C}$ and drops once more to $0.82 \pm 0.02 \times 10^4 \text{erg/cm}^3$ at $T_B = 550^\circ\text{C}$. However, without knowing the origin of the uniaxial anisotropy, it is very difficult to speculate why these changes are observed. Further STEM analysis focused at the interface between CFS and MgO is expected to provide some insight into this. The values for all the anisotropy constants have been summarized in Tab. 6.2 for the three growth temperatures.

T_B ($^{\circ}\text{C}$)	M_s (emu/cm 3)	M_{eff} (emu/cm 3)	K_c ($\times 10^4$ erg/cm 3)	K_u ($\times 10^4$ erg/cm 3)	K_{\perp} ($\times 10^5$ erg/cm 3)	α ($\times 10^{-3}$)	$\Delta H(0)$ (Oe)
< 130	1025 ± 50	1000 ± 40	1.80 ± 0.09	0.56 ± 0.02	1.6 ± 4	13.6 ± 0.3	-3.6 ± 0.9
350	1035 ± 50	1130 ± 50	3.7 ± 0.2	2.73 ± 0.01	-6.2 ± 4	6.5 ± 0.1	5.4 ± 0.4
550	1000 ± 50	1035 ± 40	2.2 ± 0.1	0.82 ± 0.02	-2.2 ± 4	–	–

Table 6.2: Magnetic parameters extracted from VSM and FMR experiments for the CFS films grown on MgO(001) at $T_B < 130^{\circ}\text{C}$, 350°C and 550°C .

Note that given the errors in M_s , the perpendicular anisotropy constant $K_{\perp} = 2\pi M_s(M_s - M_{eff})$ is subjected to large errors of around $\pm 4 \times 10^5$ erg/cm 3 . Hence, the K_{\perp} extracted for $T_B < 130^{\circ}\text{C}$ and 550°C is meaningless. Similarly, the calculated value of -6.2×10^5 erg/cm 3 for $T_B = 350^{\circ}\text{C}$, arises from the discrepancy between M_s and M_{eff} at this temperature, which might be arising from the previously mentioned errors related to VSM measurements. Therefore, all the values listed in Table 6.2 for K_{\perp} , although they appear larger than K_c and K_u , due to the uncertainty on them, they cannot be taken into consideration. All these values are indeed 1 order of magnitude smaller than the ones found for the Si-poor CFS samples in Chapter 5 (refer to the inset of Fig. 5.26a) which were attributed to strain effects. Also, it has to be mentioned that the values for M_{eff} extracted from the fits (and in turn, K_{\perp}), is quite dependent on the correct value of γ . The fitting parameters M_{eff} and γ are not easily decoupled even when including several Kittel curves in the fit (including higher frequency data on the analysis might help with this in the future). Thus, the values given in Tab. 6.2 were extracted with $\gamma = 1.76 \times 10^7$ rad s $^{-1}$ Oe $^{-1}$ (i.e. $g_e = 2.0$), which can also add to the error in K_{\perp} . This is also applicable for the K_{\perp} values listed in Tab. 6.3.

To finish the FMR analysis, the magnetic damping was investigated. Once more, the resonance linewidth was extracted by fitting the FMR signals taken along the EA (i.e. $\phi_{CFS} = 0^{\circ}$) at frequencies between 5GHz and 20GHz to the asymmetric Lorentzian distribution. ΔH was plotted as a function of frequency and analysed according to eq. (4.34). The samples grown at the lowest substrate temperatures, $T_B < 130^{\circ}\text{C}$ and $T_B = 350^{\circ}\text{C}$, show a linear behaviour which dominates over the two-magnon scattering even at high frequencies. The slope of the curves is clearly reduced at $T_B = 350^{\circ}\text{C}$ which is reflected in a smaller intrinsic damping. Indeed, the Gilbert parameter is reduced by half from $1.36 \pm 0.03 \times 10^{-2}$ at $T_B < 130^{\circ}\text{C}$ to $6.5 \pm 0.1 \times 10^{-3}$ at $T_B = 350^{\circ}\text{C}$. The value obtained here is of the same order of magnitude as the one measured by Oogane *et al.* [Oog07] for Co $_2$ MnAl films grown on MgO ($\alpha = 8 \times 10^{-3}$), and around 3 times smaller than the damping constant they measured for the CFS/MgO(001) samples annealed at 400°C ($\alpha = 2.2 \times 10^{-2}$) despite not using a Cr buffer layer. At $T_B = 550^{\circ}\text{C}$,

the linearity is lost and extrinsic contributions dominate the damping, which agrees with the introduction of magnetic inhomogeneities from the possible segregation of Mg into the film. Hence, the extraction of α is not possible in this case. The values for α , as well as $\Delta H(0)$, have also been included in Tab. 6.2 for $T_B < 130^\circ\text{C}$ and $T_B = 350^\circ\text{C}$.

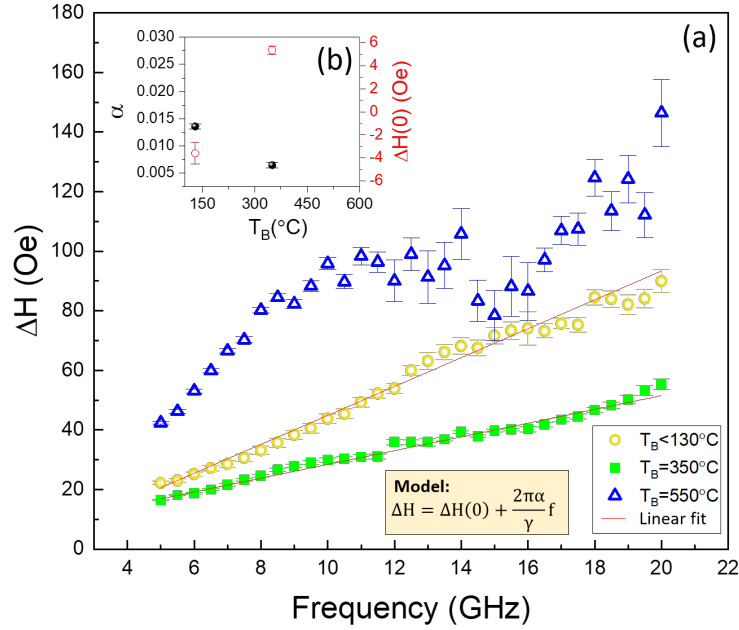


Figure 6.22: (a) ΔH as a function of the RF frequency and the corresponding linear fits for $T_B = 130^\circ\text{C}$ (yellow circles), $T_B = 350^\circ\text{C}$ (green squares) and $T_B = 550^\circ\text{C}$ (blue hollow triangles); (b) Gilbert damping parameter and $\Delta H(0)$ extracted from the linear fits in (a).

6.4 NiO capped-CFS films

After finding the optimal evaporation rates and growth temperature (350°C) for the growth of CFS on MgO(001), a series of NiO[t_{NiO}]/Fe[1]/Co₂FeSi[25]/MgO(001) multilayer structures were grown with different NiO thicknesses of $t_{\text{NiO}}=3, 5, 10$ and 20 nm to study the growth and the effects of an AFI layer on the half-Heusler alloy.

Following the preparation of the MgO(001) surface as per the recipe in § 6.2, 25 nm of CFS were deposited at 350°C using the optimized evaporation rates for Fe, Co and Si. After the growth had finished, an additional 1nm-thick Fe layer was grown by closing the shutters of the Co and Si sources. The extra Fe layer was grown to promote the crystallization of the NiO

layer on top, which grew amorphous without this buffer. When the deposition was done, the shutter of the Fe k-cell was also closed and the heating current was gradually reduced leaving the substrate to cool down to $< 100^\circ\text{C}$. When the substrate had reached temperatures between 70°C - 90°C , the sample was transferred to a second MBE chamber for the growth of NiO. The two chambers are connected through a UHV gate valve which enables the transfer to be done without breaking the vacuum. At the second chamber, the Ni source (also a k-cell), was risen to a deposition temperature of $T_{\text{Ni}} = 1425^\circ\text{C}$ and the sample was slowly brought to 250°C . When the source and substrate temperatures had stabilized, the oxygen was introduced into the vacuum chamber through a leak valve. The growth was carried out at O_2 pressures of 5×10^{-6} - 6×10^{-6} mbar at $T_B = 250^\circ\text{C}$ and at a rate of $\approx 1\text{\AA}/\text{min}$. The crystallinity of the NiO overlayer was confirmed by RHEED and the sample was subsequently taken out the chamber.

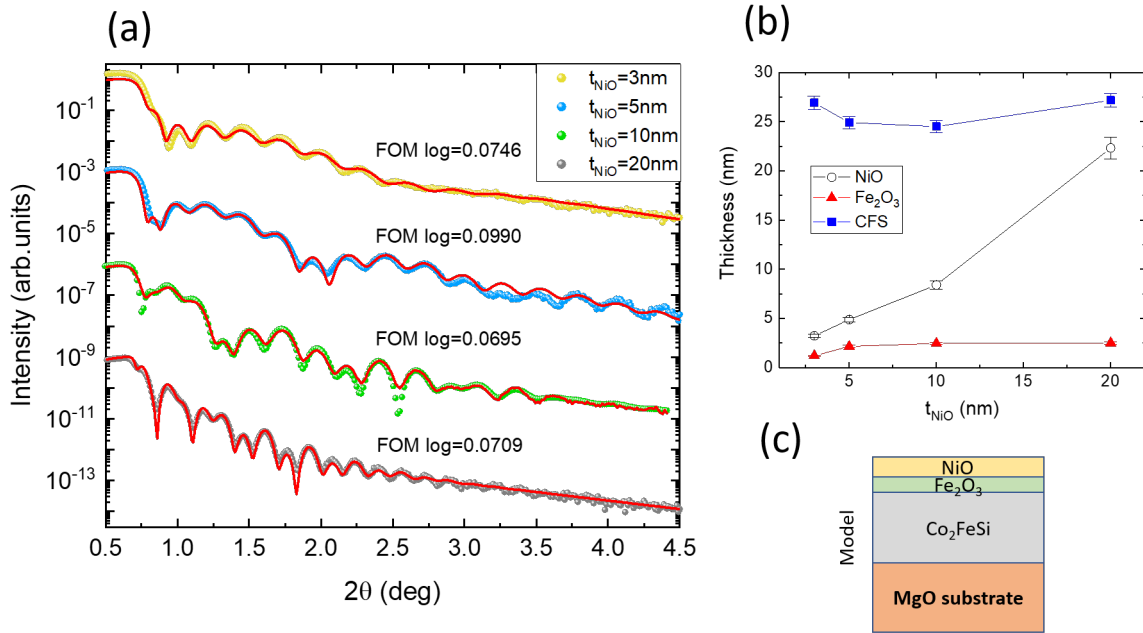


Figure 6.23: (a) XRR measurements (coloured dots) and fits (red lines) for the NiO [t_{NiO}]/Fe [1]/ Co_2FeSi [25]/MgO(001) heterostructures with $t_{\text{NiO}} = 3\text{nm}$ (yellow), 5nm (blue), 10nm (green) and 20nm (grey); (b) thickness of the 3 layers in (c) extracted from the fits; (c) 3-layer model used to fit the data.

Fig. 6.23a shows the XRR curves of the 25-nm thick CFS films capped with the NiO layer of varying thickness. As can be observed, the NiO[t_{NiO}]/Fe[1] capping results in the modulation of the original oscillatory pattern governed by the CFS/MgO interface. The period of this modulation is bigger than that of the underlying oscillation and decreases as the thickness of NiO is increased, and it is hence, mainly controlled by the NiO[t_{NiO}]/Fe[1] interface. When

$t_{\text{NiO}} = 20$ nm, the thickness of NiO approaches that of CFS and so, the distinction between the two periods becomes more difficult. The adequate model to fit this data was found to be the one in Fig. 6.23c. Initially, the parameters of single crystal Fe (i.e. $\rho_{\text{Fe}} = 0.085$ f.u./ \AA^3 and the corresponding scattering factor) were assigned to the layer between CFS and NiO according to the nominal heterostructure, but this led to poor-quality fits. The density of the Fe interlayer was then introduced as a fit parameter to improve the FOM.

The density was allowed to vary by 25%, i.e. from 0.064 to 0.106 f.u./ \AA^3 . When doing so, the density had the tendency to saturate to 0.106 f.u./ \AA^3 and the thickness of the layer to reduce to 0, while retrieving FOM values still above 0.1. This clearly indicated that the assumptions for this layer were not correct. However, because the RHEED showed crystalline features in all the stages of the growth, no amorphous layers are expected across the structure. The two possible explanations for a change in the structure of Fe can be mixing at the NiO/Fe or Fe/CFS interface (although the growth temperatures were kept low so as to minimize this) and the oxidation of Fe due to the exposure of the Fe surface to O_2 just before the growth of NiO. Nevertheless, it is difficult to find out which of these options is the most likely cause only by letting the density of the layer vary, because the interference fringes also depend on the scattering factor. After several attempts to improve the fits and based on the author's best guess, the Fe layer was substituted by a Fe_2O_3 layer with its corresponding scattering factor and $\rho_{\text{Fe}_2\text{O}_3} = 0.0066$ f.u./ \AA^3 . This is the model depicted in Fig. 6.23c. The density was once again allowed to vary by 25% and was found to converge to 0.0063 f.u./ \AA^3 . The FOM values retrieved from the fits are all below 0.1 and the fits are the red curves in Fig. 6.23a. Therefore, this model seems to represent the data more accurately, although microscopy experiments are needed to validate or reject the model.

Despite the unknown nature of the interface, the fits give reasonable values for the thickness of NiO. In Fig. 6.23b the thickness of all the layers in the model have been plotted as a function of t_{NiO} . The thickness of CFS oscillates between 24.5 ± 0.6 and 27.2 ± 0.7 nm and the thickness of the Fe_2O_3 layer takes values from 1.20 ± 0.06 to 2.5 ± 0.1 nm, much bigger than the 1 nm thickness expected for Fe. The thickness of NiO matches to a 10% with the nominal value for all the thicknesses except for $t_{\text{NiO}} = 10$ nm, where the discrepancy increases to a 20%. The SLD profile of the XRR fits has been plotted in Fig. 6.24 for the four NiO thicknesses. The substrate and air bulk-like regions have been represented in grey, whereas the interface between CFS and NiO (with the oxide layer in between) is shown in green. As can be observed, the interface region seems to increase with NiO thickness and hence, might point to a mixing between Fe and NiO. Nevertheless, as will be seen from the microscopy data (Fig. 6.26), the interface region between NiO and CFS seems more complicated than can be explained by the XRR model.

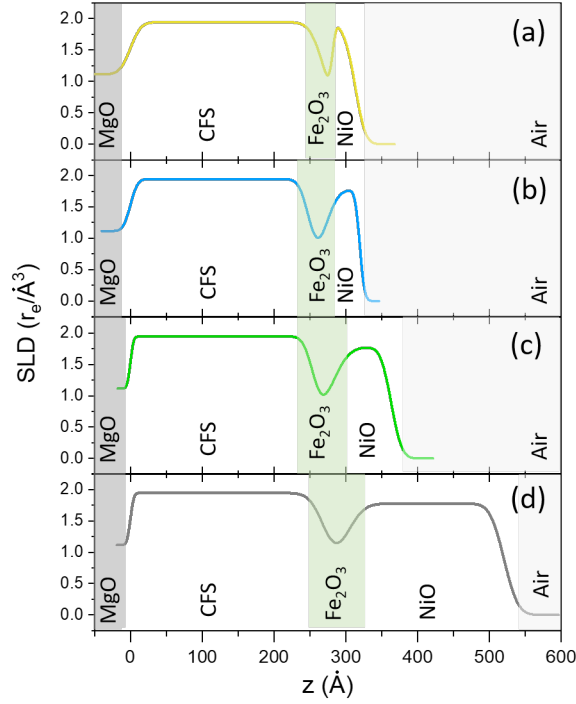


Figure 6.24: X-ray scattering length density extracted from the XRR fits in Fig. 6.23a for $t_{\text{NiO}} = 3\text{nm}$ (a), 5nm (b), 10nm (c) and 20nm (d).

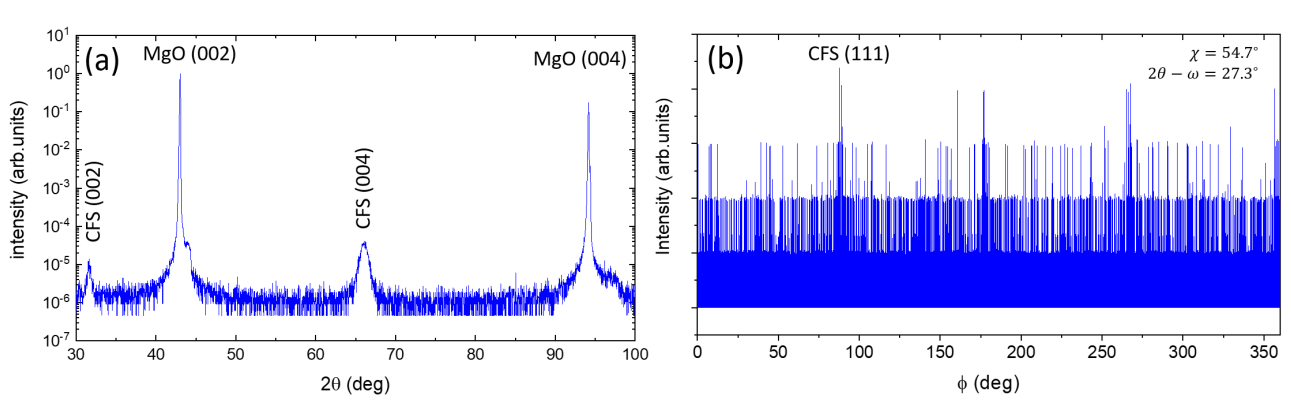


Figure 6.25: (a) Out-of-plane $2\theta - \omega$ scan aligned to MgO(002) and (b) ϕ scan aligned to CFS(111) for the NiO[20]/Fe[1]/Co₂FeSi[25]/MgO(001) sample. Even at large angles, the NiO peaks cannot be resolved for the 20nm-thick layer.

Out of plane $2\theta - \omega$ scans were performed for all the samples and similar structural order of the CFS layer was confirmed by the appearance of the usual superlattice reflections, namely CFS(002) and CFS(111), comparable to those shown by the uncapped film grown at 350°C (see Figs. 6.25a and b). However, no other diffraction peaks were observed that could indicate the presence of NiO. This is expected because NiO ($a_{\text{NiO}} = 4.17\text{\AA}$) has a lattice constant very

close to that of MgO ($a_{\text{MgO}} = 4.20\text{\AA}$) and so, any diffraction peaks will be hidden behind the substrate peaks. As for the Fe layer, this is too thin to produce any reflections in a XRD scan.

Fig. 6.26a is the cross-section of the $t_{\text{NiO}} = 10\text{ nm}$ sample taken with the JEOL-2200FS microscope showing the NiO and CFS layers grown on the MgO(001) substrate. The top Pt capping layer was grown at a later stage via magnetron sputtering. The large roughness of the CFS layer ($\approx 2\text{ nm}$) translates into an also rough NiO overlayer. The thickness of CFS is in good agreement with its nominal value and that measured by XRR ($24.5 \pm 0.6\text{ nm}$). The thickness of the layer on top of the CFS (which should include both the 10nm-NiO layer as well as the 1nm-thick Fe buffer) is $\approx 11\text{ nm}$ which also matches the expected nominal value. The HRTEM image in Fig. 6.26b shows in more detail the interface between NiO and CFS. NiO is a single-crystal and grows 45 degrees in-plane rotated with respect to CFS (i.e. without rotation respect to MgO). Nonetheless, instead of finding a 1nm-thick Fe layer between NiO and CFS, one can see a crystalline interfacial region of $\approx 3\text{-}4\text{ nm}$ with the NiO thickness consequently reduced to $\approx 7\text{ nm}$. This appears to explain the small (big) thickness of $8.4 \pm 0.4\text{ nm}$ ($2.5 \pm 0.1\text{ nm}$) measured by XRR for NiO (Fe_2O_3) in this sample. In some parts of this interface, amorphous areas are also observed, which probably relate to the oxidized regions. However, no definitive conclusions could be extracted yet about the structure/chemistry of this secondary phase between NiO and CFS.

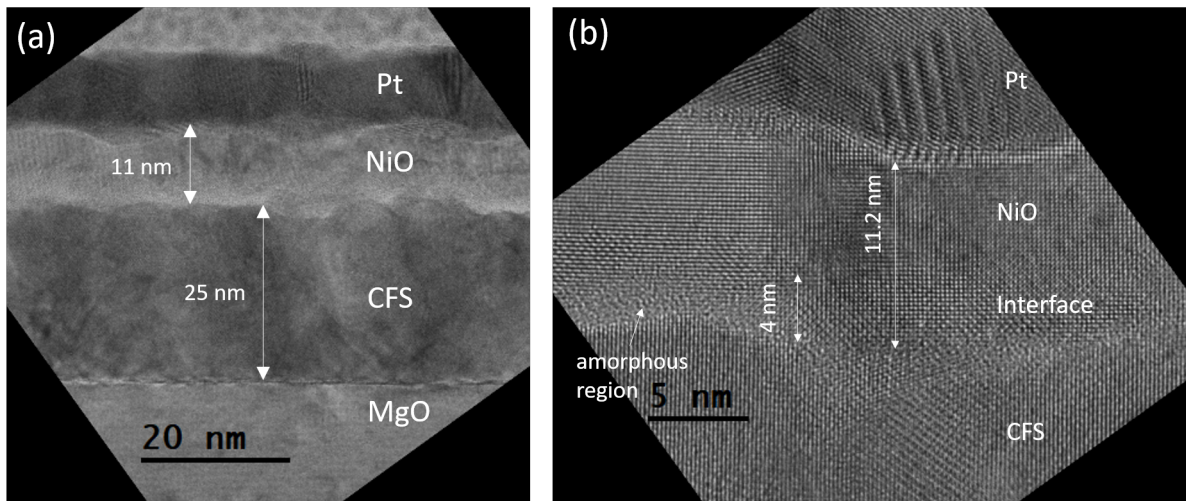


Figure 6.26: HRTEM images of the NiO[10]/Fe[1]/Co₂FeSi[25]/MgO(001) sample. (a) is an overview of the layers in cross-section, and (b) is a high magnification image focused on the interface between NiO and CFS.

The usual $H_r(\phi_{\text{CFS}})$ polar plots can be seen in Fig. 6.27 for the NiO-capped films with $t_{\text{NiO}} = 3, 5$ and 10 nm, which have been acquired and analysed in the same manner as in § 6.3.2.2. The crystallographic directions in Fig. 6.27a refer once again to the orientation of CFS. Without

doubt, the anisotropy differs from the one shown by the uncapped films in Fig. 6.20. The symmetry is again fourfold but the directions of the EAs and HAs have swapped so that the easy axes are now along $\langle 110 \rangle$ and the hard axes along $\langle 100 \rangle$. The presence of the uniaxial anisotropy along $[\bar{1}10]$ does not change, but this time it makes the two EAs inequivalent, whereas the two HAs are equally hard directions.

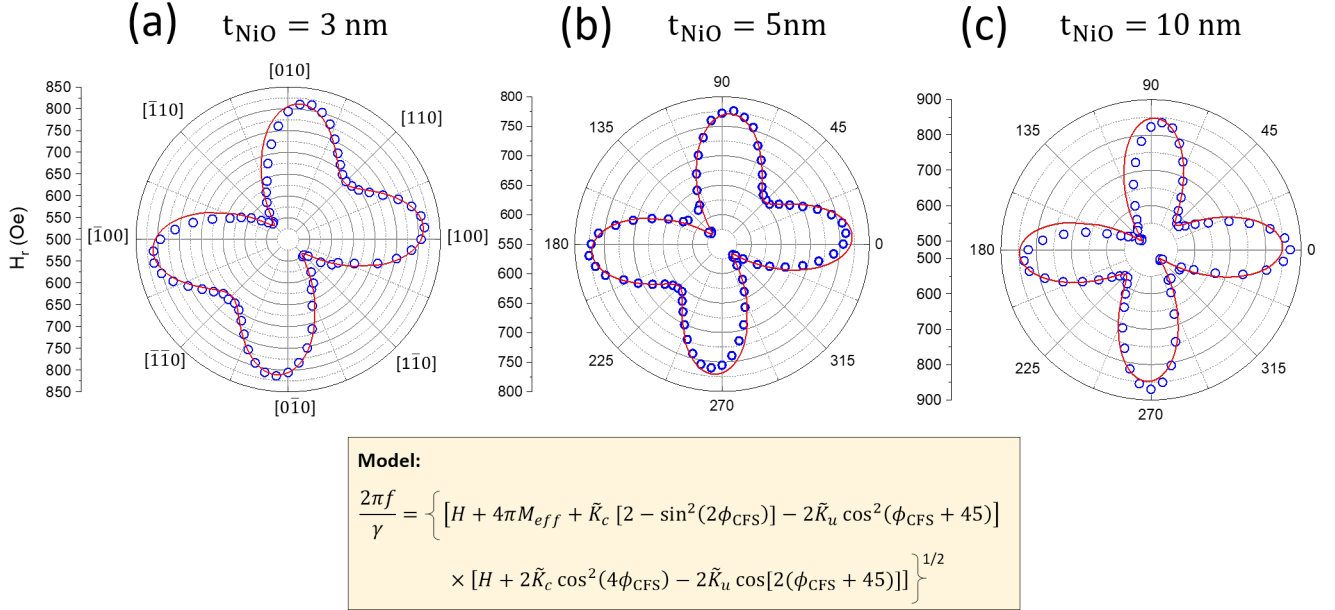


Figure 6.27: Azimuthal plots of the resonant frequency for (a) $t_{\text{NiO}}=3\text{nm}$, (b) $t_{\text{NiO}}=5\text{nm}$ and (c) $t_{\text{NiO}}=10\text{nm}$ revealing a negative K_c in all the capped films.

The change observed in the MCA agrees with the picture of a cubic MCA with $K_c < 0$. As described in § 2.1.2, when K_c changes sign, the EAs align to the $\langle 111 \rangle$ directions. Hence, projected onto the (001) sample plane, one finds the EAs along $\langle 110 \rangle$ and conversely, the HAs along the $\langle 100 \rangle$ directions. This reasoning was confirmed by the results obtained from curve fitting. When the Kittel curves were fitted to the same model used for the uncapped films, that is, a cubic MCA plus a uniaxial anisotropy component at $\phi_u = -45^\circ$, equally good fits were obtained but all of them returned negative values for K_c . The red curves in Fig. 6.27 are the models achieved when the best-fitting parameters for K_u , K_c and M_{eff} were substituted in eq. (4.30). The values retrieved for the anisotropy parameters have been collected in Tab. 6.3 along with α and M_s .

The reason for this change in K_c is currently not clear. One possibility could be changes in the chemistry of CFS from the interdiffusion of magnetic species, Fe or Ni, from the capping layers into the CFS. This could also be the reason why the saturation magnetization values measured in the VSM for the capped films are $\approx 20\%$ higher than those measured for the

uncapped films (refer to tab.6.3); although the M_s measured for the multilayer structures ($\approx 1200 \text{ emu/cm}^3$) is still close to the bulk value of CFS. The absolute values for K_c and K_u are also bigger in these films. K_{\perp} is also shown in the table but once again, it was found that this value is dependent on the value of γ used during the fitting and hence, one has to be able to decouple these two fitting parameters before giving any interpretation of the results. Despite this, the values for K_c and K_u are robust and can model accurately the polar data taken along a different RF frequency (this was indeed double-checked by fitting the data at 15GHz and obtaining the same values for the anisotropy constants).

t_{NiO} (nm)	M_s (emu/cm ³)	M_{eff} (emu/cm ³)	K_c ($\times 10^4$ erg/cm ³)	K_u ($\times 10^4$ erg/cm ³)	K_{\perp} ($\times 10^5$ erg/cm ³)	α_{110} ($\times 10^{-3}$)	$\alpha_{1\bar{1}0}$ ($\times 10^{-3}$)
3	1200 ± 50	1380 ± 60	-5.9 ± 0.3	4.2 ± 0.1	-13.6 ± 8	9.3 ± 0.2	8.6 ± 0.3
5	1200 ± 50	1420 ± 60	-4.8 ± 0.3	2.4 ± 0.2	-16.6 ± 7	9.8 ± 0.1	6.2 ± 0.1
10	1210 ± 60	1415 ± 60	-9.4 ± 0.2	1.9 ± 0.2	-16.2 ± 8	8.0 ± 0.2	7.7 ± 0.2

Table 6.3: Magnetic parameters measured with VSM and FMR on NiO [t_{NiO}]/Fe [1]/CFS [25]/MgO(001) samples with $t_{\text{NiO}} = 3\text{nm}$, 5nm and 10nm .

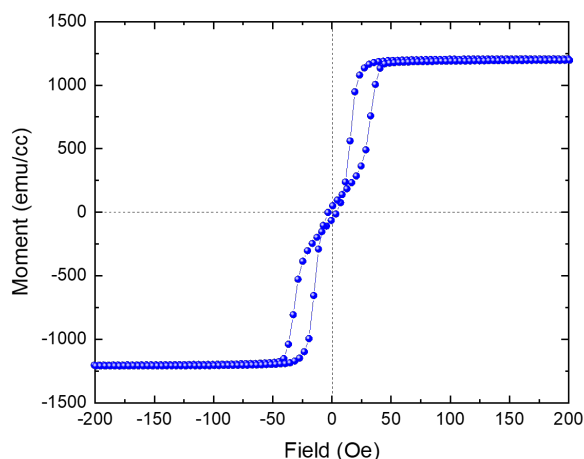


Figure 6.28: Magnetic hysteresis loop recorded along the [110] direction for $t_{\text{NiO}} = 5\text{nm}$.

The observation of the EA along the [110] direction agrees with the reports by Wang *et al.* for CFAS films grown on MgO(001) [Wan08] and by Hashimoto *et al.* for CFS films grown on GaAs(001) [Has05]. Although they also attribute the anisotropic behaviour of their films to the coexistence of a cubic and a uniaxial component, without the full angular dependence of the anisotropy, it is hard to say if their observations correspond to a positive or a negative

K_c as is our case. It is evident that the MCA in CFS films is very weak and so, it is possible that chemical/structural variations can lead to a change in K_c from positive to negative, as has already been reported for other Heusler films like Co_2MnSi in [Yil07]. The presence of the uniaxial and the cubic MCA in these films is also evidenced by the multi-step switching hysteresis loop observed along the [110] direction of one of the capped CFS films in Fig. 6.28. When H is applied along the [110] axis, the resultant hysteresis curve is not the expected square loop of an EA but has additional features. At large fields, the magnetization lies parallel to H . As H is reduced below 25 Oe, the favoured direction of M lies close to the easier $[1\bar{1}0]$ direction so that at near zero fields, M lies almost perpendicular to H . Upon field reversal, M returns to the field direction in a similar manner together with hysteresis. Ambrose *et al.* observed the same phenomenon for Co_2MnGe films in [AKP00a], which they were able to explain assuming coherent rotation of the magnetization. Nevertheless, measurements still need to be performed along the different in-plane directions to correlate the shape of the hysteresis loops and hence, the magnetic switching process (as was done in [Wan05b]), to the anisotropy profile recorded through the FMR.

6.5 Summary and conclusions

In this chapter, the growth of CFS films on MgO(001) single crystal substrates has been optimized. With that purpose, in the first part of the chapter, CFS films have been grown using different Si rates so as to find the right stoichiometry. XRD out of plane $2\theta - \omega$ measurements have shown the presence of the CFS(004) structural peak, as well as the CFS(002) superlattice reflection. A higher intensity of both reflections, as well as an out-of plane lattice constant close to bulk CFS, shows the direction to the stoichiometric CFS film at $T_{Si} = 1045^\circ\text{C}$. However, in none of the CFS films grown at low temperatures was the CFS(111) superlattice reflection observed. Hence, contrary to CFS/Si(111), where the presence of $L2_1$ -ordered grains could be demonstrated even at $< 130^\circ\text{C}$, this could not be achieved in similarly grown CFS films on MgO. In order to promote the full-structural order in CFS/MgO(001), two more CFS films were grown at elevated substrate temperatures of $T_B = 350^\circ\text{C}$ and $T_B = 550^\circ\text{C}$.

As the substrate temperature increases, various changes are observed in the structural and magnetic properties of the films. The structural order improves as T_B increases, as evidenced by the XRD measurements. The integrated intensity of both the structural CFS(004) and the CFS(002) superlattice reflection increases with T_B ; whereas the FWHM of both peaks decreases, also indicating an improvement of the crystallinity of the films. Signs of the CFS(111) superlattice reflection start appearing at $T_B = 350^\circ\text{C}$, albeit very weak, and are strongly present

at $T_B = 550^\circ\text{C}$. Although the presence of the $L2_1$ phase at $T_B = 350^\circ\text{C}$ seemed weak based on XRD, FFTs performed on HAADF-images suggest that the degree of $L2_1$ ordering might actually be stronger due to the presence of a strong 111 diffraction spot. In order to quantify and compare the B2/ $L2_1$ ratio among the three films, nanodiffraction experiments are planned on all these samples to be performed in the near future.

VSM measurements have shown that the saturation magnetization of these films is constant within error ($\approx 1000 \pm 50$ emu/cc) and very close to the bulk value of CFS (≈ 1100 emu/cc). FMR measurements have shown the coexistence of a uniaxial anisotropy superimposed on a cubic MCA which could not be observed in the previous (111)-oriented CFS films. The angular dependence of the resonant field was fitted to the appropriate model giving reliable values for the uniaxial anisotropy constant (K_u) and the cubic anisotropy constant (K_c). Although the values for M_{eff} (and K_\perp) have also been shown, it has been found that this fitting parameter is strongly coupled with γ and hence, the fitting has to be further improved to be able to extract reliable values for these two parameters. The film grown at $T_B = 350^\circ\text{C}$ is the most anisotropic film showing a K_u of $3.7 \pm 0.2 \times 10^4$ and a K_c of $2.73 \pm 0.01 \times 10^4$ erg/cm³, both of which drop at $T_B = 550^\circ\text{C}$ to $2.2 \pm 0.1 \times 10^4$ and $0.82 \pm 0.02 \times 10^4$ erg/cm³ respectively (values close to those shown by the low temperature film). The behaviour of the uniaxial anisotropy with the substrate temperature is difficult to explain given its unknown origin. The increase in K_c at $T_B = 350^\circ\text{C}$, on the other hand, correlates with a decrease in the Gilbert damping parameter.

The films grown at $T_B < 130^\circ\text{C}$ and $T_B = 350^\circ\text{C}$ show a linear dependence of the resonant linewidth with frequency, hence the intrinsic damping is dominant in this samples. The Gilbert parameter decreases by half from $13.6 \pm 0.3 \times 10^{-3}$ at $T_B < 130^\circ\text{C}$ to $6.5 \pm 0.1 \times 10^{-3}$ at $T_B = 350^\circ\text{C}$. The value obtained at $T_B = 350^\circ\text{C}$ is comparable to the α measured for the non-annealed films on Si(111). At $T_B = 550^\circ\text{C}$, the linearity is lost and the sample shows a dominant extrinsic damping mechanism. The extrinsic damping is probably related to an increment of magnetic impurities in the film as a result of outdiffusion of Mg into the film. Overall, from the structural and magnetic characterization it can be concluded that the optimal growth temperature for the growth of CFS on MgO(001) is $T_B = 350^\circ\text{C}$.

Finally, at the end of this chapter, the effects of a NiO overlayer on the MCA of the CFS films, all of them grown at $T_B = 350^\circ\text{C}$, has been shown for different NiO thicknesses. For all these films the EAs and HAs of the CFS are swapped. Whereas the EA in the uncapped films was along the $\langle 100 \rangle$ directions, the EA for the capped films is shifted towards the $\langle 1\bar{1}0 \rangle$ directions of CFS. It was demonstrated that this swap is a consequence of a change of K_c from positive to negative values. A similar change in K_c was observed in Co_2MnSi films upon increasing the annealing temperature [Yil07], although the reason is still unclear. In our case,

the most likely cause is either a change in the chemical composition of the films or the proximity effect with the AFI layer, which is subject to current research.

Chapter 7

Conclusions and Outlook

7.1 Conclusions

The present work was undertaken with two main objectives. The first was the commissioning of a MBE system for the growth of high quality $\text{Co}_2\text{FeAl}_{1-x}\text{Si}_x$ Heusler films. The second objective was the growth optimization of CFS films grown on technologically relevant substrates, namely Si(111) and MgO(001). With that aim, the effect of stoichiometry and the substrate temperature on the structural and magnetic properties of CFS has been investigated. The growth of epitaxial CFS films has been achieved with properties comparable to those reported in the literature for high quality Heusler films. This demonstrates that the MBE system developed in this thesis is effective for the growth of high quality Co-based metallic Heusler films. Finally, the growth of NiO on CFS has been also explored in the context of HM/AFM(AFI)/HMF structures.

7.1.1 CFS/Si(111)

The concentration of Si in CFS films can be traced by looking at the out-of plane lattice constant and M_s , both of which decrease with T_{Si} and hence, serve as indicators of the chemical composition of the films which can not be measured by simple planar EDS measurements. XRD has proved to be an invaluable technique to compare the structural ordering among the films through the presence of the (111) and (222) superlattice reflections. The ordering peaks have a higher integrated intensity and a smaller width when the film stoichiometry is optimum. At that point, $T_{\text{Si}} = 1045 \pm 5^\circ\text{C}$, the lattice constant has a value close to bulk CFS $a = 5.647 \pm 0.001 \text{ \AA}$, and an M_s value also close but lower than bulk, $M_s = 800 \pm 90 \text{ emu/cc}$. HAADF-STEM has confirmed the existence of B2 and L2_1 ordered grains in all the films

with $1025^\circ\text{C} \leq T_{Si} \leq 1045^\circ\text{C}$, although to quantify the degree of $L2_1$ to B2 ratio 4D-STEM measurements are still needed. HAADF-STEM has also shown changes in the CFS/Si interface among the Si-rich specimens and Si-poor specimens, which might be arising from Si-outdiffusion or the formation of secondary phases. This has to be further assessed with EELS experiments. The stoichiometry of the films has also an important impact on the magnetic damping. The damping constant increases with the addition of Si, although a local minimum is observed at $T_{Si} = 1045 \pm 5^\circ\text{C}$ which could be related to the improvement of crystallinity. The Gilbert damping at $T_{Si} = 1045^\circ\text{C}$ is $8.1 \pm 0.2 \times 10^{-3}$, comparable to the values found in literature for non-annealed CFS films [Oog07; Haz19]. Finally, FMR studies on the in-plane anisotropy have shown that even at low growth temperatures $< 130^\circ\text{C}$, interfacial effects result in the change of the uniaxial anisotropy which switches the EA from $[10\bar{1}]$ at $T_{Si} < 1040^\circ\text{C}$ to $[1\bar{1}0]$ at $T_{Si} \geq 1040^\circ\text{C}$. Because the origin of this anisotropy is unknown, it will be interesting to see if this switch is due to the changes observed in the CFS/Si interface via HAADF-STEM.

7.1.2 CFS/MgO(001)

The growth of CFS films on MgO(001) substrates has been more challenging than on Si(111) due to the larger mismatch with this substrate. The concentration of Si in the film could also be tracked by the out-of plane lattice constant and the integrated intensity of the B2 superlattice reflection. The chemical composition could this time be correlated with planar EDS. Conversely to Si(111), the growth temperature has to be risen to 350°C before the $L2_1$ superlattice reflection can be observed. Increasing the substrate temperature to 350°C additionally results in a significant improvement of the magnetic properties of the film. The Gilbert damping is reduced by half to $6.5 \pm 0.1 \times 10^{-3}$ at $T_B = 350^\circ\text{C}$, which is among the lowest values found in literature for this substrate. This value is of the same order of magnitude as the one measured for CFS on Si(111) grown at RT. Further increasing the substrate temperature to 550°C leads to an improvement of the structural ordering but at the expense of a large extrinsic damping effect revealed in the behaviour of $\Delta H(\omega)$. Hence, this high-temperature annealed film is less suitable for practical applications. The reason for such detrimental effects on the magnetic damping are still under investigation, with the first option being segregation of Mg to the CFS film. Finally, the MCA of CFS has been discussed. The MCA measured for the uncapped CFS films corresponds to the expected cubic MCA with $K_c > 0$, that is with the EAs along the $\langle 100 \rangle$ directions of CFS. However, this disagrees with the observations of other authors who find the EA along the $\langle 110 \rangle$ [Wan08; Has05].

7.1.3 NiO[t]/Fe[1]/CFS/MgO(001)

In the last part of the thesis, the influence of an AFI on CFS has been investigated in a series of NiO[t]/Fe[1]/CFS/MgO(001) structures. NiO has the same isostructure and very similar lattice constant to MgO and hence, its lattice mismatch with CFS is the same as the mismatch between CFS and MgO. NiO grows as a single crystal with the aid of a 1nm-thick Fe buffer layer. However, as a consequence of the rough CFS surface, the NiO/Fe and Fe/CFS interfaces are also rough. (S)TEM images suggest that instead of a 1nm-Fe interlayer, a thicker crystalline layer is present between NiO and CFS which needs to be characterized. XRR measurements indicate that this interlayer is not single-crystal Fe but that oxide compounds might be present from the oxidation of the Fe surface. Despite the rough interface, the AFI overlayer changes the magnetic properties of CFS and specifically has an effect on the MCA. Even for a NiO layer as thin as 3 nm, the capped-CFS films now show an EA along the $\langle 110 \rangle$. Therefore, in the NiO/Fe[1]/CFS/MgO(001) structures the EA of CFS is found along the same direction that has been reported in literature for CFS thin films [Wan08; Has05]. Although, in contrast to the works by Wand *et al.* [Wan08] and Hashimoto *et al.* [Has05] where this feature was attributed to the superimposed uniaxial anisotropy, in our case it is indubitably due to a negative value of K_c . Further work is now needed to see if the change in K_c is due to a change in the chemical composition of the CFS layer or else, due to the exchange coupling between NiO and CFS.

7.2 Future work

7.2.1 MBE growth and system development

With respect to the MBE system, several modifications can still be made to improve the versatility of the system. Provision has been made for the incorporation of other k-cells or e-beam evaporators to grow metallic capping layers such as Pt or Au. The sample manipulator and heating stage assembly would also benefit from a few changes. Such changes include the addition of a motor to allow for sample rotation, and to redesign the sample holder so that RHEED patterns can be taken at different azimuthal angles.

Moreover, other additions should be considered in the future to facilitate the maintenance of the system. Because all the growth is carried out under UHV, each time the chamber is vented, it has to be baked again. This means that at least 1 month has to pass before the base pressure of the system has returned to optimum conditions. Hence, if the frequency of interventions can be reduced, it would save the researcher a valuable amount of time and effort.

Specifically, the most helpful incorporation would be a gate valve between the turbo-pump and the vacuum chamber that maintains the vacuum if the pumps have to be stopped for a short period of time (due to for example, a brief power outage). Secondly, linear drives and individual pumping lines could be installed for each source so that one can withdraw them from the vacuum chamber, load them and put them back in without exposing the main chamber to atmospheric pressure. Finally, a buffer chamber equipped with a sample carousel would be ideal to store multiple substrates in UHV conditions. This would have been extremely helpful for the growth on Si(111) for example, in order to minimise the amount of time spent in the cleanroom doing HF-cleaning.

Regarding CFS Heusler growth, work is required to further optimise growth conditions, especially on MgO(001). The films grown on MgO(001) have turned out to be rougher than on Si(111), so attempts should be made to grow smoother films if one wants to use them in multilayer structures. The first approach in the author's opinion should be rotating the substrate during growth as this will indubitably improve film homogeneity and possibly, film roughness. If after doing so the CFS films are still rough, the roughness might be arising from the lattice mismatch between CFS and MgO. Therefore, one could try growing an MgO or a Cr buffer layer before depositing the CFS film. Because the oxide chamber used in this work is provided with Mg, the MgO interlayer would be the first option in our case. However, before doing this, it would be advisable to spend some time studying the substrate preparation method for MgO(001) as this might have an impact on the morphology of the film as well.

7.2.2 CFS/Si(111)

The CFS samples in this work show promising structural and magnetic properties, including partial $L2_1$ order and low Gilbert damping. However, certain fundamental mechanisms-correlations are still unclear. Hence, further work in these films will focus on microscopy experiments, 4D-STEM, that study the correlation between the chemical composition and the structural ordering of the grains. If important chemical variations are measured throughout the films, this means that future growth optimization has to be aimed towards the minimization of these chemical fluctuations. The first place to start would then be adding sample rotation as mentioned earlier. Although the imperfections in these films might have to be addressed before implementing them for spintronic applications, they still provide a good platform for the investigation of various interesting features such as the characterization of the Heusler/SC interface and its impact on the properties of the film. As is known, interfaces can have drastic effects on spin-polarization and in turn, on spin injection efficiency which is the most relevant

quality of $\text{Co}_2\text{FeAl}_{1-x}\text{Si}_x$ Heuslers. Changes in the CFS/Si interface in our films are evident from the behaviour of the uniaxial anisotropy. Thus, the second subject of interest will be to correlate the anisotropy with the formation of interfacial phases or other chemical changes at the interface.

7.2.3 CFS/MgO(001)

Stoichiometric CFS films grown on MgO(001) have shown comparable properties to those grown on Si(111) when the growth temperature is risen to 350°C. Future work on these films follows the same path as the CFS/Si(111) samples, but in this case focusing on the effects of growth temperature (rather than film stoichiometry) on the properties of the film. HAADF-STEM measurements are still missing on the CFS/MgO(001) samples to see how the substrate temperature affects the grain structure of the films. Similar 4D-STEM experiments are also under way and will allow to compare the $L2_1$ to B2 ratio of these films to the ones grown at RT on Si(111). Because annealing processes are prone to affect the characteristics of the interface, chemical and structural analysis of the CFS/MgO interface will also be performed. In fact, the sharpness or smoothness of the interface might also provide some insight on why these films are systematically rougher when they are grown on MgO. On the other hand, given that the mismatch of CFS with MgO is larger than with Si, studying the presence of strain in these films could also be of interest to consider introducing a buffer layer between the film and the substrate.

7.2.4 NiO[t]/Fe[1]/CFS/MgO(001)

With respect to the NiO/Fe[1]/CFS/MgO(001) heterostructures, the cause of the negative MCA and the multi-step switching mechanism of CFS should be investigated. The first step to do so in the author's opinion, is to perform a complete characterization of the multilayered structures with cross-sectional STEM-HAADF imaging and with correlated diffraction and chemical analysis, focused firstly on the bulk of the CFS layer, and secondly on the NiO/Fe and Fe/CFS interfaces. If the diffraction and chemical analysis discards that the change in K_c is due to a change in the bulk chemical composition and structure of CFS, then a more systematic study might be needed involving the growth of more heterostructures with varying thickness of the CFS layer and the Fe interlayer in order to study the coupling between NiO and CFS. Looking further ahead, one should put an effort on improving the quality of the NiO/Fe/CFS interfaces which relies on growing smoother CFS films on the MgO(001) surface.

List of abbreviations

1D	one-dimensional
2D	two-dimensional
ACE	acetone
AFI	antiferromagnetic insulator
AFM	antiferromagnetic metal
AHE	anomalous Hall effect
AMR	anisotropic magnetoresistance
BF	bright-field
CAN	cubic anisotropy
CCD	charge-coupled-device
CCFA	$\text{Co}_2(\text{Cr}_{0.6}\text{Fe}_{0.4})\text{Al}$
CFA	Co_2FeAl
CFAS	$\text{Co}_2\text{FeAl}_{0.5}\text{Si}_{0.5}$
CFGG	$\text{Co}_2\text{Fe}(\text{Ga}_{0.5}\text{Ge}_{0.5})$
CFMS	$\text{Co}_2\text{Fe}_{0.5}\text{Mn}_{0.5}\text{Si}$
CFS	Co_2FeSi
CPP	current-perpendicular-to-plane
CPW	co-planar waveguide
CVD	chemical vapor deposition
DF	dark-field
DI	deionized
DMS	diluted magnetic semiconductors
DOS	density of states
DP	diffraction pattern
EA	easy axis
ECP	electrochemical potential
EDS	energy dispersive x-ray spectrometry

EELS	electron energy-loss spectrometry
EXC	exchange coupling
FEL	fast entry lock
FIB	focused ion beam
FM	ferromagnetic metal
FMI	ferromagnetic insulator
FMR	ferromagnetic resonance
FVM	Frank van der Merwe
FWHM	full width at half maximum
GIS	gas injection system
GMR	giant magnetoresistance
HA	hard axis
HAADF	high angle annular dark field
HF	hydrofluoric acid
HM	heavy metal
HMF	half-metallic ferromagnet
HRTEM	high-resolution TEM
HTEZ	high temperature effusion cell
IG	ionization gauge
IO	insulating oxide
iSHE	inverse SHE effect
LLG	Landau-Lifshitz-Gilbert
LMIS	liquid metal ion source
LSV	lateral spin-valve
MBE	molecular beam epitaxy
MCA	magnetocrystalline anisotropy
ME	magnetoelastic
MOCVD	metal organic CVD
MS	magnetostatic
MTJ	magnetic tunnelling junction
NM	normal metal
PID	proportional-integral-derivative
PLD	pulsed laser deposition
QCM	Quartz crystal microbalance
RGA	residual gas analyzer

List of abbreviations

RHEED	Reflection High Energy Electron diffraction
ROI	region of interest
RT	room temperature
SAED	selected area diffraction
SC	semiconductor
S-FET	spin field-effect transistor
SHE	Spin Hall effect
SK	Stransky-Krastonov
SLD	scattering length density
SOC	spin-orbit coupling
SOT	spin-orbit torque
SP	spin polarisation
SSE	Spin Seebeck effect
STEM	Scanning transmission electron microscope
STO	SrTiO ₃
STT	spin transfer torque
SUSI	Silicon Sublimation Source
SV	spin-valve
T _c	Curie temperature
TEM	transmission electron microscope
TMR	tunnel magnetoresistance
TMS	tunnel magneto-Seebeck effect
TSP	titanium sublimation pump
UAN	uniaxial anisotropy
UHV	ultra-high vacuum
VNA	vector network analyzer
VSM	vibrating sample magnetometer
VW	Volmer-Weber
WEZ	standard temperature effusion cell
XAS	x-ray absorption spectroscopy
XRD	x-ray diffraction
YIG	yttrium iron garnet, Y ₃ Fe ₅ O ₁₂

Bibliography

- [AKP00a] T Ambrose, JJ Krebs, and GA Prinz. “Epitaxial growth and magnetic properties of single-crystal Co₂MnGe Heusler alloy films on GaAs (001)”. In: *Applied Physics Letters* 76.22 (2000), pp. 3280–3282.
- [AKP00b] T Ambrose, JJ Krebs, and GA Prinz. “Magnetic properties of single crystal Co₂MnGe Heusler alloy films”. In: *Journal of Applied Physics* 87.9 (2000), pp. 5463–5465.
- [Alb00] FJ Albert et al. “Spin-polarized current switching of a Co thin film nanomagnet”. In: *Applied Physics Letters* 77.23 (2000), pp. 3809–3811.
- [AM76] Neil W Ashcroft, N David Mermin, et al. *Solid state physics*. Vol. 2005. holt, rinehart and winston, new york London, 1976.
- [AM99] Rodrigo Arias and DL Mills. “Extrinsic contributions to the ferromagnetic resonance response of ultrathin films”. In: *Physical review B* 60.10 (1999), p. 7395.
- [AMS00] Hiro Akinaga, Takashi Manago, and Masafumi Shirai. “Material design of half-metallic zinc-blende CrAs and the synthesis by molecular-beam epitaxy”. In: *Japanese Journal of Applied Physics* 39.11B (2000), p. L1118.
- [And97] J. F. Anderson et al. “Surface structure and morphology of Mg-segregated epitaxial Fe₃O₄(001) thin films on MgO(001)”. In: *Phys. Rev. B* 56 (15 1997), pp. 9902–9909.
- [Bai88] Mario Norberto Baibich et al. “Giant magnetoresistance of (001) Fe/(001) Cr magnetic superlattices”. In: *Physical review letters* 61.21 (1988), p. 2472.
- [Bap18] Mukund Bapna et al. “Spin-orbit-torque switching in 20-nm perpendicular magnetic tunnel junctions”. In: *Physical Review Applied* 10.2 (2018), p. 024013.
- [Bas09] Lubna Basit et al. “Heusler compounds as ternary intermetallic nanoparticles: Co₂FeGa”. In: *Journal of Physics D: Applied Physics* 42.8 (2009), p. 084018.

- [Bil07] Claus Bilzer. “Microwave susceptibility of thin ferromagnetic films: metrology and insight into magnetization dynamics”. PhD thesis. Université Paris Sud-Paris XI, 2007.
- [Bin89] Grünberg Binasch et al. “Enhanced magnetoresistance in layered magnetic structures with antiferromagnetic interlayer exchange”. In: *Physical review B* 39.7 (1989), p. 4828.
- [Blo46] Felix Bloch. “Nuclear induction”. In: *Physical review* 70.7-8 (1946), p. 460.
- [Blu03] Stephen Blundell. *Magnetism in condensed matter*. 2003.
- [Boe17] Alexander Boehnke et al. “Large magneto-Seebeck effect in magnetic tunnel junctions with half-metallic Heusler electrodes”. In: *Nature communications* 8.1 (2017), pp. 1–7.
- [Boz93] Richard M Bozorth. *Ferromagnetism*. 1993.
- [Bro00] PJ Brown et al. “The magnetization distributions in some Heusler alloys proposed as half-metallic ferromagnets”. In: *Journal of Physics: Condensed Matter* 12.8 (2000), p. 1827.
- [But01] WH Butler et al. “Spin-dependent tunneling conductance of Fe—MgO—Fe sandwiches”. In: *Physical Review B* 63.5 (2001), p. 054416.
- [BVEJ83] KHJ v Buschow, PG Van Engen, and R Jongebreur. “Magneto-optical properties of metallic ferromagnetic materials”. In: *Journal of magnetism and magnetic materials* 38.1 (1983), pp. 1–22.
- [Cam15] Robert E Camley et al. “Handbook of Surface Science”. In: (2015).
- [Cha04] Austin Chambers. *Modern vacuum physics*. CRC Press, 2004.
- [Che20] Ping Che et al. “Efficient wavelength conversion of exchange magnons below 100 nm by magnetic coplanar waveguides”. In: *Nature communications* 11.1 (2020), pp. 1–9.
- [CSH14] Andrii V Chumak, Alexander A Serga, and Burkard Hillebrands. “Magnon transistor for all-magnon data processing”. In: *Nature communications* 5.1 (2014), pp. 1–8.
- [Cui14] Yishen Cui et al. “Magnetic damping and spin polarization of highly ordered B2 Co₂FeAl thin films”. In: *Journal of Applied Physics* 116.7 (2014), p. 073902.
- [Cul56] Bernard Dennis Cullity. *Elements of X-ray Diffraction*. Addison-Wesley Publishing, 1956.

- [CW16] C Barry Carter and David B Williams. *Transmission electron microscopy: Diffraction, imaging, and spectrometry*. Springer, 2016.
- [DD90] Supriyo Datta and Biswajit Das. “Electronic analog of the electro-optic modulator”. In: *Applied Physics Letters* 56.7 (1990), pp. 665–667.
- [Dec18] Martin Maria Decker. “Spin current induced control of magnetization dynamics”. PhD thesis. 2018.
- [DG83] RA De Groot et al. “New class of materials: half-metallic ferromagnets”. In: *Physical Review Letters* 50.25 (1983), p. 2024.
- [DP71] MI D’yakonov and VI Perel. “Spin orientation of electrons associated with the interband absorption of light in semiconductors”. In: *Soviet Journal of Experimental and Theoretical Physics* 33 (1971), p. 1053.
- [Dya07] MI Dyakonov. “Magnetoresistance due to edge spin accumulation”. In: *Physical review letters* 99.12 (2007), p. 126601.
- [Ell54] R _ J Elliott. “Theory of the effect of spin-orbit coupling on magnetic resonance in some semiconductors”. In: *Physical Review* 96.2 (1954), p. 266.
- [Eve] Everspin. *Everspin ships first ST-MRAM memory with 500X performance of flash/Computerworld*. <https://www.computerworld.com/article/2493603/everspin-ships-first-st-mram-memory-with-500x-performance-of-flash.html>.
- [Far98] Michael Farle. “Ferromagnetic resonance of ultrathin metallic layers”. In: *Reports on progress in physics* 61.7 (1998), p. 755.
- [Fel15] Claudia Felser et al. “Basics and prospective of magnetic Heusler compounds”. In: *APL materials* 3.4 (2015), p. 041518.
- [FF07] Gerhard H Fecher and Claudia Felser. “Substituting the main group element in cobalt–iron based Heusler alloys: Co₂FeAl_{1-x}Si_x”. In: *Journal of Physics D: Applied Physics* 40.6 (2007), p. 1582.
- [FH12] Brent Fultz and James M Howe. *Transmission electron microscopy and diffraction of materials*. Springer Science & Business Media, 2012.
- [FJ01] A Fert and H Jaffres. “Conditions for efficient spin injection from a ferromagnetic metal into a semiconductor”. In: *Physical Review B* 64.18 (2001), p. 184420.
- [Fon59] Simon Foner. “Versatile and sensitive vibrating-sample magnetometer”. In: *Review of Scientific Instruments* 30.7 (1959), pp. 548–557.

- [Fuj17] Y Fujita et al. “Spin transport and relaxation up to 250 k in heavily doped n-type Ge detected using Co₂FeAl_{0.5}Si_{0.5} electrodes”. In: *Physical Review Applied* 8.1 (2017), p. 014007.
- [Fur13] T Furubayashi et al. “Temperature dependence of magnetoresistive output of pseudo spin valves with Co₂Fe (Al_{1-x}Si_x) Heusler alloys and a Ag spacer”. In: *Journal of Applied Physics* 114.12 (2013), p. 123910.
- [Gan17] Kathrin Ganzhorn et al. “Temperature dependence of the non-local spin Seebeck effect in YIG/Pt nanostructures”. In: *AIP Advances* 7.8 (2017), p. 085102.
- [Gen] *GenX documentation*. https://aglavic.github.io/genx/doc/tutorials/xrr_fitting.html. Online; accessed 1-December-2021.
- [GFP11] Tanja Graf, Claudia Felser, and Stuart SP Parkin. “Simple rules for the understanding of Heusler compounds”. In: *Progress in solid state chemistry* 39.1 (2011), pp. 1–50.
- [GH00] A Gibaud and S Hazra. “X-ray reflectivity and diffuse scattering”. In: *Current Science* (2000), pp. 1467–1477.
- [Gil04] Thomas L Gilbert. “A phenomenological theory of damping in ferromagnetic materials”. In: *IEEE transactions on magnetics* 40.6 (2004), pp. 3443–3449.
- [Gil16] Daniel Gilks et al. “Polar Spinel-Perovskite Interfaces: an atomistic study of Fe₃O₄ (111)/SrTiO₃ (111) structure and functionality”. In: *Scientific reports* 6 (2016), p. 29724.
- [Gre02] JF Gregg et al. “Spin electronics—a review”. In: *Journal of Physics D: Applied Physics* 35.18 (2002), R121.
- [GS99] Lucille A Giannuzzi and Frederick A Stevie. “A review of focused ion beam milling techniques for TEM specimen preparation”. In: *Micron* 30.3 (1999), pp. 197–204.
- [Gup05] Ratnesh Gupta et al. “Influence of ion implantation on the magnetic properties of thin FeCo films”. In: *Journal of applied physics* 97.7 (2005), p. 073911.
- [Ham12] K Hamaya et al. “Estimation of the spin polarization for Heusler-compound thin films by means of nonlocal spin-valve measurements: Comparison of Co₂FeSi and Fe₃Si”. In: *Physical Review B* 85.10 (2012), p. 100404.
- [Ham16] Kohei Hamaya et al. “Finely Controlled Approaches to Formation of Heusler-Alloy/Semiconductor Heterostructures for Spintronics”. In: *Materials Transactions* 57.6 (2016), pp. 760–766.

- [Han02] Aubrey T Hanbicki et al. “Efficient electrical spin injection from a magnetic metal/tunnel barrier contact into a semiconductor”. In: *Applied Physics Letters* 80.7 (2002), pp. 1240–1242.
- [Han13] Paul M Haney et al. “Current induced torques and interfacial spin-orbit coupling: Semiclassical modeling”. In: *Physical Review B* 87.17 (2013), p. 174411.
- [Has05] M Hashimoto et al. “Epitaxial Heusler alloy Co₂FeSi/GaAs (001) hybrid structures”. In: *Applied Physics Letters* 87.10 (2005), p. 102506.
- [Has07] M Hashimoto et al. “Growth temperature dependent interfacial reaction of Heusler-alloy Co₂FeSi/GaAs (001) hybrid structures”. In: *Journal of Physics D: Applied Physics* 40.6 (2007), p. 1631.
- [Haz19] Binoy Krishna Hazra et al. “Uniaxial anisotropy, intrinsic and extrinsic damping in Co₂FeSi Heusler alloy thin films”. In: *Journal of Physics D: Applied Physics* 52.32 (2019), p. 325002.
- [Haz20] Binoy Krishna Hazra et al. “Magneto-optical Kerr microscopy investigation of magnetization reversal in Co₂FeSi Heusler alloy thin films”. In: *AIP Advances* 10.6 (2020), p. 065017.
- [Heu03] Friedrich Heusler. “Über magnetische manganlegierungen”. In: *Verhandlungen der Deutschen Physikalischen Gesellschaft* 5 (1903), p. 219.
- [HHR19] Georg Hoffmann, Jens Herfort, and Manfred Ramsteiner. “Spin generation in completely MBE-grown Co₂FeSi/MgO/GaAs lateral spin valves”. In: *Physical Review Materials* 3.7 (2019), p. 074402.
- [Hir13] Atsufumi Hirohata et al. “Heusler-alloy films for spintronic devices”. In: *Applied Physics A* 111.2 (2013), pp. 423–430.
- [Hit] *Hitachi products*. <https://www.hitachi-ies.co.jp/english/products/air/scroll/features.htm>. Accessed: 9-June-2019.
- [HM09] Mark C Hickey and Jagadeesh S Moodera. “Origin of intrinsic Gilbert damping”. In: *Physical review letters* 102.13 (2009), p. 137601.
- [HSH03] Fr Heusler, W Starck, and E Haupt. “Magnetisch-chemische studien”. In: *Verh. Dtsch. Phys. Ges* 5 (1903), pp. 219–232.
- [HSL13] PJ Hasnip, JH Smith, and VK Lazarov. “Ab initio studies of disorder in the full Heusler alloy Co₂FexMn_{1-x}Si”. In: *Journal of Applied Physics* 113.17 (2013), 17B106.

- [Hua19] Xiufeng Huang et al. “Spin Hall magnetoresistance in Co₂MnSn/IrMn/Pt heterostructures”. In: *Journal of Magnetism and Magnetic Materials* 477 (2019), pp. 62–67.
- [Hua20] SY Huang et al. “Pure spin current phenomena”. In: *Applied Physics Letters* 117.19 (2020), p. 190501.
- [Hus18] Sajid Husain et al. “Spin pumping in the Heusler alloy Co₂FeAl/MoS₂ heterostructure: Ferromagnetic resonance experiment and theory”. In: *Physical Review B* 98.18 (2018), p. 180404.
- [Ide] *Ideal Vacuum catalog*. https://www.idealvac.com/files/literature/Sec_02_Ideal_Vacuum_Rotary_Vane.pdf. Accessed: 9-June-2019.
- [Ike08] S Ikeda et al. “Tunnel magnetoresistance of 604% at 300 K by suppression of Ta diffusion in Co/Fe/B/MgO/Co/Fe/B pseudo-spin-valves annealed at high temperature”. In: *Applied Physics Letters* 93.8 (2008), p. 082508.
- [Ino03] Koichiro Inomata et al. “Large tunneling magnetoresistance at room temperature using a Heusler alloy with the B2 structure”. In: *Japanese journal of applied physics* 42.4B (2003), p. L419.
- [Ino08] K Inomata et al. “Site disorder in Co₂Fe(Al, Si) Heusler alloys and its influence on junction tunnel magnetoresistance”. In: *Physical Review B* 77.21 (2008), p. 214425.
- [Ish08] Takayuki Ishikawa et al. “Fabrication of fully epitaxial Co₂MnSi/MgO/Co₂MnSi magnetic tunnel junctions”. In: *Journal of Applied Physics* 103.7 (2008), 07A919.
- [JFVW01] Friso Jacobus Jedema, AT Filip, and BJ Van Wees. “Electrical spin injection and accumulation at room temperature in an all-metal mesoscopic spin valve”. In: *Nature* 410.6826 (2001), pp. 345–348.
- [Joh96] MT Johnson et al. “Magnetic anisotropy in metallic multilayers”. In: *Reports on Progress in Physics* 59.11 (1996), p. 1409.
- [Jul75] Michel Julliere. “Tunneling between ferromagnetic films”. In: *Physics letters A* 54.3 (1975), pp. 225–226.
- [Jun16] JW Jung et al. “Enhancement of magnetoresistance by inserting thin NiAl layers at the interfaces in Co₂FeGa_{0.5}Ge_{0.5}/Ag/Co₂FeGa_{0.5}Ge_{0.5} current-perpendicular-to-plane pseudo spin valves”. In: *Applied Physics Letters* 108.10 (2016), p. 102408.

- [KC01] Walter S Knodle and Robert Chow. “Molecular beam epitaxy: Equipment and practice”. In: *Handbook of thin film deposition processes and techniques*. Elsevier, 2001, pp. 381–461.
- [KFF07] Hem C Kandpal, Gerhard H Fecher, and Claudia Felser. “Calculated electronic and magnetic properties of the half-metallic, transition metal based Heusler compounds”. In: *Journal of Physics D: Applied Physics* 40.6 (2007), p. 1507.
- [Kim12] Takashi Kimura et al. “Room-temperature generation of giant pure spin currents using epitaxial Co₂FeSi spin injectors”. In: *NPG asia materials* 4.3 (2012), e9–e9.
- [Kit51] Charles Kittel. “Ferromagnetic resonance”. In: (1951).
- [KL54] Robert Karplus and JM Luttinger. “Hall effect in ferromagnetics”. In: *Physical Review* 95.5 (1954), p. 1154.
- [Kos05] MP Kostylev et al. “Spin-wave logical gates”. In: *Applied Physics Letters* 87.15 (2005), p. 153501.
- [Kri16] Kannan M Krishnan. *Fundamentals and applications of magnetic materials*. Oxford University Press, 2016.
- [Kub17] Takahide Kubota et al. “Current perpendicular-to-plane giant magnetoresistance using an L₁2 Ag₃Mg spacer and Co₂Fe_{0.4}Mn_{0.6}Si Heusler alloy electrodes: Spacer thickness and annealing temperature dependence”. In: *Physical Review Materials* 1.4 (2017), p. 044402.
- [Kud19] Kohei Kudo et al. “Great Differences between Low-Temperature Grown Co₂FeSi and Co₂MnSi Films on Single-Crystalline Oxides”. In: *ACS Applied Electronic Materials* 1.11 (2019), pp. 2371–2379.
- [Kue16] Balati Kuerbanjiang et al. “The role of chemical structure on the magnetic and electronic properties of Co₂FeAl_{0.5}Si_{0.5}/Si (111) interface”. In: *Applied Physics Letters* 108.17 (2016), p. 172412.
- [Kue18] Balati Kuerbanjiang et al. “Effect of annealing on the structure and magnetic properties of Co₂FeAl_{0.5}Si_{0.5} thin films on Ge(111)”. In: *Journal of Alloys and Compounds* 748 (2018), pp. 323–327. ISSN: 0925-8388.
- [Kum17] Ankit Kumar et al. “Temperature-dependent Gilbert damping of Co₂FeAl thin films with different degree of atomic order”. In: *Physical Review B* 96.22 (2017), p. 224425.

- [LC17] Weiwei Lin and CL Chien. “Electrical detection of spin backflow from an antiferromagnetic insulator/Y 3 Fe 5 O 12 interface”. In: *Physical review letters* 118.6 (2017), p. 067202.
- [Lei21] L Leiva et al. “Giant spin Hall angle in the Heusler alloy Weyl ferromagnet Co 2 MnGa”. In: *Physical Review B* 103.4 (2021), p. L041114.
- [Li18] Songtian Li et al. “Enhanced current-perpendicular-to-plane giant magnetoresistance by improvement of atomic order of Co₂FeSi Heusler alloy film through Ag doping”. In: *AIP Advances* 8.7 (2018), p. 075230.
- [Lin16] Weiwei Lin et al. “Enhancement of thermally injected spin current through an antiferromagnetic insulator”. In: *Physical review letters* 116.18 (2016), p. 186601.
- [LL35] E. LIFSHITS L. LANDAU. In: *Phys. Zeitsch. der Sow.* 8.153 (1935).
- [LL72] Chih-Shun Lu and Owen Lewis. “Investigation of film-thickness determination by oscillating quartz resonators with large mass load”. In: *Journal of Applied Physics* 43.11 (1972), pp. 4385–4390.
- [Loo14] Li Ming Loong et al. “Investigation of the temperature-dependence of ferromagnetic resonance and spin waves in Co₂FeAl_{0.5}Si_{0.5}”. In: *Applied Physics Letters* 104.23 (2014), p. 232409.
- [Lüt01] Hans Lüth. *Solid surfaces, interfaces and thin films*. Vol. 4. Springer, 2001.
- [MM33] Nevill Francis Mott and Harrie Stewart Wilson Massey. “Theory of atomic collisions”. In: *Theory of Atomic Collisions* (1933).
- [MNS04] Yoshio Miura, Kazutaka Nagao, and Masafumi Shirai. “Atomic disorder effects on half-metallicity of the full-Heusler alloys Co₂(Cr_{1-x}Fe_x)Al: A first-principles study”. In: *Physical Review B* 69.14 (2004), p. 144413.
- [MRK17] R Mohankumar, M Manivel Raja, and J Kumar. “Effect of substrate on the structural and magnetic properties of DC sputtered Co₂FeSi full Heusler alloy thin films”. In: *Journal of Crystal Growth* 468 (2017), pp. 220–224.
- [MU01] J Mathon and A Umerski. “Theory of tunneling magnetoresistance of an epitaxial Fe/MgO/Fe (001) junction”. In: *Physical Review B* 63.22 (2001), p. 220403.
- [Mun89] H Munekata et al. “Diluted magnetic III-V semiconductors”. In: *Physical Review Letters* 63.17 (1989), p. 1849.

- [MY07] Takao Marukame and Masafumi Yamamoto. “Tunnel magnetoresistance in fully epitaxial magnetic tunnel junctions with a full-Heusler alloy thin film of $\text{Co}_2\text{Cr}_{0.6}\text{Fe}_{0.4}\text{Al}$ and a MgO tunnel barrier”. In: *Journal of applied physics* 101.8 (2007), p. 083906.
- [Nak07] TM Nakatani et al. “Structure, magnetic property, and spin polarization of $\text{Co}_2\text{FeAl}_x\text{Si}_{1-x}$ Heusler alloys”. In: *Journal of Applied Physics* 102.3 (2007), p. 033916.
- [Ned15] Zlatko Nedelkoski et al. “The effect of atomic structure on interface spin-polarization of half-metallic spin valves: $\text{Co}_2\text{MnSi}/\text{Ag}$ epitaxial interfaces”. In: *Applied Physics Letters* 107.21 (2015), p. 212404.
- [Ned16a] Zlatko Nedelkoski et al. “Controlling the half-metallicity of Heusler/Si (1 1 1) interfaces by a monolayer of Si–Co–Si”. In: *Journal of Physics: Condensed Matter* 28.39 (2016), p. 395003.
- [Ned16b] Zlatko Nedelkoski et al. “Realisation of magnetically and atomically abrupt half-metal/semiconductor interface: $\text{Co}_2\text{FeSi}_{0.5}\text{Al}_{0.5}/\text{Ge}$ (111)”. In: *Scientific reports* 6.1 (2016), pp. 1–8.
- [Oka05] S Okamura et al. “Large tunnel magnetoresistance at room temperature with a Co_2FeAl full-Heusler alloy electrode”. In: *Applied Physics Letters* 86.23 (2005), p. 232503.
- [Oki13] Soichiro Oki et al. “Generation and Detection of a Pure Spin Current Using Co-Based Heusler-Alloy Spin Injector and Detector: Comparison of Co_2MnSi and Co_2FeSi ”. In: *ECS Transactions* 50.10 (2013), p. 245.
- [Oki17] S Oki et al. “Robust spin-current injection in lateral spin valves with two-terminal Co_2FeSi spin injectors”. In: *AIP Advances* 7.5 (2017), p. 055808.
- [OL02] D Ozkaya L et al. “Effect of Ga implantation on the magnetic properties of permalloy thin films”. In: *Journal of Applied Physics* 91.12 (2002), pp. 9937–9942.
- [Oog06] M Oogane et al. “Large tunnel magnetoresistance in magnetic tunnel junctions using Co_2MnX ($X = \text{Al}, \text{Si}$) Heusler alloys”. In: *Journal of Physics D: Applied Physics* 39.5 (2006), p. 834.
- [Oog07] Mikihiko Oogane et al. “Magnetic damping constant of Co_2FeSi Heusler alloy thin film”. In: *Journal of applied physics* 101.9 (2007), 09J501.

- [Oog15] M Oogane et al. “Magnetic damping constant in Co-based full heusler alloy epitaxial films”. In: *Journal of Physics D: Applied Physics* 48.16 (2015), p. 164012.
- [Oza83] K Ozawa et al. “Oblique incidence effects in evaporated iron thin films”. In: *Journal of magnetism and magnetic materials* 35.1-3 (1983), pp. 289–292.
- [Par04] Stuart SP Parkin et al. “Giant tunnelling magnetoresistance at room temperature with MgO (100) tunnel barriers”. In: *Nature materials* 3.12 (2004), pp. 862–867.
- [Par98] J-H Park et al. “Direct evidence for a half-metallic ferromagnet”. In: *Nature* 392.6678 (1998), pp. 794–796.
- [Pat19] N Patra et al. “Pulsed laser deposited Co₂FeSi Heusler alloy thin films: Effect of different thermal growth processes”. In: *Journal of Alloys and Compounds* 804 (2019), pp. 470–485.
- [Pet13] B Peters et al. “Epitaxial films of Heusler compound Co₂FeAl_{0.5}Si_{0.5} with high crystalline quality grown by off-axis sputtering”. In: *Applied Physics Letters* 103.16 (2013), p. 162404.
- [PM76] Daniel T Pierce and Felix Meier. “Photoemission of spin-polarized electrons from GaAs”. In: *Physical Review B* 13.12 (1976), p. 5484.
- [Qu13] D Qu et al. “Intrinsic spin Seebeck effect in Au/YIG”. In: *Physical review letters* 110.6 (2013), p. 067206.
- [Ram08] M Ramsteiner et al. “Co₂FeSi/GaAs/(Al, Ga)As spin light-emitting diodes: Competition between spin injection and ultrafast spin alignment”. In: *Physical Review B* 78.12 (2008), p. 121303.
- [Ras00] EI Rashba. “Theory of electrical spin injection: Tunnel contacts as a solution of the conductivity mismatch problem”. In: *Physical Review B* 62.24 (2000), R16267.
- [Rat18] Ashutosh Rath et al. “Reduced interface spin polarization by antiferromagnetically coupled Mn segregated to the Co₂MnSi/GaAs (001) interface”. In: *Physical Review B* 97.4 (2018), p. 045304.
- [Rav02] Bruce Ravel et al. “Atomic disorder in Heusler Co₂MnGe measured by anomalous x-ray diffraction”. In: *Applied physics letters* 81.15 (2002), pp. 2812–2814.
- [Ris00] Delia Ristoiu et al. “Manganese surface segregation in NiMnSb”. In: *Applied Physics Letters* 76.17 (2000), pp. 2349–2351.
- [Roy14] Kuntal Roy. “Ultra-low-energy computing paradigm using giant spin Hall devices”. In: *Journal of Physics D: Applied Physics* 47.42 (2014), p. 422001.

- [RS08] Daniel C Ralph and Mark D Stiles. “Spin transfer torques”. In: *Journal of Magnetism and Magnetic Materials* 320.7 (2008), pp. 1190–1216.
- [Sak06a] Y Sakuraba et al. “Giant tunneling magnetoresistance in Co₂MnSi/Al-O/Co₂MnSi magnetic tunnel junctions”. In: *Applied Physics Letters* 88.19 (2006), p. 192508.
- [Sak06b] Y Sakuraba et al. “Magnetic tunnel junctions using B₂-ordered Co₂MnAl Heusler alloy epitaxial electrode”. In: *Applied physics letters* 88.2 (2006), p. 022503.
- [Sán13] JC Rojas Sánchez et al. “Spin-to-charge conversion using Rashba coupling at the interface between non-magnetic materials”. In: *Nature communications* 4.1 (2013), pp. 1–7.
- [Sau59] G Sauerbrey. “Verwendung von schwingquarzen zur mikrowagung”. In: *Z. Phys* 155 (1959), p. 289.
- [Sch00] G Schmidt et al. “Fundamental obstacle for electrical spin injection from a ferromagnetic metal into a diffusive semiconductor”. In: *Physical Review B* 62.8 (2000), R4790.
- [Sch07] H Schneider et al. “Structural, magnetic and transport properties of Co₂FeSi Heusler films”. In: *Journal of Physics D: Applied Physics* 40.6 (2007), p. 1548.
- [Sin15] Jairo Sinova et al. “Spin hall effects”. In: *Reviews of Modern Physics* 87.4 (2015), p. 1213.
- [Sin21] Braj Bhusan Singh et al. “High spin mixing conductance and spin interface transparency at the interface of a Co₂Fe_{0.4}Mn_{0.6}Si Heusler alloy and Pt”. In: *NPG Asia Materials* 13.1 (2021), pp. 1–11.
- [SJ16] Meltem Sezen and M Janecek. “Focused Ion Beams (FIB)—Novel methodologies and recent applications for multidisciplinary sciences”. In: *Modern Electron Microscopy in Physical and Life Sciences* (2016).
- [Slo02] JC Slonczewski. “Currents and torques in metallic magnetic multilayers”. In: *Journal of magnetism and magnetic materials* 247.3 (2002), pp. 324–338.
- [Slo96] John C Slonczewski et al. “Current-driven excitation of magnetic multilayers”. In: *Journal of Magnetism and Magnetic Materials* 159.1 (1996), p. L1.
- [Smi55] J Smit. “Ferromagnetic resonance absorption in BaFe₁₂O₁₉, a highly anisotropic crystal”. In: *Philips Res. Rep.* 10 (1955), pp. 113–130.

- [Sou98] RJ Soulen et al. “Measuring the spin polarization of a metal with a superconducting point contact”. In: *science* 282.5386 (1998), pp. 85–88.
- [Str03] A Stroppa et al. “Electronic structure and ferromagnetism of Mn-doped group-IV semiconductors”. In: *Physical Review B* 68.15 (2003), p. 155203.
- [STT09] A Sakuma, Y Toga, and H Tsuchiura. “Theoretical study on the stability of magnetic structures in the surface and interfaces of Heusler alloys, Co_2MnAl and Co_2MnSi ”. In: *Journal of Applied Physics* 105.7 (2009), p. 07C910.
- [Suk12] Hiroaki Sukegawa et al. “Spin-transfer switching in full-Heusler Co_2FeAl -based magnetic tunnel junctions”. In: *Applied Physics Letters* 100.18 (2012), p. 182403.
- [Tez06] N Tezuka et al. “175% tunnel magnetoresistance at room temperature and high thermal stability using $\text{Co}_2\text{FeAl}_{0.5}\text{Si}_{0.5}$ full-Heusler alloy electrodes”. In: *Applied physics letters* 89.25 (2006), p. 252508.
- [TNS09] Yota Takamura, Ryosho Nakane, and Satoshi Sugahara. “Analysis of L 2 1-ordering in full-Heusler Co_2FeSi alloy thin films formed by rapid thermal annealing”. In: *Journal of Applied Physics* 105.7 (2009), 07B109.
- [Tru10] Simon Trudel et al. “Magnetic anisotropy, exchange and damping in cobalt-based full-Heusler compounds: an experimental review”. In: *Journal of Physics D: Applied Physics* 43.19 (2010), p. 193001.
- [Tso98] Maxim Tsoi et al. “Excitation of a magnetic multilayer by an electric current”. In: *Physical Review Letters* 80.19 (1998), p. 4281.
- [Uch08] K Uchida et al. “Observation of the spin Seebeck effect”. In: *Nature* 455.7214 (2008), pp. 778–781.
- [Uem07a] T Uemura et al. “Structural and magnetic properties of $\text{Co}_2\text{Cr}_{0.6}\text{Fe}_{0.4}\text{Al}$ thin films epitaxially grown on GaAs substrates with MgO interlayer”. In: *Thin Solid Films* 515.20-21 (2007), pp. 8013–8016.
- [Uem07b] Tetsuya Uemura et al. “Analysis of magnetic anisotropy for $\text{Co}_2\text{Cr}_{0.6}\text{Fe}_{0.4}\text{Al}$ thin films epitaxially grown on GaAs”. In: *Journal of Magnetism and Magnetic Materials* 310.2 (2007), e696–e698.
- [Uem08] Tetsuya Uemura et al. “Epitaxial growth and characterization of Co_2MnSi thin films on GaAs with MgO interlayer”. In: *Physica E: Low-dimensional Systems and Nanostructures* 40.6 (2008), pp. 2025–2027.

- [Vah14] Mahmoud Vahidi et al. “Fabrication of highly spin-polarized $\text{Co}_2\text{FeAl}_{0.5}\text{Si}_{0.5}$ thin-films”. In: *APL Materials* 2.4 (2014), p. 046108.
- [VF93] T Valet and A Fert. “Theory of the perpendicular magnetoresistance in magnetic multilayers”. In: *Physical Review B* 48.10 (1993), p. 7099.
- [Vig10] G Vignale. “Ten years of spin Hall effect”. In: *Journal of superconductivity and novel magnetism* 23.1 (2010), pp. 3–10.
- [WAKA13] KL Wang, JG ALZATE, and P KHALILI AMIRI. “Low-power non-volatile spintronic memory: STT-RAM and beyond: Emerging non-volatile memories: magnetic and resistive technologies”. In: *Journal of physics. D, Applied physics (Print)* 46.7 (2013).
- [Wan05a] W. H. Wang et al. “Magnetic properties and spin polarization of Co_2MnSi Heusler alloy thin films epitaxially grown on $\text{GaAs}(001)$ ”. In: *Phys. Rev. B* 71 (14 2005), p. 144416.
- [Wan05b] WH Wang et al. “Magnetic properties and spin polarization of Co_2MnSi Heusler alloy thin films epitaxially grown on $\text{GaAs}(001)$ ”. In: *Physical Review B* 71.14 (2005), p. 144416.
- [Wan08] Wenhong Wang et al. “Preparation and characterization of highly L_2-1 -ordered full-Heusler alloy $\text{Co}_2\text{FeAl}_{0.5}\text{Si}_{0.5}$ thin films for spintronics device applications”. In: *Applied Physics Letters* 92.22 (2008), p. 221912.
- [Wan18] Mengxing Wang et al. “Field-free switching of a perpendicular magnetic tunnel junction through the interplay of spin-orbit and spin-transfer torques”. In: *Nature electronics* 1.11 (2018), pp. 582–588.
- [Wen12] Zhenchao Wen et al. “Magnetic tunnel junctions with perpendicular anisotropy using a Co_2FeAl full-Heusler alloy”. In: *Applied Physics Express* 5.6 (2012), p. 063003.
- [Wij91] HPJ Wijn. “Alloys and compounds of 3d elements with main group elements”. In: *Magnetic Properties of Metals*. Springer, 1991, pp. 95–158.
- [Win12] Jürgen Winterlik et al. “Design scheme of new tetragonal Heusler compounds for spin-transfer torque applications and its experimental realization”. In: *Advanced Materials* 24.47 (2012), pp. 6283–6287.
- [Wol15] Lukas Wollmann et al. “Magnetism in tetragonal manganese-rich Heusler compounds”. In: *Physical Review B* 92.6 (2015), p. 064417.

- [Wur06] Sabine Wurmehl et al. “Investigation of Co₂FeSi: The Heusler compound with highest Curie temperature and magnetic moment”. In: *Applied physics letters* 88.3 (2006), p. 032503.
- [Xia10] Jiang Xiao et al. “Theory of magnon-driven spin Seebeck effect”. In: *Physical Review B* 81.21 (2010), p. 214418.
- [Yam10] S Yamada et al. “Significant growth-temperature dependence of ferromagnetic properties for Co₂FeSi/Si (111) prepared by low-temperature molecular beam epitaxy”. In: *Applied Physics Letters* 96.8 (2010), p. 082511.
- [Yas10] Miho Yasaka. “X-ray thin-film measurement techniques”. In: *Rigaku J* 26.2 (2010), pp. 1–9.
- [Ye13] Jun Ye et al. “Determination of magnetic anisotropy constants in Fe ultrathin film on vicinal Si (111) by anisotropic magnetoresistance”. In: *Scientific Reports* 3.1 (2013), pp. 1–6.
- [YF02] ZG Yu and ME Flatté. “Spin diffusion and injection in semiconductor structures: Electric field effects”. In: *Physical Review B* 66.23 (2002), p. 235302.
- [YH18] Fengyuan Yang and P Chris Hammel. “FMR-driven spin pumping in Y₃Fe₅O₁₂-based structures”. In: *Journal of Physics D: Applied Physics* 51.25 (2018), p. 253001.
- [Yil07] Resul Yilgin et al. “Anisotropic intrinsic damping constant of epitaxial Co₂MnSi Heusler alloy films”. In: *Japanese journal of applied physics* 46.3L (2007), p. L205.
- [Yua04] Shinji Yuasa et al. “Giant room-temperature magnetoresistance in single-crystal Fe/MgO/Fe magnetic tunnel junctions”. In: *Nature materials* 3.12 (2004), pp. 868–871.
- [YWC13] FJ Yang, C Wei, and XQ Chen. “Half-metallicity and anisotropic magnetoresistance of epitaxial Co₂FeSi Heusler films”. In: *Applied Physics Letters* 102.17 (2013), p. 172403.
- [Zan10] M Zander et al. “Epitaxial Heusler alloy Co₂FeSi films on Si (1 1 1) substrates grown by molecular beam epitaxy”. In: *Journal of Physics D: Applied Physics* 43.30 (2010), p. 305004.
- [Zhu01] HJ Zhu et al. “Room-temperature spin injection from Fe into GaAs”. In: *Physical Review Letters* 87.1 (2001), p. 016601.

- [ZW74a] K.R.A. Ziebeck and P.J. Webster. “A neutron diffraction and magnetization study of Heusler alloys containing Co and Zr, Hf, V or Nb”. In: *Journal of Physics and Chemistry of Solids* 35.1 (1974), pp. 1–7. ISSN: 0022-3697.
- [ZW74b] KRA Ziebeck and PJ Webster. “A neutron diffraction and magnetization study of Heusler alloys containing Co and Zr, Hf, V or Nb”. In: *Journal of Physics and Chemistry of Solids* 35.1 (1974), pp. 1–7.